Department of Physics
University of Fribourg (Switzerland)

Institut für Physik
Johannes Gutenberg Universität Mainz (Germany)

An accurate combined ^{3}He/Cs magnetometer with fT sensitivity for the nEDM experiment at PSI

THESIS

presented to the Faculties of Science of the

University of Fribourg (Switzerland)
and the
Johannes Gutenberg Universität Mainz (Germany)

in consideration for the award of the academic grade of *Doctor rerum naturalium*

by

Hans-Christian Koch

from

Munich (Germany)

2015

Accepted by the Faculty of Science of the University of Fribourg (Switzerland) and the Department of Physics of the University of Mainz (Germany) upon the recommendations of

Names removed in accordance with the regulations for the protection of privacy

Defended, 15 October 2015, Mainz

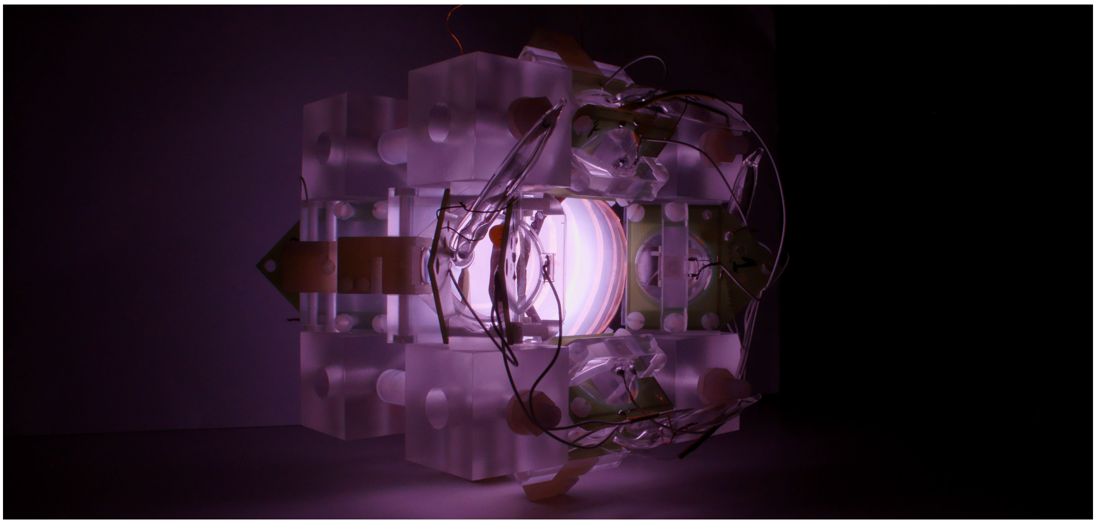

Abstract

This work describes the development, construction and examination of a magnetometer for the accurate and precise measurement of weak magnetic fields. The magnetometer is envisioned to be used in high precision fundamental physics experiments, e.g., the search for the electric dipole moment of the neutron. The device is based on the simultaneous detection of the free spin precession of nuclear polarized ^{3}He gas by multiple optically pumped Cesium magnetometers. It is shown that Cesium magnetometers provide a reliable and versatile way of measuring the ^{3}He Larmor frequency and a convenient alternative to the use of superconducting quantum interference devices for this purpose. A prototype magnetometer was built and it's performance investigated at the magnetically shielded room of Physikalisch-Technische Bundesanstalt. The sensitivity of the magnetometer as a function of the measurement time is experimentally investigated and it is proven that the device performs Cramér-Rao lower bound limited field measurements on short timescales ($< 500\,\mathrm{s}$) while the sensitivity becomes limited by the stability of the applied magnetic field for longer times. Measurements of a $\sim 1\,\mu\mathrm{T}$ magnetic field with a relative precision of better than 5×10^{-8} in 100 s integration time are presented. It is shown that the sensitivity of the device can be scaled by the number of applied Cesium magnetometers to virtually any desired value. A gradiometric measurement technique is demonstrated which allows to suppress periodic magnetic perturbations. The dependence of the combined magnetometer's sensitivity on the parameters of operation of the Cesium magnetometers used for readout is theoretically studied and application-specific merits and drawbacks of different modes of operation are discussed. A semi-empirical formula is derived that allows to predict the achievable sensitivity of the combined magnetometer and is found to be in excellent agreement with the experimental results. The ultimate intrinsic sensitivity of the magnetometer is estimated using this formula and implications for the second generation neutron electric dipole moment experiment at Paul Scherrer Institute are discussed. An experimental method for measuring the degree of polarization and Rabi-flipping angle of the ^{3}He spin polarization is also presented which is important for the application in high precision experiments.

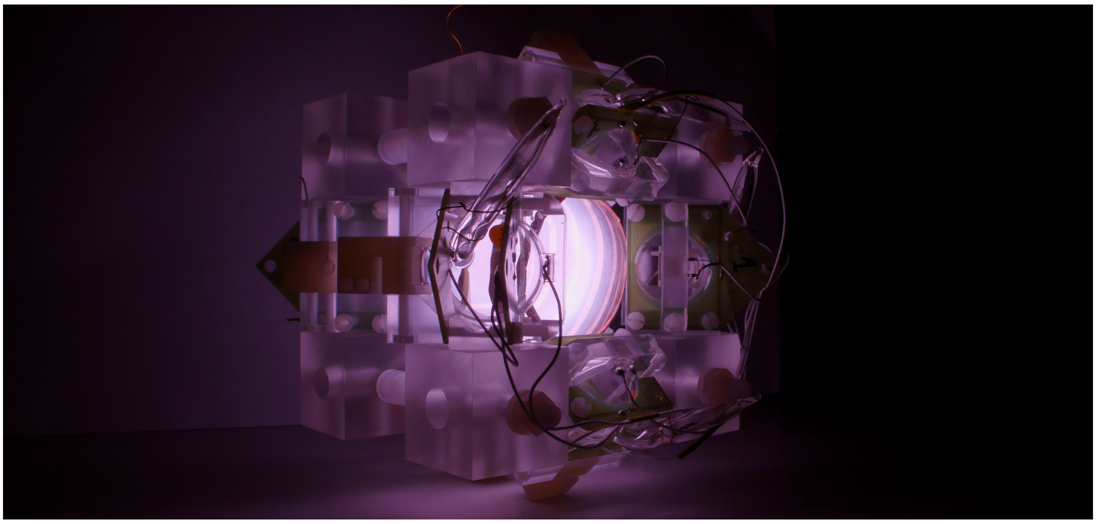

Zusammenfassung

Diese Arbeit beschreibt die Entwicklung, Konstruktion und Untersuchung eines Magnetometers zur exakten und präzisen Messung schwacher Magnetfelder. Diese Art von Magnetometer eignet sich zur Anwendung in physikalischen hochpräzisions Experimenten wie zum Beispiel der Suche nach dem elektrischen Dipolmoment des Neutrons. Die Messmethode beruht auf der gleichzeitigen Detektion der freien Spin Präzession Kern-Spin polarisierten ^{3}He Gases durch mehrere optisch gepumpte Cäsium Magnetometer. Es wird gezeigt, dass Cäsium Magnetometer eine zuverlässige und vielseitige Methode zur Messung der ^{3}He Larmor Frequenz und eine komfortable Alternative zur Benutzung von SQUIDs für diesen Zweck darstellen. Ein Prototyp dieses Magnetometers wurde gebaut und seine Funktion in der magnetisch abgeschirmten Messkabine der Physikalisch Technischen Bundesanstalt untersucht. Die Sensitivität des Magnetometers in Abhängigkeit von der Messdauer wurde experimentell untersucht. Es wird gezeigt, dass für kurze Messperioden ($< 500\,$s) Cramér-Rao limitierte Messungen möglich sind während die Sensitivität bei längeren Messungen durch die Stabilität des angelegten Magnetfeldes limitiert ist. Messungen eines $\sim 1\,\mu$T Magnetfeldes mit einer relativen Genauigkeit von besser als 5×10^{-8} in $100\,$s werden präsentiert. Es wird gezeigt, dass die Messgenauigkeit des Magnetometers durch die Zahl der zur Detektion der ^{3}He Spin Präzession eingesetzten Cäsium Magnetometer skaliert werden kann. Prinzipiell ist dadurch eine Anpassung der Messgenauigkeit an jegliche experimentellen Bedürfnisse möglich. Es wird eine gradiometrische Messmethode vorgestellt, die es erlaubt den Einfluss periodischer magnetischer Störungen auf die Messung zu unterdrücken. Der Zusammenhang zwischen der Sensitivität des kombinierten Magnetometers und den Betriebsparametern der Cäsium Magnetometer die zur Spin Detektion verwendet werden wird theoretisch untersucht und anwendungsspezifische Vor- und Nachteile verschiedener Betriebsarten werden diskutiert. Diese Zusammenhänge werden in einer Formel zusammengefasst die es erlaubt, die erwartete Sensitivität des Magnetometers zu berechnen. Diese Vorhersagen befinden sich in perfekter Übereinstimmung mit den experimentellen Daten. Die intrinsische Sensitivität des Magnetometers Prototyps wird auf Basis dieser Formel theoretisch bestimmt. Ausserdem wird die erwartete Sensitivität für die Anwendung im Rahmen des Experiments der nächsten Generation zur Bestimmung des elektrischen Dipolmoments des Neutrons am Paul Scherrer Institut abgeschätzt. Des weiteren wird eine bequeme experimentelle Methode zur Messung des Polarisationsgrades und des Rabi Flip-Winkels der ^{3}He Kernspin Polarisation vorgestellt. Letztere Messung ist sehr wichtig für die Anwendung in hochpräzisions Experimenten.

Contents

Part I

Motivation and theoretical background

Chapter 1

The search for the neutron electric dipole moment

One of the big challenges that today's fundamental research is confronted with is the quest for the processes underlying the formation and properties of the universe we inhabit. According to the standard model of cosmology, the universe emerged from the Big Bang, an event in which equal amounts of matter and anti-matter have been created. In the evolution of the early universe particles and their corresponding anti-particles should have annihilated and we should basically be left with radiation only. Nevertheless, and in strong contrast to this prediction, we live in a matter abundant universe, while failing to observe the respective amount of anti-matter. The development of this imbalance between matter and anti-matter, the so called baryon asymmetry of the universe (BAU), can only be explained assuming certain symmetry violating processes. The existence of a permanent electric dipole moment of the neutron (nEDM) would violate parity (P) and time reversal (T) and thus, assuming (CPT) conservation [LZ57], violate (CP). Finding an nEDM would make up for a new source of CP violation to explain the BAU. The search for the nEDM is thus closely tied to the most fundamental questions of cosmology.

1.1 The nEDM and its implications for physics

An electric dipole moment (EDM) is the electrical equivalent of a magnetic moment. In the simplest picture it can be understood as an ensemble of two opposite point charges q_+ and q_- displaced by a distance $|\vec{r}|$ leading to an EDM $\vec{d}$ of

$$\vec{d} = |q|\vec{r}, \tag{1.1}$$

with $\vec{r}$ pointing from negative to positive charge. For a spatially extended charge distribution $\rho_c(\vec{x})$ Eq. 1.1 is replaced by

$$\vec{d} = \int \rho_c(\vec{x}) d\vec{r}. \tag{1.2}$$

Assuming the co-existence of an nEDM d_n and the neutron's magnetic moment μ_n [GRL91] the interaction Hamiltonian with external magnetic $\vec{B}$ and electric fields $\vec{\mathcal{E}}$ is given by

$$H_{ext} = -\frac{\mu_\mathrm{n}}{I}\vec{I}\cdot\vec{B} - \frac{d_\mathrm{n}}{I}\vec{I}\cdot\vec{\mathcal{E}}. \tag{1.3}$$

Since the neutron is a fermion ($I = 1/2$) and, from all that we know, electrically neutral, a single quantum number $m_I = \pm 1/2$ is sufficient to describe its quantum state. This implies that a possible nEDM would have to be oriented along $\pm\vec{I}$, since otherwise an additional quantum number would be needed to fully describe the neutron's state. Fig. 1.1 shows the effect of a parity transformation (left) and time reversal transformation (right) on the neutron assuming an nEDM $\vec{d}_\mathrm{n}$ initially aligned with $\vec{I}$. Under the parity operation, the nEDM is inverted, $\vec{d}_\mathrm{n} \rightarrow -\vec{d}_\mathrm{n}$ while the spin $\vec{I}$ is invariant. Time reversal has the opposite effect, inverting the spin $\vec{I} \rightarrow -\vec{I}$ while leaving $\vec{d}_\mathrm{n}$ unchanged. The neutrons emerging state under both, the (T) and (P) operation, is thus different from the initial state, demonstrating the parity and time-reversal symmetry violation.

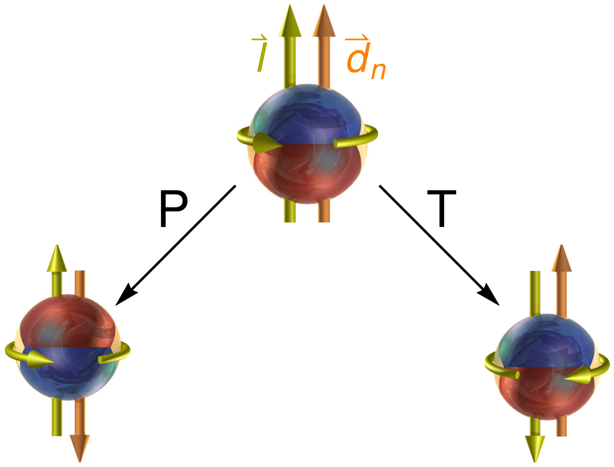

FIGURE 1.1: Violation of parity (P) and time reversal symmetry (T) of the neutron assuming the existence of an nEDM.

As stated in the introduction, the BAU continues to strongly puzzle cosmologists. The imbalance between matter and anti-matter can be quantified in terms of the baryon to photon ratio. Recent measurements of the cosmic microwave background by the WMAP[1] mission [KSD+11] have yielded a value of

$$\eta_{\mathrm{asym}} = \frac{\eta_{\mathrm{baryon}}}{\eta_{\gamma}} = 6.15(15) \times 10^{-10}. \tag{1.4}$$

In 1967, A.D.Sakharov formulated three criteria that would have to be fulfilled in order for such an imbalance to occur [Sak67], viz.,

- a violation of the baryon number symmetry (B),
- a violation of both, the charge conjugation symmetry (C) and the combined symmetry of charge conjugation and parity (CP),
- thermal inequilibrium.

The standard model of particle physics (SM) introduces two sources of CP violation through the complex phase of the CKM-matrix[KM73] and the θ-term of the strong interaction in quantum chromodynamics[JR76]. The problem is that the predicted amount of CP-violation arising from these processes is far too low to explain the BAU. Within the SM one expects a baryon asymmetry of only $\eta_{\mathrm{asym}} \approx 10^{-18}$ [RT99], which is roughly nine orders of magnitude below the measured value of Eq. (1.4). On the other hand, the smallness of the nEDM implies a tuning of the θ parameter mentioned above to very small values [PR05]. This fact is known as the strong CP problem and it remains unexplained why the parameter is so small. The magnitude of the nEDM predicted by the SM is $\sim 3 \times 10^{-32}\,\mathrm{e \cdot cm}$[GLYO+84]. An experimental observation of an nEDM larger than this value is therefore a direct proof for physics beyond the SM. Experimental constraints for the nEDM also provide tests for new theories. They can be ruled out when predicting an nEDM in the experimentally accessible range which one fails to observe.

The first measurement of the nEDM dates back to 1950 and was undertaken by Purcell and Ramsey in an effort to experimentally confirm or rule out parity conservation in the strong interaction[PR50]. The most recent and most sensitive measurement of the nEDM was done by the Sussex-Rutherford-ILL collaboration with an apparatus described below. It yielded a result of $d_{\mathrm{n}} = 0.2 \pm 1.5_{\mathrm{statistical}} \pm 0.7_{\mathrm{systematic}} \times 10^{-26}\mathrm{e \cdot cm}$ [BDG+06]. This led to currently accepted upper limit for the existence of an nEDM $d_{\mathrm{n}} < 2.9 \times 10^{-26}\,\mathrm{e \cdot cm}$ [90%C.L.].

---

[1] Wilkinson Microwave Anisotropy Probe

classification	energy range $E_{kin}(eV)$	velocity range v (m/s)
fast neutrons	$> 500 \times 10^3$	$> 10^7$
epithermal neutrons	$25 \times 10^{-3} < ... < \uparrow$	$2200 < ... < \uparrow$
thermal neutrons	$\sim 25 \times 10^{-3}$	~ 2200
cold neutrons	$0.05 \times 10^{-3} < ... < \uparrow$	$100 < ... < \uparrow$
very cold neutrons (VCN)	$360 \times 10^{-9} < ... < \uparrow$	$8 < ... < \uparrow$
ultracold neutrons (UCN)	$< 360 \times 10^{-9}$	< 8

TABLE 1.1: Classification of neutrons according to their kinetic energy.

1.2 The nEDM experiment at PSI

At Paul Scherrer Institut (PSI) in Villigen, Switzerland, an experiment is being conducted that aims at pushing the experimental limit for the existence of an nEDM. The measurements are performed using Ramsey's method of separated oscillating fields on stored ultracold neutrons (UCN) generated by a superthermal source. In this paragraph I will thus give a short introduction into the properties and production of UCN followed by a brief description of the current and future nEDM experiment at PSI. In the context of the next generation experiment, n2EDM, possible systematic errors of the measurement due to geometric phase effects will be explained. Controlling these systematics is the major motivation for the implementation of a ^{3}He/Cs magnetometer in the next stage of the experiment.

1.2.1 Ultracold neutrons

Unbound neutrons can be loosely classified according to their kinetic energy. A rough summary of the widely used classifications is given in Table. 1.1. The group with energies below $E_{kin} \leq 360\,\text{neV}$ are called ultracold neutrons (UCN). They are of particular interest to experimentalists because they can be trapped in vessels made of suitable materials or in inhomogeneous magnetic fields. This allows the construction of experiments in which measurements are conducted on stored neutrons. This type of experiments offers much longer observation times compared to beam experiments, a fact which can in many cases be exploited to yield higher measurement sensitivities.

The production of UCN usually starts with a strong source, e.g., a nuclear reactor or a spallation source that provides a high flux of thermal neutrons. Different techniques are then applied to reduce the neutrons' kinetic energy to the neV range. Conceptually one distinguishes thermal- and superthermal sources, depending on the technique of energy depletion. In a thermal source, which was historically the first approach, the neutrons are exposed to a cold moderator, e.g., liquid deuterium at $\sim 20-25\,\text{K}$. They thermalize with their environment and the resulting energy spectrum of the moderated neutrons peaks around $\sim 2\,\text{meV}$. Further cooling by thermodynamical means becomes very challenging, given that also a considerable heat load is produced by the (spallation or fission) process that generates the neutrons. However, due to Boltzmann statistics, even at this temperature a considerable amount of neutrons will be found in the neV energy range. This number can be further increased by shifting the spectrum using vertical beam extraction, where the neutrons lose energy in the Earth's gravitational field ($\sim 1\,\text{neV/m}$). Their kinetic energy can also be reduced in ballistic collisions with co-propagating surfaces, both of which processes are applied at Institut Laue Langevin (ILL) in Grenoble, France, currently hosting one of the strongest UCN sources worldwide[SNS$^+$86]. The nEDM experiment was therefore formerly installed in the UCN-experimental area of ILL.

Superthermal UCN sources, on the other hand, use a different mechanism. The neutrons are still premoderated, e.g., by liquid deuterium. In a subsequent step they are brought into contact with a suitable converter material, usually a solid deuterium crystal. The relevant process for down-conversion consists in single phonon excitations in the converter lattice. Through this highly inelastic process a neutron may deposit most of its residual energy in a single collision within the converter[GRL91]. One speaks in this context of downscattering. The counter-acting effect of up-scattering, in which a neutron withdraws energy from the converter, is less probable since the neutrons and the converter are not in thermodynamical equilibrium. This design has the potential of achieving higher UCN densities than the thermal source concept and was thus also adapted in the construction of the spallation-based UCN source at PSI. Other superthermal UCN sources have been recently built for example at Johannes Gutenberg Universität Mainz[Lau10], using a TRIGA-reactor as neutron source, and at Los Alamos National Laboratory, USA [SMB$^+$13].

1.2.2 Experimental technique

The nEDM experiment at PSI measures the precession frequency of stored UCN that are exposed to parallel $\uparrow\uparrow$ ($\xi = \hat{\mathcal{E}} \cdot \hat{B} = +1$) and anti parallel $\uparrow\downarrow$ ($\xi = \hat{\mathcal{E}} \cdot \hat{B} = -1$) electric and magnetic fields. The precession frequencies assuming perfectly aligned homogeneous fields and the existence of an nEDM can be calculated from the field interaction Hamiltonian Eq. (1.3) and are

$$\omega_{\uparrow\uparrow} = \omega_{\xi=+1} = \frac{2}{\hbar}\left|\mu_\mathrm{n} B_{\uparrow\uparrow} + d_\mathrm{n}\mathcal{E}\right| \qquad \text{and} \qquad \omega_{\uparrow\downarrow} = \omega_{\xi=-1} = \frac{2}{\hbar}\left|\mu_\mathrm{n} B_{\uparrow\downarrow} - d_\mathrm{n}\mathcal{E}\right| \tag{1.5}$$

for the two cases. For the parallel configuration the frequency is increased with respect to the magnetic Larmor frequency $\omega_{\mathrm{L,n}} = 2\mu_\mathrm{n} B/\hbar$ while for the anti-parallel case it is reduced. The existence of an nEDM would thus manifest itself in a dependence of the neutron precession frequency on the relative direction of the two fields. In comparing the results for the two cases $\Delta\omega_\mathrm{n} = \omega_{\uparrow\uparrow} - \omega_{\uparrow\downarrow} = \omega_{\xi=+1} - \omega_{\xi=-1}$ the electric contribution $\omega_{E,n} = 2d_\mathrm{n}\mathcal{E}/\hbar$ can be measured and the nEDM calculated via

$$d_\mathrm{n} = \frac{\hbar\Delta\omega_\mathrm{n}}{4\mathcal{E}}, \tag{1.6}$$

assuming that the electric and magnetic fields in the two configurations have exactly the same magnitude.

The precession frequencies are measured using Ramsey's method of separated oscillating magnetic fields [Ram49] [Ram50]. In this method the interference of a reference oscillator at ω_R with the UCNs' precession frequency $\omega_{\mathrm{L,n}}$ is observed. The basic concept is sketched in Fig. 1.2. The upper (red) curve shows the reference oscillation, the middle (blue) curve can be understood as any transverse (S_x or S_y) component of the UCN spin polarization. At the beginning of a cycle the UCN are polarized along the direction of the holding field $\hat{B}_0$. A first resonant ($\omega_\mathrm{R} \approx \omega_{\mathrm{L,n}}$) rf pulse[2] applied perpendicular to $\hat{B}_0$ during a time τ flips the spins by $\pi/2$ and and brings the two oscillations in phase. Then $\vec{B}_1(t)$ is switched off and the UCN are let to precess freely in the holding field $\vec{B}_0$ for a time T_p. Their precession frequency $\omega_{\mathrm{L,n}} = \gamma_\mathrm{n} B_0$ depends on the magnetic field and they accumulate a phase $\phi_\mathrm{n} = \omega_{\mathrm{L,n}} T_p$. The phase accumulated by the reference oscillator during this time is $\phi_\mathrm{R} = \omega_\mathrm{R} T_p$. In case $\omega_\mathrm{R} \neq \omega_{\mathrm{L,n}}$ a phase difference $\Delta\phi_{\mathrm{R,n}} = (\omega_\mathrm{R} - \omega_{\mathrm{L,n}})T_p$ will have built up between the UCN precession and the reference oscillator after the free precession time. A second rf pulse which is phase coherent to the first one is applied after the precession time T_p. If $\Delta\phi_{\mathrm{R,n}} \neq 0$ this will result in an incomplete spin-flip during the second rf interaction. In a last step the resulting flipping angle of the UCN is analyzed using a polarization sensitive neutron detector from which the phase difference can be calculated. Details of the measurement procedure and data analysis can be found in [Zen13] and will not be further described here. We still note for further reference that the anticipated sensitivity per Ramsey cycle, taking only the counting statistics as a source of error into account, is given by

$$\sigma_{d_\mathrm{n}} = \frac{\hbar}{2\alpha T_p \mathcal{E}\sqrt{N_\mathrm{n}}} \tag{1.7}$$

where N_n is the number of detected neutrons at the end of the cycle and α is the degree of polarization[3] of the UCNs after the storage [HMP$^+$00].

---

[2] The underlying mathematical description in terms of the Bloch equations is detailed in Chapter. 2.

[3] The parameter α is referred to as *visibility parameter* since it can be expressed as $\alpha = \frac{N_\mathrm{max} - N_\mathrm{min}}{N_\mathrm{max} + N_\mathrm{min}}$ where $N_{\mathrm{max,\,min}}$ are the UCN counts at the top and bottom of a Ramsey fringe.

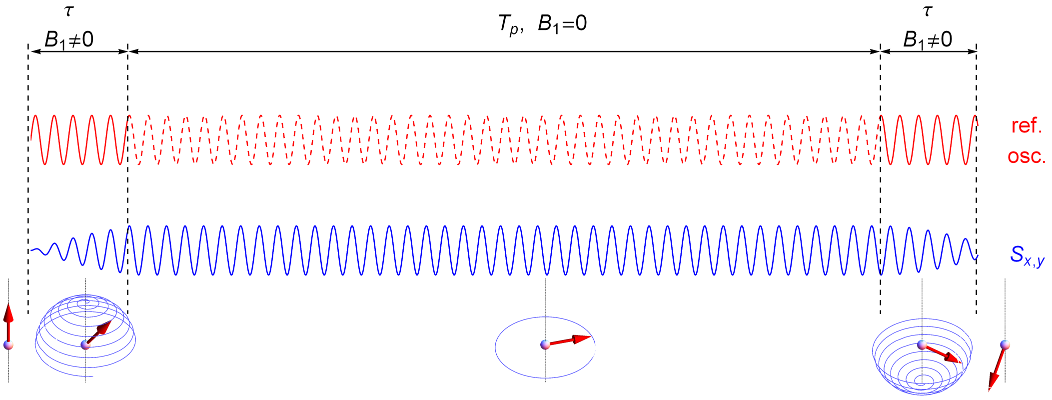

FIGURE 1.2: Ramsey's method of seperately oscillating fields. Reference oscillator (top, red), transverse component of neutron polarization (middle, blue) and visualization of neutron spin vector (bottom). The spin of the UCN is initially aligned with the magnetic field B_0. (from left to right) During a time τ an oscillating magnetic field $\vec{B}_1(t) \perp \vec{B}_0$ with frequency $\omega_\mathrm{R} \approx \omega_\mathrm{L,n}$ is applied to flip the spins by $\pi/2$. Afterwards the UCN are let to precess freely for a time T_p. At the end a second $\pi/2$ pulse is applied that is in phase to the first one. In case $\omega_\mathrm{R} \neq \omega_\mathrm{L,n}$ the spins will not be completely flipped with respect to the initial state. The deviation from a perfect π flip is proportional to $\cos\left(\Delta\phi_\mathrm{R,n}\right)$ where $\Delta\phi_\mathrm{R,n}$ is the phase difference accumulated during the time T_p. See text for more details.

For typical experimental parameters at PSI [4] the count-rate limited sensitivity Eq. (1.7) evaluates to $\sigma_{d_\mathrm{n}} = 2.6 \times 10^{-24}$ ecm.

1.2.2.1 Current nEDM experiment at PSI

A precursor version of the present nEDM apparatus was developed at ILL and operated there until 2009[5]. It was transferred to PSI because of the higher UCN density expected at the new PSI-UCN source. Since then significant upgrades have been made to the apparatus in order to yield a higher measurement sensitivity. The goal is to push the current upper limit for the nEDM from $2.9 \times 10^{-26}\,\mathrm{e \cdot cm}$[90%C.L.] measured in [BDG+06] to $5 \times 10^{-27}\,\mathrm{e \cdot cm}$[95%C.L.] which will be an improvement by almost one order of magnitude. The experiment in its current state is briefly described in the following.

The apparatus uses a single cylindrical neutron storage chamber of ~ 0.5 m diameter and ~ 0.12 m height with a vertical orientation of the rotational symmetry axis. A sketch of the apparatus is shown in Fig. 1.3. The precession chamber is installed in a vacuum tank that is enclosed by a cylindrical four layer mu-metal shield. A large $\cos(\theta)$ coil wound around the vacuum tank provides a homogeneous magnetic field of ~ $1\,\mu$T inside the apparatus. The cylinder faces of the neutron precession chamber are laid out as electrodes and a high voltage (≤ 200 kV) can be applied to the upper one to generate the electric field inside the chamber. A mechanical switch installed below the magnetic shield allows filling the chamber with UCN or emptying it into a neutron detector mounted underneath. The UCN are produced by the PSI spallation source and polarized outside before being filled into the spectrometer. The magnetic field inside the apparatus is monitored in two ways, by a ^{199}Hg co-magnetometer and an array of 16 optically pumped Cesium magnetometers (CsOPMs). The CsOPMs are compact modules developed by the Atomic Physics group of University of Fribourg (FRAP) and installed at dedicated positions directly above and below the precession chamber. These magnetometers will be described in great detail in Sec. 3.1. The measurements at their respective positions are used to monitor temporal fluctuations and assess information about the spatial dependence of the field. The spatial information is important

---

[4] 2014/2015 measurement runs: $\mathscr{E} = 1.08\,\mathrm{kV/cm}$, $T_p = 200\,\mathrm{s}$, $N_\mathrm{n} = 8 \times 10^3$, $\alpha = 0.65$.

[5] This is why it is internally referred to as oILL from *old ILL*

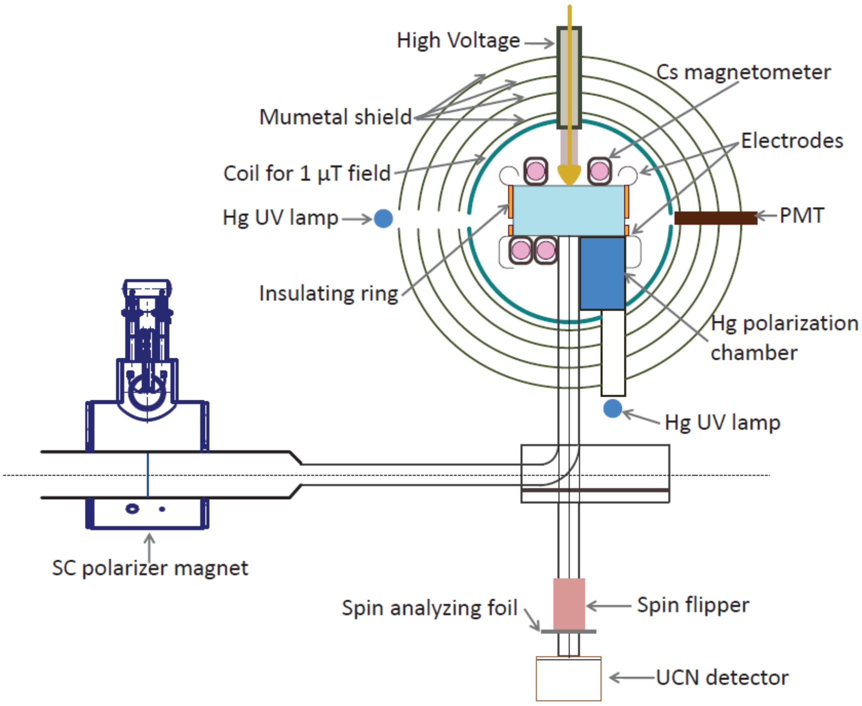

FIGURE 1.3: The current nEDM spectrometer at PSI[BBB$^+$11].

for improving the field-homogeneity inside the apparatus. This is done using several correction coils installed at certain positions. Field homogeneity is particularly important to avoid systematic measurement errors detailed later and to maintain a long coherence time of the UCN polarization. The second tool applied to control the magnetic field is a ^{199}Hg co-magnetometer that is briefly described in Sec. 3.4.2. To this aim polarized ^{199}Hg is injected into the UCN in the storage volume and simultaneously precesses with the neutrons during the measurement time. The readings of this magnetometer thus provide a volume- (and time-) averaged measurement of the magnetic field inside the precession chamber. These measurements are used to correct for changes of the neutron precession frequency caused by fluctuations of the magnetic field. The direction of the electric field can be changed by applying positive or negative high voltage to the the top electrode. A typical nEDM measurement run with the current apparatus takes typically $\sim 300\,\mathrm{s}$ and consists of the following steps.

Filling of UCN ($\sim 20\,\mathrm{s}$)

Filling of ^{199}Hg

^{199}Hg spin flip

First neutron spin flip

Free precession of both species ($\sim 200\,\mathrm{s}$)

Second neutron spin flip

Emptying and polarization sensitive detection of UCN

From Eq. (1.5) we see that precise knowledge of the magnetic fields $B_{\uparrow\uparrow}$ and $B_{\uparrow\downarrow}$ is crucial. As we can deduce from Eq. (1.6), the uncertainty of the nEDM measurement is directly connected to the uncertainty of the fre-

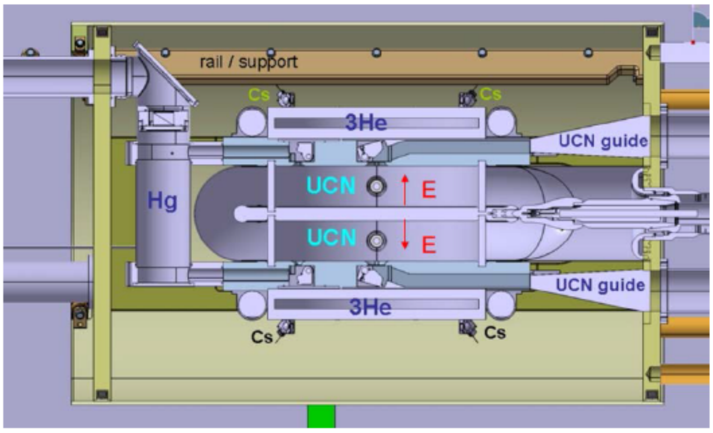

FIGURE 1.4: Preliminary design of n2EDM precession chamber.

quency measurement,

$$\sigma_{\mathrm{n}} = \frac{\hbar \sigma_{\omega}}{4\mathscr{E}}. \tag{1.8}$$

When the magnetic fields are different for the two configurations, $B_{\uparrow\uparrow} \neq B_{\uparrow\downarrow}$, for example due to a drift, this introduces an additional uncertainty of the frequency difference $\sigma_{\omega}^{B} = \gamma_{\mathrm{n}}(B_{\uparrow\uparrow} - B_{\uparrow\downarrow})$, where γ_{n} is the neutron's gyromagnetic ratio [MTN12]. In order not to deteriorate the statistical sensitivity of the measurement we have to assure that

$$\sigma_{\omega}^{B} < \sigma_{\omega}. \tag{1.9}$$

Inserting Eq. (1.8) and (1.7) into Eq. (1.9) yields an expression for the maximum acceptable statistical fluctuation of the magnetic field between two Ramsey cycles ($\uparrow\uparrow$, $\uparrow\downarrow$). One finds

$$\sigma_{B} < \frac{2}{\alpha T \sqrt{N}} \approx 0.9\,\mathrm{pT} \tag{1.10}$$

for the current typical values given in the previous section. This implies the necessity for measuring the magnetic field with a precision comparable to Eq. (1.10). This is currently achieved using the ^{199}Hg co-magnetometer briefly described in Sec. 3.4.2.

1.2.2.2 n2EDM

Currently planning is ongoing for a next generation nEDM experiment (n2EDM) at PSI. Introducing several new experimental techniques but still relying on the *room temperature in vacuum environment* concept, it is envisioned to improve the experimental limit on the nEDM by another order of magnitude to $d_{\mathrm{n}} < 5 \times 10^{-28}\,\mathrm{e \cdot cm}[95\%\mathrm{C.L.}]$. The major efforts that will be taken to improve the performance with respect to oILL are briefly outlined in the following. Special emphasis is laid on the inclusion of a ^{3}He magnetometer into the new experiment.

The details of the design are still subject of discussion but a preliminary sketch of the n2EDM spectrometer is shown in Fig. 1.4. Unlike the current experiment, the n2EDM apparatus will employ a double-chamber type of geometry which allows to measure the neutron precession frequency in $\uparrow\uparrow$ and $\uparrow\downarrow$ configuration simultaneously. This concept eliminates the errors introduced by fluctuations of the magnetic field discussed above for the current experiment. As in oILL, ^{199}Hg will be used as a co-magnetometer inside the neutron precession chambers but a laser will be employed for polarization and readout of the ^{199}Hg spin precession. This will increase the sensitivity of the co-magnetometer [Fer13].

In addition, large, flat cylindrical ^{3}He magnetometer vessels ($\sim 10\,\mathrm{l}$ each) are foreseen to be placed above and below the UCN double-chamber. The magnetometer cells will have the same cross-section as the neutron precession chamber and will thus be traversed (to a good aproximation) by the same magnetic flux. An external compact polarizer unit (ECPU) which was developed in the frame of a previous PhD thesis[Kra12] at University of Mainz provides the polarized ^{3}He gas. The ECPU works in a cyclic mode of operation on a closed gas circuit. It polarizes a sufficient quantity of ^{3}He from a reservoir to fill the magnetometer vessels at a pressure of $\sim$ 1 mbar. While the nEDM measurement is running, the next batch of ^{3}He is already prepared and held available in a storage cell. Upon request the ECPU evacuates the magnetometer cells and fills them with the freshly polarized gas. The removed batch is being cleaned by a getter and recycled into the reservoir. The ECPU is comprehensively described in a recent publication[KKD$^+$14] where also the polarization maintaining gas transfer into a magnetical shield was investigated. From the results we conclude that transfer losses can be kept negligibly small. After the gas is filled in, the ^{3}He spin polarization is initially aligned with the holding field $\vec{B}_0$ in the experiment. A resonant rf pulse is applied to flip the magnetization by $\pi/2$ and start the free precession. The spin precession of polarized ^{3}He in the magnetometer cells will be detected by CsOPMs. The detailed investigation of this detection technique is the main subject of this thesis. The measured ^{3}He Larmor frequency corresponds to the volume averaged magnetic field in the ^{3}He cells. The need for incorporating a ^{3}He magnetometer into the n2EDM apparatus is discussed in the next section.

A large number of CsOPMs will surround the whole spectrometer stack, not only for the readout of ^{3}He but also to obtain a dense grid of magnetic field measurements over the whole experimental volume. In addition to the standard rf-driven scalar CsOPMs, other types of CsOPMs are being developed that can yield information about the vector components of the magnetic field [ABB$^+$15c] or have less sources of systematic errors [GKBW15] (see Sec. 3.1). An improved magnetic shielding and a new B_0-coil-system will provide an even more stable and homogeneous magnetic environment for the experiment. New developments are also being made in improving polarization-sensitive UCN detectors [ABB$^+$15b] and the performance of the UCN source is constantly being improved and optimized. This will lead to better neutron counting statistics which will directly affect the sensitivity of the nEDM measurement, as can be seen from Eq. (1.7).

1.2.2.3 Significance of ^{3}He magnetometry for n2EDM

As mentioned above, the double chamber design of n2EDM will make the experiment insensitive against drifts of the magnetic field since measurements in the $\uparrow\uparrow$ and $\uparrow\downarrow$ configurations are performed simultaneously. Transverse components of the magnetic field however represent a source of systematic errors that has to be carefully controlled when aiming for high precision nEDM measurements. The reason lies in the so called geometric phase effects that occur for neutral particles with a magnetic moment that move and precess in a magnetic field with transverse components. A shift of the ensemble averaged Larmor frequency, referred to as Ramsey-Bloch-Siegert shift (RBS), is predicted[Ram55], the magnitude of which is given by

$$\Delta\omega_{RBS} = \sqrt{(\omega_0 - \omega_\mathrm{r})^2 + \omega_\mathrm{xy}^2} - (\omega_0 - \omega_\mathrm{r}) \approx \frac{\omega_\mathrm{xy}^2}{2\,(\omega_0 - \omega_\mathrm{r})}\,. \tag{1.11}$$

Here, $\omega_0 = -\gamma B_\mathrm{0z}$ denotes the unperturbed Larmor frequency of the particle precessing in a homogeneous magnetic field $\vec{B}_\mathrm{0z} = B_\mathrm{0z}\hat{z}$ and $\omega_\mathrm{xy} = -\gamma B_\mathrm{xy}$ is the Larmor frequency associated with a transverse component of the field rotating at frequency ω_r in the $\left(\hat{x}, \hat{y}\right)$ plane. The transverse components B_xy may have different origins two of which are discussed in this context. Since *physical* magnetic fields (in the absence of sources) have to obey the homogeneous Maxwell equation $\vec{\nabla}\cdot\vec{B} = 0$, the existence of a longitudinal gradient $\partial B_\mathrm{0z}/\partial z \neq 0$ will inevitably give rise to such transverse components. Considering an axially-symmetric case with respect to $\hat{z}$ they can be identified as

$$\vec{B}_{0xy} = -\frac{\partial B_\mathrm{0z}}{\partial z}\frac{\vec{r}}{2}\,. \tag{1.12}$$

A second source of transverse field components arises for particles moving at velocity $\vec{v}$ perpendicular to a homogeneous electric field $\vec{\mathscr{E}}$. By virtue of Lorentz transformations it can be shown that the particle will experience an effective magnetic field

$$\vec{B}_v = \frac{\vec{\mathscr{E}} \times \vec{v}}{c^2} \tag{1.13}$$

in its rest-frame. The geometric phase effects arising from $\vec{B}_{0xy}$ and $\vec{B}_v$ and their significance for EDM measurements are comprehensively discussed in [PHS$^+$04]. It is shown there, that for a trap with circular cross-section of radius R_{trap} in the $(\hat{x},\hat{y})$ plane particles can be considered exhibiting equilibrium motion on near-spherical orbits. In general both orbits with opposite senses of rotation will be equally populated and the trapped particles will experience a transverse magnetic field rotating at $|\omega_r| \approx |v_{\text{xy}}|/R_{\text{trap}}$ where $|v_{\text{xy}}|$ is the particle's transverse velocity component. Re-examining the numerator of Eq. (1.11), one finds three terms

$$\omega_{\text{xy}}^2 = \gamma^2 \vec{B}_{\text{xy}}^2 = \gamma^2 \left(\vec{B}_{0xy} + \vec{B}_v\right)^2 \tag{1.14}$$

$$= \left(\frac{\partial B_{0\text{z}}}{\partial z}\frac{\vec{r}}{2}\right)^2 + \left(\frac{\vec{\mathscr{E}} \times \vec{v}}{c^2}\right)^2 - \frac{\partial B_{0\text{z}}}{\partial z}\vec{r} \cdot \frac{\vec{\mathscr{E}} \times \vec{v}}{c^2} \tag{1.15}$$

that contribute to the RBS. The last term in Eq. (1.15) is the most relevant one in the context of EDM measurements because it is linear in $\vec{\mathscr{E}}$. It can thus produce a frequency shift correlated to the relative direction of $\vec{\mathscr{E}}$ and $\vec{B}_{0\text{z}}$ which will be falsely interpreted as an EDM signal d_{f}. The considerations presented so far equally hold for the UCN in the nEDM precession chamber and for the ^{199}Hg atoms of the co-magnetometer. However, the two species fall in different regimes that are distinguished by the ratio $|\omega_{\text{r}}|/|\omega_0| < 1$ for the UCN and $|\omega_{\text{r}}|/|\omega_0| > 1$ for ^{199}Hg and ^{3}He respectively. For both cases the geometric phase induced false EDM effect can be calculated, according to[PHS$^+$04] one finds

$$d_{\text{f}}^{(\text{n})} = -1.1 \times 10^{-27}\,\text{e}\cdot\text{cm} \qquad \text{for the UCN and} \tag{1.16}$$

$$d_{\text{f}}^{(\text{Hg})} = 1.3 \times 10^{-26}\,\text{e}\cdot\text{cm} \qquad \text{for the } ^{199}\text{Hg}. \tag{1.17}$$

This calculation assumes a realistic magnetic field gradient of $\partial B_{0\text{z}}/\partial z = 1\,\text{nT/m}$ and a UCN spectrum with $v_{\max} = 4.1\,\text{m/s}$. When, as in oILL, the ^{199}Hg Larmor frequency is used to normalize the UCN precession frequency, the (much larger) false EDM of the mercury is transferred to the neutron data which produces an even larger false nEDM

$$d_{\text{f}}^{\text{Hg}\to\text{n}} = \frac{|\gamma_{\text{n}}|}{|\gamma_{\text{Hg}}|} d_{\text{f}}^{\text{Hg}} = 5 \times 10^{-26}\,\text{e}\cdot\text{cm}. \tag{1.18}$$

Recent measurements at oILL dedicated to the investigation of geometric phase induced false EDM effects confirm these results [ABB$^+$15a]. From Eq. (1.18) it becomes clear how crucial the precise knowledge and control of the magnetic field gradients inside the apparatus is when opting for nEDM measurements beyond the $10^{-27}\,\text{e}\cdot\text{cm}$ precision. As stated in [PHS$^+$04], it is the volume averaged gradient $\langle \partial B_{0\text{z}}/\partial z \rangle$ which is of importance in this context.

The pancake-magnetometer design introduced above provides an elegant method to measure this gradient. The precession frequency from each ^{3}He magnetometer cell corresponds to the volume averaged magnetic field inside the vessel and since they cover essentially the same magnetic flux as the neutron precession chamber $\langle \partial B_{0\text{z}}/\partial z \rangle$ can be readily calculated. Because the ^{3}He cells are located outside the strong electric field they will not be prone to the geometric phase effects related to the electric field. As will be detailed in Sec. 3.2.3 the decay time of ^{3}He is very sensitive to the total magnetic field gradient, its measurement represents a convenient tool to experimentally optimize the field homogeneity. Furthermore the shift of the ^{3}He atoms' ensemble-averaged precession frequency caused by the (pressure-dependent) field averaging of the ^{3}He atoms (compare Sec.3.3) in the presence of magnetic gradients can potentially be exploited. Since the ECPU will provide the unique possibility to fill polarized ^{3}He gas at different pressures into the magnetometer cells, this effect could possibly open a way towards a direct measurement of the transverse magnetic field gradients, as one can see from Eq. (3.41).

Chapter 2

Spin dynamics

This thesis deals to a large extent with the interaction of spin-1/2 particles with external magnetic fields. This section is therefore devoted to reviewing the basic concepts and formalisms describing this interplay. We will introduce the Bloch vector and density matrix description that parametrize the polarization of an ensemble of angular momentum carrying atoms. The time evolution of spin-1/2 systems under the influence of magnetic fields will be described in terms of the suprisingly simple Bloch equation. These formalisms will be used to describe the behavior of polarized ^{3}He in the magnetic field and allow us to theoretically model the signals of the CsOPMs in later chapters. The introduction presented here is strongly inspired by a comprehensive discussion of the subject that can be found in the scriptum to a lecture of Prof. A. Weis[Wei07].

2.1 The Bloch equations

An atom can carry different types of angular momentum caused by its electronic and nuclear angular momentum configuration determined by the electronic (spin) angular momentum $\vec{S}$, the electronic orbital momentum $\vec{L}$ and the nuclear (spin) angular momentum $\vec{I}$. A magnetic moment is associated with each angular momentum via

$$\vec{\mu}_{\mathcal{O}} = \pm \frac{g_{\mathcal{O}} \mu_{\mathrm{B}}}{\hbar} \vec{\mathcal{O}}, \tag{2.1}$$

where $\mathcal{O}$ is the type of angular momentum ($\vec{L}$, $\vec{S}$, $\vec{I}$ or $\vec{F}$) and $g_{\mathcal{O}}$ the corresponding Landé factor. The g factor measures the ratio between the magnetic moment expressed in units of the Bohr magneton μ_{B}[1] and the angular momentum measured in units of $\hbar$ for the specific type of angular momentum. From Eq. (2.1) we see, that the magnetic moment is always parallel or anti-parallel to the direction of the angular momentum. In general the total angular momentum $\vec{F}$ of the atom will be the sum of the electronic and nuclear contributions

$$\vec{F} = \vec{L} + \vec{S} + \vec{I} = \vec{J} + \vec{I}. \tag{2.2}$$

A relation equivalent to Eq. 2.1 holds for $\vec{\mu}_{\mathrm{F}}$.

A quantum mechanical spin 1/2 particle such as the neutron or the ^{3}He atom in a magnetic field is a particular case. It represents a two level system since its basis only consists of two eigenfunctions that may be labeled $|a\rangle$ and $|b\rangle$. When the quantization axis is chosen as the direction of the applied magnetic field $\vec{B} = (0, 0, B_z)$ they identify the sign of the spin's projection onto $\vec{B}$. A single atom always exists in a pure state, meaning a coherent superposition of its energy eigenstates. One can thus always expand the state vector in that basis as

$$\begin{aligned} |\psi\rangle &= a|a\rangle + b|b\rangle \\ &= |a|\,|a\rangle + |b|e^{i\delta\phi}|b\rangle \end{aligned} \tag{2.3}$$

---

[1] The Bohr magneton is defined as a positive number in this notation, $\mu_{\mathrm{B}} = \frac{|q_{e^-}|\hbar}{2m_e}$. The sign in Eq. 2.1 depends on the charge of the particle, e.g. (-) for an electron and (+) for a proton. For the neutron the sign is also (-).

Here a and b are the complex amplitudes, e.g., the (square root of the) probabilities that a measurement will find the particle in the state $|a\rangle$ or $|b\rangle$, respectively. In the second line of Eq. (2.3) the complex amplitudes are expressed in terms of their magnitude and phase and it was taken into account that one can only ascribe a relative phase $e^{i\delta\phi}$ to the two components. Taking the normalization condition $|a|^2 + |b|^2 = 1$ into account, only two real parameters are thus needed to parametrize the polarization. Unlike for $F > 1/2$, the polarization of a spin 1/2 particle can be expressed as a vector in real three-dimensional space, the so called Bloch vector $\vec{\mathscr{S}}$. The requirement that the wave function is normalized to 1 is equivalent to the statement that the single particle is in a pure state and implies that the Bloch vector is also normalized to 1. The Bloch vector can then be identified with the (normalized) quantum mechanical expectation value of the particle's spin operator

$$\vec{\mathscr{S}} = \begin{pmatrix} \mathscr{S}_x \\ \mathscr{S}_y \\ \mathscr{S}_z \end{pmatrix} = \begin{pmatrix} 2\Re(a^* b) \\ 2\Im(a^* b) \\ |b|^2 - |a|^2 \end{pmatrix} = \frac{\langle \hat{\vec{F}} \rangle}{\hbar F} \tag{2.4}$$

and describes a vector that lies on the surface of a sphere (the so-called Blochsphere) around the origin. The polarization can be equally well parametrized by a density operator[2] $\hat{\zeta} = |\psi\rangle\langle\psi|$. In a basis $(|\phi_i\rangle, |\phi_j\rangle)$ the matrix representation of this operator is given by $\zeta_{i,j} = \langle\phi_i|\psi\rangle\langle\psi|\phi_j\rangle$, e.g., in the basis $(|a\rangle, |b\rangle)$ we find

$$\zeta_{i,j} = \begin{pmatrix} |a|^2 & ab^* \\ a^* b & |b|^2 \end{pmatrix}. \tag{2.5}$$

The diagonal- and off-diagonal elements of the density matrix are called populations and coherences, respectively. By comparing Eq. (2.4) and Eq. (2.5) we see that the coherences are related to the $\mathscr{S}_x$ and $\mathscr{S}_y$ components while the population difference, and thus the longitudinal polarization, is reflected by $\mathscr{S}_z$. The distinction between populations and coherences depends on the chosen basis since the diagonal and off-diagonal elements can be mixed by coordinate transformations. If the density matrix is expressed in a given basis $(|\phi_i\rangle, |\phi_j\rangle)$ and the particle is in one of these states all components of the matrix, except for the population of this specific state, become zero.

The relation between the density matrix and the Bloch vector for a spin-1/2 particle can also be written

$$\zeta = \frac{1}{2}(\mathbb{1} + \vec{\sigma} \cdot \vec{\mathscr{S}}), \tag{2.6}$$

where $\vec{\sigma}$ is a vector, the components of which are the Pauli matrices.

An *ensemble* of spin 1/2 particles can in general not be described by a wave function[3]. Unlike a single particle, which is always in a pure state, the ensemble can be partially polarized, it is then an incoherent mixture (mixed state). The density matrix formalism however still works and the ensemble polarization can still be expressed in terms of a Bloch vector. However, the Bloch vector is not normalized to 1 any more ($|\vec{\mathscr{S}}| \leq 1$). The (mixed) ensemble can be divided into sub-ensembles which are each in a pure state. For the spin 1/2 particle there exist $k = 2$ such sub-ensembles, generally one has $k = 2F + 1$ sub-ensembles for a particle of spin F. The ensemble averaged density operator is then the weighted sum of the sub-ensemble's average density operators,

$$\overline{\zeta} = \sum_{\alpha=1}^{k} w_\alpha \overline{\zeta^{(\alpha)}} \tag{2.7}$$

where the weighting factor $w_\alpha = \frac{N_\alpha}{N}$ denotes the probability to find a particle in the sub-ensemble α. For each sub-ensemble the average density operator is defined as $\overline{\zeta^{(\alpha)}} = |\psi^{(\alpha)}\rangle\langle\psi^{(\alpha)}|$. We see, that an imbalance in the populations of the sub-ensembles correspond to a (partial) polarization of the ensemble.

---

[2] Note that in the literature the symbol ρ is widely used for the density operator. However we use the symbol ζ to avoid confusion with the square root power spectral noise density which will play an important role later.

[3] Except the case when all particles are in the same state, in which case the ensemble is said to be in a pure state or, equivalently, to be 100 % polarized.

When an atom that carries angular momentum is exposed to an external magnetic field $\vec{B} = (0, 0, B_{\mathrm{z}})$, the degeneracy of the Zeeman sublevels is lifted, the energy shift of a level $|F, m\rangle$ is

$$\Delta E_{\mathrm{F,m}} = -\left\langle F, m|\vec{\mu}\cdot\vec{B}|F, m\right\rangle = \frac{g_{\mathrm{F}}\mu_{\mathrm{B}}B_{\mathrm{z}}}{\hbar}\hbar m = m\hbar\omega_L = \gamma B_{\mathrm{z}}\hbar m\,, \tag{2.8}$$

where

$$\omega_L = \frac{g_{\mathrm{F}}\mu_{\mathrm{B}}}{\hbar}B_{\mathrm{z}} \tag{2.9}$$

is the Larmor frequency and $\gamma_{\mathrm{F}} = \frac{g_{\mathrm{F}}\mu_{\mathrm{B}}}{\hbar}$ is the gyromagnetic ratio. A characteristic frequency $\omega_L = \gamma B$ can thus be assigned to every spin system exposed to a magnetic field, that corresponds to the energy difference between adjacent Zeeman substates divided by $\hbar$. Classically, the magnetic field exerts a torque $\vec{\mu}\times\vec{B}$ on the magnetic moment thereby interacting with the spin as

$$\frac{d}{dt}\left(\vec{F}\right) = \dot{\vec{F}} = \vec{\mu}_{\mathrm{F}}\times\vec{B}\,. \tag{2.10}$$

This is the classical equation of motion for a magnetic moment in a magnetic field. Using Ehrenfest's Theorem, one sees that this equation of motion also holds for the Bloch vector (since it is the expectation value of a quantum mechanical operator) of a single atom and finds a set of three equations,

$$\dot{\vec{\mathscr{S}}} = \vec{\omega}\times\vec{\mathscr{S}}\,, \tag{2.11}$$

called the Bloch equations. Applying the density matrix formalism one can also show that the same equations describe the evolution of the ensemble's Bloch vector under the influence of a magnetic field.

An analytical solution for Eq. 2.11 can be found for the simple case where $|\vec{\mathscr{S}}|$ and $\vec{B}$ are constant. To illustrate this, we consider a magnetic field $\vec{B} = (0, 0, B)$ along one of the laboratory axes, $\hat{z}$, the solution of 2.11 then becomes

$$\vec{\mathscr{S}}(t) = \begin{pmatrix} c_1\cos(\mathrm{B}\gamma t) + c_2\sin(\mathrm{B}\gamma t) \\ c_1\sin(\mathrm{B}\gamma t) - c_2\cos(\mathrm{B}\gamma t) \\ c_3 \end{pmatrix}, \tag{2.12}$$

where the c_i are constants defining the initial conditions. The solutions 2.12 obviously describe the propagation of the spin initially aligned along $\vec{\mathscr{S}}(t = 0) = (c_1, c_2, c_3,)$ on a cone with half opening-angle $\arctan(\sqrt{c_1^2 + c_2^2}/c_3)$ around $\hat{z}$ at an angular velocity $\omega_L = \gamma B$, the free spin precession. The next step of complication is taking build-up and relaxation of the spin polarization into account, meaning $\frac{d}{dt}|\vec{\mathscr{S}}| \neq 0$. In the laboratory, polarization build-up is usually achieved by optical pumping, e.g., by irradiating the medium with resonant, circularly polarized light that transfers angular momentum to the atoms. More detailed descriptions of the optical pumping process for ^{3}He and Cs are given in Sec. 3.2.2 and 3.1.1. Relaxation describes the tendency of a polarized medium to return to its thermodynamical equilibrium state. From a conceptual point of view the relaxation processes can be classified by whether they are caused by a (temporal or spatial) inhomogeneity of the magnetic field or not. However, a rather phenomenological approach is often taken to include them into the mathematical framework of the Bloch equations. One way is by adding a relaxation term that depends on the deviation of the system from equilibrium. The relaxation is then characterized by two time constants T_1 and T_2 that describe the decay of longitudinal and transverse polarization components, each of which may comprise multiple different processes. Considering the concept of populations and coherences that was addressed above, we expect that the magnetic-field-induced contributions to the T_1 and T_2 time are interwoven, since the distinction between populations(longitudinal polarization) and coherences(transverse polarization) depends on the point of view. This was beautifully proven by different authors investigating spin relaxation in the presence of inhomogeneous static and oscillating fields [CSH88] [CWC$^+$88] [McG90] [SHD91] [AAB$^+$]. Other relaxation mechanisms include collisions with container walls and inter-atomic collisions. The different relaxation processes and their importance in the scope of the depolarization of ^{3}He are discussed in

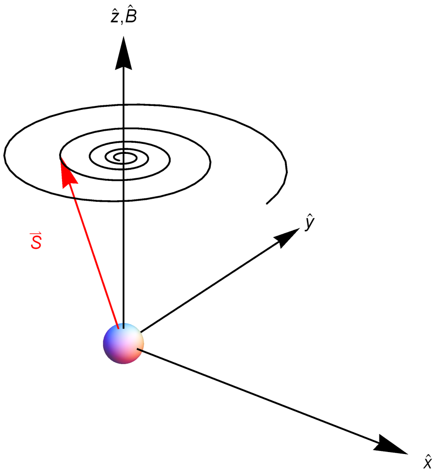

FIGURE 2.1: Decay and precession of spin polarization in an external magnetic field. The transversal component of the polarization is decaying and causes the spin vector moves inwards on the spiral eventually reaching its equilibrium value $\vec{\mathscr{S}}_{eq} = (0, 0, S_{z,eq})$.

more detail in Sec. 3.2.3. In the frame of the Bloch equations, the standard approach is to introduce a relaxation matrix

$$\Gamma_{ij} = \begin{pmatrix} \Gamma_2 & 0 & 0 \\ 0 & \Gamma_2 & 0 \\ 0 & 0 & \Gamma_1 \end{pmatrix}, \tag{2.13}$$

where Γ_1 and Γ_2 are the effective longitudinal and transverse relaxation rates, respectively. They take the intrinsic relaxation[4] rates $\gamma_{1,2}$ and the pumping rate Γ_p into account, $\Gamma_{1,2} = \gamma_{1,2} + \Gamma_p$. Including relaxation, Eq. (2.11) reads

$$\dot{\vec{\mathscr{S}}} = -\gamma \vec{B} \times \vec{\mathscr{S}} - \Gamma(\vec{\mathscr{S}} - \vec{\mathscr{S}}_{eq}), \tag{2.14}$$

where $\vec{\mathscr{S}}_{eq}$ is the equilibrium state of the system mentioned above which depends on the optical pumping rate and the decay rates.

Two special cases are worth noting to illustrate the behavior:

- When the initial polarization is aligned with $\vec{\mathscr{S}}_{eq}$ (purely longitudinal), it will decay (grow) at the effective relaxation rate Γ_1 to its equilibrium value.

- When the initial polarization has a transverse component and its longitudinal component equals the longitudinal equilibrium polarization we get precession of the spin polarization around the magnetic field at the Larmor frequency and decay at a rate Γ_2. An example for this case is given in Fig. 2.1.

The general case is a superposition of longitudinal and transverse relaxation. While Eq. (2.14) basically suffices to take account of the evolution of ^{3}He polarization in a constant magnetic field, an additional level of complexity is needed to model the signals of the CsOPMs used. There, additional oscillating magnetic fields have to be included which generally leads to a situation for which the Bloch equations can no longer be solved analytically. Still, approximative analytical solutions can be found, using the so called rotating-wave approximation

---

[4] in the absence of resonant light and oscillating fields

(RWA) that is discussed in Sec. 3.1.2. Such problems are often simplified by moving to a different coordinate frame, a technique that we will demonstrate in the next section for the simple case discussed above.

2.1.1 Larmor's theorem

For some problems the equations of motion can be more easily solved in a rotating coordinate frame. This can be understood by Larmor's theorem, from which it follows that the trajectory of a charged particle that has a velocity component perpendicular to a magnetic field will perform a circular motion around the field in the plane perpendicular to it. The inverse statement is that in a rotating coordinate system particles will follow trajectories appearing to be caused by the interaction with a static magnetic field along the rotation axis. If we choose a coordinate frame rotating around $\hat{z} = \hat{B}_0$ at angular speed $\tilde{\omega}$, the coordinate transformation is given by the rotation matrix

$$R(-\tilde{\omega}t, \hat{x})_{ij} = \begin{pmatrix} \cos(-\tilde{\omega}t) & \sin(-\tilde{\omega}t) & 0 \\ -\sin(-\tilde{\omega}t) & \cos(-\tilde{\omega}t) & 0 \\ 0 & 0 & 1 \end{pmatrix}. \tag{2.15}$$

Applying 2.15 to both sides of 2.14, after some basic algebraic manipulations, yields

$$\frac{d}{dt}\left(\vec{\mathscr{S}}'\right) = (\vec{\omega}_L - \vec{\tilde{\omega}}) \times \vec{\mathscr{S}}' - \Gamma(\vec{\mathscr{S}}' - \vec{\mathscr{S}}'_{eq}), \tag{2.16}$$

the equation of motion for the spin $\vec{\mathscr{S}}' = R\vec{\mathscr{S}}$ in the rotating coordinate frame. Here, $\vec{\tilde{\omega}} = (0, 0, -\vec{\tilde{\omega}})$ and $\vec{\omega}_L = (0, 0, \omega_L)$ denote the rotation vectors of the coordinate frame and the Larmor precession, respectively. It is apparent that in the rotating frame the spin obeys an equation of motion for a magnetic field $B' = B - \frac{\tilde{\omega}}{\gamma}$ which is reduced by the virtual field $\tilde{\omega}/\gamma$ arising from the fact that the rotating coordinate frame is not an inertial system. In the special case where $\tilde{\omega} = \omega_L$, the effective field is zero and the spin becomes static in the rotating frame. Once a solution $\vec{\mathscr{S}}'(t)$ has been found in the rotating frame, the appropriate counter-rotation has to be applied to it to get the solution $\vec{\mathscr{S}}(t) = R^{-1}\vec{\mathscr{S}}'(t)$ in the laboratory frame.

Chapter 3

Magnetometry

As introduced in Chapter 2, the time-evolution of a spin system depends of the magnetic field it is exposed to. One can make use of the proportionality between $|\vec{B}|$ and the Larmor frequency to measure the magnetic field. The choice of the spin system depends on the particular application, each species offering specific merits and drawbacks. Alkali metals are widely used because they have low optical excitation energies, typically ~ eV, which are optically accessible. Conversely, the excited energy levels in ^{3}He are not optically accessible from the ground state which results in a high inertness against external influences and a long coherence time. In this chapter different types of magnetometers which are of significance for the described work will be discussed. The focus is laid on CsOPMs and ^{3}He for obvious reasons, but three other magnetometers (^{199}Hg, SQUID, FSP-Cs) which are related in a broader context will also be addressed briefly.

3.1 Optically pumped cesium magnetometers

In this thesis, optically pumped cesium magnetometers were used to measure the ^{3}He nuclear spin precession. An array of CsOPMs is also used in the nEDM experiment to monitor the magnetic field at different positions within the apparatus. In the following sections their basic working principle will be explained and theoretical expressions for the signals they deliver will be derived. Different modes of operation and their merits and drawbacks in the frame of the ^{3}He application are discussed.

3.1.1 Optical pumping of Cs and optically detected magnetic resonance

Cesium has only one stable isotope, ^{133}Cs with a hydrogen-like electronic configuration [Xe]6s^1 in the outer shell and a nuclear spin of $I = 7/2$. Due to the hyperfine interaction, its $6S_{1/2}$ ground state (a $^2S_{1/2}$ state) splits by 9.19 GHz into two sublevels with total angular momentum quantum numbers $F = 4$ and $F = 3$. The lowest excited state is the $6P_{1/2}$ level (a $^2P_{1/2}$ state), that again splits into two sublevels with $F' = 4$ and $F' = 3$ spaced by 1.38 GHz. The $\mathrm{Cs}-\mathrm{D}_1$ line comprises all transitions between $6P_{1/2}$ and $6S_{1/2}$, the hyperfine splitting in both states is large enough to produce four resolved, Doppler broadened lines. A schematic plot of the Cs energy levels is given in Fig. 3.1. In a weak magnetic field each hyperfine level splits into $2F+1$ Zeeman sublevels, characterized by their magnetic quantum number m_F.

A magnetic field B_0 lifts the degeneracy of the Zeeman sublevels. The splitting between two adjacent Zeeman substates depends on the modulus of the magnetic field $|B_0|$ and the Landé factor g_F of the respective state. For weak magnetic fields the splitting is given by

$$\Delta E_{m_F,m_F+1} = E_{m_F} - E_{m_F+1} = \mu_B g_F |B_0|, \tag{3.1}$$

where μ_B is the Bohr magneton. In the experiments described here, the $\mathrm{Cs}-\mathrm{D}_1$ transition $6S_{1/2}$, $F = 4 \rightarrow 6P_{1/2}$, $F = 3$ was used, since it yields the largest spin polarization. A resonant, circularly (σ^+ or σ^-) polarized laser beam at $\lambda = 894.1$ nm is used to drive the transition. The photons of the beam carry an angular momentum

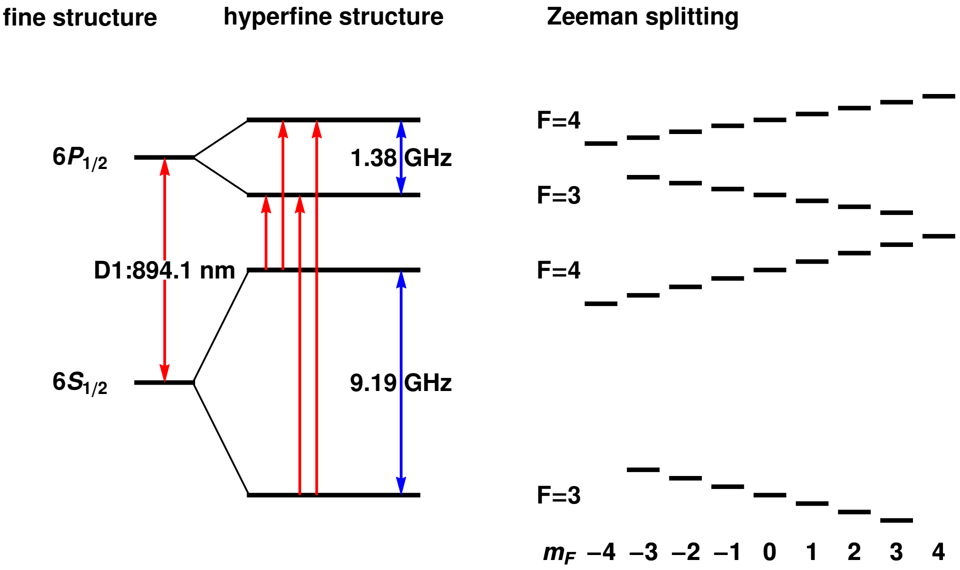

FIGURE 3.1: Energy level diagram of Cs with weak magnetic field applied. Splittings not to scale.

aligned with the $\vec{k}_{\mathrm{Cs}}$ vector of the beam. Since angular momentum has to be conserved, absorption of a circularly polarized photon transfers the atom to a Zeeman sublevel with a magnetic quantum number increased or decreased by one, $\Delta m_F = \pm 1$, depending on the light helicity. There exist three different decay channels for the relaxation of the excited $6P_{1/2}$ state, leading to possible changes of m_F by $0, -1, +1$. The probability of each channel is given by the square of the respective Clebsch-Gordan coefficient. Fluorescence photons are emitted in arbitrary directions, the probability of emission along the pump beam is thus very small and each absorption of a photon in the pumping process will thus decrease the transmitted power of the pump beam. The process of absorption and reemission of a photon is called an optical pumping cycle. Each optical pumping cycle thus changes the magnetic quantum number of the atom by $\Delta m_F = 0, 1, 2$ when considering σ^+ pumping (cf. Fig. 3.2). Thus, there is a finite probability for the atom to end up in a state with increased m_F, but no means by which m_F can be decreased during a pumping cycle. This leads to a net increase of the atom's angular momentum quantum number when going through multiple pumping cycles. The optical pumping process comes to a halt, when the atom has reached the $6S_{1/2}$, $F = 4$, $m_F = 3$ or $6S_{1/2}$, $F = 4$, $m_F = 4$ state, since there exist no $6P_{1/2}$, $F = 3$, $m_F \geq 4$ states to which the atom could be excited by a $\Delta m_F = +1$ transition. For this reason the $6S_{1/2}$, $F = 4$, $m_F = 3$ and $m_F = 4$ states are often called dark states, since no fluorescence occurs. After a short transient phase, all Cs atoms in $F = 4$ are pumped to the dark states, no absorption occurs anymore, the pump beam is virtually not attenuated by the medium. If the medium is now irradiated with a resonant rf field, meaning that the energy of the rf-photons matches the splitting between adjacent Zeeman sublevels (Eq. (3.1)), absorption or stimulated emission of an rf photon can drive transitions between these states. These rf-induced transitions bring population back from a dark Zeeman substate to a bright state and the atom then has to go through at least one pumping cycle, thus absorb at least one photon from the σ^+ pump beam, to reach the dark state again. Since only resonant rf photons are absorbed, i.e.,

$$E_{\mathrm{rf}} = \hbar\omega_{\mathrm{rf}} = \Delta E_{m_F, m_F+1}\,, \tag{3.2}$$

their frequency is a measure of $|B_0|$. The advantage of this experimental scheme is that the absorption of rf photons can be measured optically by monitoring the attenuation of the pump beam in the medium[1]. The

---

[1] In This context the process is sometimes described as a quantum amplifier. An rf photon has a very small energy $\propto \nu_{\mathrm{rf}} = 3.5\,\mathrm{kHz}$ but its absorption is correlated to the absorption of a photon that has an energy $\propto \nu_\gamma = 334\,\mathrm{THz}$. This represents an energy amplification of $\sim 10^{11}$.

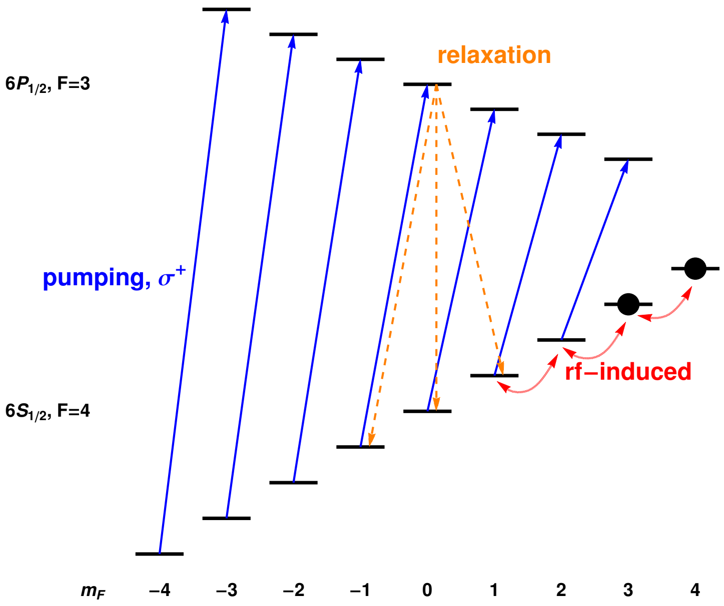

FIGURE 3.2: Close-up on the used $6S_{1/2}, F = 4 \rightarrow 6P_{1/2}, F = 3$ transition of Cs. The σ^+ pump laser drives transitions (blue) shifting the population towards higher m_F values. Relaxation (orange) can result in decrease, increase or maintaining of m_F. Resonant rf-photons drive transitions (red) between adjacent Zeeman sublevels, thereby depopulating the dark states (black disks) again. Splittings not to scale.

CsOPMs used in this study build on that optically detected magnetic resonance (ODMR) process to measure the magnetic field [GBS⁺06]. ODMR can be modeled as a three step process [BGK⁺02]:

(1) *Pumping*, angular momentum is transferred from the resonant circularly polarized light to the atoms. The medium becomes polarized.

(2) *Evolution in the dark*, the polarized atoms interact with the applied magnetic field(s) in the absence of light and acquire a phase $\sim |\omega_L t|$.

(3) *Probing*, the phase of the atoms after evolution is measured by a second interaction with a (not necessarily different) polarized resonant light beam.

In the continuously running CsOPMs described here, all three processes happen in parallel.
The gyromagnetic ratio of the $6S_{1/2}, F = 4$ state can be calculated via

$$\gamma_{\mathrm{Cs}} \equiv \gamma_F = \frac{\mu_B}{\hbar} g_F\,, \tag{3.3}$$

with

$$g_F = \frac{g_J}{2}\frac{F(F+1)+J(J+1)-I(I+1)}{F(F+1)} + \frac{g_I}{2}\frac{F(F+1)-J(J+1)+I(I+1)}{F(F+1)} \tag{3.4}$$

being the respective Landé factor. Inserting the values $g_J = 2.00254032(20)$ and $g_I = -0.00039885395(52)$ from [AIV77] yields $g_4 = 0.249968542(25)$ and finally

$$\frac{\gamma_4^{\mathrm{Cs}}}{2\pi} = 3.49862110(36)\,\frac{\mathrm{Hz}}{\mathrm{nT}}\,. \tag{3.5}$$

3.1.2 Lineshapes of M_x magnetometers

We will now derive analytical expressions for the expected signals from such a magnetometer. We assume (as always throughout this thesis) a magnetic field aligned with the z axis $\hat{z} = \hat{B}_0$. The CsOPMs are designed as M_x

magnetometers [GBS$^+$06], meaning that the $\vec{k}_{\mathrm{Cs}}$ vector of the pump light is at a 45° angle with respect to $\vec{B}_0$. For generality we assume an rf-field oscillating at an angle θ_{rf} with respect to $\hat{z}$ [2]. The described geometry of the CsOMP is shown in Fig. 3.3. To derive the expected magnetometer signal, we set up the Bloch equation

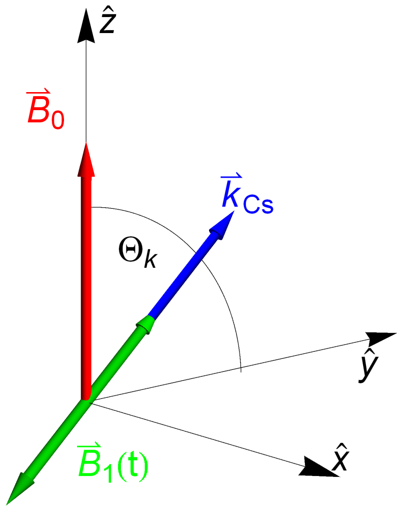

FIGURE 3.3: Geometry of modified M_x magnetometer. The magnetic field is along $\hat{z}$ (red), the $\vec{k}_{\mathrm{Cs}}$ (blue) of the laser beam and the oscillating rf field $\vec{B}_1(t)$ (green) are at an angle θ_k with respect to $\hat{z}$.

Eq. 2.14 for this problem. Therefore we decompose the oscillating field $\vec{B}_1$ in two components, one oscillating along $\hat{z}$ and one along $\hat{y}$. The component along $\hat{y}$ we again decompose into two counter-rotating fields in the $(\hat{x}, \hat{y})$-plane. The oscillating rf field thus takes the form

$$\vec{B}_1(t) = 2\sqrt{2}B_1 \begin{pmatrix} 0 \\ \sin(\omega t)\sin(\theta_k) \\ \cos(\omega t)\cos(\theta_k) \end{pmatrix} = B_z + \vec{B}_y = \vec{B}_z + \vec{B}_+ + \vec{B}_- \qquad \text{with} \tag{3.6}$$

$$\vec{B}_z = 2B_1 \begin{pmatrix} 0 \\ 0 \\ \cos(\omega t)\cos(\theta_k) \end{pmatrix}, \qquad \vec{B}_y = 2B_1 \begin{pmatrix} 0 \\ \sin(\omega t)\sin(\theta_k) \\ 0 \end{pmatrix} \qquad \text{and} \tag{3.7}$$

$$\vec{B}_+ = B_1\sin(\theta_k) \begin{pmatrix} -\sin(\omega t) \\ \cos(\omega t) \\ 0 \end{pmatrix}, \qquad \vec{B}_- = B_1\sin(\theta_k) \begin{pmatrix} \sin(\omega t) \\ \cos(\omega t) \\ 0 \end{pmatrix}. \tag{3.8}$$

Now we transform to a coordinate system rotating at angular velocity ω around $\hat{z}$. The effective field in the rotating frame is, according to Larmor's theorem that was introduced in Sec. 2.1.1,

$$\vec{B}_{eff} = \begin{pmatrix} -\omega_1\sin(\theta_k)\sin(2\omega t) \\ \omega_1\sin(\theta_k)(1+\cos(2\omega t)) \\ 1/\sqrt{2}\omega_1\cos(\omega t) + \omega_0 - \omega \end{pmatrix} 1/\gamma_{\mathrm{Cs}}. \tag{3.9}$$

Here we have made the replacements $\omega_0 = B_0\gamma_{\mathrm{Cs}}$ and $\omega_1 = B_1\gamma_{\mathrm{Cs}}$. We see that one of the counter-rotating components becomes constant in this frame, while the other rotates at -2ω. At this point we will make two approximations. First we will neglect all components rotating at -2ω, since their effects will average out for every

---

[2] In former versions of the magnetometer modules, the rf-fields were oriented at 90° with respect to $\vec{k}_C s$ and $\hat{B}_0$. In the former version this could lead to a systematic effect occurring when the $\vec{k}_{\mathrm{Cs}}$ was not exactly at 45° angle with respect to $\vec{B}_0$, the so called rf-projection phase error.

integer number of rotations, this assumption is known as the rotating wave approximation (RWA). Secondly we will neglect the oscillating component along $\hat{z}$ since it does not drive a magnetic resonance. Finally we end up with the Bloch equation in the rotating frame

$$\frac{d}{dt}\left(\vec{\mathscr{S}}'\right) = \vec{\omega}_{eff} \times \vec{\mathscr{S}}' - \Gamma(\vec{\mathscr{S}}' - \vec{\mathscr{S}}'_{\text{eq}}), \tag{3.10}$$

where the effective field in the RWA is given by

$$\omega_{eff} = \gamma_{\text{Cs}} \vec{B}_{eff} = \begin{pmatrix} 0 \\ \omega_1 \sin(\theta_k) \\ \omega_0 - \omega \end{pmatrix}. \tag{3.11}$$

The equilibrium polarization in the rotating frame is given by

$$\vec{\mathscr{S}}'_{eq} = S_0 (\hat{k} \cdot \hat{B}_0) \hat{B}_0, \tag{3.12}$$

where S_0 is a parameter that depends on the laser power. Since in the rotating frame now all remaining magnetic fields are constant we can assume that after a transient phase the spin will become static in that frame. To find this steady state solution, we set $\frac{d}{dt}\left(\vec{\mathscr{S}}'\right) = 0$ in Eq. 3.10. The remaining linear system of algebraic equations for the three spin components $\vec{\mathscr{S}}' = (u, v, w)$ can be solved analytically. In order to get the solutions in the lab frame, we apply the inverse rotation $\vec{\mathscr{S}} = R(-\omega t, \hat{z}) \vec{\mathscr{S}}'$ to the steady state solution. The time dependent signal $P_{\text{Pd}}(t)$ detected by the photodiode (PD) of the magnetometer will depend on the transmitted light-power, e.g., the absorption of the atomic medium and is proportional to the projection of the spin (in the lab frame) on the $\vec{k}_{\text{Cs}}$ of the laser beam,

$$P_{\text{Pd}}(t) = \vec{\mathscr{S}} \cdot \hat{k}. \tag{3.13}$$

Usually the (transimpedance amplified) PD signal is fed into a lockin amplifier (LIA) which is referenced at ω. The in-phase (IP) and quadrature (Q) components of the oscillating signal are given by

$$IP = \frac{\omega}{\pi} \int_0^{2\pi/\omega} P_{\text{Pd}}(t) \cos(\omega t) dt \qquad \text{and} \qquad Q = \frac{\omega}{\pi} \int_0^{2\pi/\omega} P_{\text{Pd}}(t) \sin(\omega t) dt. \tag{3.14}$$

Finally, the calculation yields, introducing the detuning $\delta\omega = \omega_0 - \omega$,

$$IP = S_0 \frac{\delta\omega}{\Gamma_2^2(\delta\omega^2 + \Gamma_1 + \frac{\omega_1^2}{\Gamma_2} \sin^2(\theta_k))} \sin^2(\theta_k) \cos(\theta_k) \omega_1 \Gamma_1 \tag{3.15}$$

and

$$Q = S_0 \frac{-1}{\Gamma_2^2(\delta\omega^2 + \Gamma_1 + \frac{\omega_1^2}{\Gamma_2} \sin^2(\theta_k))} \sin^2(\theta_k) \cos(\theta_k) \omega_1 \Gamma_1 \Gamma_2 \tag{3.16}$$

for the in-phase and quadrature component, respectively. The structure of these equations becomes a bit clearer when we set all relaxation rates equal $\Gamma_1 = \Gamma_2 = \Gamma$ and introduce the normalized detuning $x = \frac{\delta\omega}{\Gamma}$ and the rf-saturation parameter $S_{\text{rf}} = \left(\frac{\omega_1}{\Gamma}\right)^2$, yielding the simpler forms

$$IP = S_0 \frac{x}{x^2 + 1 + S_{\text{rf}} \sin^2(\theta_k)} \sin^2(\theta_k) \cos(\theta_k) \sqrt{S_{\text{rf}}} \tag{3.17}$$

and

$$Q = S_0 \frac{-1}{x^2 + 1 + S_{\text{rf}} \sin^2(\theta_k)} \sin^2(\theta_k) \cos(\theta_k) \sqrt{S_{\text{rf}}} \tag{3.18}$$

which can be clearly identified with dispersive- and absorptive Lorentzians. Instead of Eq. (3.15) and (3.16) we can also express the magnetometer signal in terms of its amplitude R and phase φ, yielding

$$R = \sqrt{IP^2 + Q^2} = \frac{S_0 \sin^2(\theta_k) \cos(\theta_k) \sqrt{\Gamma_2^2 + \delta\omega^2}\, \omega_1 \Gamma_1}{\Gamma_1(\Gamma_2^2 + \delta\omega^2) + \sin^2(\theta_k) \Gamma_2 \omega_1^2} \qquad \text{and} \tag{3.19}$$

$$\tan(\varphi) = \frac{Q}{IP} = -\frac{\Gamma_2}{\delta\omega}. \tag{3.20}$$

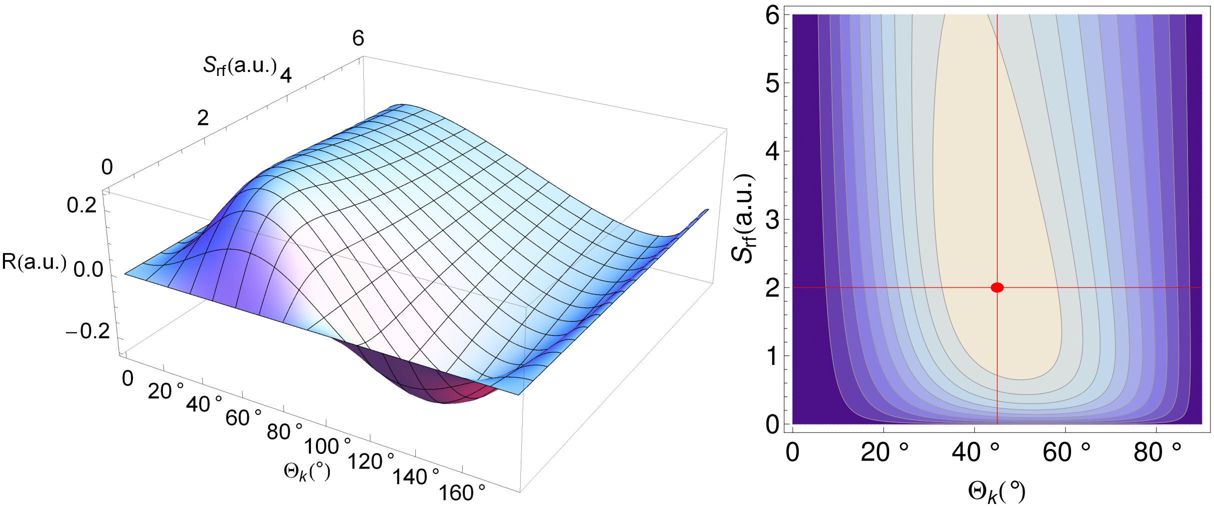

(a) (b)

FIGURE 3.4: (a) Three dimensional plot and (b) contour representation of R-signal amplitude as a function of S_{rf} and θ_k. The red dot in (b) is the point of highest amplitude at $\theta_k = \pi/4$, $S_{\mathrm{rf}} = 2$ which was chosen as the working point.

When we examine Eq. (3.19), we find that the amplitude of the R-signal on resonance ($x = 0$) depends on the rf saturation parameter and θ_k. A plot of this dependence is shown in Fig. 3.4. While the dependence on S_{rf} is rather shallow, the θ_k dependence is steep and the maximum amplitude for very low rf intensities ($S_{\mathrm{rf}} \ll 1$) is obtained at $\theta_k = 54.7356°$. For non vanishing rf powers the amplitude attains a global maximum at $\theta_k = 45°$ and $S_{\mathrm{rf}} = 2$, this working point is marked as a red dot in Fig. 3.4. Since the magnetometer is most sensitive for maximal amplitude, this is usually the preferred magnetometer geometry and was also chosen for the CsOPMs used here. When we replace $\theta_k \to 45°$ in Eq. (3.19), it takes the simpler form

$$R = \sqrt{IP^2 + Q^2} = \frac{S_0 \sqrt{S_{\mathrm{rf}}}}{2\sqrt{2}(x^2 + 1 + S_{\mathrm{rf}}/2)} \sqrt{x^2 + 1}. \tag{3.21}$$

3.1.3 Modes of operation

There are different possible ways to operate a CsOPM for continuous field measurements two of which will be described in the following. The method of choice depends mainly on the desired application. Prior to setting up a continuous measurement, a so called sweep response is recorded for each individual CsOPM to obtain the actual Larmor frequencies and linewidths of each sensor. This is done by scanning (“sweeping”) ω_{rf} over the resonance and demodulating the PD signal at the instantaneous ω_{rf}. Phase and amplitude curves of such a sweep response are shown in 3.6. These sweep responses also serve as calibration measurements for the later data analysis.

In the **fixed frequency** mode of continuous operation (FF-mode) a constant rf-frequency ω_{rf} is used to drive the CsOPMs. A connection scheme is depicted in Fig. 3.5. This frequency is chosen such that it is close to or on the magnetic resonance ($\omega_{\mathrm{L,Cs}} \sim \omega_{\mathrm{rf}}$) of the CsOPM. The CsOPM’s photodiode signal is demodulated at ω_{rf} to obtain the phase signal of the magnetometer. A change in the magnetic field B_0 results in a change of the CsOPM’s Larmor frequency and thus translates into a change of the magnetometer’s phase. When the rf frequency is close to the resonance, meaning that the detuning $\delta\omega = \omega_{\mathrm{L,Cs}} - \omega_{\mathrm{rf}}$ is small, the phase has a linear dependence on the detuning, as we see from Eq. (3.20). A prerequisite for FF-mode to be applicable is that the magnetic field B_0 is sufficiently stable, e.g., that it does not drift by more than a one linewidth equivalent field magnitude. A larger drift would result in the CsOPM being driven far off resonance which would lead to a

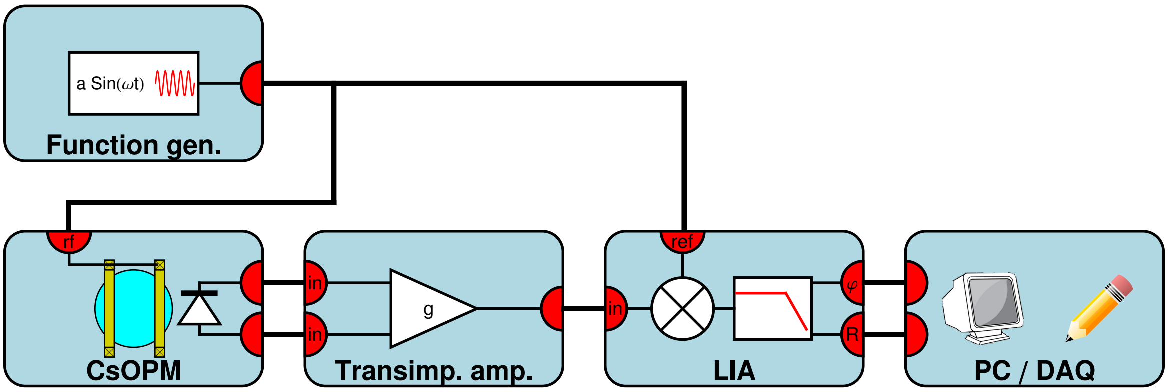

FIGURE 3.5: Electrical connection scheme for FF-mode of CsOPM operation. The function generator delivers an oscillating voltage to drive the rf-coils of the CsOPM, the same signal is also fed into the LIA as reference for demodulation. The PD signal from the CsOPM is transimpedance amplified and then passed to the LIA. The demodulated LIA signals are recorded.

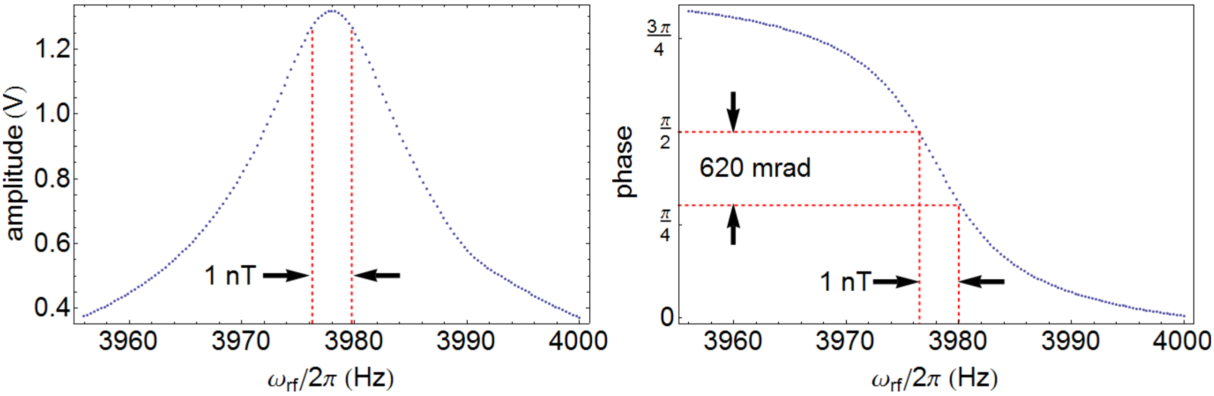

FIGURE 3.6: Amplitude (left) and phase (right) response of CsOPM when the ω_{rf} is swept over the magnetic resonance.

drastically decreased sensitivity (see Sec. 12.2.4). The FF-mode offers an easy way to measure small fluctuations of the magnetic field through the phase signal. The complication that arises with this mode of operation is that the primary measurement data is a phase signal which is not very intuitive. For further analysis, the phase signal can be rescaled to magnetic units using a technique described in Sec. 7.1. We already note here that from the fact that in FF mode the drive frequency ω_{rf} is in general not identical to the CsOPMs resonance frequency $\omega_{L,Cs}$ a bandwidth limitation of the system arises. This will be more thoroughly discussed in Sec. 4.4 where the two modes of operation are reviewed in the scope of their suitability for ^{3}He FSP readout.

In the **phase-stabilized** mode of continuous operation (PS-mode), the rf-frequency is dynamically adjusted to follow the actual Larmor frequency of the magnetometer ($\omega_{rf}(t) = \omega_{L,Cs}(t)$). This is done by demodulating the photodiode signal at the instantaneous $\omega_{rf}(t)$ and using the phase signal to drive a voltage controlled oscillator (VCO) to stabilize the phase to its on-resonance value [KBC$^+$09] by suitable frequency changes. This feedback circuit is called a phase-stabilization loop (PSL) and this mode of operation is currently used to drive the CsOPMs employed in the nEDM experiment at PSI. An appropriate phase shift is introduced by the LIA to obtain a zero crossing of the phase signal on resonance, the phase signal can then be used to drive a simple feedback loop consisting of a VCO and a PID controller. Contrary to the FF-mode, variations of the magnetic field are translated into a change of ω_{rf}, since $\omega_{rf} = \omega_{L,Cs}$. Variations of the phase signal are strongly suppressed, since the magnetometers phase is being actively stabilized by the PSL. The advantage of the PS-mode is that

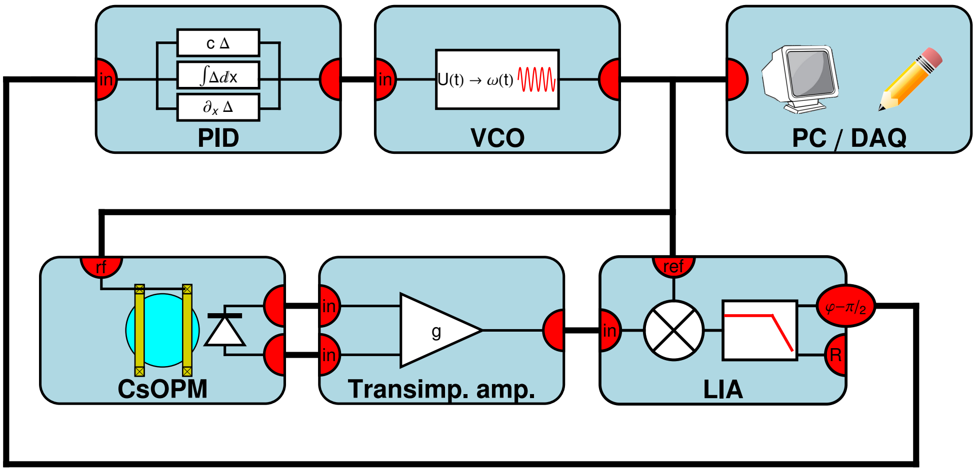

FIGURE 3.7: Electrical connection scheme for PS-mode of CsOPM operation. As before, the PD signal from the CsOPM is transimedance amplified and sent to the LIA. The phase output of the LIA is shifted by $-\pi/2$ and fed in to a PID that drives a VCO. The VCO finally is generating the oscillating voltage to drive the CsOPMs rf-coils and supplies a reference to the LIA. The rf frequency signal is recorded.

the magnetometer can track variations of the magnetic field that are much larger than the one-linewidth equivalent field magnitude without loss of sensitivity because ω_{rf} is always kept on resonance. Since the CsOPM is (ideally) always driven at its resonance frequency, the bandwidth limitation mentioned above is not present in this mode.

3.1.4 Arrays of multiple CsOPMs

When it comes to simultaneously operating an array of multiple, closely-spaced CsOPMs, it is advisable to drive them all at the same frequency ω_{rf}. This avoids one sensor being parasitically driven by the rf field of another, an effect known as crosstalk. The FF-mode can be applied for driving multiple CsOPMs, when ω_{rf} is chosen such that it is within the linewidth of all CsOPMs. This is, of course, only possible when the $\vec{B}_0$ field is sufficiently homogeneous, e.g., the local Larmor frequencies of the individual CsOPMs do not differ by more than the linewidth of the magnetic resonance ($\Gamma_2/2\pi \sim 7\,\mathrm{Hz}$). Large inhomogeneities of $\vec{B}_0$ would render it impossible to choose a common rf-frequency within the resonance linewidth of all CsOPMs. Furthermore the B_0 field and its gradients have to be sufficiently stable since its drift by more than a one-linewidth equivalent field change would result in all or some CsOPMs being driven far off resonance. In most of the measurements presented in this work, the FF-mode approach was followed for an array of eight CsOPMs belonging to the ^{3}He/Cs magnetometer. In this case, where the CsOPMs of the ^{3}He/Cs combined magnetometer are approximately spaced by 10 cm (compare Chapter. 5), this corresponds to a maximum acceptable gradient of

$$\frac{\partial B_0}{\partial x, y, z} \leq \frac{2\,\mathrm{nT}}{10\,\mathrm{cm}}. \tag{3.22}$$

3.2 ^{3}He magnetometry

In this section the processes relevant for the creation of nuclear polarization (optical pumping) and its decay (relaxation) in ^{3}He will be reviewed. These dynamics are a research topic in itself and their investigation goes beyond the scope of this thesis. Here, polarized ^{3}He was rather used as a tool to study magnetometric effects.

I will thus keep this section compact and leave the deeper study of this subject to the interested reader by the given references.

3.2.1 The ^{3}He atom

^{3}He is a stable isotope of helium with a natural abundance of 0.000137 %[Lab00]. Its nucleus only consists of two protons and one neutron, and thus it carries a nuclear spin $I = 1/2$ and a magnetic moment[PFR93]

$$\mu_{\mathrm{He}} = -1.158671471(14) \times 10^{-3} \mu_B\,, \tag{3.23}$$

with μ_B being the Bohr magneton. The magnetic moment will interact with an external magnetic field $\vec{B}_0$ in the way described in Sec. 2.1, its time evolution governed by the Bloch equations. The Larmor frequency $\omega_{\mathrm{L,He}}$ is connected to the field via the familiar relation

$$\omega_{\mathrm{L,He}} = \gamma_{\mathrm{He}} \left|\vec{B}_0\right|\,, \tag{3.24}$$

where

$$\gamma_{\mathrm{He}}/2\pi = 32.43410084(81)\,\mathrm{Hz}/\mu\mathrm{T} \tag{3.25}$$

is the ^{3}He's gyromagnetic ratio [MTN12]. In this work ^{3}He was polarized by suitable techniques described in the following and a sample cell of polarized gas was used as a magnetometric probe. Since it is the nuclear spin which is being polarized it is very secluded and will not interact with its environment except through its magnetic moment. This immunity to a number of effects that may influence electronic spin systems, such as resonant electromagnetic radiation, makes ^{3}He a probe for **absolute** magnetic field measurements. Besides its magnetic properties ^{3}He has also a very large absorption cross section for neutrons, this is why it is widely used in neutron detectors. Rising security demands have recently spurred the request for ^{3}He and prices have risen to around 1000 EUR for one liter at atmospheric pressure. To satisfy the demands, ^{3}He is commercially produced in high flux nuclear reactors. Fortunately, the amount of ^{3}He needed in the studies presented here is very small and price is not an issue in this context.

3.2.2 Optical pumping of ^{3}He

In contrast to the cesium atom, the ^{3}He nucleus can not be polarized by direct optical pumping and more elaborated schemes have to be applied. One approach is to transfer spin polarization from one species (typically an alkali vapor) that can be easily optically pumped to the ^{3}He by exchange collisions[BCV60]. This technique is referred to as spin exchange optical pumping (SEOP) and was historically the first successful approach to polarizing ^{3}He. However, with the availability of strong lasers in the infra-red range, the so-called metastable exchange optical pumping (MEOP) technique has widely become the method of choice. The application of this technique to ^{3}He was first described in [CSW63]. With the availability of high intensity lasers at the wavelength of 1083 nm, the MEOP technique has become the method of choice allowing to achieve a polarization exceeding $p = 50\,\%$ in weak magnetic fields ($B = 2\,\mathrm{mT}$) and at low pressures ($\sim 1\,\mathrm{mbar}$) [LNTC00]. The MEOP technique was also applied in the frame of this thesis. We shall therefore describe it in detail in the following.

The MEOP process is an optical pumping scheme in which a metastable state serves as a ground state. A weak gas discharge is maintained in the sample cell containing ^{3}He typically at about $\sim 1\,\mathrm{mbar}$ pressure. This discharge (highly) excites a small fraction, typically at the ppm level[Bat11] of atoms in the $1\,^1S_0$ ground state by electron-gas collisions which decay and eventually end up in the $2\,^3S_1$ state which has a long lifetime. This $2\,^3S_1$ state is called a metastable state because its radiative decay to the ground state is forbidden[3]. The lifetime is practically limited by the diffusion rate of the excited atoms to the cell walls, where collisions cause the decay [CSW63]. Typical values are $\tau \sim 1\,\mathrm{ms}$ for cells of $\sim 5\,\mathrm{cm}$ length/diameter in the mbar pressure range [Bat11]. Resonant circularly polarized light at $\lambda \approx 1083\,\mathrm{nm}$ induces transitions between the metastable $2\,^3S_1$

---

[3] The decay is possible but changes the multiplicity, therefore it is strongly hindered.

Transition	$\lambda(nm)$	rel. intensity
C_1	1083.184	0.03556
C_2	1083.166	0.37482
C_3	1083.164	2
C_4	1083.163	1.29767
C_5	1083.157	1.29767
C_6	1083.140	0.29185
C_7	1083.137	0.03556
C_8	1083.056	0.29185
C_9	1083.030	0.37482

TABLE 3.1: Transitions between the 2^3S_1 states and the 2^3P states in ^{3}He at zero magnetic field. The resonant wavelength and the relative intensity of each transition is given [CMN+02].

states and the 2^3P_J states thereby transferring angular momentum to the atoms ($\Delta m_F = +1$ in case of σ^+ light). The populations in the Zeeman-substates of each hyperfine level of the 2^3P_J states are to first order equalized during their lifetime of typically $10^{-7}s$ by collisional mixing[Sch67]. This leads to a largely isotropical decay back into the metastable 2^3S_1 state ($\Delta m_F = \pm 1, 0$). The decay itself thus does not lead to a net change of the m_F quantum number but the angular momentum transfer during absorption leads to a net electronic polarization of the metastable state. In the metastable state the hyperfine interaction couples the electronic and nuclear angular momenta. The timescale of this interaction is $\tau = 2.23 \times 10^{-10}$ s which is much shorter than the lifetime of the metastable state [RP70]. This coupling thus creates a nuclear polarization of the metastable 2^3S_1 state. When these nuclear spin polarized metastable atoms collide with ^{3}He atoms in the ground state the nuclear polarization is transferred to the ground state via

$$^3\overset{\curvearrowright}{\mathrm{He}}(2^3S_1) + {}^3\mathrm{He}(1^1S_0) \rightarrow {}^3\mathrm{He}(2^3S_1) + {}^3\overset{\curvearrowright}{\mathrm{He}}(1^1S_0)\,, \tag{3.26}$$

where $\curvearrowright$ denotes the nuclear spin polarized atom. MEOP ows its name to these metastable exchange collisions during which the electron hull is exchanged between a metastable and a ground state atom through the formation of a short lived molecule [Hap72]. Figure 3.8 shows the hyperfine structure and the Zeeman substates of the concerned levels and the possible transitions. The transitions are labeled $C_1 - C_9$ in the order of rising energies following a nomenclature introduced in [NL85]. The corresponding transition wavelengths and relative intensities are given in Table 3.1. Due to Doppler broadening (~ 2GHz[Bat11]), the lines $C_1 - C_7$ are not resolved and can therefore not be selectively driven at room temperature (c.f. Fig. 6.4). This makes them inappropriate for optical pumping, since the achievable degree of polarization is then limited to small values by the fact that optical pumping on C_1 and C_3 creates a spin polarization of opposite sign than pumping on C_2, C_4, C_5, C_6, C_7 [NL85]. Therefore, the C_8 or C_9 transitions are usually chosen, as was done in the frame of this thesis. Figure 3.9 shows a simplified picture of the pumping scheme when σ^+ light is used for optical pumping.

3.2.3 Relaxation mechanisms in ^{3}He

The nuclear polarization of a ^{3}He gas sample decays over time, a phenomenon known as relaxation which was already introduced in Sec. 2.1, where we have also seen that relaxation is governed by two different time constants, the longitudinal- and transverse relaxation times T_1 and T_2 respectively. In the following we will describe the different relaxation mechanisms in ^{3}He and quantify their significance under the given experimental conditions.

Relaxation in the gas discharge

The gas discharge necessary for optical pumping promotes ground state atoms into various, highly excited states. In case the gas is already (partially) nuclear spin polarized, also atoms in the desired nuclear-spin-

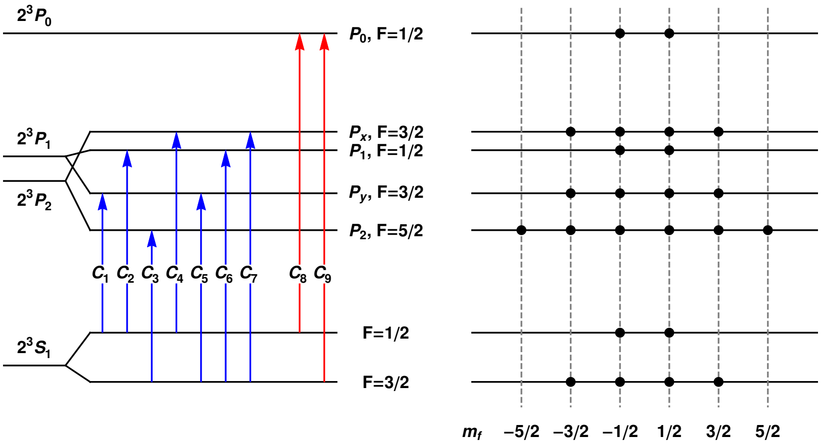

FIGURE 3.8: Left: Level diagram showing the hyperfine structure of $2\,^3S$ and $2\,^3P$ states of ^{3}He. The possible transitions are labeled according to the nomenclature introduced in [NL85]. The C_8 and C_9 transition relevant for the optical pumping process are highlighted in red. Right: Zeeman substates for each level (at $B = 0$). Splittings not to scale.

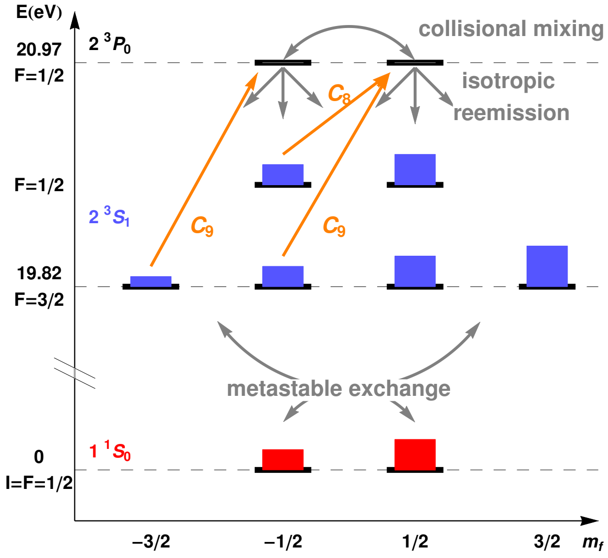

FIGURE 3.9: Optical pumping scheme of ^{3}He using σ^+ light. The C_8 and C_9 transitions are drawn. The process shifts the population in the ground state to higher m_F values thereby creating nuclear polarization. See text for details.

oriented state *parallel* to $\hat{B}_0$ will be subject to such excitations. Some of them will be transferred into states with non-zero electronic angular momentum $l \neq 0$. In these states the hyperfine interaction couples electronic and nuclear angular momentum and leads to the emission of polarized fluorescence radiation[4] in the process of de-excitation by which the nuclear spin may be flipped. This will effectively depolarize the metastable population which then depolarizes the ground state in metastability exchange collisions. The discharge itself thus counteracts the optical pumping process, the strength of the depolarizing effect depends on the intensity of the discharge. On one hand the pumping rate grows with discharge intensity due to the higher absorption, on the other hand the equilibrium polarization which can be reached becomes smaller due to the inherent depolarization mechanism[LNTC00]. Since the total pumping time was a non-critical parameter during the experiments described here, a very weak discharge was usually chosen in order to maximize the achievable polarization. In sufficiently homogeneous fields the discharge represents the strongest relaxation mechanism and limits the decay time to typically several minutes in the absence of pump light[Wol04]. Since the discharge is only needed during optical pumping, it does not impose a limitation on the lifetime of the polarization *in the dark*. The other relaxation mechanisms detailed in the following occur in the dark and need to be considered independently.

Wall relaxation

Relaxation due to wall collisions is a major polarization loss mechanism in ^{3}He. Bare or coated cells made from different types of glass are usually the recipients of choice. In the scope of this thesis an uncoated cell made from borosilicate glass was used (c.f. Sec. 5.1). Polarized ^{3}He atoms colliding with the container walls interact with ferro- or para-magnetic impurities in the wall material. Two types of interactions have to be considered, these are dipolar interactions with ferromagnetic iron contaminations and Fermi contact interactions with paramagnetic dangling bonds in the glass matrix. It was recently shown that the latter process dominates the de-polarization behavior under normal conditions and that the influence of ferromagnetic contaminants had been overestimated in the past [SHO$^+$06]. The relaxation rate $1/T^{\text{wall}}$ attributed to this effect is pressure independent but scales with the surface to volume ratio S/V of the vessel,

$$\frac{1}{T^{\text{wall}}} = \eta_r \frac{S}{V}. \tag{3.27}$$

Here, the relaxivity η_r is a material dependent parameter that quantifies the strength of the wall-collision induced depolarization effect. For standard borosilicate glass, measured relaxivities range between 0.1 – 1 h/cm[FTW69] [JDS03]. The wall relaxation affects longitudinal and transverse polarization likewise which has to be considered when estimating the achievable T_2 time.

Relaxation due to magnetic field gradients

The presence of a spatially or temporally inhomogeneous magnetic field represents a further relaxation mechanism. In a simple approach this effect can be explained by the fact that not all atoms are exposed to the same magnetic field, which leads to a relative dephasing of their precessions. Relaxation of ^{3}He in static field gradients has been studied by different authors [McG90] [CSH88][5]. Cates et al have shown that the process substantially depends on the *relative pressure* parameter,

$$\frac{\omega_{\text{L,He}} R^2_{\text{cell}}}{D} = \frac{\tau_d}{\tau_l}. \tag{3.28}$$

That is the ratio of the characteristic time $\tau_d = R^2_{\text{cell}}/D$ the atoms need to diffuse through the cell of radius R_{cell} (at diffusion constant D) and a characteristic precession time $\tau_l = 1/\omega_{\text{L,He}}$. Different situations are met

---

[4] Since the degree of polarization of the fluorescence light depends on the polarization of the ground state, this effect can be exploited to measure the nuclear polarization of the gas sample. Usually the polarization of the 668 nm radiation emitted on the $3\,^1D \rightarrow 2\,^1P_1$ transition is examined for this purpose[BNL92].

[5] Cates et al. have extended their treatment to oscillating magnetic fields in a second publication in which they beautifully demonstrate how the interplay of longitudinal and transverse relaxation can be understood in the context of the rotating frame description[CWC$^+$88].

when this parameter is $\gg 1$ or $\ll 1$, in the first case one speaks of the high pressure limit while the second case is called the low pressure regime. The first case represents a situation where the mobility of the atoms is restricted within the cell, the dynamics of the spins are mostly governed by the magnetic field at their individual position. In the second case the atoms have enough time to *sample* the whole cell volume during one Larmor precession cycle, this situation is often called motional narrowing regime[6]. In this regime the atoms' precession frequencies are rather reflecting the average magnetic field in the cell than the field at their instantaneous position. The effect of relative dephasing of the spins mentioned above is therefore not as pronounced as in the high pressure limit and this leads to an increased lifetime of the polarization. The self diffusion coefficient for ^{3}He at 1 torr $\approx$ 1.3 mbar and $T = 300\,\mathrm{K}$ was measured by Barbé et al. [BLL74] and found to be

$$D = 1440(80)\,\mathrm{cm}^2/\mathrm{s}. \tag{3.29}$$

Using this value we readily estimate that $\frac{\omega_{\mathrm{L,He}} R_{\mathrm{cell}}^2}{D} = \frac{\tau_d}{\tau_l} \approx 1.8$ in our case. We are working at the interface of both regimes, on the high pressure side rather, though, not overly pronounced. The longitudinal relaxation rate due to magnetic field gradients is[CSH88]

$$\frac{1}{T_1^{\mathrm{grad,HP}}} \approx \frac{D}{\Omega_0^2}\left(|\vec{\nabla}\Omega_{1,x}|^2 + |\vec{\nabla}\Omega_{1,y}|^2\right) \qquad \text{in the high pressure limit and} \tag{3.30}$$

$$\frac{1}{T_1^{\mathrm{grad,LP}}} \approx \frac{8R_{\mathrm{cell}}^4}{175D}\left(|\vec{\nabla}\Omega_{1,x}|^2 + |\vec{\nabla}\Omega_{1,y}|^2\right) \tag{3.31}$$

at low relative pressures. For the transverse relaxation rates Cates et al. find

$$\frac{1}{T_2^{\mathrm{grad,HP}}} \approx \frac{8R_{\mathrm{cell}}^4}{175D}\left(|\vec{\nabla}\Omega_{1,z}|^2\right) \qquad \text{in the high pressure limit and} \tag{3.32}$$

$$\frac{1}{T_2^{\mathrm{grad,LP}}} \approx \frac{1}{2T_1^{\mathrm{grad,LP}}} + \frac{1}{T_2^{\mathrm{grad,HP}}} = \frac{4R_{\mathrm{cell}}^4}{175D}\left(|\vec{\nabla}\Omega_{1,x}|^2 + |\vec{\nabla}\Omega_{1,y}|^2 + 2|\vec{\nabla}\Omega_{1,z}|^2\right) \tag{3.33}$$

in the low pressure limit. For both cases we have introduced

$$\vec{\Omega}_1 = \begin{pmatrix} \Omega_{1,x} \\ \Omega_{1,y} \\ \Omega_{1,z} \end{pmatrix} = \gamma_{\mathrm{He}} \vec{B}_1 \tag{3.34}$$

being the perturbation of the mean[7] Larmor frequency at the position $\vec{r}$ due to a local deviation of the magnetic field from its mean value $\vec{B}_1(\vec{r}) = \vec{B}(\vec{r}) - \vec{B}_0$. Gradient relaxation is an important relaxation mechanism, this explains the need to work in preferably homogeneous magnetic fields.

Relaxation by inter-atomic collisions

The ^{3}He atoms will collide with each other in the magnetometer cell. The rate of collisions depends on the gas pressure P_{He} in the cell and on the temperature T. During these collisions, angular momentum may be transferred by dipolar interaction. This process thus represents a relaxation mechanism. At room temperature ($T = 300\,\mathrm{K}$) the corresponding relaxation rate evaluates to [NBC+93]

$$\frac{1}{T_1^{\mathrm{He\text{-}He}}} \approx \frac{P_{\mathrm{He}}}{2.9 \times 10^6}, \tag{3.35}$$

where P_{He} is given in units of bar. The process is thus completely neglegible at the pressures concerned here ($P_{\mathrm{He}} \sim 1\,\mathrm{mbar}$). However, in the presence of paramagnetic atoms in the cell the effect is much stronger. In

---

[6] The nomenclature may seem misleading at first, because the *motion* of the atoms is not *narrowed* at all. The term refers to the narrowing of the spectral line corresponding to the free spin precession signal due to the increased lifetime.

[7] In this context *mean* denotes the cell-volume average, e.g., $\vec{B}_0 = \frac{1}{V}\int \vec{B}(\vec{r})dV$. Note, that $\vec{B}_1$ is assumed to have a zero mean value over the cell volume.

case of a contamination of the sample with oxygen, e.g., at a partial pressure of P_{O_2} one expects a dipolar-interaction-induced relaxation rate[SHM95]

$$\frac{1}{T_1^{\mathrm{He-O_2}}} \approx \frac{P_{O_2}}{2.5}\,. \tag{3.36}$$

This explains why considerable effort is made in order produce a very clean and pure ^{3}He sample cell. The technical steps to achieve this are detailed in Sec. 5.1, and if followed carefully, one can assume that the impurities are reduced to a level at which this relaxation mechanism plays only a negligible role under normal conditions.

The effective decay time

After reviewing the major relaxation mechanisms for ^{3}He in the previous sections, an approximative expression for the expected experimental decay rate of the ^{3}He FSP signal can be given. Under the conditions met in the frame of this thesis we expect wall-relaxation and gradient relaxation to be the dominant processes. The rate at which the FSP signal is expected to decay under these assumption is thus given by

$$\frac{1}{T_2^*} \approx \frac{1}{T_2^{\mathrm{grad}}} + \frac{1}{T^{\mathrm{wall}}} \tag{3.37}$$

where T^{wall} and T_2^{grad} are to be taken from Eqns. (3.27),(3.33) respectively.

3.2.4 Detection of ^{3}He spin precession

The concept of employing polarized ^{3}He for magnetometry is very appealing and as such not new. The same property that qualifies ^{3}He as an absolute magnetometric probe, i.e., its inertness against environmental influences except the magnetic field, represents however an experimental difficulty that has to be overcome. Unlike in alkali-atomic magnetometers, the spin precession can not be measured by optical methods[8]. Therefore many experiments rely on the detection of the rotating magnetic field produced by the precessing ^{3}He nucleus (see Sec. 4.1 for details). The use of pick-up coils is straightforward for this purpose and widespread through the literature. However, the application of this concept finds its limitations when working in weak holding fields B_0 where the precession frequency $\omega_{\mathrm{L,He}}$ is very low which reduces the strength of the magnetic induction $\propto \omega_{\mathrm{L,He}}$. We can roughly estimate the signal to noise density ratio achievable in such an experiment assuming a $n = 10$-windings pickup coil of surface area $1\,\mathrm{cm}^2$ and electrical resistance $R = 1\,\Omega$. If Johnson noise at room temperature is assumed to be the only source of the measurement noise we expect for the noise density

$$\rho_{\mathrm{Jhn}} = \sqrt{4k_B T R} \approx 130\,\mathrm{pV_{rms}}/\sqrt{\mathrm{Hz}}\,. \tag{3.38}$$

Assuming further a ^{3}He-FSP induced magnetic field oscillation amplitude of $b_{\mathrm{He}} \sim 50\,\mathrm{pT_{rms}}$[9] and a holding field of $B_0 \sim 1\,\mu\mathrm{T}$ which corresponds to a precession frequency $f_{\mathrm{He}} \approx 32\,\mathrm{Hz}$ we obtain an induced voltage signal with amplitude $\mathrm{A_{ind}}$ on the order of

$$\mathrm{A_{ind}} = n b_{\mathrm{He}} f_{\mathrm{He}} 2\pi \approx 10\,\mathrm{pV_{rms}}\,. \tag{3.39}$$

A very unfavorable situation, indeed.

For low field applications, a different solution had to be sought and more recently superconducting quantum interference devices (SQUIDs) have been very successfully employed to detect the ^{3}He FSP magnetic field [HGK+13],[GHK+10]. SQUIDs are well suited for this application due to their high sensitivity (see Sec. 3.4.3 for details) but their operation is only possible in a cryogenic environment. This restricts their use in many applications, for example in the nEDM experiment, where the integration of cryogenic infrastructure into the experimental apparatus poses a severe technical obstacle. The virtue of the approach followed in this thesis

---

[8] Except in the presence of the gas discharge.

[9] ,which is already a large amplitude, compare Sec. 4.1,

is that it opens a simple, remote way to detect the ^{3}He FSP in low magnetic fields at room temperature. The idea of using alkali magnetometers for this purpose was already brought up and impressively demonstrated by C.Cohen-Tannoudji and co-workers in 1969 [CTDRHL69]. However they applied a rubidium magnetometer and were rather interested in measuring the static magnetic field produced by the polarized ^{3}He gas. Since then, for obvious reasons, the application of optical magnetometers to detect NMR signals [LSB$^+$08] or polarization of noble gases [YGK$^+$04] has attracted growing scientific interest. For a comprehensive review of the recent developments in this field, the reader is referred to [BBDM13]. The general feasibility of employing a discharge lamp-pumped cesium magnetometer to measure the ^{3}He FSP was qualitatively shown in the context of a PhD thesis[Kra12] concerned with the construction of an automated ^{3}He polarizer system and the results were recently published [KKD$^+$14]. However the achievable magnetometric sensitivity was not investigated in that study. In the main body of this thesis the application of laser pumped cesium magnetometers as readout for the ^{3}He FSP will be described in great detail.

3.3 Systematic effects in atomic magnetometers

All magnetometers described so far, as well as the nEDM measurement proper, are based on measuring the precession frequency of an ensemble of spin-polarized particles (atoms). Different systems may rely on electronic spin, such as the CsOPMs, or nuclear spin, like in ^{3}He magnetometry, the ^{199}Hg magnetometer mentioned in Sec. 3.4.2 and the nEDM measurement. In the applications discussed here a rather large number of particles ($\sim 10^{18}$ for ^{3}He) is involved in the measurement process. These particles are confined to a measurement volume, e.g., the ^{3}He sample cell, the neutron precession chamber or the Cs magnetometer cell respectively. We have to be aware that the measured Larmor frequency will in general represent an ensemble average of all particles involved. There are certain systematic effects which influence the measured frequency. They may arise either from the properties of the magnetic field and the dynamics of the particles therein, the manipulation of the spin system in the measurement process or a combination of both. Additional effects have to be considered in the presence of other external perturbations, e.g., electric fields or magnetic field inhomogeneities. In this section a brief review of the systematic effects that are relevant for the magnetometers under study is given.

The light shift

Optical magnetometers rely on detecting the Larmor frequency by measuring the attenuation of a resonant light beam in the polarized medium. While being operationally very convenient, this technique introduces a possible systematic effect, the so called *light shift*. This frequency shift is caused by the alteration of the atomic energy levels due to the interaction with (near) resonant polarized light[Kas63]. Its magnitude depends on the the intensity, the polarization and the detuning from resonance of the light. For perfectly resonant light the effect vanishes. The light shift falls into the category of systematic effects inherent to the measurement process of optical magnetometers. The CsOPMs and the ^{199}Hg magnetometer are both potentially prone to this effect. For ^{3}He the effect does not play a role because the detection of the spin precession is not done optically so that the ^{3}He energy levels are not affected by the detection system.

Regime dependent field averaging

As was discussed in the context of the gradient-induced relaxation of ^{3}He (see Sec. 3.2.3), the evolution of the ensemble polarization depends on the dynamic regime in the sample cell. Besides the effect on the relaxation time already mentioned, a frequency shift is also predicted[CSH88] that follows the relations

$$\delta\omega_0^{\mathrm{avg,HP}} \approx \frac{R_{\mathrm{cell}}^2}{10\omega_0}\left(|\vec{\nabla}\Omega_{1,x}|^2 + |\vec{\nabla}\Omega_{1,y}|^2\right) \qquad \text{in the high pressure regime and} \tag{3.40}$$

$$\delta\omega_0^{\mathrm{avg,LP}} \approx \frac{83\omega_0 R_{\mathrm{cell}}^6}{15750 D_{\mathrm{He}}^2}\left(|\vec{\nabla}\Omega_{1,x}|^2 + |\vec{\nabla}\Omega_{1,y}|^2\right) \qquad \text{for the motional narrowing regime.} \tag{3.41}$$

Again, we have to remember that this derivation assumes a weak linear inhomogeneity with zero volume average strictly perpendicular to the homogeneous holding field. The problem traces back to the fact that the volume- (or ensemble-) averaged modulus of the magnetic field $\langle|\vec{B}(\vec{r})|\rangle$ is in general different from the modulus of the volume- (or ensemble-) averaged magnetic field $|\langle\vec{B}(\vec{r})\rangle|$. Following the considerations presented in [PHS$^+$04],[CSH88] and briefly reproduced in Sec.3.2.3, one realizes that the high pressure limit is an averaging of the first type ,$\langle|\vec{B}(\vec{r})|\rangle$. At slow precession frequencies and high mobility of the particles on the other hand we expect an averaging process that rather corresponds to the second type, $|\langle\vec{B}(\vec{r})\rangle|$. The limiting case of the second type can be treated analytically. One can show[Jac62] that the average over a spherical volume, that does not contain sources, of any *physical* field[10] is equal to the field at the center of the sphere, e.g.,

$$\frac{1}{V_{\text{cell}}}\int\limits_{V_{\text{cell}}}\vec{B}(\vec{r})dV=\vec{B}(\vec{r}_c)\,, \tag{3.42}$$

when the center of the sphere is located at $\vec{r}_c$. This agrees with Eq. (3.41), which scales with $\sim D^{-2}$ and thus with the square of the pressure for an ideal gas. We conclude that only in this special case the measured Larmor frequency would correspond to the magnetic field at the cell center and be independent of eventual inhomogeneities of the magnetic field. In the general case, the measurement reflects a volume average which depends on the magnetic field gradients. We note that the shift also vanishes for perfectly uniform fields. The magnitude of the frequency shift, that is, the deviation from the ideal case, has to be evaluated for each specific spin system under study independently. Even for spatially constant gradients only, where Eq. (3.41) holds, this poses a non trivial problem because it relies on the precise knowledge of the dynamical regime in the magnetometer cell, e.g., the diffusion coefficient D. Different cases have to be considered when the particle's mean free path is limited by the container dimensions or rather by inter-particle collisions. Accounts for these effects regarding ^{199}Hg and UCN are given in [PHS$^+$04]. For the ^{3}He cell used in the scope of this thesis we can estimate the magnitude of the effect assuming cylindrical symmetry as in Eq. (1.12) and a constant longitudinal gradient[11] of $\frac{\partial B_z}{\partial z}=1\,\text{pT/mm}$. Using Eqns. (3.41),(3.40) together with the diffusion coefficient from Eq. (3.29) and assuming a holding field of $B_0=1\,\mu\text{T}$ we find

$$\delta B^{\text{avg,HP}}\approx 0.06\,\text{fT}\qquad\text{in the high pressure limit and}\tag{3.43}$$

$$\delta B^{\text{avg,LP}}\approx 0.01\,\text{fT}\qquad\text{in the low pressure limit}\,,\tag{3.44}$$

when scaled to magnetic field units.

Ramsey-Bloch-Siegert shifts in electric fields

For particles moving in an electric field yet another effect has to be taken into account, as was already discussed in Sec. 1.2.2.3. From the interaction with the electric field arises a magnetic field $\sim\vec{\mathscr{E}}\times\vec{v}$ in the rest frame of the moving particle. The equation for the RBS Eq. (1.15) contains linear and quadratic terms in $\vec{\mathscr{E}}$, the linear term vanishes for vanishing magnetic field gradients but the quadratic term persists. Again the magnitude of this shift considering the whole ensemble of particles depends on the dynamic regime and the geometry of the sample cell. These effects are being intensively studied in the context of the nEDM project, the reader is referred to [PHS$^+$04],[ABB$^+$15a] for further information.

Bloch-Siegert shift for driven magnetometers

The Bloch-Siegert shift comes into play in driven magnetometers when a linearly oscillating rather than a rotating rf field is applied. For reasons of convenience this is done in the CsOPMs used in this work and in the nEDM project at PSI. It was demonstrated in Sec. 3.1.2, that this gives rise to a counter-rotating rf field at the double frequency $\omega_r=2\omega_{\text{rf}}$ in the rest frame of the spin. There, the line shapes of the M_x magnetometer were

---

[10] Fulfilling the homogeneous Maxwell equation $\vec{\nabla}\cdot\vec{B}(\vec{r})=0$

[11] Fields of this homogeneity can reliably achieved in well shielded environments, e.g., the nEDM experiment at PSI.

derived in the RWA which consists in neglecting this $2\omega_{\rm rf}$ component. The effect of this field on the resonance frequency can be estimated using Eq. (1.11). We assume an amplitude $B_1 \sim 2\,\rm nT$ of the linear rf field oscillating at $\omega_{\rm rf} = \gamma_{\rm Cs} B_0$ (on resonance). From Eq. (3.8) we deduce the amplitude of the rotating field, $\frac{B_1}{2\sqrt{2}}$. Inserting this into Eq. (1.11) and dividing by the gyromagnetic ratio yields

$$\delta_B^{\rm BS} \approx \frac{B_1^2}{16 B_0} \approx 0.25\,\rm pT, \tag{3.45}$$

where $B_0 = 1\,\mu\rm T$ was used to obtain the numerical result.

Bloch-Siegert shift in the combined ^{3}He/Cs magnetometer

Because of the thematic contiguity we will already discuss here the possibility of a Bloch-Siegert shift of the ^{3}He Larmor frequency arising from the rf fields driving the CsOPMs. For this purpose we consider the geometry of the ^{3}He/Cs prototype magnetometer described in Chapter 5. The ^{3}He cell is surrounded by eight CsOPMs, their cell centers being at a distance $\sim 5\,\rm cm$ from the ^{3}He cell center. We start by estimating the effect of a single CsOPM's rf coils on the ^{3}He cell. We make a very rough approximation modeling the rf coils of the CsOPMs as two magnetic dipoles oriented along the same direction $\hat{x}'$ and spaced by the distance of the PCBs $d = 1.5\,\rm cm$. The strength of these dipoles is scaled such, that they produce a field $B_1(\vec{r}_{\rm Cs}) = |\vec{B}_1(\vec{r}_{\rm Cs})| = 2\,\rm nT$ in their middle, at the center of the Cs cell $\vec{r}_{\rm Cs} = (0,0,0)$. Based on these assumptions we calculate the magnetic field at the position of the ^{3}He cell center $\vec{r}_{\rm He} = (0, 0.05\,\rm m, 0)$ and find

$$B_1(\vec{r}_{\rm He}) = |\vec{B}_1(\vec{r}_{\rm He})| \approx 1\,\rm nT. \tag{3.46}$$

We further assume that only the component of $\vec{B}_1$ perpendicular to $\hat{B}_0$

$$B_{1,\perp}(\vec{r}_{\rm He}) = \vec{B}_1(\vec{r}_{\rm He}) \cdot \hat{n} \approx 0.7\,\rm nT, \tag{3.47}$$

produces a frequency shift. Here, $\hat{n}$ is a unit vector perpendicular to $\hat{B}_0$. We now calculate the effect of the magnetic field rotating at $\omega_r = \gamma_{\rm Cs} B_0$ with amplitude $B_{1,\perp}(\vec{r}_{\rm He})$ on the ^{3}He resonance frequency using again Eq. (1.11). The shift of $\omega_{\rm L,He}$ translates into a systematic shift of the measured field

$$|\delta B^{\rm BS,He/Cs}| \approx 2.3\,\rm fT \tag{3.48}$$

under these assumptions, where we have used again $B_0 = 1\,\mu\rm T$. In a worst case scenario the rf fields of all eight CsOPMs would interfere constructively at the ^{3}He cell center, leading to an eight-fold increase of $B_{1,\perp}(\vec{r}_{\rm He})$. Since the shift is quadratic in $B_{1,\perp}(\vec{r}_{\rm He})$ this would give rise to a 64-fold increased

$$|\delta B^{\rm BS,He/Cs}| \approx 150\,\rm fT. \tag{3.49}$$

In the design of the prototype such problems were foreseen and the CsOPM were placed in a highly symmetrical way (see Chapter. 5). The idea is that each sensor has a symmetric counterpart which has its rf-coil connected in reversed polarity so that the rf-fields average to zero at the ^{3}He cell center. A shift of the magnitude given in Eq. (3.49) is comparable to the statistical sensitivity of the SQUID magnetometer reading the ^{3}He precession (compare Chapter. 12). An effect from switching the CsOPM's rf fields on and off was not observed in this data.

3.4 Other types of magnetometers

In the following, three more types of magnetometers will be briefly addressed. They are not of major importance for the measurements described in this thesis, however, they are of significance in a broader frame. For further information on these systems the reader is referred to the literature.

3.4.1 Cs magnetometers based on free spin precession

A different class of cesium magnetometers that is recently being investigated with rising interest are CsOPMs based on free spin precession (FSP-Cs). Because of their increasing significance for the nEDM project they will be briefly described here. In contrast to magnetometers that use the ODMR process, where the Cs spin precession is driven by an oscillating rf-field, these magnetometers rely on detecting the unperturbed precession of the Cs polarization. This scheme has the intriguing advantage that the measurements are free of all the potential systematic errors associated with the presence of a driving rf field (Bloch-Siegert shift, accuracy of initial phase setting, instability of phase setting) that were discussed above[12].

Although different schemes of operation exist, one common feature distinguishes the FSP-Cs from the driven CsOPMs described before. In the latter, optical pumping, evolution and detection of the spin take place simultaneously, they are continuously measuring. In the FSP-Cs however, optical pumping is temporally separated from the evolution and detection process, the measurements are thus done in a sequential way. Two approaches have been successfully demonstrated recently. In the first approach the Cs vapor is optically pumped by intensity modulated circularly polarized light incident at angle of $\theta_k = 90\,^\circ$ with respect to the holding field $\vec{B}_0$. The modulation frequency is chosen to match the Larmor frequency of the atomic medium in the applied field[GW13]. After the pumping process[13], the light-power is significantly reduced and the modulation switched off. During the subsequent measurement period[14] the attenuation of the less intense, constant power beam in the polarized medium is measured using a photodiode. Measurements with this type of sensor are described in [GKBW15] and show promising results. A conceptually beautiful feature of this scheme is that, in contrast to the driven CsOPMs detailed above, it does not produce any magnetic perturbances during operation[15]. This makes it particularly interesting in the frame of the nEDM project since it eliminates the cross-talk problem and eliminates the risk of unwanted magnetic interferences. A second scheme of FSP-Cs magnetometer that was recently explored [ABB$^+$15c] works with a constant intensity pump-light but then uses a short, intense magnetic rf pulse at the beginning of the measurement period to start the Cs spin precession. Both types of FSP-Cs also permit obtaining vector information about the magnetic field by using multiple readout beams at different angles.

3.4.2 Hg magnetometer

The current (and future) nEDM experiment at PSI employs a Hg co-magnetometer, this is why a short overview of this type of magnetometer is given here. Mercury has seven stable isotopes $\mathrm{A_{Hg}}$ with $A = (196, 198, 199, 200, 201, 202, 204)$ of which only the two odd ones carry a nuclear spin and can thus be optically pumped. For the magnetometric application, ^{199}Hg was chosen since it has a spin 1/2 and larger g factor. The $6^1S_0 \rightarrow 6^3P_1$ transition is used to optically pump the ^{199}Hg and create nuclear spin polarization. The transition frequency corresponds to an optical wavelength of $\lambda_{Hg} = 253.7\,\mathrm{nm}$. The magnetometer measures the volume-averaged magnetic field inside the neutron precession chamber of the experiment. To this aim Hg vapor is extracted by heating either a ^{199}Hg enriched droplet of elementary mercury or a HgO compound. The vapor is collected in a preparation chamber situated below the neutron precession chamber and polarized along B_0. Directly after filling the neutrons, the polarized Hg vapor is fed into the precession chamber via a separate inlet. A $\pi/2$ flip is applied and the Hg magnetization's precession is measured by monitoring corresponding power modulation of a resonant polarized light beam traversing the neutron precession chamber and impinging on a photo-multiplier or -diode. A detailed account of the PSI ^{199}Hg co-magnetometer is given in [Fer13]. We just note here that the magnetometer yields time averaged measurements of a $\sim 1\,\mu\mathrm{T}$ magnetic field with uncertainties as low as $\sim 20\,\mathrm{fT}$ in a 100 s integration time. The readings of this magnetometer may comprise systematic

---

[12] This type of magnetometer exhibits a yet unexplained systematic measurement error which is described in [GKBW15] and remains to be investigated. However, there is strong experimental evidence indicating that this error does not occur when the angle between the magnetic field and the pump beam is exactly $\theta_k = 90\,^\circ$.

[13] Typically 20 ms

[14] Typically 80 ms

[15] This type of magnetometer is therefore called *magnetically silent.*

effects of different origins, e.g., the light shift discussed above, the geometric phase effect (Sec. 1.2.2.3) due to interactions with the strong electric field applied in the precession chamber and effects related to the volume-averaging of the magnetic field by the atoms (Sec. 3.3). The effect of the light shift has been evaluated to be $\sim 6\,\mathrm{fT}$ in a $1\,\mu\mathrm{T}$ magnetic field for well controlled experimental parameters[Fer13]. The ^{199}Hg gyromagnetic ratio is only known with a $\sim 10^{-6}$ relative precision [Cag60][MTN12], which limits the absolute accuracy of the magnetometer to $\sim 1\,\mathrm{pT}$. In the next stage of the nEDM experiment the ^{3}He/Cs magnetometer would thus be an excellent candidate to complement and improve the magnetic field monitoring in the neutron precession chamber.

3.4.3 SQUID

During the measurements carried out at PTB in an investigation of the ^{3}He/Cs magnetometer performance described in Chapter 6ff., a SQUID magnetometer was used simultaneously to detect the ^{3}He FSP. As mentioned in Sec. 3.2.4, SQUIDs have been already successfully applied for this purpose[BHK^{+}07]. At PTB a 304 channel DC-vector SQUID system is permanently installed inside a magnetically shielded room. A SQUID magnetometer detects single fluxon changes of the magnetic flux through a superconducting ring electrode exploiting the Josephson effect. In a vector SQUID these rings are oriented along different spatial directions to yield vector information about the magnetic flux. In order to keep these rings in a superconducting state the magnetometer has to be operated at very low temperatures. This requires that the device is enclosed in a dewar and the use of liquid helium to cool it to $\sim 4\,\mathrm{K}$. Since a SQUID measures changes of the flux in units of quanta, its magnetometric sensitivity is very high, typically on the order of $\sim 1\,\mathrm{fT}/\sqrt{\mathrm{Hz}}$. A SQUID is usually operated in a mode where the magnetic flux generated by the measured field is actively compensated by suitable coils[16]. This makes it possible to track changes of the magnetic field over a wider range. While having this superb sensitivity to field changes, it is not possible to measure the absolute magnetic field with such a device. However in the scope of detecting the ^{3}He-FSP, this does not impose a restriction because the information about the absolute field is contained in the ^{3}He FSP frequency.

---

[16] This demands of course very low-noise current sources for driving the coils and actually a current source designed for this purpose was used during the measurements to generate the B_0 coil-current.

Part II

The ^{3}He/Cs combined magnetometer

Chapter 4

Principle of ^{3}He magnetometry

In this chapter the basic concepts underlying the detection of the ^{3}He free spin precession (FSP) by CsOPMs will be discussed. From the spatial and temporal dependence of the magnetic field created by the polarized ^{3}He and the properties of the CsOPM in M_x-configuration an optimized detection geometry is derived which dictates the design of the magnetometer prototype described in Chapter 5. The two different modes of operation of CsOPMs presented in Sec. 3.1.3 are reviewed concerning their suitability for readout of ^{3}He-FSP signals.

4.1 Magnetic field produced by the polarized ^{3}He sample

We will first examine the magnetic field that is created by a sample of polarized ^{3}He gas contained in a spectroscopy cell. For this we consider an ensemble of N_{He} ^{3}He atoms, each carrying a magnetic moment of identical magnitude μ_{He} and arbitary orientation $\hat{\mu}_{\mathrm{i}}$. The magnetic moments are tiny dipoles, the field created at a position $\vec{\mathrm{r}}$ by a single magnetic moment $\vec{\mu}_{\mathrm{i}} = \hat{\mu}_{\mathrm{i}}\mu_{\mathrm{He}}$ located at $\vec{\mathrm{r}}_{0\mathrm{i}}$ is well known [Jac62] and reads

$$\vec{B}_{\mu,i}(\vec{r}) = \frac{3(\vec{r}-\vec{r}_{0\mathrm{i}})(\hat{\mu}_{\mathrm{i}}\cdot(\vec{r}-\vec{r}_{0\mathrm{i}})) - \hat{\mu}_{\mathrm{i}}\,|\vec{r}-\vec{r}_{0\mathrm{i}}|^2}{|\vec{r}-\vec{r}_{0\mathrm{i}}|^5}\,\frac{\mu_{\mathrm{He}}\mu_0}{4\pi} \tag{4.1}$$

where $\mu_{He} = -2.127624\mu_N$, with $\mu_N = 5.0507832410^{-27}\mathrm{J/T}$ being the nuclear magnetic moment and $\mu_0 = 4\pi \times 10^{-7}\,\mathrm{Newton/Ampere}^2$ is the vacuum permeability. An arbitary distribution of such magnetic dipoles located at positions $\vec{r}_{0\mathrm{i}}$ creates a magnetic (far-)field at the position $\vec{\mathrm{r}}$ that is given by the sum of all contributions from the individual dipoles

$$\vec{B}_{\mu}(\vec{r}) = \sum_{\mathrm{i}} \vec{B}_{\mu,i}\,, \tag{4.2}$$

as long as $|\vec{\mathrm{r}} - \vec{r}_{0\mathrm{i}}| \gg |\vec{r}_{\mathrm{i}} - \vec{r}_{\mathrm{j}}|$. In case of a polarized gas, a fraction $0 \leq p \leq 1$ of the total number N_{He} of dipoles will be aligned along the same direction $\hat{\mu}$, p is a measure for the degree of polarization. When we consider a homogeneous distribution of dipoles filling an arbitrary volume V, the far field is given by the integral

$$\vec{B}(\vec{r}) = \frac{p\mu_0\mu_{\mathrm{He}}N_{\mathrm{He}}}{4\pi V}\int_V dV\vec{B}_{\mu,i}(\vec{r})\,, \tag{4.3}$$

where the number of atoms can be found using the ideal gas law. We now consider the case of an ensemble with spherical symmetry around $\vec{r}_0 = \vec{0}$ and polarization p, which describes the spherical sample cell used in our later experiments. In this case the calculation of the produced magnetic field simplifies, the far-field can be calculated assuming a single macroscopic magnetic moment with magnitude $N_{\mathrm{He}}\cdot p\cdot\mu_{\mathrm{He}}$ and orientation $\hat{\mu}$ located at the center of the sphere. This yields

$$\vec{B}_{\mathrm{He}}(\vec{r}) = \frac{3\vec{r}(\hat{\mu}\cdot\vec{r}) - \hat{\mu}\,|\vec{r}|^2}{|\vec{r}|^5}\,\frac{N_{\mathrm{He}}p\mu_{\mathrm{He}}\mu_0}{4\pi} \tag{4.4}$$

for the magnetic field. For the experiments conducted in the frame of this thesis we find, using the ideal gas law, $PV = Nk_BT$, the number of ^{3}He atoms $N_{\mathrm{He}} = \frac{PV}{k_BT} = 2.04\cdot 10^{18}$, Eq. (4.4) thus yields a magnetic field in the

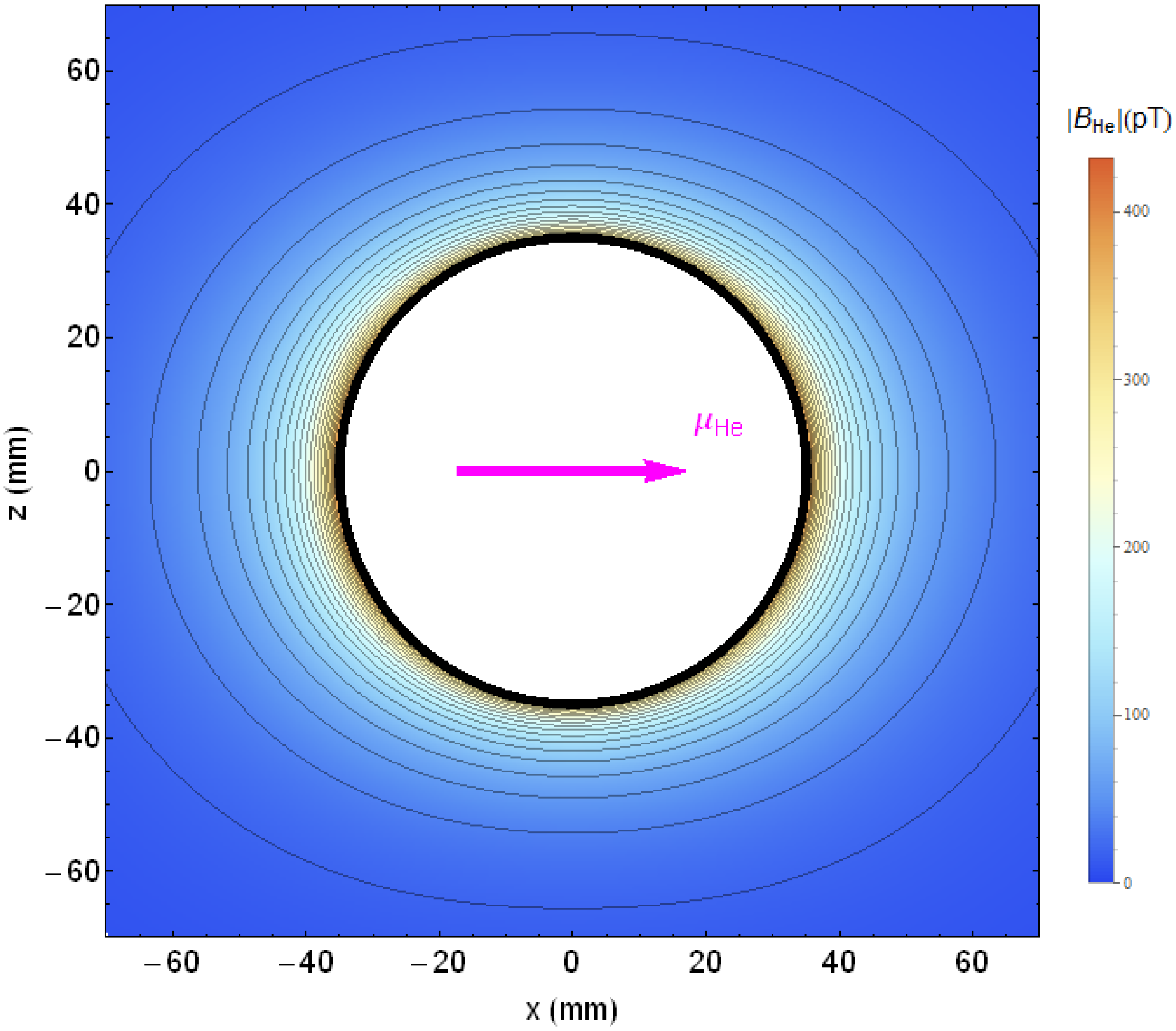

FIGURE 4.1: Modulus $|\vec{B}_{\mathrm{He}}|$ of magnetic field produced by a 70 mm diameter spherical ^{3}He cell filled with 100 % polarized gas at a pressure of 1 mbar according to Eq. (4.4).

pT range. Figure 4.1 visualizes the result for a magnetization pointing along $\hat{x}$. When the magnetic moments of a polarized gas sample precess in an external magnetic field, this results in the macroscopic magnetization rotating around the $\vec{B}_0$ direction with an angular velocity given by its Larmor frequency $\omega_{\mathrm{L,He}}$. Introducing standard spherical coordinates

$$\vec{r} = \begin{pmatrix} r\sin(\theta)\cos(\phi) \\ r\sin(\theta)\sin(\phi) \\ r\cos\theta \end{pmatrix}, \tag{4.5}$$

the time dependent orientation of the macroscopic sample magnetization $\hat{\mu}(t)$ can be expressed by

$$\hat{\mu}(t) = R(\omega_{\mathrm{L,He}}t, \hat{B}_0)\hat{\mu}(t=0), \tag{4.6}$$

where $R(\omega_{\mathrm{L,He}}t, \hat{B}_0)$ is the time dependent rotation matrix acting on the initial orientation $\hat{\mu}(t=0)$. We assume in the following a homogeneous, constant magnetic field aligned with the $\hat{z}$-axis, $\vec{B}_0 = (0, 0, B_0)$ and a magnetization initially oriented along $\hat{\mu}(t=0) = \hat{x}$. The time dependent magnetic field produced at a position $\vec{r}$ by the precessing magnetization can then be found by replacing $\vec{\mu}_{\mathrm{i}} \to \vec{\mu}(t)$ in Eq. (4.4), leading to

$$\vec{B}_{\mathrm{He}}(\vec{r}, t) = \frac{N_{\mathrm{He}} p \mu_{\mathrm{He}} \mu_0}{4\pi r^3} \begin{pmatrix} \frac{1}{4}\left(-\cos(\omega_{\mathrm{L,He}}t)\,(1+3\cos(2\theta)) + 6\cos(\omega_{\mathrm{L,He}}t - 2\phi)\sin(\theta)^2\right) \\ -\cos(\theta)^2\sin(\omega_{\mathrm{L,He}}t) + \frac{1}{2}\left(\sin(\omega_{\mathrm{L,He}}t) - 3\sin(\omega_{\mathrm{L,He}}t - 2\phi)\right)\sin(\theta)^2 \\ 3\cos(\omega_{\mathrm{L,He}}t - \phi)\cos(\theta)\sin(\theta) \end{pmatrix}. \tag{4.7}$$

Of course, this result only holds under the above assumption that the sample cell is spherical, an assumption that we will follow throughout the whole thesis.

4.2 Optimized detection geometry of ^{3}He/Cs magnetometer

As described in Sec. 3.2, the combined magnetometer concept is based on measuring the Larmor frequency of freely precessing ^{3}He using CsOPMs. For this, a sample of ^{3}He gas contained in a sealed glass cell centered at the origin is exposed to a homogeneous, constant magnetic field $\vec{B}_0$. The total magnetic field in the vicinity of the sample cell will be a superposition of the constant holding field and the time-dependent magnetic field produced by the ^{3}He FSP

$$\vec{B}(\vec{r}, t) = \vec{B}_0 + \vec{B}_{\mathrm{He}}(\vec{r}, t). \tag{4.8}$$

A CsOPM located near the ^{3}He cell will measure the modulus of the total magnetic field at its respective position $\vec{r}_{\mathrm{Cs}}$. In the experiments described here the holding field was $\sim 1\,\mu$T. The field given by Eq. (4.4) and shown in Fig. 4.1 in the previous section, is only on the order of pico Teslas even in close vicinity of the ^{3}He cell, thus $|\vec{B}_0| >> |\vec{B}_{\mathrm{He}}|$. For the modulus of the total magnetic field we thus find, assuming a holding field along $\hat{z}$,

$$|\vec{B}(\vec{r}, t)| = |\vec{B}_0 + \vec{B}_{\mathrm{He}}(\vec{r}, t)| = \left| \begin{pmatrix} 0 \\ 0 \\ B_0 \end{pmatrix} + \begin{pmatrix} B_{He,x}(\vec{r}, t) \\ B_{He,y}(\vec{r}, t) \\ B_{\mathrm{He,z}}(\vec{r}, t) \end{pmatrix} \right| \tag{4.9}$$

$$= \sqrt{(B_{\mathrm{He,x}}(\vec{r}, t))^2 + B_{\mathrm{He,y}}(\vec{r}, t)^2 + (B_0 + B_{\mathrm{He,z}}(\vec{r}, t))^2} \approx B_0 + B_{\mathrm{He,z}}(\vec{r}, t). \tag{4.10}$$

This approximation shows that for perturbations of the $\vec{B}_0$ field which are small compared to $|\vec{B}_0|$, the CsOPMs are to first order only sensitive to the component of the perturbation along $\hat{B}_0$. Figure 4.2 shows a map of the $\hat{z}$ component $B_{\mathrm{He,z}}$ of the magnetic field in the ($\hat{x}$,$\hat{z}$) plane produced by a polarized ^{3}He sample contained in a spherical cell when the magnetization is aligned along $\hat{x}$ (more details in the figure caption). From Eq. (4.7), it is evident that the $\hat{z}$-component of the magnetic field produced by the magnetization precessing at an angular velocity $\omega_{\mathrm{L,He}}$ in the $(\hat{x}, \hat{y})$ plane is of the form

$$B_{\mathrm{He,z}}(\vec{r}, t) = b(r,\theta)\cos(\omega_{\mathrm{L,He}}t - \phi), \tag{4.11}$$

where the amplitude

$$b(r,\theta) = b_{\mathrm{He}} = \frac{N_{\mathrm{He}} p \mu_{\mathrm{He}} \mu_0}{4\pi r^3}\cos(\theta)\sin(\theta) \tag{4.12}$$

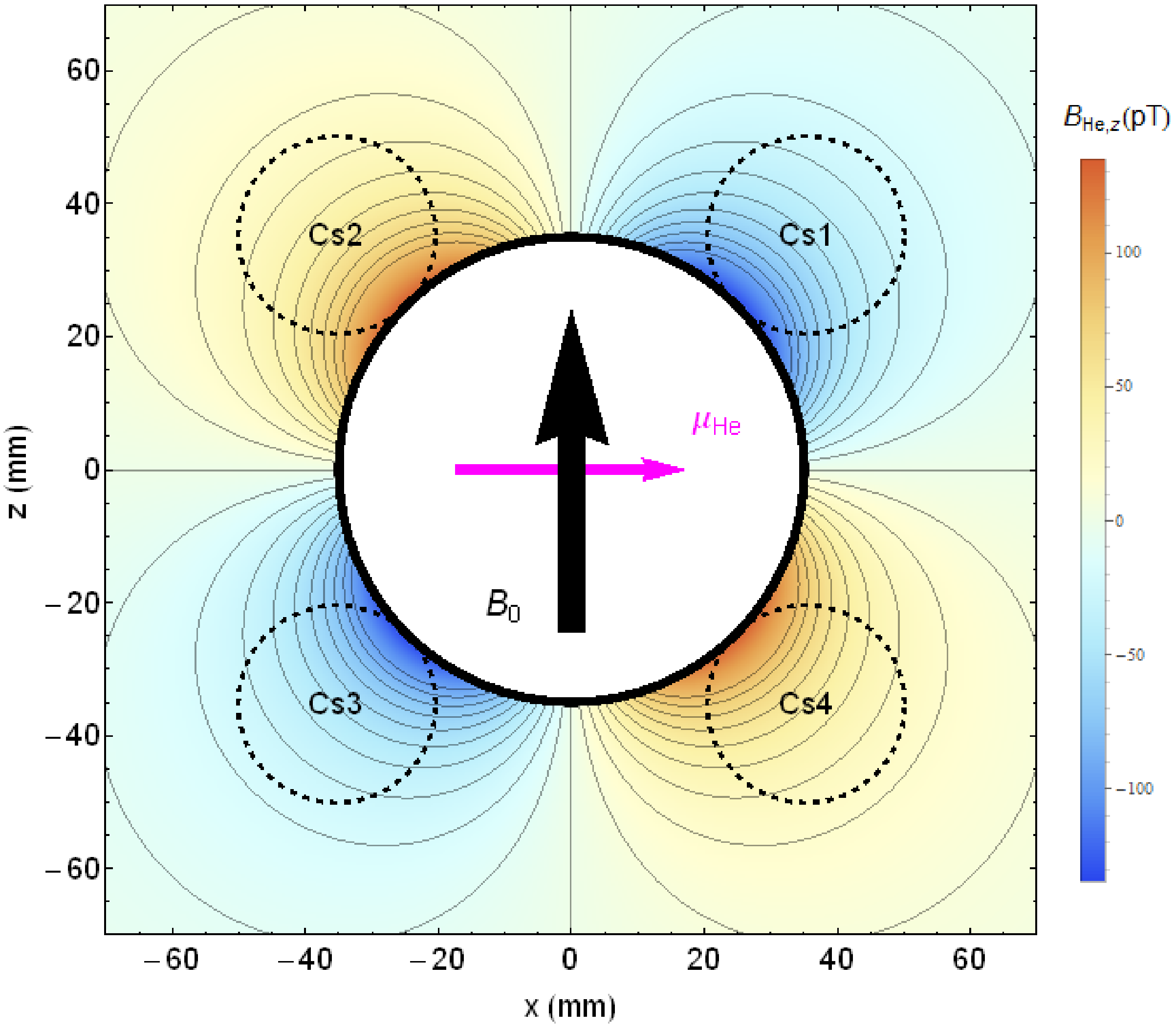

FIGURE 4.2: $\hat{z}$ -component of magnetic field produced by a polarized ^{3}He sample in a spherical cell. The ^{3}He magnetization μ_{He} is oriented along $\hat{x}$, the magnetic (holding) field points along $\hat{z}$. Positive (negative) values of $B_{\mathrm{He,z}}$ denote that the magnetic field at this position is increased (decreased). Positions of CsOPMs are also drawn, the geometry corresponds to the prototype magentometer described in Chapter 5. The simulation assumes a ^{3}He polarization of 100 % and a pressure of 1 mbar.

is independent of the coordinate ϕ and has the characteristic $|\vec{r}-\vec{r}_0|^{-3}$ dependence of a dipole field on the distance from the source. The z-component of the total magnetic field at the CsOPMs position is thus given by

$$B_z(\vec{r},t) = B_{0,z} + B_{\mathrm{He,z}} = B_0 + b(r,\theta)\cos(\omega_{\mathrm{L,He}}t - \phi)\,. \tag{4.13}$$

Equation 4.13 shows that the z-component B_z of the total magnetic field (to which the CsOPM is only sensitive to first order) will oscillate around B_0 at the ^{3}He Larmor frequency $\omega_{\mathrm{L,He}}$. Since the magnetic field is inferred from $\omega_{\mathrm{L,He}}$, and a large amplitude of this oscillation is beneficial to our ability to determine this frequency we are aiming to maximize this amplitude. A detailed description of the factors affecting the precision of frequency estimation of a sinusoidal signal is given in Chapter 7. It is easy to see from Eq. (4.12) that $b(r,\theta)$ will be maximized for minimal r and $\theta^* \in \{\pi/4, 3\pi/4\}$. The points $\vec{r}(r,\theta=\theta^*,\phi)$ form two cones around $\hat{z}$ with half opening angle $\phi = 45°$ and tips centered at $\vec{r}_0$. The minimum distance $r_{\mathrm{min}} = |\vec{r}-\vec{r}_0|$ at which the CsOPMs can be placed is defined by the radii of the ^{3}He cell ($r_{\mathrm{He}} = 35\,\mathrm{mm}$) and the Cs cell ($r_{\mathrm{Cs}} = 15\,\mathrm{mm}$), $|\vec{r}-\vec{r}_0|_{\mathrm{min}} = r_{\mathrm{He}} + r_{\mathrm{Cs}} = 50\,\mathrm{mm}$. The calculation yields a maximum amplitude

$$b_{\mathrm{He,max}} = b(r_{\mathrm{min}},\theta^*,\phi) = 34\,\mathrm{pT_{rms}} \tag{4.14}$$

for a 100 % polarized 1 mbar spherical cell. The demand to maximize the amplitude by placing the CsOPMs on a 45° cone as close as possible to the ^{3}He cell defines the optimum detection geometry for a ^{3}He/Cs magnetometer based on a spherical ^{3}He cell and M_x-CsOPMs. For other ^{3}He cell shapes, like the flat cylinders foreseen for n2EDM, the optimum position has to be evaluated individually and may not anymore be independent of ϕ. Nevertheless a minimal distance between CsOPM and ^{3}He cell is always desirable.

4.3 ^{3}He phase relations for multiple CsOPMs

The considerations presented in the preceding section leave only a single free parameter for the placement of the Cs readout sensors, viz., their angular position ϕ on the 45° cone. When we examine the phase relation $\Delta\phi$ between the ^{3}He FSP signals of two different CsOPMs, we find that it is independent of $|\vec{r}|$ but related to their relative angular position. Two CsOPMs Cs_{i} and Cs_{j} located at angular positions (θ_{i}, ϕ_{i}) and (θ_{j}, ϕ_{j}) respectively will, according Eq. (4.11), see time dependent magnetic fields

$$B_{i,z} \sim \cos(\theta_{\mathrm{i}})\sin(\theta_{\mathrm{i}})\cos(\omega_{\mathrm{L,He}}t-\phi_{\mathrm{i}}) \qquad \text{and} \qquad B_{j,z} \sim \cos(\theta_{\mathrm{j}})\sin(\theta_{\mathrm{j}})\cos(\omega_{\mathrm{L,He}}t-\phi_{\mathrm{j}})\,. \tag{4.15}$$

The phase difference is thus given by

$$|\Delta\phi| = |\mathrm{sign}\left(\cos(\theta_{\mathrm{i}})\sin(\theta_{\mathrm{i}})\right)\phi_{\mathrm{i}} - \mathrm{sign}\left(\cos(\theta_{\mathrm{j}})\sin(\theta_{\mathrm{j}})\right)\phi_{\mathrm{j}}|\,. \tag{4.16}$$

Figure 4.3a shows the spherical ^{3}He cell with the 45° cones of highest signal amplitude assuming the magnetization is precessing in the ($\hat{x}$-$\hat{y}$)-plane around $\vec{B}_0$ aligned with $\hat{z}$. Three CsOPMs $Cs_{i,j,k}$ are drawn at positions (θ, $\phi_{i,j,k}$) to illustrate the definitions of the angles. In Fig. 4.3b the time dependence of the $\hat{z}$ component of the total magnetic field at their respective positions is shown, as expected from Eq. 4.13. The phase shift between the different signals is visible, corresponding to Eq. (4.16). A particularly interesting situation arises when two CsOPMs are dephased by $|\Delta\phi| = \pi$, such as Cs_{j} and Cs_{k} in Fig. 4.3. In this case a difference signal can be constructed from the two oscillations by substracting one from the other. This so-called gradiometer signal has interesting properties which can become useful for certain applications. The gradiometric measurement approach will be discussed in more detail in Chapter 10. Here we just note that as a consequence of Eq. (4.16) a pair of CsOPMs has $\left|\Delta\phi\right| = \pi$ and can thus form a gradiometer (and is called a gradiometer pair) when they are either symmetric with respect to $\hat{B}_0 = \hat{z}$ or with respect to the plane perpendicular to $\hat{B}_0$ intersecting at the center of the ^{3}He cell.

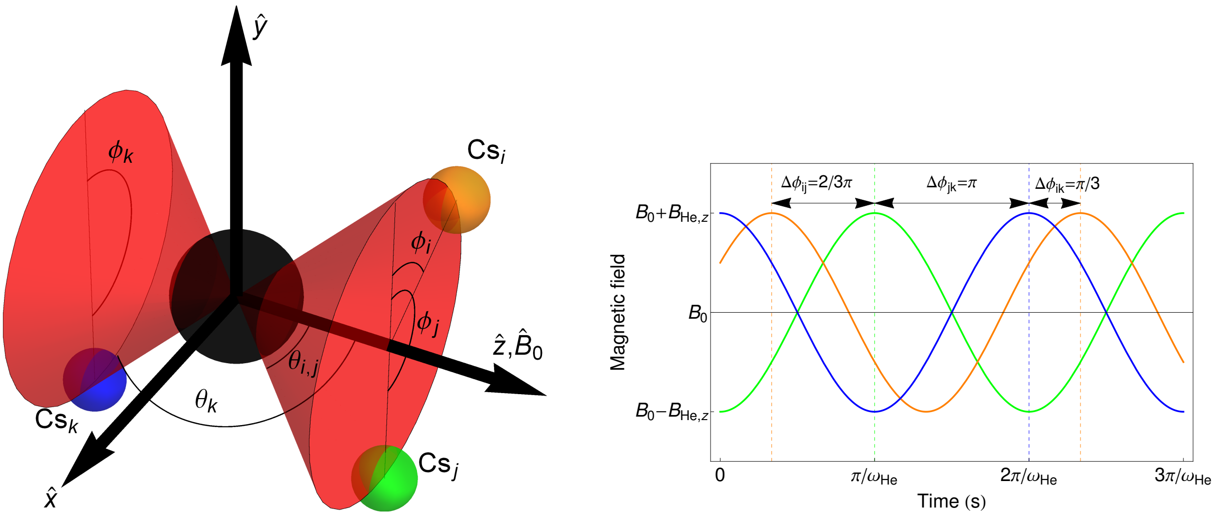

(a) (b)

FIGURE 4.3: (a) ^{3}He cell (black) with 45° cones (red) of highest signal amplitude for magnetization rotating in the ($\hat{x}$-$\hat{y}$)-plane. CsOPMs Cs_i (orange), Cs_j (green) and Cs_k (blue) are centered on these cones at different angular positions $\phi_\mathrm{i} = \pi/3$, $\phi_{j,k} = \pi$, $\theta_{i,j} = \pi/4$ and $\theta_\mathrm{k} = 3\pi/4$. The magnetic field is pointing along $\hat{z}$. Size and distance of spheres are not to scale. (b) Magnetic field measured by Cs_i (orange), Cs_j (green) and Cs_k (blue) as a function of time to visualize the phase-shift relation Eq. (4.16). The signals are dephased by $\Delta\phi_{ij} = 2/3\pi$, $\Delta\phi_{jk} = \pi$ and $\Delta\phi_{ik} = \pi/3$ respectively.

4.4 Modes of operation and ^{3}He FSP readout

We will now review the two different modes of operation of CsOPMs introduced in Sec. 3.1.3 in view of their use as ^{3}He FSP readout sensors. In FF-mode the CsOPM is driven at a constant rf frequency while in PS-mode a feedback loop keeps the magnetometer on resonance by dynamically readjusting the drive frequency. Generally both techniques are possible, but arguments will be presented which led to most measurements being performed in the FF-mode.

In both cases, the oscillating magnetic field produced by the ^{3}He FSP will modulate the magnetic field at the CsOPMs position according to Eq. (4.13) thereby changing the local Larmor frequency $\omega_{\mathrm{L,Cs}}(\vec{r},t)$. We first address the FF-mode of operation and derive an expression for the expected phase signal of a CsOPM detecting ^{3}He FSP referring to the notation that was introduced in Sec. 3.1.2. The phase of the CsOPM is given by Eq. (3.20),

$$\tan(\varphi) = -\frac{\Gamma_2}{\delta\omega}, \tag{4.17}$$

where $\delta = \omega_{\mathrm{L,Cs}} - \omega_{\mathrm{rf}}$ is the detuning from resonance. We assume the total magnetic field being a superposition of the static field $(0,0,B_0)$ and the ($\hat{z}$ component of the) oscillating magnetic field produced by the ^{3}He FSP $\big(0,0,b_{\mathrm{He}}\sin(\omega_{\mathrm{L,He}}t)\big)$. Inserting this into Eq. (4.17) yields

$$\tan(\varphi) = \frac{-\Gamma_2}{\omega_{\mathrm{L,Cs}}(t) - \omega_{\mathrm{rf}}} = \frac{-\Gamma}{\omega_0 + \gamma_{\mathrm{Cs}} b \sin(\omega_{\mathrm{L,He}}t) - \omega_{\mathrm{rf}}}. \tag{4.18}$$

Note, that in FF-mode, the rf-frequency ω_{rf} is kept constant. In order to obtain a simplified expression, we separate the phase into a constant on-resonance contribution φ_0 and a time-dependent term $\Delta\varphi(t)$ describing the change due to the oscillating ^{3}He field. We thus have for the phase

$$\varphi(t) = \varphi_0 + \Delta\varphi(t)\,. \tag{4.19}$$

Inserting Eq. (4.19) into the LHS of Eq. (4.18) we find

$$\tan(\varphi) = \tan(\varphi_0 + \Delta\varphi) = \frac{\sin(\varphi_0 + \Delta\varphi)}{\cos(\varphi_0 + \Delta\varphi)} \tag{4.20}$$

$$= \frac{\sin(\varphi_0)\cos(\Delta\varphi) + \cos(\varphi_p)\sin(\Delta\varphi)}{\cos(\varphi_0)\cos(\Delta\varphi) - \sin(\varphi_p)\sin(\Delta\varphi} = -\frac{\cos(\Delta\varphi)}{\sin(\Delta\varphi)} \tag{4.21}$$

$$\approx -\frac{1}{\Delta\varphi}. \tag{4.22}$$

Here we have used the on-resonance value $\varphi_0 = -\pi/2$ calculated from Eq. (4.17) assuming $\delta = 0$ to obtain Eq. (4.21). In the last step, leading to Eq. (4.22) the assumption has been made that $\Delta\varphi \ll \varphi_0$, which is justified since in the measurements presented here $B_0 \sim \mu$T while $b_{\mathrm{He}} \sim$ pT. Combining Eq. (4.22) and Eq. (4.18) leads to

$$\Delta\varphi(t) = \frac{\omega_{\mathrm{L,Cs}} - \omega_{\mathrm{rf}}}{\Gamma_2} \tag{4.23}$$

and inserting this result into Eq. (4.19), we find an expression for the expected phase signal

$$\varphi(t) = \varphi_0 + \frac{\omega_{\mathrm{L,Cs}} - \omega_{\mathrm{rf}}}{\Gamma_2} \tag{4.24}$$

$$= \varphi_0 + \frac{\omega_0 - \omega_{\mathrm{rf}}}{\Gamma_2} + \frac{\gamma_{\mathrm{Cs}} b_{\mathrm{He}} \sin(\omega_{\mathrm{L,He}} t)}{\Gamma_2}. \tag{4.25}$$

The first term of Eq. (4.25) is the on-resonance phase offset, the second term describes an additional phase offset that depends on the detuning of the rf-frequency from the magnetic resonance and the third term introduces a modulation of the phase due to the ^{3}He FSP. Note that φ_0 may also contain an additional phase offset introduced by the LIA. This result obtained in Eq. (4.25) justifies the use of the fit functions introduced in Sec. 7.3 for the analysis of the measured phase signal.
In the PS-mode the feedback loop will dynamically readjust the rf-frequency of the magnetometer to follow changes of the Larmor frequency. Assuming an infinite bandwidth of the PID that stabilizes the magnetometer's phase, the output (rf-) frequency would have the form

$$\omega_{\mathrm{rf}} = \omega_{\mathrm{L,Cs}} = \gamma_{\mathrm{Cs}}\left(B_0 + b_{\mathrm{He}}\cos(\omega_{\mathrm{L,He}} t)\right) = \omega_0 + \gamma_{\mathrm{Cs}} b_{\mathrm{He}} \cos(\omega_{\mathrm{L,He}} t) \tag{4.26}$$

while the phase signal would become constant.

4.4.1 Considerations on bandwidth

From what is discussed in Sec. 3.1, it is apparent that the CsOPM can be understood as a driven oscillator system. In FF-mode, the drive frequency ω_{rf} is in general not identical to the resonance frequency $\omega_{\mathrm{L,Cs}}$. In PS-mode, in the ideal case, the magnetometer is always driven at its resonance frequency. These two conditions lead to different implications for the bandwith of the CsOPM in the two modes of operation. Any driven oscillator shows a transient phase change when the detuning $\delta\omega = \omega_{\mathrm{L,Cs}} - \omega_{\mathrm{rf}}$ changes. This can be either due to a change of the drive frequency at constant resonance frequency or a change of the resonance frequency at constant drive frequency. The latter case applies for a CsOPM operated in FF-mode in a changing magnetic field. The time the oscillator (CsOPM) needs to adapt to such a change is connected to the quality factor Q of the oscillator. For the CsOPM this can be written as

$$Q = \frac{\omega_{\mathrm{L,Cs}}}{2\Gamma_2} \tag{4.27}$$

where Γ_2 is the transverse relaxation rate. This effect introduces a frequency-dependent response of the FF-driven CsOPM to changes of the B_0 field. The transfer function represents a first order low-pass filter that emerges from the general expression

$$T(f) = \frac{1}{(1 + (\tau 2\pi f)^2)^{n/2}} \tag{4.28}$$

for $n = 1$ and time constant $\tau = 1/\Gamma_2$ being the lifetime of the Cs polarization [BWW03]. For typical values achieved in the paraffin-coated Cs magnetometer cells ($\Gamma/2\pi \approx 6\,\mathrm{Hz}$), the lifetime is roughly $\tau_{\mathrm{Cs}} \approx 26\,\mathrm{ms}$ which corresponds to a -3dB cutoff frequency of $f_{\text{-3dB}} \approx 6\,\mathrm{Hz}$. This bandwidth limitation has to be taken into account when the true value b_{He} of the oscillating field created by the ^{3}He FSP is to be calculated and will be adressed in Sec. 7.1. As we will see in Sec. 12.2.3, it also brings important implications for the achievable signal to noise ratio.

In order to adequately describe the response of a CsOPM in FF-mode, low-pass filtering involved in the lock-in detection also has to be taken into account. During the measurements with ^{3}He/Cs, 4th order filters with cutoff frequency $f_{-3dB} < 100\,\mathrm{Hz}$ were usually chosen which have some attenuating effect already at the ^{3}He Larmor frequency $\omega_{\mathrm{L,He}}/2\pi$. The theoretical transfer function $T_{\mathrm{tot}}(f)$ of the complete signal treatment chain is then given by

$$T_{\mathrm{tot}}(f) = T_{\mathrm{LIA}}(f)\,T_{\mathrm{Cs}}(f)\,, \tag{4.29}$$

where $T_{\mathrm{LIA}}(f)$ and $T_{\mathrm{Cs}}(f)$ are the transfer functions of the low-pass filters of the LIA and the one associated with the lifetime of the Cs polarization, respectively. Both can be calculated according to Eq. (4.28).

To compare these predictions to the experimental reality and check for additional bandwidth limitations in the system, the phase response of the CsOPMs in FF-mode was measured. This was done by applying small oscillating magnetic fields of identical amplitude but varying frequency f_{mod} parallel to the $\vec{B}_0$ field. The amplitudes of the CsOPM response at the respective frequencies were extracted from FFT spectra of the phase signals. The results of these measurements are shown in Fig. 4.4, represented by the dots. Also shown are the theoretical functions $T_{\mathrm{LIA}}(f)$ (Fig. 4.4(a)), $T_{\mathrm{Cs}}(f)$ (Fig. 4.4(b,c), dashed lines) and $T_{\mathrm{tot}}(f)$ (Fig. 4.4(b,c), solid lines). It can be seen, that $T_{\mathrm{Cs}}(f)$ dominates $T_{\mathrm{tot}}(f)$ at low frequencies. The experimental points are in excellent agreement with the theoretically predicted frequency response $T_{\mathrm{tot}}(f)$ for both sensors (Cs1, red and Cs3, blue) shown in the plot. We thus conclude, that the transfer function of the signal treatment chain is adequately described by Eq. (4.29) and no additional bandwidth limitations are present.

The situation is substantially different for the CsOPM operated in PS-mode. Here, it is the PSL that adapts to a change of the detuning and the CsOPM is (ideally) always driven on resonance. As a consequence the properties of the PSL dominate the response of the CsOPM, in the ideal case it becomes independent of the linewidth Γ_2 [GBS+06][1]. As we have seen, changes of the magnetic field δB lead to changes of the CsOPMs phase signal $\delta\phi$ (in the absence of bandwidth limitations). In the PS-mode of CsOPM operation a PSL actively stabilizes the phase by making the PSL-frequency (rf-frequency) identical (*locking*) to the Larmor frequency $\omega_{\mathrm{L,Cs}}$ of the CsOPM $\omega_{\mathrm{rf}} = \omega_{\mathrm{PSL}} = \omega_{\mathrm{L,Cs}}$. We consider a DC magnetic field and a superimposed oscillating component of amplitude δB oscillating at frequency f, as it is encountered for the detection of the ^{3}He FSP signal in a constant holding field. The PSL is generating an error signal

$$\delta\phi_{\mathrm{PSL}} = \delta\phi - \frac{\delta\omega_{\mathrm{PSL}}}{\Gamma_2} \tag{4.30}$$

which is minimized in the feedback loop. The minimization will only work properly if the PSL bandwidth $f_{\mathrm{BW,PSL}}$ is larger than the oscillation frequency $f_{\mathrm{BW,PSL}} \gg f$. Even at sufficient bandwidth a finite phase error (error signal) $\delta\phi_{\mathrm{PSL}}$ is maintained, the magnitude of which depends on the gain characteristics of the PSL via

$$\delta\omega_{\mathrm{PSL}} = \delta\phi_{\mathrm{PSL}}\kappa(f)\,, \tag{4.31}$$

where $\kappa(f)$ is a gain factor at the signal frequency f. From Eq. (4.30) we see that for a properly working PSL the full magnetic oscillation amplitude is given by

$$\delta B = \frac{\Gamma_2\delta\phi_{\mathrm{PSL}} + \delta\omega_{\mathrm{PSL}}}{\gamma_{\mathrm{Cs}}}\,. \tag{4.32}$$

---

[1] This situation has some parallels to a operation amplifier that is used in a feedback loop. The OpAmp has a free running gain which corresponds to the magnetometers $1/\Gamma$ in this case. In the feedback though, the gain of the whole circuit will be defined by the loop characteristics, just like the CsOPMs response is determined by the phase feedback loop.

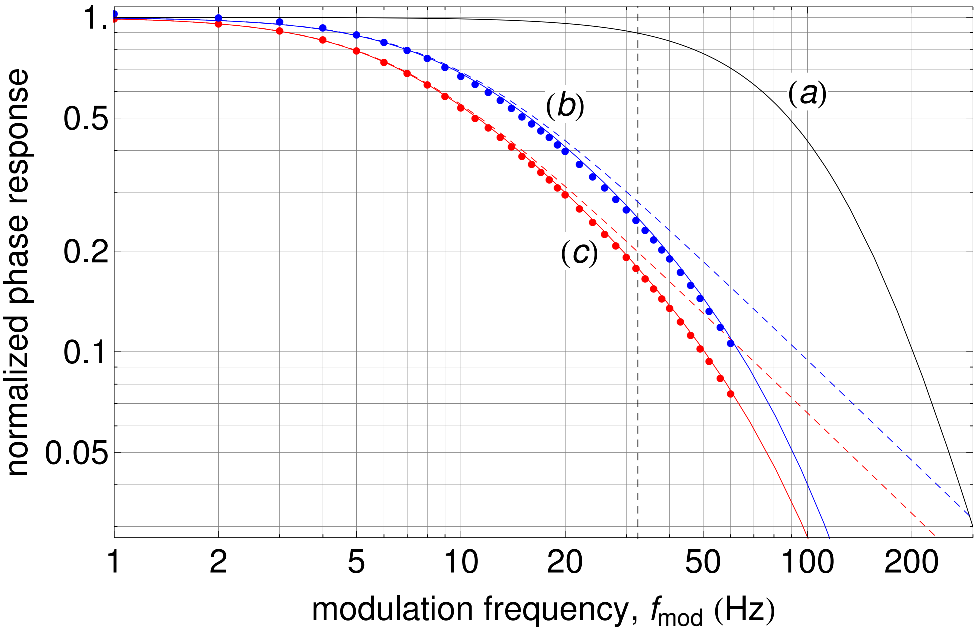

FIGURE 4.4: Theoretical and measured phase response of CsOPM running in FF-mode. (a) Transfer function T_{LIA} of LIA demodulator filter calculated according to Eq. (4.28) ($\tau = 1.16$ ms, 4-th order). (b,c) dashed lines: Transfer functions T_{Cs} of two CsOPMs, corresponding to 1st order filter with $\tau = 1/\Gamma_2$. The lifetimes are $\tau_{\text{Cs3}} \approx$ 17 ms for the blue curve and $\tau_{\text{Cs1}} \approx 24$ ms for the red curve respectively. (b,c) Solid lines: Combined transfer functions $T_{\text{LIA}} T_{\text{Cs}}$ for two CsOPMs. The dots represent experimentally measured points. The dashed vertical line indicates the ^{3}He precession frequency at 1 μT typically encountered in the experiments described here. See text for more details.

Combining this with Eq. (4.31), we obtain

$$\delta B = \frac{\delta\omega_{\text{PSL}}}{\gamma_{\text{Cs}}}\left(\frac{\Gamma_2}{\kappa(f)} + 1\right). \tag{4.33}$$

The PSLs used in our experiments are built in features of the lockin amplifier ZI-HF2 from Zurich Instruments. Since it is non-trivial to calculate the transfer function T_{PSL} of such a PSL, it was experimentally measured. To this aim, as in the measurement in the FF-mode, small magnetic fields oscillating at different frequencies f_{mod} were superimposed on the constant B_0 field. The response of the PS-driven CsOPM to these oscillating fields was investigated by extracting the amplitudes of the oscillating $\delta\omega_{\text{PSL}}$ and $\delta\phi_{\text{PSL}}$ components from FFT spectra of the respective signals. Rescaled to magnetic units, these are

$$\delta B_\omega = \delta\omega_{\text{PSL}}/\gamma_{\text{Cs}} \qquad \text{and} \qquad \delta B_\phi = \delta\phi_{\text{PSL}}\Gamma_2/\gamma_{\text{Cs}}\,. \tag{4.34}$$

A plot of these amplitudes as a function of the signal frequency is shown in Fig.4.5 for two PSLs of different bandwidth. It can be seen that Eq. (4.32) holds true for signals within the bandwidth of the PSL, the full magnetic oscillation amplitude is recovered in the PSL signals. We also note that for high bandwidth (and high gain $\kappa(f)$) the remaining error signal $\delta\phi_{\text{PSL}}$ becomes negligibly small. The fact that the bandwidth limitation due to the lifetime of the Cs polarization is lifted in this mode of operation rises the question if the resulting increase in signal amplitude goes hand in hand with an increased SNDR. This question will be addressed in Sec. 12.2.7.

4.4.2 Readout mode - Conclusion

Of course, a high bandwidth of the system is desirable, however, a number of arguments finally led to preferring the FF-mode over the PS-mode in most measurements of the ^{3}He FSP, they are discussed below.

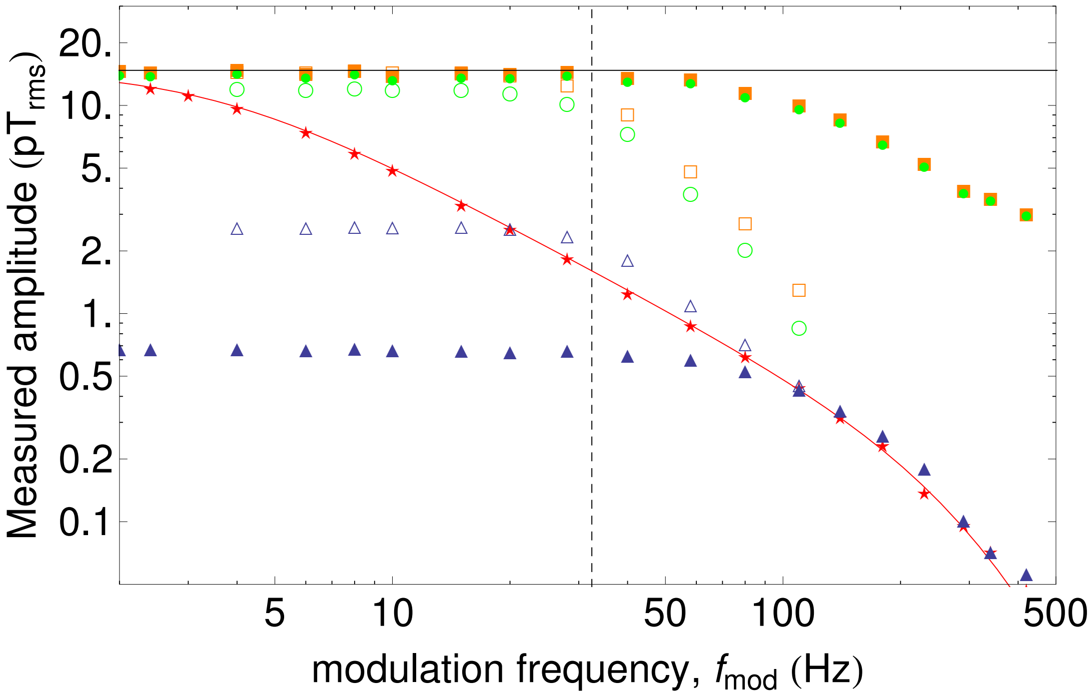

FIGURE 4.5: Measurement of the transfer function of a PSL used to stabilize the CsOPM's phase. Measurements for two different PSLs with $f_{BW,PSL} = 30$ Hz (open symbols) and $f_{BW,PSL} = 100$ Hz (filled symbols) are shown. The magnetic field amplitudes δB_ω and δB_ϕ reflected in the frequency and phase signals from Eq.(4.34) are denoted by the green circles and blue triangles respectively. The total field amplitude δB according to Eq. (4.32) is represented by orange squares. The red stars display a measurement of identical signals by the same CsOPM driven in FF-mode, the solid line connecting the points is again the fitted transfer function $T_{tot}(f)$. From this fit the true magnetic field oscillation amplitude was extracted which is given by the solid horizontal line. The dashed vertical line indicates the ^{3}He precession frequency at 1 μT typically encountered in the experiments described here.

The strongest argument is that the PSL circuit adds a new level of complexity to the system. As we have seen in the previous sections, the phase response of the FF-mode driven CsOPM can be consistently predicted from the measurement parameters. For the PS-mode the exact relations are more complicated and harder to derive due to the unknown properties of the PSL circuit.

The system becomes even more complex when the simultaneous operation of multiple CsOPMs is considered. As described in Sec. 3.1.4, crosstalk is an effect that arises when CsOPMs at different albeit closely-spaced frequencies are operated in spatial vicinity. This would be deemed to happen if the readout CsOPMs were individually driven in PS-mode. Since this has to be avoided, a so-called master-slave scheme, where one CsOPM (master) is run in PS-mode and all remaining sensors (slaves) are driven at the same frequency would have to be employed. This approach has the disadvantage that, since the master dictates the CsOPM drive frequency, it can not be chosen freely to have optimal overlap with all resonances which might lead to a reduced sensitivity of the system. Furthermore, due to the spatio-temporal dependence of the magnetic field created by the ^{3}He FSP, this scheme will *entangle* the readings of the different sensors in a complicated manner.

Let us assume that a PSL with high enough bandwidth to follow the ^{3}He oscillation stabilizes the master and dictates the drive frequency of the slaves. Depending on the relative position of the master and the slaves with respect to the ^{3}He cell this will lead to increased (or decreased) ^{3}He FSP signal amplitudes on the different slaves. The direction of change depends on the phase relation Eq. (4.16) between the two sensors[2]. In contrast to the FF-mode, the individual sensors are no longer independent but depend all on the master CsOPM and their signals are qualitatively different. Not only that this complicates data analysis, in this scheme the whole system will suffer from problems that affect the master, and which thus might, in the worst case, corrupt a whole measurement and not only that of a single sensor.

Because of these considerations all measurements that were to be quantitatively analyzed were performed in the FF-mode of operation. The PS mode was still used for testing and optimizing the apparatus where it is a valuable tool due to its capability to follow large magnetic field changes. This decision should not be misinterpreted as the FF-mode being the superior mode of operation for ^{3}He FSP readout. Which mode proves to be more advantageous depends on the specific application and will have to be judged based on the specific experimental conditions. Given the high achievable bandwidth, the PS-mode remains a very interesting topic for further investigations.

---

[2] This mode of operation actually represents a *hardwired* version of a gradiometer that will be discussed in Chapter 10.

Chapter 5

Prototype construction

In this chapter the design and construction of the prototype magnetometer is described. It was built after various test with simpler measurement arrangements at Universities of Mainz and Fribourg. Its optimal detection geometry is dictated by the considerations presented in Sec. 4.2. As also discussed in that section, certain relative positions between the CsOPMs with respect to the ^{3}He cell are preferable since they lead to phase offsets between the ^{3}He-FSP signals on different sensors that can be exploited in gradiometric measurements. Based on these demands, the design of the prototype magnetometer evolved quite naturally. I will restrict myself to vital components of the combined magnetometer proper here, the ^{3}He cell, the CsOPMs, the elements constituting the mechanical structure of the prototype and the auxiliary parts necessary for preparation and manipulation of the ^{3}He polarization. Details of other parts of the measurement setup, such as amplifiers, lasers and DAQ are given in Sec. 6.1 where the measurements are described.

5.1 The ^{3}He cell

A spherical geometry was chosen for the ^{3}He sample cell of the magnetometer since then the magnetic field produced by the polarized ^{3}He has a dipole shape, as shown in Sec. 4.1. The spherical symmetry simplifies calculations of the field and leaves maximal freedom to the design. It has been shown[FTW69][JDS03] that long ^{3}He spin coherence times can be achieved in uncoated cells made from standard Duran glass. The high transmission ($\sim 90\,\%$,[Gro14]) in the infrared spectrum, at the wavelength of the ^{3}He pump light $\lambda = 1083\,\mathrm{nm}$ and its easy handling during manufacturing made Duran the material of choice. The cell was produced by the glassblower of the Institute of Physics of University of Mainz. It has a diameter of $69-72\,\mathrm{mm}$ and wall thickness of approximately $2\,\mathrm{mm}$, thus a volume of $\sim 140\,\mathrm{ml}$. It was equipped with a thin glass tube terminated by a flange to connect it to the ^{3}He filling system. The cell shows some variations of the index of refraction of the glass over the surface, visible by inspection with the bare eye. These are probably due to internal stress during the manufacturing process and of course undesired since they might influence the polarization of the ^{3}He pump light but can hardly be avoided. Thus the cell was later installed in the magnetometer in an orientation such that the surface traversed by the pump light had minimal imperfections.

A specialized gas handling system exists at University of Mainz that allows evacuation, baking and filling of sample cells, to which the cell was connected after having been thoroughly cleaned with acetone and isopropanol. It was evacuated while being kept at a temperature of $\sim 400\,^\circ\mathrm{C}$ over a period of approximately 1 day. This procedure serves to evaporate and pump away possible contaminations such as remaining water that would increase the depolarization rate of ^{3}He. The cell was first filled with ^{4}He gas at a low pressure and a gas discharge was ignited inside. The optical spectrum of the gas discharge was inspected with a simple prism spectrometer to verify that no emission lines different than those expected from ^{4}He were present. Since no contaminations were found in the spectrum, the ^{4}He was again pumped away and the cell heated and evacuated for another $\sim 24\,\mathrm{h}$. Prior to filling with ^{3}He the heating was switched off and the cell cooled down to room temperature. The ^{3}He gas from a reservoir was led through a liquid nitrogen cold trap and a titanium subli-

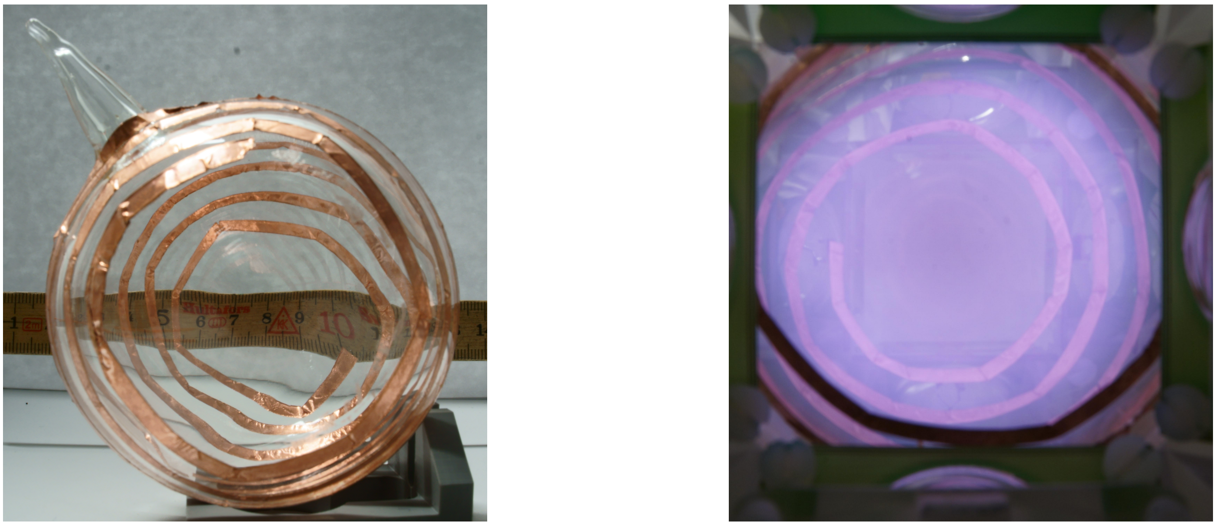
(a)
(b)

FIGURE 5.1: (a) Photograph of ^{3}He cell with early version of spiral copper electrodes. Appendix from filling stem is visible in the upper left. Folding ruler in the back serves to demonstrate lensing effects caused by curvature and imperfections of the glass. (b) ^{3}He cell with ignited gas-discharge mounted inside the magnetometer prototype. The illumination gets weaker towards the cell walls and is strongest in the volume accessible by the pump light.

mation getter before being filled into the gas handling system. After the pressure in the system had reached a value of ~ 1 mbar, the cell was shut off with a valve and immediately sealed and disconnected by melting the stem close to the cell.

Since for optical pumping of the ^{3}He a gas discharge is needed, the cell had to be equipped with electrodes on its outside. These electrodes should allow to maintain a homogeneous discharge in the entire cell volume while still leaving a large area of the cell cross section open for the pump light to traverse it. After tests with various electrode geometries it was found that a spiral shape best suited these requirements. The electrodes were made from self adhesive copper foil and glued to the outside of the cell.

5.2 Cs magnetometer modules

The CsOPMs used in the combined magnetometer are based on modules that were developed by the Atomic Physics Group at the University of Fribourg (FRAP) for the nEDM experiment. Modules of this type have been reported to yield intrinsic magnetometric sensitivities as low as $15\,\mathrm{fT}/\sqrt{\mathrm{Hz}}$ [CBD$^+$09]. More details on their sensitivity and factors limiting sensitivity are given in Chapter 12. They consist of an evacuated, paraffin-coated 30 mm diameter spherical glass cell with a small appendix [CBD$^+$09]. The appendix is connected to the main cell volume by a capillary and holds a droplet of Cs so that the cell volume is filled with Cs vapor that is in thermal equilibrium with the droplet in the appendix. Since the vapor pressure of Cs is rather high, the vapor has sufficiently high optical density at room temperature already. The capillary plays a crucial role to decrease depolarization of pumped Cs atoms by collisions with the bulk metal droplet. It restricts the exchange of atoms between the main volume and the droplet, thereby minimizing this effect. The inner walls of the cell are coated with paraffin to reduce relaxation of atoms due to wall collisions. The coating ensures a long-lived coherence of the polarization created by optical pumping (typically ~ 30 ms) [CBD$^+$09]. Two coils laid out in Helmholtz configuration on printed circuit board (PCB) are enclosing the cell to apply rf magnetic fields. A compact mounting module holds the optical fiber delivering the 894 nm pump light in place and also contains a linear polarizer and $\lambda/4$ plate to circularly polarize the laser beam and a lens to collimate it before traversing the cell. A pho-

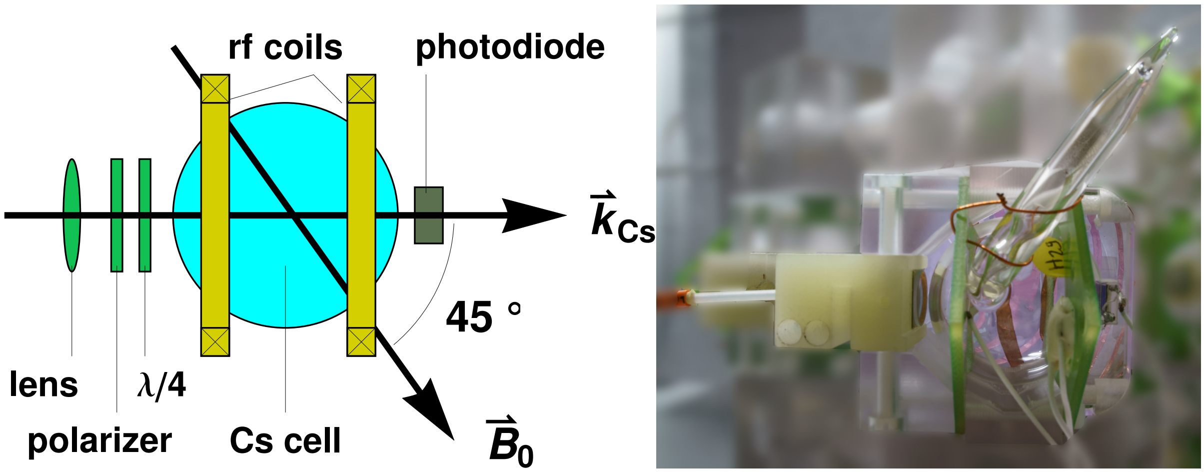

(a) (b)

FIGURE 5.2: (a) Schematic sketch of CsOPM. The pump light enters from the left and passes through polarization and beam shaping optics before traversing the cell on the opposite side of which the transmission is measured by a photodiode. Rf coils in Helmholtz configuration laid out on PCB are installed to produce the oscillating field $\vec{B}_1(t)$along $\vec{k}_{\mathrm{Cs}}$, which is at 45° with respect to $\vec{B}_0$. (b) Photograph of one of the CsOPMs installed in the prototype magnetometer.

todiode is installed on the opposite side of the cell to measure the transmitted light. A schematic drawing of a CsOPM is shown in Fig. 5.2a. The CsOPMs are modified true scalar M_x magnetometers with a detection geometry as described in Sec. 3.1. Analytical expressions for the signals and line-shapes of such magnetometers have been derived in Sec. 3.1.2 and also apply here. Only minor mechanical modifications have been made to the standard FRAP modules to adapt them to the application in the combined magnetometer. The Cs cells, polarization and beam-shaping optics and rf-coils remained unchanged. The redesigned components include a new holder for the photodiode and mounts for the fiber connector block that contains the optical elements and are described in the next section.

5.3 Mechanical structure

The mechanical parts which were to be designed, e.g., the combined ^{3}He/Cs magnetometer prototype had to fulfill the following requirements:

Mechanically hold the ^{3}He cell and the CsOPMs in place satisfying the optimal detection geometry derived in Sec. 4.2.

Provide suitable orientation of all CsOPMs to maximize their sensitivity, e.g., $\sphericalangle(\vec{k}_{\mathrm{Cs}}, \vec{B}_0) = 45^\circ$ (cf. Sec. 3.1.2).

Provide appropriate mounting of the rf-coils of the CsOPMs and the optical fibers delivering the $Cs-D_1$ pump light to ensure $\vec{k}_{\mathrm{Cs}} \parallel \vec{B}_{\mathrm{rf}}$.

Leave enough cross section of the ^{3}He cell perpendicular to $\hat{B}_0$ open for optical pumping.

Host a maximum number of CsOPMs to improve measurement statistics of the combined device.

Have suitable symmetry to form a maximum number of gradiometer pairs as described in Sec. 4.3.

Offer the possibility to measure magnetic field gradients in all three directions by the CsOPMs.

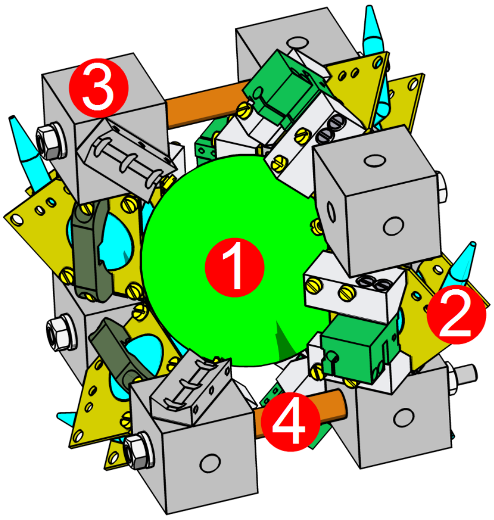

FIGURE 5.3: CAD drawing of prototype magnetometer. One corner and two CsOPMs left away for better visibility. ① spherical ^{3}He cell, ② CsOPM, ③ corner cube, ④ connection rod.

Have appropriate symmetry to allow easy interpolation of the magnetic field at the ^{3}He cell position by CsOPMs.

Have appropriate symmetry so that the rf-fields from the CsOPMs cancel at the ^{3}He cell center (see Sec. 3.3).

Allow for easy modification, e.g. replacement of the ^{3}He cell or the CsOPMs.

Be compact, transportable, nonmagnetic and operational in vacuum.

Following these requirements led to the design shown in Fig. 5.3. The spherical ^{3}He cell (c.f. Fig. 5.3,①) is located in the center of a cubical structure which holds eight CsOPMs (c.f. Fig. 5.3,②) on its edges and is $(110\,\mathrm{mm})^3$ in total size. The prototype magnetometer is symmetric with respect to a plane perpendicular to $\hat{B}_0$ passing through the center of the ^{3}He cell. It can be easily disassembled into two symmetric halves, each holding four CsOPMs. The CsOPMs are positioned according to the optimal detection geometry and, due to the symmetry, in such a way that eight gradiometer pairs can be formed (see Chapter 10 for more details). The CsOPMS are arranged such that pairs of them lie on three mutually perpendicular axes. The distance between ^{3}He cell and the Cs cells is as small as possible, meaning that the cells are touching except for variations of the cell radii. As it was pointed out in Sec.5.1, the ^{3}He cell is not strictly spherical due to the manner of its production. Therefore the distances between the ^{3}He cell-center and the centers of the individual Cs cells vary. They can be estimated to be $r_c = 50(1)\,\mathrm{mm}$. The key structural parts of the assembly are the corner-cubes (c.f. Fig. 5.3,③). All parts of the CsOPMs are mounted to these cubes thereby providing mechanical stability to the CsOPMs proper while also mechanically connecting adjacent CsOPMs thus defining the relative positions of the sensors in the symmetry plane. The two symmetric halves are held together by four rods (c.f. Fig. 5.3,④) also connecting to the corner cubes.

All parts were designed using Autodesk® Inventor® software which offered high flexibility in the planing phase and easy communication with the mechanical workshop during manufacturing. They were produced from polycarbonate by the mechanical workshop of University of Fribourg using nonmagnetic tools. Polycarbonate was chosen for its vacuum compatibility, since it has only a modest outgassing. Although this was not done in the frame of this thesis, it was envisioned that the combined magnetometer might be tested inside the current

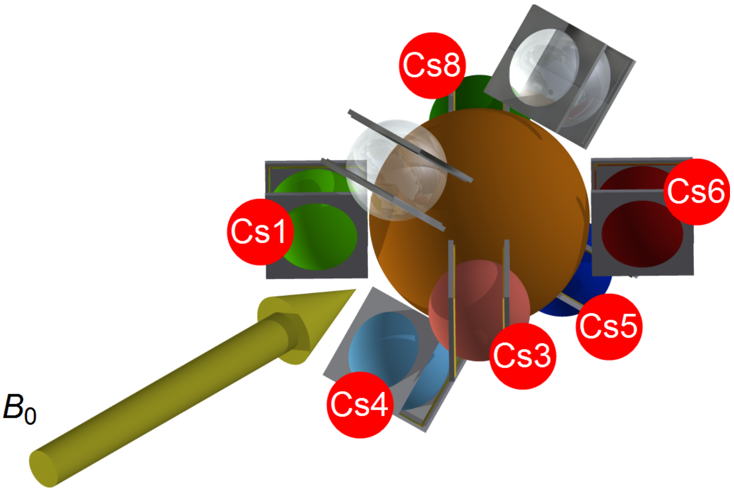

FIGURE 5.4: Schematic drawing of combined magnetometer prototype introducing nomenclature and color-coding of CsOPMs. The two transparent modules are Cs2 (further left) and Cs7 (further right) which were excluded from most of the analysis since they were handled by a different data acquisition system (see Sec.6.1.4 for details). The large sphere in the center is the ^{3}He cell.

nEDM experimental chamber together with the Hg-magnetometer. Since this would require operation in vacuum, all parts were already planned according to these requirements. This includes for example all sack-holes having venting channels to allow efficient evacuation. For the later analysis it is useful to uniquely identify the individual CsOPMs. For this purpose we introduce the nomenclature shown in Fig.5.4. The names are persistently assigned to an individual CsOPM throughout the whole thesis. Whenever colors will be used to identify readings from different CsOPMs, they will refer to Fig.5.4. Colors were chosen such, that lighter and darker variants of the same base color are given to CsOPMs that can form a gradiometer pair along the $\hat{B}_0$ axis (c.f. Sec.4.3).

5.4 Auxiliary parts

In order to make the setup easy to handle and allow reproducible measurements, all additional components needed for the operation of the magnetometer prototype were assembled to form a compact unit. The full setup is shown in Fig. 5.5. The magnetometer rests on four feet (c.f. Fig. 5.5,⑤) made from polycarbonate which have cylindrical pins protruding from the top that slide into corresponding holes on the corner cubes of the magnetometer. The feet are fixed to a nonmagnetic mounting plate (c.f. Fig. 5.5,⑥) and thus the magnetometers position and orientation is reproducible and well defined while still allowing easy removal for inspection. As stated in Sec. 3.2.2, a wide diameter beam of circularly polarized light is needed to pump the ^{3}He. A compact plastic bench (c.f. Fig. 5.5,②) that holds the optical components necessary for preparation of the ^{3}He pump beam is installed at one end of the mounting plate. These are (from right to left) a holder to which the optical fiber from the 1083 nm laser attaches, a $\lambda/2$ plate, lenses forming a telescope, a polarizing beam-splitter cube and a $\lambda/4$ plate. The lenses are used to expand the laser beam in order to illuminate a large cross section of the ^{3}He cell. For efficient polarization the pump light is aligned with the direction of the magnetic field $\hat{k}_{\mathrm{He}} = \hat{B}_0$. After the pump light has traversed the ^{3}He cell it is back-reflected onto itself by a mirror (c.f. Fig. 5.5,③) for a second passage through the cell in order to increase pumping efficiency. A set of Helmholtz coils (c.f. Fig. 5.5,④) is mounted around the magnetometer that can produce a magnetic field perpendicular to $\hat{k}_{\mathrm{He}}$. These coils are used to apply resonant oscillating magnetic fields to manipulate the ^{3}He polarization after optical pumping, e.g., a $\pi/2$ pulse to start the FSP.

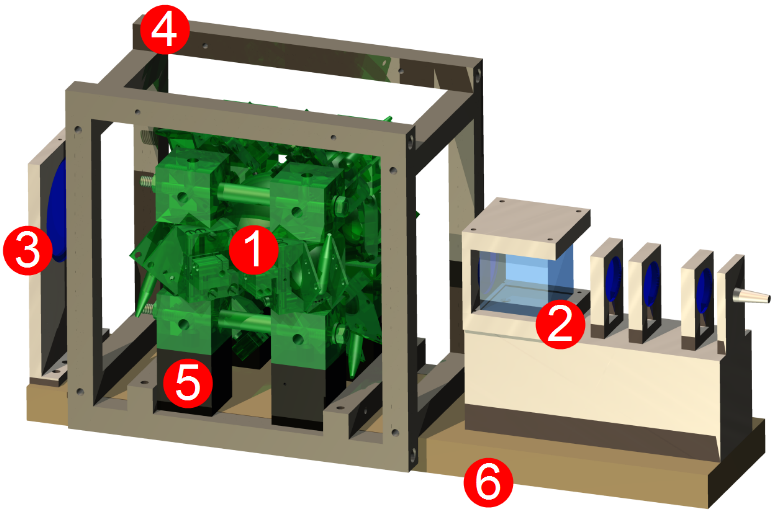

FIGURE 5.5: Prototype magnetometer ① with auxiliary components needed for operation. ② bench holding optics for ^{3}He pump beam preparation, ③ mirror, ④ Helmholtz coil for ^{3}He spin-flip, ⑤ magnetometer feet, ⑥ mounting plate. See text for details.

Chapter 6

Characterization of the magnetometer at PTB

After its general functionality had been demonstrated at Mainz and Fribourg, the magnetometer was taken for further tests to Physikalisch Technische Bundesanstalt (PTB), Berlin. PTB hosts one of the magnetically most silent experimental environments on earth, the Berlin magnetically shielded room 2 (BMSR-2). All the necessary experimental equipment was brought to Berlin for a one-week measurement campaign.

6.1 Experimental setup

In the following, the experimental setup at PTB is described. More details on specific components are given in the subsections. A photograph of the combined magnetometer prototype during measurements at BMSR-2 is shown in Fig. 6.1. A sketch of the general experimental scheme in top-view is displayed in Fig. 6.2. A static, homogeneous holding field of $\sim 1\mu$ T was generated inside BMSR-2 using a large coil system (Fig. 6.2,③ and Fig. 6.1,②) and the ^{3}He/Cs magnetometer (Fig. 6.2,① and Fig. 6.1,①) on its board holding the auxiliary parts described in Sec. 5.4 was placed inside. The magnetometer was located underneath a dewar (Fig. 6.2,② and Fig. 6.1,②) which holds a vector SQUID system provided by PTB. The lasers (Fig. 6.2,⑤) for pumping of ^{3}He and Cs were kept outside the magnetic shielding on a table behind BMSR-2. Their light was fed to the experiment via optical fibers (red line in Fig. 6.2). From the same place the electric currents were supplied (brown line in Fig. 6.2) to the coil system to produce the $\vec{B}_0$ field and the rf-field needed for the FSP-initializing spin flip. The

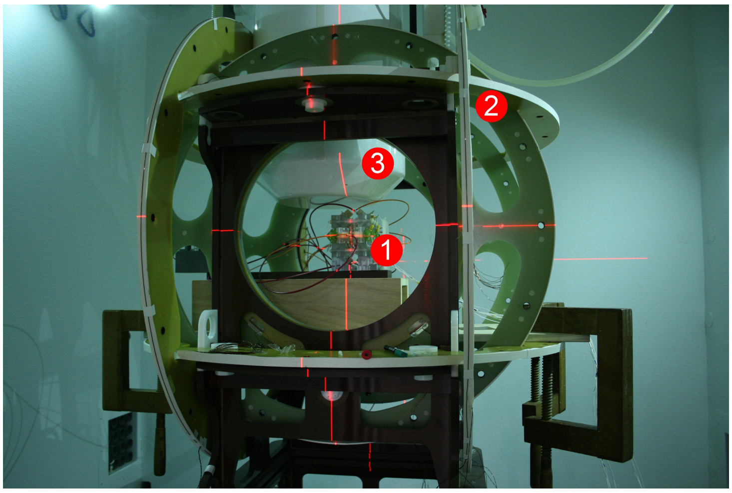

FIGURE 6.1: Photograph of the magnetometer prototype during operation at PTB. ①^{3}He/Cs magnetometer, ②three-axis coil system, ③dewar containing SQUID magnetometer. The red laser cross-hair centered at the magnetometer prototype was used for positioning.

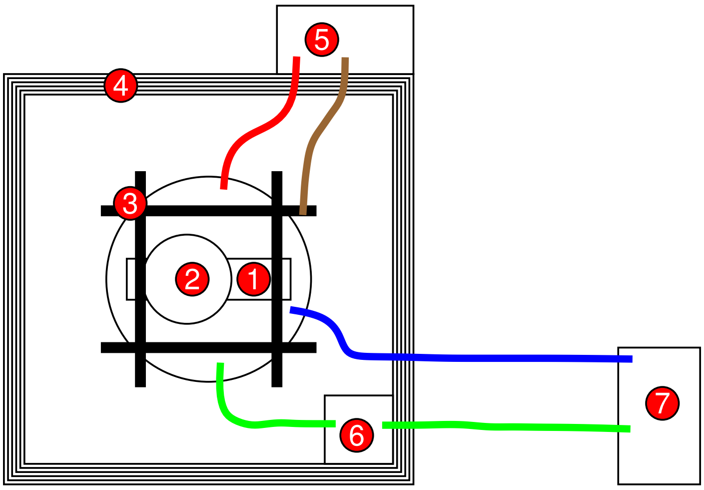

FIGURE 6.2: Schematic drawing of measurement setup at PTB (top view). ① Combined ^{3}He/Cs magnetometer, ② dewar with SQUID system, ③ 3-axis coil system, ④ multilayer magnetic shielding, ⑤ Cs-laser, ^{3}He-laser, supplies for coils, ⑥ transimpedance amplifier, ⑦ DAQ. For details, see text.

measurement signals (green line in Fig. 6.2) were transimpedance-amplified (Fig. 6.2,⑥) inside the shield and then fed to the LIAs (Fig. 6.2,⑦). The rf-coils of the CsOPMs were driven by the same LIA (blue line in Fig. 6.2). In general, a measurement begins with building up ^{3}He spin polarization by MEOP as described in Sec. 3.2.2. This process takes typically 5 – 10 min. Then the He-laser and discharge is switched off and for a short time a weak resonant oscillating magnetic field is applied perpendicular to $\vec{B}_0$ to flip the ^{3}He magnetization by $\pi/2$ and start the FSP (more details on the flipping procedure are given in Chapter 8). Finally the FSP signal is recorded by the CsOPMs and eventually the SQUID system. The measurement period can be as long as ~ 12 h since the ^{3}He polarization is very long-lived.

6.1.1 BMSR2

The BMSR-2 consists of a 7-layer MUMETALL[1] cube and additional aluminum layer, all enclosed in a large rf-shield. Its inner experimental area has dimensions of $3 \times 3 \times 3m^3$. Holes are provided in the walls to feed electrical and optical conducts into the shield. A 304 channel liquid He cooled vector-DC-squid magnetometer is installed at the ceiling which can be flexibly positioned in the chamber[BHK$^+$07]. A three dimensional Helmholtz coil system [HGH$^+$10] was employed to provide the necessary magnetic fields inside the chamber. The coils are made from fiber reinforced plastic and are mechanically connected to form a solid unit. The largest coil pair of the system was used to generate a horizontally oriented B_0 field. For some measurements a second pair was used to produce an oscillating field for the ^{3}He spin flip. The coil current was delivered by a device[2] originally designed to generate currents for the compensation coils used in SQUIDs. It is designed to have extremely low technical noise characteristics which was also proven during measurements.

6.1.2 The Cs pump laser

An extended cavity diode laser[3] with wavelength 894.2 nm and nominal power of 30 mW was used to drive the CsOPMs. A photograph of the Cs-laser and its components is shown in Fig. 6.3. The frequency of the laser is actively stabilized to the Cs-D1 $F = 4 \rightarrow F = 3$ transition by a commercial system[4]. In this system, a Doppler-

---

[1] Registered trademark of Vacuumschmelze GmbH & Co. KG

[2] Model: Magnicon CSE-1

[3] Model: Toptica DL PRO 100

[4] Model: TEM-Messtechnik CoSy-Cs

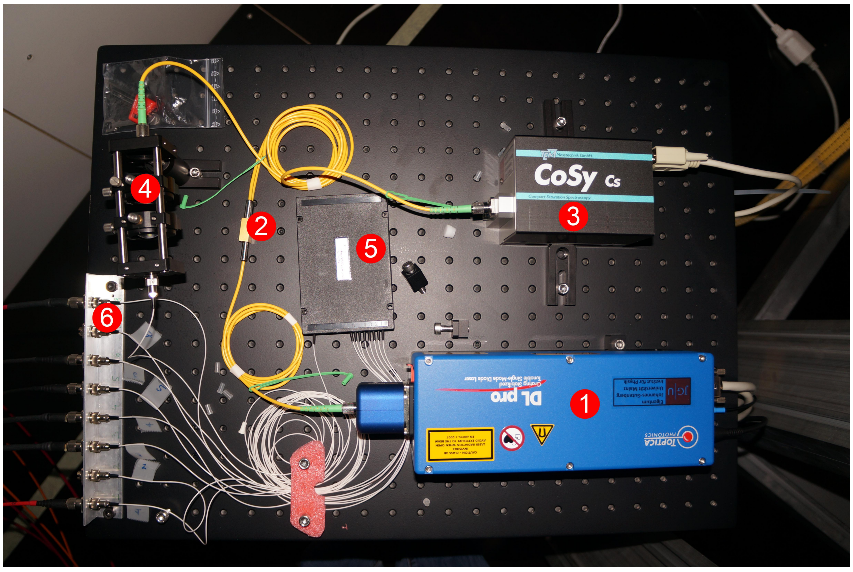

FIGURE 6.3: Photograph of the laser system used to drive the CsOPMs. The components are ① Toptica DL-Pro 100 laser module, ② 1/10 fiber splitter, ③ saturated absorption spectroscopy module, ④ mounting system for insertion of variable attenuators, ⑤ 1 → 8 fiber splitter, ⑥ connector bank for output fibers leading to CsOPMs.

free absorption signal is obtained by saturation spectroscopy, from which an error signal is derived using a LIA. A PID stabilizes this error signal by controlling the laser diode current and voltage of the piezo that defines the length of the cavity. The beam is coupled into a single-mode fiber and then distributed to eight multimode fibers by a fibersplitter, one for each CsOPM. Between the single-mode fiber and the fiber-splitter, variable optical attenuators can be inserted to adjust the output power. The multimode fibers had a length of 3 m each and are represented by the red line in Fig. 6.2.

6.1.3 The ^{3}He pump laser

For optical pumping of the ^{3}He a 2 W ytterbium-doped fiber laser[5] with specified linewidth of 2 GHz at 1083 nm was employed. The laser resided outside of the magnetic shield, its light was brought to the experiment by a 3 m long polarization maintaining fiber. The wavelength of the laser can be adjusted by changing the voltage on the piezo which effectively changes the length of the laser cavity. For pumping it was manually tuned to the C_8 or C_9 transition of ^{3}He. To this aim a weak fraction of the beam, which is provided on a monitor fiber, was sent through a ^{3}He reference cell outside the magnetic shield. A gas discharge was burning in the cell and the fluorescence was observed with a photodiode. The measured spectrum is shown in Fig.6.4 as a function of the tune-value set to the laser module. The C_8 or C_9 transition lines can be unambiguously identified due to their large spacing to the other transitions and the contrast is high enough to be used for tuning. After a short warm-up period, the laser wavelength was quite stable and only minor, if any readjustment was necessary during optical pumping ($\sim$ 8 min). Inside BMSR2 the neccessary optical components for beamshaping and polarization manipulation were mounted on a nonmagnetic optical table next to the ^{3}He/Cs magnetometer as described in Sec. 5.4.

In the course of the measurements it turned out that the fiber connector (FC) of the fiber feeding the experiment was slightly magnetic. Since a quick replacement was impossible, the distance between the FC and the ^{3}He cell was maximized.

---

[5] Model: Keopsys KPS-STD-BT-YFL-1083-05-GIGA-PM-11-CO

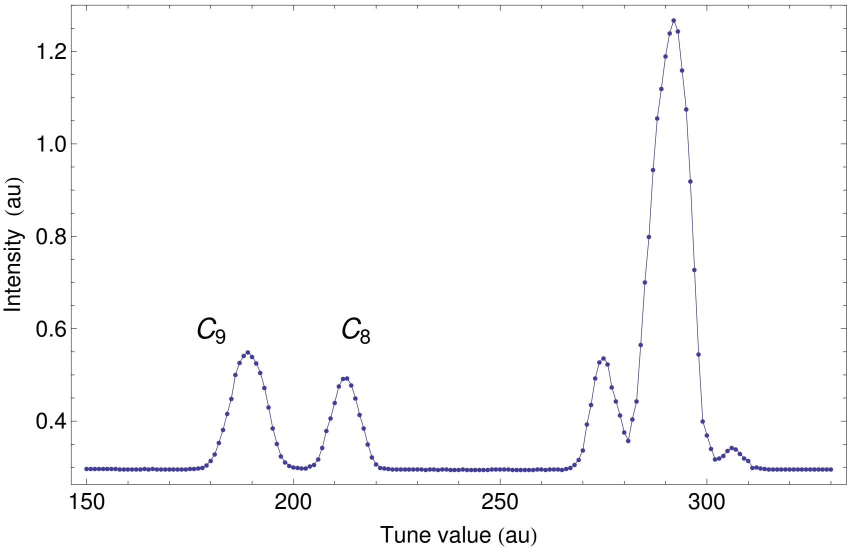

FIGURE 6.4: Fluorescence spectrum of ^{3}He measured in the reference cell used for frequency adjustment. The intensity of the fluorescence light is shown as a function of the tuning value of the laser module. The C_8 and C_8 absorption lines that were used for optical pumping are clearly visible. Compare Fig. 3.8 for the nomenclature of the lines.

6.1.4 Data acquisition

The photodiode signals from the CsOPMs were fed into an eight channel transimpedance amplifier located inside BMSR-2. The amplifier has a specifically tailored gain profile, matched to the requirements of handling signals of CsOPMs in weak fields. Such photodiode signals usually consist of a small modulation ($\sim 0.1\,\mu$A) that contains the measurement information on a large, constant background ($\sim 3\,\mu$A). Therefore the amplifier has a relatively low DC- amplification of 10^4 V/A and a considerably higher AC amplification of 2.53×10^7 V/A. It was placed inside BMSR-2 to minimize AC pickup on the PD cables, which then would be amplified along with the signals thus having a much larger influence than pickup on the already amplified signals. The outputs of the transimpedance amplifier were connected via BNC cables to the inputs of several LIAs. Additionally, each cable was connected to an eight channel data logger[6] that recorded the signals at 32 bit digitization depth and sample rate of ~ 44 kHz. The LIAs are the heart of the DAQ system, they were not only used to demodulate the measurement signals but also provided the rf-frequency to drive the coils of the CsOPMs and served for datalogging. Six CsOPM signals were handled on three identical digital 2-channel LIAs[7] (ZI-LIA). The ZI-LIAs offer a built in logging functionality which was employed to directly record the demodulated phase signals of the six connected sensors. The data was recorded at a sampling rate of 450 Hz and a 14 bit digitization depth. Unfortunately, the two remaining sensors had to be handled by two different [8] LIAs (SR-LIA) because no fourth ZI-LIA was available. This caused some minor inconvenience, the transimpedance amplified signals had to be attenuated before the SR-LIA to match its 1 V input range. The demodulated signals from the SR-LIAs were then fed into a ZI-LIA device via AUX inputs for recording. In retrospect this solution is to be considered as being sub-optimal because the AUX in of the ZI-LIA has an input range of 10 V, the signal only a dynamic range of ~ 1 V. This mismatch results in digitization noise which is visible on the signals of these two sensors. Generally the signal processing chain for these two sensors is not as clean and fully understood which is why they were left out in parts of the analysis.

All three devices feature a functionality that allows to reference the internal (quartz) oscillators to an externally

---

[6] Model: National Instruments NI USB6366

[7] Model: Zurich Instruments ZI HF2

[8] Models: Stanford Research SR810 and SR830

provided frequency. A rubidium atomic clock[9] was used to provide a stable timebase for the ZI-LIAs, the SR-LIAs and the data-logger. Unfortunately, the SQUID DAQ were not referenced to this timebase; this resulted in a notable discrepancy between simultaneous SQUID and ^{3}He/Cs measurements which are described in detail in 11.2.2. A computer-controlled function generator was used to produce a digital signal-train encoding the current date and time of the measurement. This signal was recorded by the ZI-LIAs and the data-logger on separate channels simultaneously with the measurement signals. This allowed to synchronize the data recorded by the four different devices in the off-line analysis by matching these timestamps. The three ZI-LIAs could be synchronized to better than $\Delta t = 1/f_{\mathrm{SR}}$, where $f_{\mathrm{SR}} = 450\,\mathrm{Hz}$ is the DAQ sampling rate using this method.

---

[9] Model: Stanford Research SRS PRS10

Part III

Results

Chapter 7

Data analysis

In this chapter the mathematical toolbox for analyzing the measurement data will be introduced. The methods described here were implemented in dedicated Mathematica codes and the data was analyzed after the measurement had been taken. These techniques will be referred to when used in the following which allows to keep the experimental sections shorter. The procedure of rescaling the measured CsOPM phase signals to magnetic units will be discussed (Sec. 7.1). I will address the problem of frequency estimation by fit routines (Sec. 7.3) with special attention being given to the influence of noise on the estimation process (Sec. 7.4). Mathematical formalisms such as the Cramér-Rao lower bound and the Allan standard deviation will be introduced and their significance in the context of the present study explained (Sec. 7.2, Sec. 7.5).

7.1 Rescaling to magnetic units

As described in Sec. 4.4, the primary measurement data in the FF-mode of operation are phase signals. Several operations, such as determining the ^{3}He FSP frequency, can directly be performed on this data. For other investigations, for example to obtain the value of the magnetic field B_0 at the CsOPMs position, rescaling to magnetic units is necessary. Also it is much more intuitive to express the experimental noise in units of $\mathrm{fT}/\sqrt{\mathrm{Hz}}$ rather than $\mathrm{rad}/\sqrt{\mathrm{Hz}}$. The parameters of the functional dependence that connects a magnetometer's phase reading to the magnetic field at its location is different for each individual CsOPM. Furthermore, due to a subtlety in the CsOPMs response to magnetic field changes, it also depends on the frequency of the magnetic disturbance measured by the CsOPM. The sweep responses described in Sec. 4.4 form the basis of all rescaling procedures.

7.1.1 Rescaling for DC fields

The sweep responses described in Sec. 4.4 and displayed in Fig. 3.6 serve as calibration measurements for the rescaling. From Eq. (3.20), the expected lineshape of the phase response is known, a function

$$\varphi(\omega) = \varphi_0 + \arctan\left(\frac{-\Gamma_2}{\omega_0 - \omega_{\mathrm{rf}}}\right) \tag{7.1}$$

is then fit to the phase response signal to obtain the resonance frequency $\omega_0 = \omega_{\mathrm{L,Cs}}$, the linewidth Γ_2 and the phase offset φ_0. In case of the FF-mode of operation we can use Eq. (4.18) to obtain the relation

$$B_0 = \omega_{\mathrm{L,Cs}}/\gamma_{\mathrm{Cs}} = \left(\frac{-\Gamma_2}{\tan(\varphi - \varphi_0)} + \omega_{\mathrm{rf}}\right)\frac{1}{\gamma_{\mathrm{Cs}}}\,, \tag{7.2}$$

between the measured phase φ and the magnetic field B_0. Here, ω_{rf} is the constant drive frequency and the other parameters were obtained from the sweep response.

7.1.2 Rescaling for AC fields

While the dependence of the CsOPM's phase on the magnetic (DC) field described in the previous section is rather straightforward, additional corrections have to be applied for time-dependent magnetic fields. This is due to bandwidth limitations of the CsOPMs which have different origins that were discussed in Sec. 4.4.1. These effects have to be considered when opting to accurately calculate the amplitude b_{He} of the oscillating magnetic field created by the ^{3}He FSP. It becomes particularly important when amplitude comparisons between different CsOPMs are to be made since τ_{Cs} and thus the transfer function depends on the individual Cs-cell properties via the linewidth Γ_2. To correct for such effects arising from bandwidth limitations, the transfer function $T_{\mathrm{tot}}(f)$ of the signal treatment chain that was calculated in Eq. (4.29) has to be known. The magnetic amplitudes obtained in the DC-rescaling procedure via Eq. (7.2) can then be multiplied by the inverse of $T_{\mathrm{tot}}(f)$ at the respective frequency to obtain the true magnetic field amplitude. For the true value of the ^{3}He FSP amplitude b_{He} we thus obtain

$$b_{\mathrm{He}} = b'_{\mathrm{He}} \frac{1}{T_{\mathrm{tot}}(\omega_{\mathrm{L,He}})} . \tag{7.3}$$

As can be seen from Fig. 4.4, these bandwidth limitations significantly change the ^{3}He FSP amplitudes. An example for the application is given in Sec. 12.2.6 where the true field is calculated from a number of running magnetometers.

7.2 Cramér-Rao lower bound

The data analysis relies to a large extent on estimating the frequency of sinusoidal signals; this makes it necessary to investigate this procedure from a more theoretical point of view. In the course of this thesis the question of sensitivity of the combined magnetometer will be addressed (Chapter 12), meaning how precisely (i.e., with which statistical uncertainity) can a magnetic field be measured in a given time. Since the magnetic fields are calculated from the measured Larmor frequencies according to Eq. (3.24), the field estimation uncertainty ΔB_0 scales in the same way as the frequency estimation error $\Delta\omega_{\mathrm{L,He}}$, i.e.,

$$\Delta B_0 = \Delta\omega_{\mathrm{L,He}} / \gamma_{\mathrm{He}} . \tag{7.4}$$

It is intuitive to expect that the achievable precision of each frequency estimation will depend on the signal parameters, e.g., the amplitude, the measurement noise and the measurement time. The rigorous mathematical treatment of this problem was done by Cramér and Rao in [RR45], [Cra46] who derived a lower limit for the variance of the frequency estimate from a *coherent* single-tone sinusoidal signal affected by white noise. This so called Cramér-Rao lower bound (CRLB) is based on information theoretical considerations, a short derivation of which is given in Appendix A. The result is important since it serves as a theoretical limit for the estimation processes used in the data analysis and thus sets a theoretical limit on the achievable magnetometric sensitivity for given measurement parameters (such as signal amplitude, noise, measurement time).
We consider a single tone sinusoidal signal with constant rms amplitude

$$a^{rms}_{\mathrm{He}} = a/\sqrt{2} \qquad \text{and frequency} \qquad \omega_{\mathrm{L,He}} = 2\pi f_{\mathrm{He}} \tag{7.5}$$

affected by (white) Gaussian amplitude noise $\mathscr{G}$ with variance $\sigma^2_{\mathscr{G}}$. Gaussian noise has a constant power spectral density ρ^2, to which the variance relates via

$$\sigma^2_{\mathscr{G}} = \rho^2 f_{\mathrm{BW}} , \tag{7.6}$$

where f_{BW} is the measurement bandwidth that is connected to the sampling rate $f_{\mathrm{SR}} = 1/T_{\mathrm{SR}}$ through Shannon's sampling theorem via

$$f_{\mathrm{BW}} = f_{\mathrm{SR}}/2 = \frac{1}{2T_{\mathrm{SR}}} . \tag{7.7}$$

We further define the signal to noise-density ratio (SNDR)[1] as the ratio between the rms-amplitude of a signal

---

[1] This definition may seem trivial, but it has in fact an impact on many other quantities introduced in the following. This choice often allows to express quantities of interest in a more general way, independent of the measurement bandwidth. We note that according to the definition Eq. (7.8), the unit of the SNDR is $\sqrt{\mathrm{Hz}}$.

and the square root power spectral density of the noise. For the ^{3}He FSP signal in particular this means that

$$SNDR = \frac{a_{\mathrm{L,He}}^{rms}}{\rho} . \tag{7.8}$$

We model the measurement data as a discrete time series of equi-spaced points

$$S_n = a_{\mathrm{He}}^{rms} \sin(\omega_{\mathrm{L,He}} n T_{\mathrm{SR}} + \phi_0) + \mathcal{G}(n) \qquad \text{with} \qquad n \in \mathbb{N}, \tag{7.9}$$

where $\mathcal{G}(n)$ is the noise contribution to the n-th data point. The CRLB of a frequency estimation from such a discrete-sample signal of constant amplitude has been derived in [RB74] and reads

$$\sigma_{\mathrm{f}}^2 \geq \frac{6}{(2\pi)^2 \, \mathrm{SNDR}^2 \, T_{\mathrm{M}}^3} , \tag{7.10}$$

where T_{M} is the measurement time. For later reference we also introduce the corresponding CRLB for magnetic field estimation from a ^{3}He FSP signal that is related to Eq. (7.10) via[2] Eq. (3.24) and reads

$$\sigma_{\mathrm{B}}^2 \geq \frac{6}{\mathrm{SNDR}^2 \, T_{\mathrm{M}}^3 \gamma_{\mathrm{He}}^2} \qquad \text{or} \qquad \sigma_{\mathrm{B}} \geq \frac{\sqrt{6}\rho}{a_{\mathrm{L,He}}^{rms} \, T_{\mathrm{M}}^{3/2} \gamma_{\mathrm{He}}} , \tag{7.11}$$

where γ_{He} is the ^{3}He gyromagnetic ratio given by Eq. (3.25). A similar bound $\sigma_{\mathrm{f,dec}}^2$ can be found for an exponentially damped oscillation [GHK+10] $a(t) \sim e^{-t/T_2^*}$ that differs from Eq. (7.10) by the factor

$$C(T_{\mathrm{M}}, T_{\mathrm{SR}}, T_2^*) = \frac{T_{\mathrm{M}}^3}{6 \, T_{\mathrm{SR}}^3} \cdot \frac{(1 - e^{-2T_{\mathrm{SR}}/T_2^*})^3 \, (1-\alpha)}{e^{-2T_{\mathrm{SR}}/T_2^*} (1-\alpha)^2 - (T_{\mathrm{M}}/T_{\mathrm{SR}})^2 \, \alpha (1 - e^{-2T_{\mathrm{SR}}/T_2^*})^2} \tag{7.12}$$

where

$$\alpha = e^{-2T_{\mathrm{M}}/T_2^*} \tag{7.13}$$

and T_2^* is the time constant of the decay of the signal amplitude. It thus holds

$$\sigma_{\mathrm{f,dec}}^2 = \sigma_{\mathrm{f}}^2 \cdot C(T_{\mathrm{M}}, T_{\mathrm{SR}}, T_2^*) . \tag{7.14}$$

The factor Eq. (7.12) takes damping into account, or more intuitively spoken, complies with the fact that with shrinking amplitude also the information content of the signal diminishes. In the limiting case of vanishing damping, $C(T_{\mathrm{M}}, T_{\mathrm{SR}}, T_2^*)$ becomes unity and Eq. (7.14) reduces to Eq. (7.10). Under the assumption of a sufficiently high sampling rate, e.g., $T_{\mathrm{SR}} \ll 2\pi/\omega_{\mathrm{He}}$, an approximative form of Eq. (7.12) independent of T_{SR} can be found. It reads

$$C(r) = \frac{e^{2/r} - 1}{3r^3 \cosh\left(\frac{2}{r}\right) - 3r\left(r^2 + 2\right)} , \tag{7.15}$$

with $r = T_2^*/T_{\mathrm{M}}$ being the ratio of the decay and measurement time. A plot of Eq. (7.15) is shown in Fig. 7.1. The behavior of $C(r)$ is of high importance, since the ^{3}He FSP signals will in general have an exponentially decaying amplitude due to relaxation of the polarization. Examination of Fig. 7.1 shows, however, that the relaxation can be neglected for measurement times that are short compared to the decay time, e.g., $T_{\mathrm{M}} \ll T_2^*$ or $r \gg 1$. For such short measurement times, the signal amplitude can be considered constant and simple fit functions like Eq. (7.16) can be used to extract the signal parameters. As we will see in a later chapter (Chapter 9), the decay time of ^{3}He polarization in the measurements presented here was significantly longer than the typical measurement timescale ($T_2^* \approx 13000\,\mathrm{s} \gg \mathrm{T_M} \sim 100\,\mathrm{s}$), which allows this simple treatment to be used throughout most of the data analysis.

---

[2] We note that Eq. (7.10) is valid for all frequency estimation processes. The corresponding field-CRLB then depends on the gyromagnetic ratio of the spin species under study.

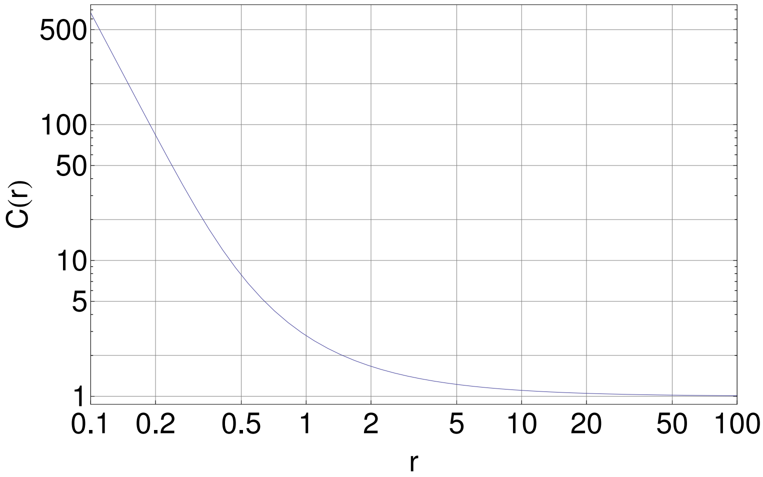

FIGURE 7.1: Plot of the CRLB degradation function $C(r)$ for a damped sine wave as a function of $r = T_2^*/T_\mathrm{M}$, the ratio of decay to measurement time.

7.3 Fitting

As stated Sec. 4.4, most measurements were done in the FF-mode of operation. There the expected phase signal of a CsOPM measuring the ^{3}He FSP has also been theoretically derived. This leads quite naturally to choosing the function

$$f(t) = f_0 + f_1 \sin(\omega_{\mathrm{L,He}} t + f_2) \tag{7.16}$$

to describe the phase signal of the CsOPMs (cf. Eq. (4.25)), which describes a single tone oscillation on a constant offset. As noted before, this assumes a stable magnetic field and only holds for timescales on which the decay of ^{3}He polarization can be neglected. The built-in function "NonlinearModelFit" of Mathematica was used which performs a least mean squares algorithm to estimate the parameters of the model function. Under the condition that only white Gaussian noise is affecting the measurement signal, this routine should yield an unbiased estimator and the fit uncertainity should correspond to the measurement uncertainty.

7.4 Noise-level correction

In general, as described in Sec. 7.3, the magnetic field is calculated from the measurement signal by estimating the ^{3}He Larmor frequency using a fit routine. A crucial part of the data analysis is the determination of the measurement uncertainty since this defines the magnetometer sensitivity. The assumption that the uncertainties of the estimate produced by the fit routine reflect the measurement uncertainties does not hold any more when the data is affected by other than Gaussian noise. Since the CsOPM phase signals undergo low-pass filtering in the LIA, it is expected that the noise is correlated to a certain degree.

For an unfiltered signal sampled at a rate $f_{SR} = 1/T_\mathrm{SR}$, the bandwidth is equal to $f_{BW} = f_{SR}/2$, due to Shannon's sampling theorem. A different case applies for a filtered signal; here the bandwidth is limited by the filter characteristics rather than by the sampling rate. The noise equivalent power bandwidth (NEPBW) of a low pass filter is defined as the equivalent bandwidth of an ideal brickwall-filter[3] that transmits the same integral white noise power (cf. Fig. 7.2). Generally, the NEPBW can be calculated from the transfer function $T(f)$ of the filter under consideration according to

$$\int_0^\infty T_\mathrm{Brick}(f)^2 df = \int_0^{\mathrm{NEPBW}} 1 df \equiv \int_0^\infty T(f)^2 df, \tag{7.17}$$

---

[3] An ideal low pass brickwall-filter has a rectangular transfer function T_Brick which jumps from unity to zero at the bandwidth limit. $T_\mathrm{Brick} = 1$ for $f \leq \mathrm{NEPBW}$ and $T_\mathrm{Brick} = 0$ for $f > \mathrm{NEPBW}$.

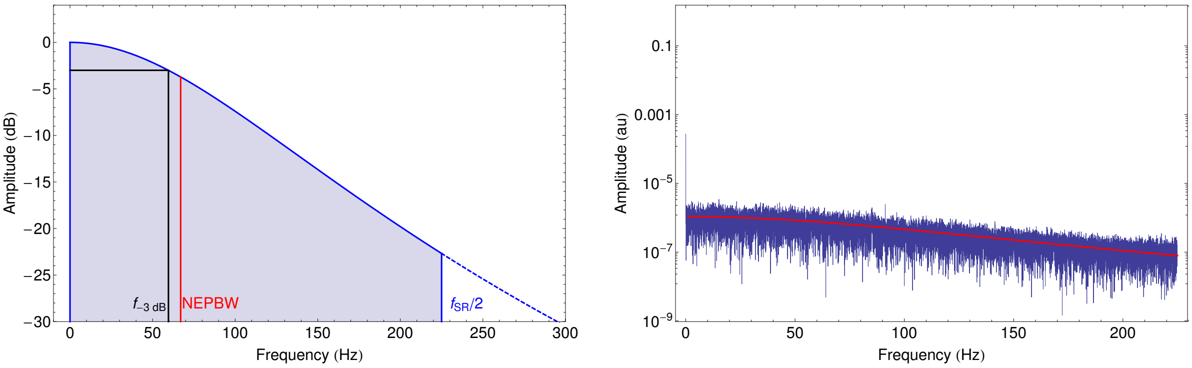

FIGURE 7.2: Transfer function $T_{\mathrm{LIA}}(f)$ of low-pass with $\tau = 1.16\,\mathrm{ms}$, $n = 4$ (left). Three characteristic frequencies are shown: The -3dB cutoff frequency $f_{-3dB} = 59.6\,\mathrm{Hz}$ (black), the NEPBW = 67.1 Hz (red) and the bandwidth limit $f_{SR}/2$ due to a finite sampling rate (blue). An FFT spectrum of the noise track from a phase signal (right) shows the effect of the filtering on the data in the frequency domain. The red line is (theoretically) obtained from a white noise spectrum filtered by a low-pass with the given characteristics and adequately describes the experimentally observed spectrum.

where the upper integration bound on the right hand side has to be replaced by the bandwidth f_{BW} used during the recording (e.g. by sampling at a rate $f_{\mathrm{SR}} = 2 f_{\mathrm{BW}}$) of the filter output. A typical filter transfer function is drawn in Fig. 7.2 (left) together with different characteristic frequencies. As shown in Fig. 7.2 (right), the noise spectrum of the LIA phase data is clearly not Gaussian. The observed shape matches well the prediction arising from an initially flat noise floor after filtering by a low-pass described by $T_{\mathrm{LIA}}(f)$ (red line)[4]. For a non-Gaussian noise floor, the estimation precision of the frequency will only depend on the noise level under the peak, i.e., the signal to noise ratio. Since the uncertainties calculated by the fit routine are derived from the fit residuals, they will only reflect the true measurement uncertainties when the noise has a constant power spectral density (PSD). To deal with this situation, and still obtain realistic uncertainties from the fit routine, the noise under the peak ρ_{He} is estimated from an FFT spectrum and a variance corresponding to Gaussian noise of this PSD at a bandwidth of $f_{SR}/2$ manually imposed to the fit. Figure 7.3 illustrates the procedure.

---

[4] Having still in mind the considerations presented in Sec. 4.4.1, one might wonder why the FFT of the noisetrack in Fig. 7.2(right) is adequately described by the transfer function $T_{\mathrm{LIA}}(f)$ only, neglecting $T_{\mathrm{Cs}}(f)$. The reason is that the white noise present in the system is strongly dominated by the photocurrent shotnoise, as can be seen from a calculation presented in Sec. 12.2. This noise is substantially different from noise arising from magnetic perturbations as described in Sec. 7.1.2, since it does not depend on the ODMR process in the CsOPM. As a consequence it is also not affected by the bandwidth limitations arising from the lifetime of the Cs-polarization but by the LIA filter only. This also leads to important implications for the SNDR which are presented in Sec. 12.2.3.

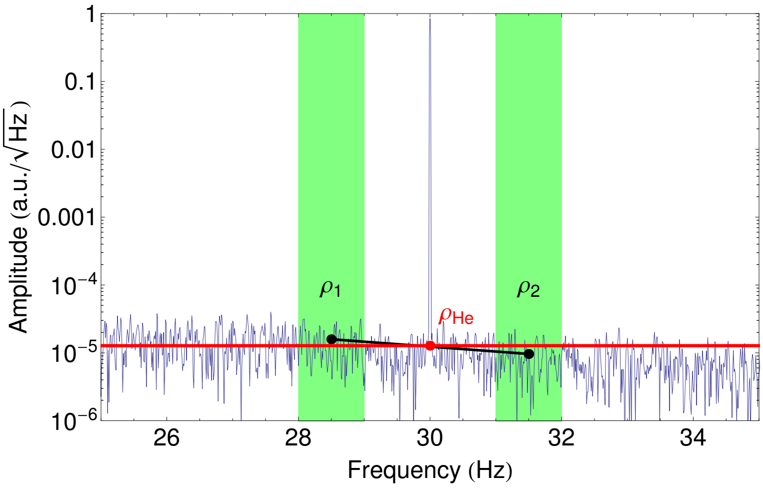

FIGURE 7.3: Sketch to illustrate noise correction procedure. The noise levels in two frequency intervals (green) enclosing the peak are measured (ρ_1, ρ_2, black dots). Then the noise under the peak (ρ_{He}, red dot) is estimated by a linear interpolation. A variance corresponding to a constant square root noise power spectral density over the whole acquisition rate-limited bandwidth is imposed on the fit routine. The procedure proved to be robust for reasonable width and spacing of the two intervals.

7.5 Allan standard deviation

In the course of the thesis the question of sensitivity of the ^{3}He/Cs magnetometer will be addressed. There, we will make use of a mathematical tool that is common in the scientific community investigating the temporal stability of clocks. This so-called Allan variance (AV), and its square root, the Allan standard deviation (ASD) will be mathematically introduced here without further discussion. Its significance for the measurements in the scope of this thesis will be explained in Chapter 12, where it is actually used. Detailed accounts of its properties and application are given in [SAHW90].

We consider a set of data

$$y_i = \langle x(t) \rangle_\tau \,, \tag{7.18}$$

where each point corresponds to the temporal expectation value of a quantity $x(t)$ (in our case frequency, or magnetic field) measured over a given integration time τ. The AV is then defined as

$$\sigma^2_{Allan}(\tau) = ASD^2(\tau) = \frac{1}{2}\langle (\Delta y)^2 \rangle \,, \tag{7.19}$$

where $\langle\,\rangle$ denotes the average value of the quantity in the brackets and $(\Delta y)^2 = (y_{i+1} - y_i)^2$ is the squared difference of two consecutive values of the data set. Usually a graphical representation of $ASD(\tau)$ as a fuction of τ will be presented that reflects the dependence of the ASD on the integration time. These ASD plots can help to distinguish the different sources of noise / instability affecting the measurement variable $x(t)$.

In the presence of white noise only, the ASD is identical to the classical standard deviation. This identity results in some implications for the ASD's dependence on the integration time, which we will discuss now.

When a signal with a magnitude proportional to the magnetic field (or Larmor frequency), $x_i = x(t_i) \propto |B_0|$ is analyzed, the process that produces the temporal expectation value in in Eq. (7.18) is a simple statistical averaging. This case applies when the phase signal of a CsOPM or the reading of a SQUID, both in the absence of the ^{3}HeFSP are considered. The $x_i = x(t_i)$ are statistically independent (field, frequency) measurements, the time dependence of the ASD is

$$ASD(\tau) \propto \frac{1}{\tau^{1/2}} \,. \tag{7.20}$$

Due to the short coherence time (on the order of milliseconds) these values have to be considered as independent.

When the ^{3}He signal is considered, the situation is different. The ^{3}He could be measured either by CsOPMs or SQUIDs. The primary measurement data is a *coherent* oscillation and we are interested in the average frequency over an integration time τ. Each point y_i will thus be an estimate of this oscillation frequency over a time τ. In the best case, these estimates will be CRLB limited and the ASD will have the same time dependence as $\sqrt{\sigma_{\mathrm{f}}^2}$ in Eq. (7.11),

$$ASD(\tau) \propto \frac{1}{\tau^{3/2}}\,. \tag{7.21}$$

The uncertainty of an $ASD(\tau)$ value depends on the ratio between the total measurement time of recorded data used in the computation T_{tot} and τ and was derived in [BCC$^+$71]. An expression for the relative uncertainty ΔASD is given by

$$\frac{\Delta ASD}{ASD} = \frac{1}{\sqrt{2(T_{\mathrm{tot}}/\tau - 1)}}\,. \tag{7.22}$$

This implies that in order to have small errors on the $ASD(\tau)$ values for large τ, the signal has to be measured for a very long time. For the ASD plots shown in this thesis we usually calculate $ASD(\tau)$ up to values of $\tau = T_{\mathrm{tot}}/5$, which leads to an uncertainty of $\Delta ASD = 33\,\%$ for the last point shown, using Eq. (7.22).

7.6 Mean values

Throughout the data analysis we will often face the situation of having to calculate mean values of multiple measurements. For a set of independent measurement values v_i having uncertainities Δv_i the weighted mean $\widetilde{v}$ will be calculated using the formula

$$\widetilde{v} = \frac{\sum \frac{v_i}{\Delta v_i^2}}{\sum \frac{1}{\Delta v_i^2}}\,. \tag{7.23}$$

The standard error of $\widetilde{v}$ is then given by

$$\Delta \widetilde{v} = \left(\sum \frac{1}{\Delta v_i^2} \right)^{-1/2}\,. \tag{7.24}$$

Chapter 8

^{3}He spin flip

Prior to a measurement, after polarization, the ^{3}He spins have to be flipped out of the direction of the $\vec{B}_0$ field in order to start the FSP. In the experiments described here, this was done by irradiation with a resonant oscillating magnetic field perpendicular to the main field. The spin-flip angle depends on the amplitude and frequency of these oscillating fields and the duration of the irradiation. For obvious reasons, we opt to reproducibly flip the spin exactly by $\pi/2$. This is of particular importance having the nEDM application in mind. It was shown[Len09] that a precise control of the flipping angle is necessary to exclude an influence of the magnetic field created by the ^{3}He polarization on the UCN precession. In this section, a method will be introduced that allows to experimentally control the flipping angle.

8.1 The spin flip in the RWA

In Chapter 2 the Bloch equations were introduced and in Sec. 3.1.2 they were used to derive the lineshapes of an M_x magnetometer in the RWA. A similar case applies when we use a resonant oscillating field to flip the ^{3}He magnetization after polarization to start the FSP. However here, the decay mechanisms can be neglected in the theoretical treatment since the ^{3}He polarization is much longer lived than that of Cs. We thus consider a static magnetic field $\vec{B}_0 = B_0\hat{z}$ and an oscillating perpendicular field $\vec{B}_{\rm rf}(t) = B_{\rm rf}\cos(\omega_{\rm rf}t)\hat{x}$. Now, in analogy to the procedure in Sec. 3.1.2, we move to a coordinate frame rotating at $\omega_{\rm rf}$. In the RWA, $B_{\rm rf}$ becomes static in that frame and we get an additional field $-\omega_{\rm rf}/\gamma_{\rm He}$ along $\hat{z}$, the effective field is $(B_{\rm rf}, 0, B_0 - \omega_{\rm rf}/\gamma_{\rm He})$. Using Mathematica, the Bloch equations can be solved in the rotating frame and the solution in the laboratory frame found by applying the back-rotation. When assuming a spin polarization $|\vec{S}| = 1$ initially oriented along $\hat{z}$ and defining $\delta\omega = \omega_0 - \omega_{\rm rf}$, the expression reduces to

$$\vec{S}(t) = \begin{pmatrix} \frac{e^{-ct}\omega_1}{2}\left(\frac{(e^{ct}-1)^2(\omega_0-\omega_{\rm rf})\cos(\omega_{\rm rf}t)}{c^2} + \frac{(e^{2ct}-1)\sin(\omega_{\rm rf}t)}{c}\right) \\ \frac{e^{-ct}\omega_1}{2}\left(\frac{(e^{ct}-1)^2(\omega_0-\omega_{\rm rf})\sin(\omega_{\rm rf}t)}{c^2} + \frac{(e^{2ct}-1)\cos(\omega_{\rm rf}t)}{c}\right) \\ -\frac{(\omega_0-\omega_{\rm rf})^2+\omega_1^2\cosh(ct)}{c^2} \end{pmatrix} = \begin{pmatrix} \frac{\omega_1}{\Omega^2}\left(\delta\omega(1-\cos(\Omega t))\cos(\omega_{\rm rf}t) + \Omega\sin(\Omega t)\sin(\omega_{\rm rf}t)\right) \\ \frac{\omega_1}{\Omega^2}\left(\delta\omega(1-\cos(\Omega t))\sin(\omega_{\rm rf}t) - \Omega\sin(\Omega t)\cos(\omega_{\rm rf}t)\right) \\ \frac{\delta\omega^2+\omega_1^2\cos(\Omega t)}{\Omega^2} \end{pmatrix}, \tag{8.1}$$

where we have introduced $\omega_1 = \gamma_{\rm He}B_{\rm rf}$ and

$$c = \sqrt{-\omega_0^2 + 2\omega_0\omega_{\rm rf} - \omega_{\rm rf}^2 - \omega_1^2} \equiv i\Omega \tag{8.2}$$

with $\Omega = \sqrt{\delta\omega^2 + \omega_1^2}$. Equation (8.1) describes the motion of $\vec{S}$ on a sphere in a direction and by an angle that depend on the strength and frequency of the oscillating field $\vec{B}_{\rm rf}$. The result is visualized in Fig. 8.1 for three different values of detuning from resonance. We see, that for a large detuning the spin is only partially flipped (c.f. Fig. 8.1a). When $\omega_{\rm rf}$ approaches ω_0 (c.f. Figs. 8.1b,8.1c) the flip angle increases until the spin completely reverses its orientation. From Eq. (8.1), we can directly conclude a relation for the flip-angle as a function of

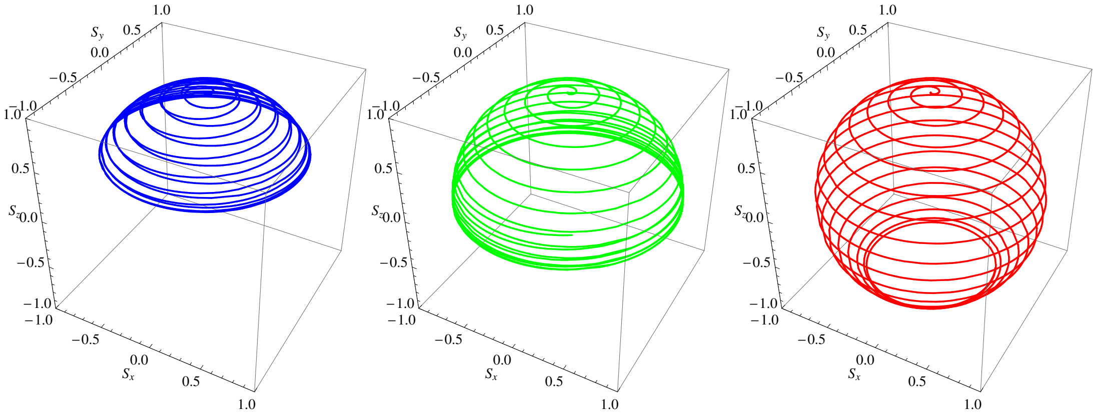

(a) (b) (c)

FIGURE 8.1: The spin vector moves on the surface of the Bloch sphere, according to Eq. (8.1). For all three plots, the parameters $B_{\mathrm{rf}} = 30\,\mathrm{nT}, B_0 = 1\,\mu\mathrm{T}, t = 0.5\,\mathrm{s}$ and $\gamma = \gamma_{\mathrm{He}}$ were chosen. They differ by the frequency of the applied oscillating field, $\omega_{\mathrm{rf}} = 0.95\omega_0$ in (a), $\omega_{\mathrm{rf}} = 0.97\omega_0$ in (b) and $\omega_{\mathrm{rf}} = 0.99\omega_0$ in (c).

time:

$$\theta_{\mathrm{flip}} = \arccos\left(\frac{\delta\omega^2 + \omega_1^2\cos(\Omega t)}{\Omega^2}\right), \tag{8.3}$$

which reduces to the well known expression

$$\theta_{\mathrm{flip}} = B_{\mathrm{rf}}\gamma_{\mathrm{He}}t \tag{8.4}$$

for a resonant field $\omega_{\mathrm{rf}} = \omega_0$. Although very simple, this equation is not really practical from an experimental point of view since the field B_{rf} might not necessarily be well known. During the measurements at PTB we followed an experimental approach to determine suitable flip parameters, which is described in the following.

8.2 Experimental determination of flip parameters

In order to investigate the flipping procedure, ^{3}He was polarized along $\vec{B}_0$ and a weak magnetic field oscillating at ω_{rf} perpendicular to $\vec{B}_0$ was produced by applying a small voltage from a function generator to a suitable coil (BMSR-2-y). A reasonable amplitude B_{rf}, typically on the order of nT, and frequency ω_{rf} for the rf-field was chosen. The rf frequency should be as close as possible to the ^{3}He resonance frequency $\omega_{\mathrm{L,He}}$, a reasonable value can be inferred from measurements of the CsOPMs resonances $\omega_{\mathrm{L,Cs}}$. During this procedure, the phase signals of the CsOPMs (driven in FF-mode) were inspected on the oscilloscope and recorded.

One would expect that the signals can be qualitatively deduced from the following considerations: The CsOPMs measure the modulus of the magnetic field at their specific position. After optical pumping, when the ^{3}He magnetization points along $\hat{B}_0$, no precession occurs. There is only a constant offset magnetic field produced by the polarized ^{3}He sample that adds to the main field, yielding $\vec{B}_{\mathrm{Tot}} = \vec{B}_0 + \vec{B}_{\mathrm{off}}(\theta_{\mathrm{flip}})$. When we consider the magnetization being gradually driven out of the $\hat{B}_0$ direction, precession starts. With increasing flip angle the offset component $\vec{B}_{\mathrm{off}}(\theta_{\mathrm{flip}})$ decreases, while the oscillatory component $\vec{B}_{\mathrm{He}}(t,\theta_{\mathrm{flip}}) = a_{\mathrm{He}}(\theta_{\mathrm{flip}})\cos(\omega_{\mathrm{He}}t)$ gains in amplitude. The total field can be described by $\vec{B}_{\mathrm{Tot}}(t,\theta) = \vec{B}_0 + \vec{B}_{\mathrm{off}}(\theta_{\mathrm{flip}}) + \vec{B}_{\mathrm{He}}(t,\theta_{\mathrm{flip}})$. This trend peaks at a flip angle of $\theta_{\mathrm{flip}} = \pi/2$ with respect to $\hat{B}_0$, where the oscillation amplitude $a_{\mathrm{He}}(\theta_{\mathrm{flip}})$ is maximum and the offset $\vec{B}_{\mathrm{off}}(\theta_{\mathrm{flip}})$ vanishes. For flip angles $\theta_{\mathrm{flip}} > \pi/2$ the oscillation amplitude starts to decrease again and an offset field with opposite sign starts to build up until the magnetization has completely reversed its orientation. Then the procedure starts from the beginning. The result is a slow oscillation corresponding to the change of the S_z component during the spin flip and an overlaid fast oscillation with changing amplitude originating from

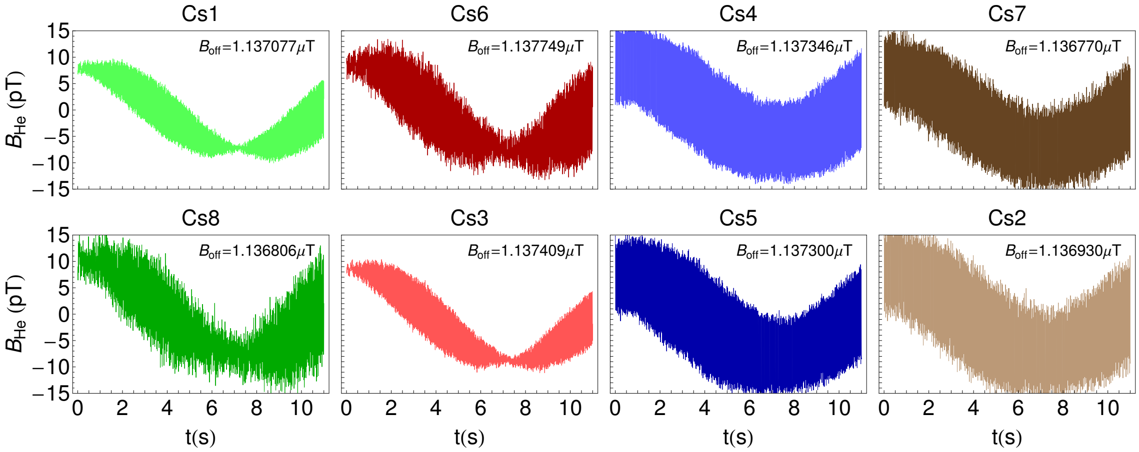

FIGURE 8.2: Signals of all eight CsOPMs showing the Rabi nutation of ^{3}He magnetization. All plots have common abscissa, the ordinate of each plot is shifted by an individual amount B_{off} denoted in the plot to a common range around zero. The magnetization is flipped by approximately $3\pi/2$. One sees that there are two qualitatively different types of signals. For the four sensors on the left (Cs1,Cs8, Cs6, Cs3), the underlying fast oscillation vanishes at the peak-amplitude points of the slow oscillation, for the other sensors (Cs4, Cs5, Cs2, Cs7) it does not. Explanation, see text.

the precession, so change of the S_x and S_y components. Besides different offsets due to local differences of the B_0 field at the positions of the individual sensors, one would expect the signals from all CsOPMs to look qualitatively identical from these considerations.

Figure 8.2 showing the signals of all eight CsOPMs during a flip reveals that this is not the case. There are two distinct classes of signals that qualitatively look similar, the signals from Cs1, Cs3, Cs6, Cs8 and those from Cs2, Cs4, Cs5, Cs7. The first group exhibits the behavior that is expected from the above considerations, the points where $\theta_{\text{flip}} = 0, \pi$ can be clearly identified with the points of the curves where the underlying fast oscillation vanishes (around 0 s and 7 s). The second group does also show a slow oscillation with an underlying faster one, but the fast oscillation does not die out at the $\theta_{\text{flip}} = 0, \pi$ points.

The explanation for this lies in the direct effect of the applied rf-field on the measurement signal that we have neglected in the above considerations. The CsOPMs measure the modulus of the magnetic field at their position, $\omega_{\text{L,Cs}} \propto |\vec{B}|$. In Sec. 4.2, it was shown that for small transverse magnetic fields ($B_x, B_y \ll B_z$) the approximation $|\vec{B}| \approx B_z$ is justified. Here, we are now dealing with oscillating, far off-resonant transverse fields that may not necessarily be considered small. When examining the influence of such transverse fields, one finds that their impact on the CsOPM signal is substantially different, depending on the direction in which they are applied with respect to the CsOPM geometry. Figure 8.3 shows the M_x geometry and two perturbing transverse oscillating fields $\vec{B}_{1p}$ and $\vec{B}_{2p}$. While $\vec{B}_{1p}$ lies in the *detection plane*[1], $\vec{B}_{2p}$ is perpendicular to it. It is non-trivial (or even impossible) to find analytical solutions of the Bloch equations for this case, but the effect can be modeled numerically[2]. The result of such a simulation is that the CsOPM response exhibits a *fast* and a *slow* direction, meaning that oscillating fields applied perpendicular to $\vec{B}_0$ but lying in the *detection plane* (like $\vec{B}_{1p}$ in Fig. 8.3) affect the CsOPM signal very quickly while reactions to fields applied perpendicular to both $\vec{B}_0$

---

[1] See Fig. 8.3 for definition of this term.

[2] The effect has been experimentally observed by the FRAP group already in 2010. To my knowledge, there is yet no analytical theoretical description of it.

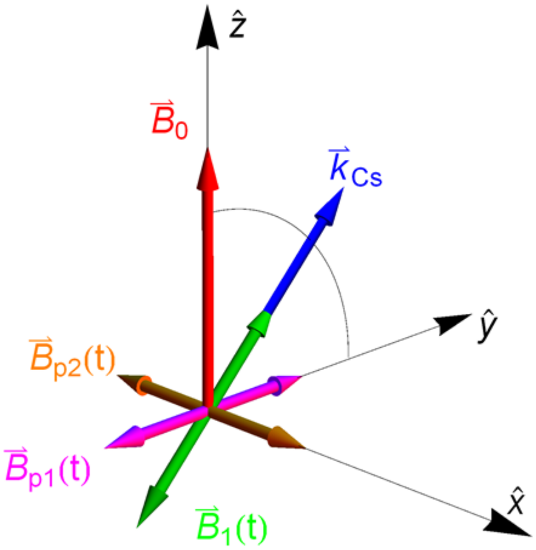

FIGURE 8.3: Geometry of M_x magnetometer. $\vec{B}_1$ is the rf field resonant with the Cs transition. $\vec{B}_0$ and $\vec{B}_1$ lie in the $\hat{z}$-$\hat{y}$ plane (*detection plane*) in this plot. $\vec{B}_{1p}$ and $\vec{B}_{2p}$ are off-resonant oscillating magnetic fields. $\vec{B}_{1p}$ also lies in the *detection plane*, while $\vec{B}_{2p}$ is perpendicular to it.

and the *detection plane* (like $\vec{B}_{2p}$ in Fig. 8.3) are much slower. [3] When inspecting the geometry of the combined ^{3}He/Cs magnetometer prototype, we find that there are two groups of CsOPMs for which the *detection plane* coincides either with the $\hat{z}$-$\hat{y}$ (Cs2, Cs4, Cs5, Cs7) or the $\hat{z}$-$\hat{x}$ (Cs1, Cs3, Cs6, Cs8) plane. Since the oscillating magnetic field to flip the ^{3}He magnetization was applied along $\hat{y}$, it will affect these two groups of sensors very differently. For the first group (Cs2, Cs4, Cs5, Cs7) the perturbation is *in-plane*, or along the *fast axis* and thus has a strong effect on the CsOPM signals. This explains why the underlying oscillation in the corresponding plots of Fig. 8.2 is comparatively large and never completely dies out. For the second group of sensors the perturbation is perpendicular to the detection plane, the frequency of the applied rf-field is too fast to strongly affect the signals of these CsOPMs, the lineshapes qualitatively match the expectations from the considerations at the beginning of this section. This assumption was also verified by a measurement in which ^{3}He remained unpolarized and the pure effect of the rf-field on the CsOPM signals was examined.

The rigorous mathematical description of the signals observed during flipping is quite demanding. In the following, a simple approach that suffices to determine the rf-pulse parameters to achieve a flipping of the ^{3}He magnetization by an arbitrary angle is presented. It consists in extracting the frequency ω_z of the slow oscillation on the CsOPM signals that corresponds to the change of S_z during a flip with fixed, reasonable, but not necessarily known parameters $\omega_{\mathrm{rf}} \approx \omega_{\mathrm{L,He}}$ and B_{rf}. This is done by fitting a simple sinusoidal function

$$f(t) = a_0 + a\sin(\omega_z t + \phi_0) \tag{8.5}$$

to the data recorded during the flipping. Figure 8.4 demonstrates the fitting for the Rabi patterns recorded by six CsOPMs[4] using Eq. (8.5). The results are visualized in Figs. 8.5a, 8.5b. It can be seen that the extracted values of ω_z agree within their uncertainties. A weighted mean of all six sensors $\widetilde{\omega}_z = 0.422066(13)$ rad/s and its uncertainty were calculated according to Eqns. (7.23),(7.24) and are denoted by the red line and the shaded region around it. Once ω_z is known, the necessary rf-irradiation time to achieve a desired flip angle θ_{flip} for this

---

[3] It turns out that for a CsOPM running at a Larmor frequency $\omega_{\mathrm{L,Cs}} \approx 3.5$ kHz oscillating fields along the *slow* axis have to be in the sub-Hertz range to be visible as oscillations of the CsOPM signal while fields along the *fast* axis can be on the order of ~ kHz.

[4] During these measurements, only six CsOPMs were recorded.

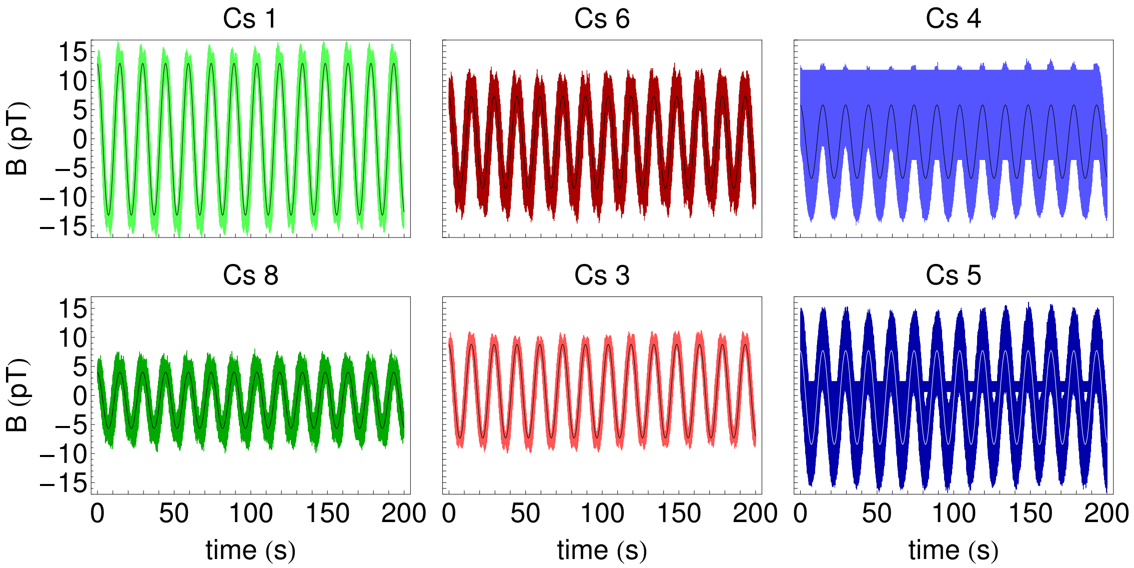

FIGURE 8.4: Signals from six CsOPMs during a continuous spin-flipping process and their fit of the corresponding Rabi nutation by Eq. (8.5). The ordinate of all signals was artificially shifted to a region around zero to simplify the visualization.

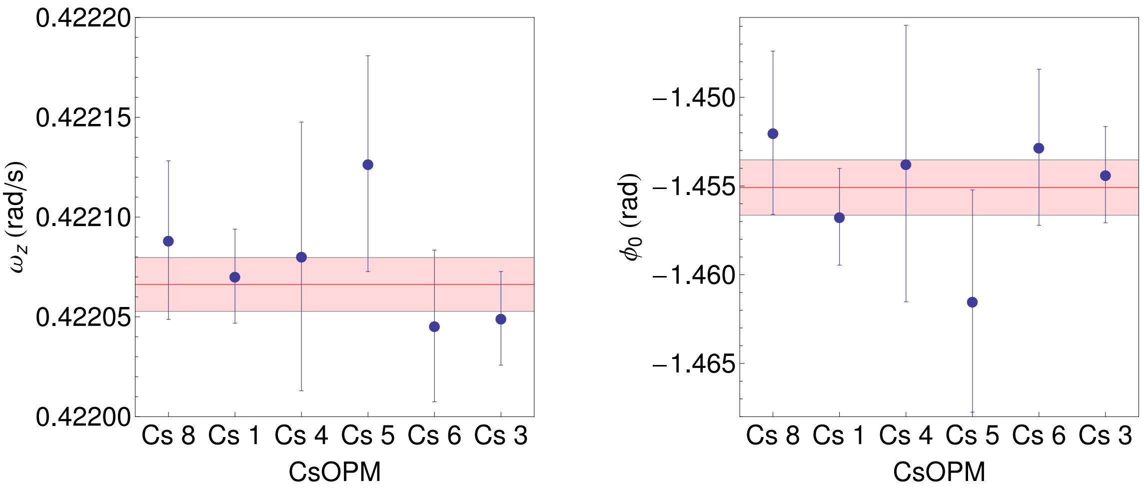

(a)

(b)

FIGURE 8.5: Visualization of fit results from Rabi patterns. (a) Slow oscillation frequency ω_z and 1σ confidence band, determined by fits of Eq. (8.5) to the data shown in Fig. 8.4. (b) Phase offsets determined by the fits, as consistency check.

set of ω_{rf} and B_{rf} can be calculated via

$$T_\theta = \frac{\theta_{\mathrm{flip}}}{\omega_z}\,. \tag{8.6}$$

These parameters can then be used in a successive measurement, of course assuming that the main field $\vec{B}_0$ does not change in the meantime. In any case it is advisable to record the CsOPM signals already during the spin flip of a measurement. Then the above method can be applied during data analysis to check the achieved flip angle.

Chapter 9

Decay time

For various reasons the decay time of the ^{3}He polarization is a parameter of interest. From a practical point of view it sets the possible timescale of uninterrupted measurements for the combined magnetometer. From the scientific point of view it contains important information on the magnetic field gradients as described in Sec. 3.2. In the following chapter, measurements of the decay time and their implications during the tests at PTB are described.

9.1 Measurement of ^{3}He decay time

Decay times on the order of hours were expected from previous tests and the literature [HGK$^+$13] and long running measurements are needed to assess this value with sufficient precision. Therefore these measurements were usually done over night. The ^{3}He sample was freshly polarized, precession started and the phase signals from the CsOPMs recorded for $\sim 12\,$h. The data was then analyzed by subdividing the time series into 44 s long time slices for which the FSP amplitude can be assumed to be constant. These slices were individually fit using the function Eq. (7.16) to extract the amplitude $a(t)$ of the ^{3}He FSP for each subset. The DC-scaled amplitudes[1] as a function of time can then be fit with an exponentially decaying function

$$a(t) = a_0\, e^{-t/T_2^*} \tag{9.1}$$

to extract the effective decay time T_2^*. When inspecting the fit residuals, it became apparent that Eq. 9.1 does not properly describe the time dependence of the amplitudes. Especially in the beginning of the measurement the residuals showed some structure and did not have a Gaussian distribution. Such a behaviour had been observed and described already in [Tul13] and is considered to be caused by a relaxation of the magnetic shield. During opening of the magnetic shield, the innermost layer is exposed to a relatively strong magnetic field that enters through the open cabin doors. The mu-metal is brought to a different equilibrium magnetization in this strong field from which it relaxes again after closure. A composite fit function

$$a(t) = a_1\, e^{-t/T_2^{(1)}} + a_2\, e^{-t/T_2^{(2)}}\,, \tag{9.2}$$

that empirically takes the shield relaxation into account by introducing a second time constant $T_2^{(2)}$ can be used to model this behavior.

The effect is demonstrated for the signals of a single CsOPM (Cs1) in Fig. 9.1. The amplitudes as a function of time and the two fit functions Eqns. (9.1) and (9.2) that describe the decay of polarization are shown in the upper semi logarithmic plot. In the two lower plots the corresponding fit residuals are shown, upper (red) for the fit by Eq. (9.1) and lower (green) for Eq. (9.2). While some clear structure is visible in the upper residual plot, the fit by Eq. (9.2) yields Gaussian-distributed residuals. It was thus concluded that Eq. (9.2) adequately

---

[1] Note that these amplitudes do not reflect the true magnitude of the oscillating field created by the ^{3}He FSP since no AC-rescaling was applied to simplify data analysis. In any case the decay constant is not affected by that rescaling.

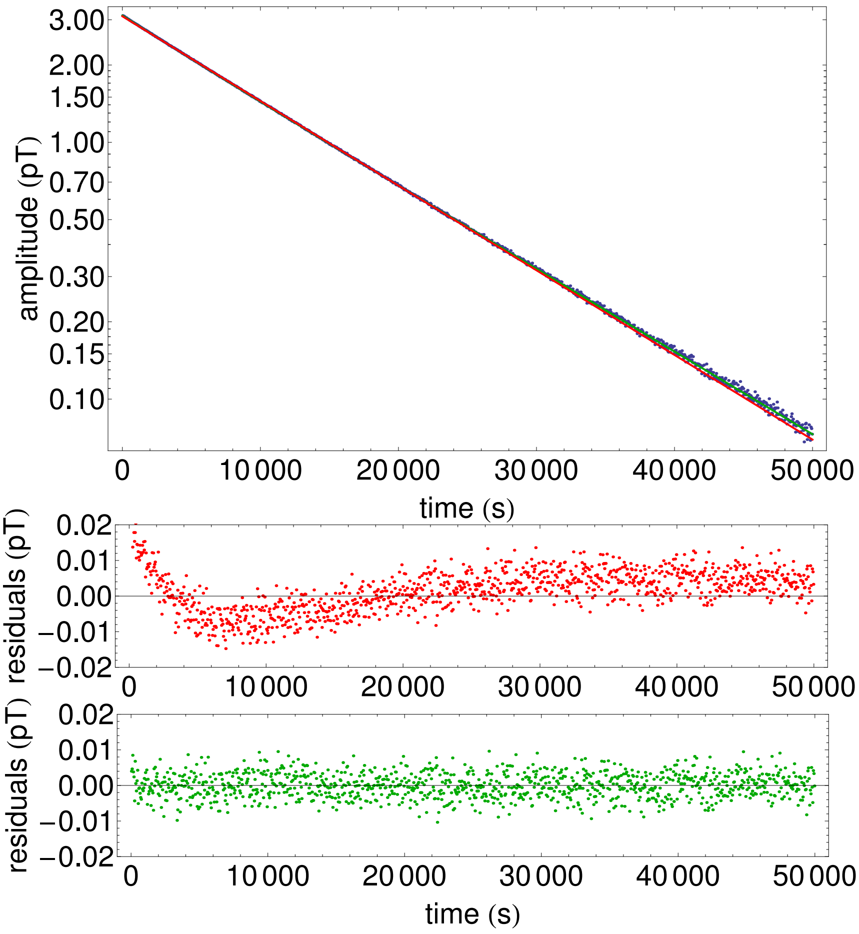

FIGURE 9.1: Decay of ^{3}He FSP signal amplitude. In the upper figure the extracted amplitude $a(t)$ is plotted as a function of time. Two different functions were fit to these points to extract the decay time. The red solid line depicts the fit by the simple exponentially decaying function Eq. (9.1). The green line represents a fit by the composite function Eq. (9.2). They are hardly distinguishable in the upper plot, but inspection of the fit residuals shows that the simple decay (middle plot, red) does not adequately model the data. The composite function does much better, its residuals do not show any structure (lower plot, green). See text for explanation.

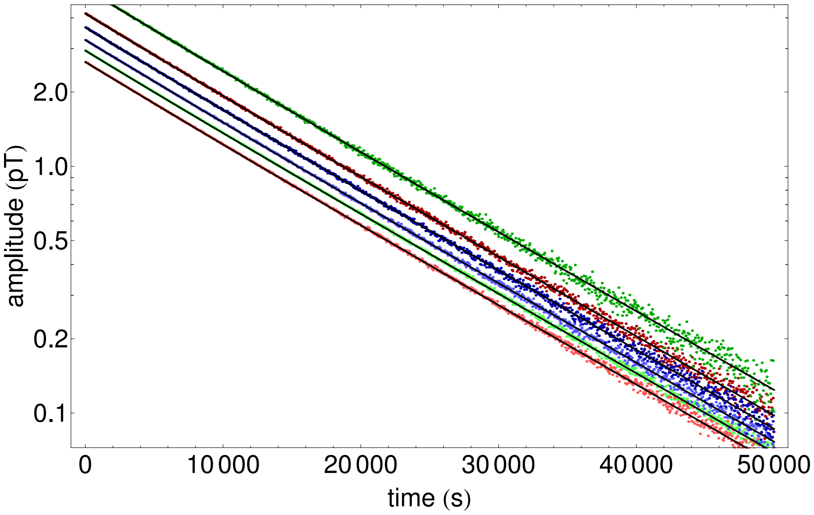

FIGURE 9.2: Semi-logarithmic plot of ^{3}He FSP amplitudes $a(t)$ as a function of time for six CsOPMs simultaneously measuring the same ^{3}He FSP. The exponential character of the relaxation is clearly visible. Fits of CsOPM data sets by Eq. (9.2) are denoted as solid lines.

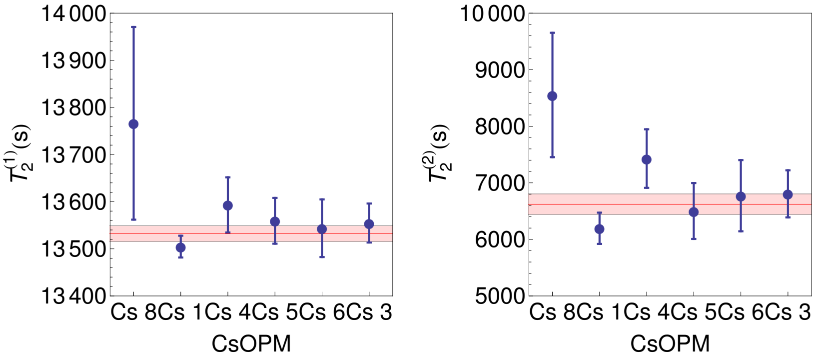

FIGURE 9.3: Visualization of the $T_2^{(1)}$ and $T_2^{(2)}$ time constants. The solid red lines display the weighted mean of all six readings, the shaded band around it indicates the 1σ confidence region. It can be seen that the measured decay times agree within their uncertainties.

describes the decay and it was also used to analyze the signals from the other CsOPMs. In total six CsOPMs measured the same ^{3}He FSP simultaneously, their extracted amplitudes as a function of time and the fits thereof are shown in Fig. 9.2. The individual curves are shifted by values that depend on the initial signal amplitude of the corresponding sensor. Figures 9.3 visualize the $T_2^{(1)}$ and $T_2^{(2)}$ and their uncertainties. The measurement uncertainties differ largely for the individual sensors due to different signal to noise ratios. This issue will be more deeply discussed in Chapter 12. It is visible that the decay times measured by the individual sensors agree within their uncertainties, a result that was expected, but still is comforting to see. This justifies the calculation of a mean value from the set of measured decay times using Eqns. (7.23) and (7.24). We find for the mean decay times

$$\widetilde{T}_2^{(1)} = 13532(17)\,\mathrm{s} \qquad \text{and} \qquad \widetilde{T}_2^{(2)} = 6621(183)\,\mathrm{s} \tag{9.3}$$

respectively. It is worth noting that much longer decay times have been measured at BMSR-2 and are reported in the literature [HGK+13]. The rather short relaxation times encountered here are most probably due to the presence of relatively large magnetic field gradients. However, this result is important because it justifies neglecting the decaying character of the signal in the data analysis up to rather long measurement times. The benefits of this simplification have been addressed already in Chapter 7.

Chapter 10

Cs-gradiometer measurements

One of the nice features that the combined magnetometer prototype offers arises from the fact that the ^{3}He FSP signals from different CsOPMs have specific phase relations (c.f. Sec. 4.3). This effect can be exploited to increase the signals of interest and suppress unwanted perturbations. For this purpose differential signals are set up by selecting a pair of CsOPMs on which the ^{3}He FSP signals have a phase shift of π and subtracting one signal from the other. Such a pair of CsOPMs is called a gradiometer pair and from the high symmetry of the magnetometer prototype's geometry it follows that eight such pairs can be formed. In the first section we will address the question whether the formation of gradiometer signals has an impact on the achievable precision of the frequency estimations. In the second section experimental examples for this technique will be shown.

10.1 Gradiometer pairs and CRLB

To model the situation we encounter when dealing with dephased and in-phase signals on different CsOPMs, we consider two signals

$$S_a(t) = a_1 \sin(\omega_1 t) + a_2 \sin(\omega_2 t) + \mathscr{G}_a \qquad \text{and} \qquad S_b(t) = b_1 \sin(\omega_1 t + \pi) + b_2 \sin(\omega_2 t) + \mathscr{G}_b\,. \tag{10.1}$$

Both signals contain frequency components ω_1 and ω_2 and are affected by Gaussian amplitude noise $\mathscr{G}$ with power spectral densities ρ_a^2 and ρ_b^2 respectively. The ω_1 component is dephased by π between the two signals, the ω_2 components oscillate in-phase on both signals[1]. When we construct the sum and difference of the two signals, we find

$$S_-(t) = S_a(t) - S_b(t) = a_1 \sin(\omega_1 t) - b_1 \sin(\omega_1 t + \pi) + (a_2 - b_2)\sin(\omega_2 t) + \mathscr{G}_a + \mathscr{G}_b \tag{10.2}$$

$$= (a_1 + b_1)\sin(\omega_1 t) + (a_2 - b_2)\sin(\omega_2 t) + \mathscr{G}_a + \mathscr{G}_b \tag{10.3}$$

$$= A_1 \sin(\omega_1 t) + A_2 \sin(\omega_2 t) + \mathscr{G}_{a+b} \tag{10.4}$$

and similarly

$$S_+(t) = S_a(t) + S_b(t) = a_1 \sin(\omega_1 t) + b_1 \sin(\omega_1 t + \pi) + (a_2 + b_2)\sin(\omega_2 t) + \mathscr{G}_a + \mathscr{G}_b \tag{10.5}$$

$$= (a_1 - b_1)\sin(\omega_1 t) + (a_2 + b_2)\sin(\omega_2 t) + \mathscr{G}_a + \mathscr{G}_b \tag{10.6}$$

$$= B_1 \sin(\omega_1 t) + B_2 \sin(\omega_2 t) + \mathscr{G}_{a+b}\,. \tag{10.7}$$

We see, that the amplitude of the in-phase component of the differential signal is

$$A_2 = a_2 - b_2\,, \tag{10.8}$$

while the π-dephased component has an amplitude

$$A_1 = a_1 + b_1 \tag{10.9}$$

---

[1] The considerations presented here can be generalized to arbitrary dephasing, but for the sake of simplicity we restrict the discussion to signals having a constant phase difference of π here.

on the differential signal. The in-phase amplitudes thus subtract while the π-dephased ones add up. The attenuation of the in-phase component's amplitude in the difference signal is referred to as common noise suppression and we will later exploit this effect. For the sum signal, the situation is somehow reversed. We have

$$B_2 = a_2 + b_2\,, \tag{10.10}$$

and

$$B_1 = a_1 - b_1\,. \tag{10.11}$$

The noise $\mathscr{G}_{a+b}$ of the differential (and sum-) signal has a power spectral density

$$\rho^2_{a+b} = \rho^2_a + \rho^2_b \tag{10.12}$$

since the noise powers of the two signals add, assuming uncorrelated noise on both signals[2]. We can now examine the SNDR of $S(t)_-$ and $S(t)_+$ and compare them to those of $S(t)_a$ and $S(t)_b$. Following the definition in Eq. (7.8), we find initial values

$$SNDR_a(\omega_1) = \frac{a_1}{\sqrt{2}\rho_a} \quad \text{and} \quad SNDR_a(\omega_2) = \frac{a_2}{\sqrt{2}\rho_a} \tag{10.13}$$

for the ω_1 and ω_2 components on $S_a(t)$ and similarly

$$SNDR_b(\omega_1) = \frac{b_1}{\sqrt{2}\rho_b} \quad \text{and} \quad SNDR_b(\omega_2) = \frac{b_2}{\sqrt{2}\rho_b} \tag{10.14}$$

for the SNDRs on $S_b(t)$. The differential signal $S(t)_-$ will exhibit SNDRs of

$$SNDR_-(\omega_1) = \frac{A_1}{\sqrt{2}\rho_{a+b}} = \frac{a_1 + b_1}{\sqrt{2(\rho^2_a + \rho^2_b)}} \quad \text{and} \tag{10.15}$$

$$SNDR_-(\omega_2) = \frac{A_2}{\sqrt{2}\rho_{a+b}} = \frac{a_2 - b_2}{\sqrt{2(\rho^2_a + \rho^2_b)}} \tag{10.16}$$

for the two frequency components, respectively. For the sum signal $S(t)_+$ we obtain

$$SNDR_+(\omega_1) = \frac{B_1}{\sqrt{2}\rho_{a+b}} = \frac{a_1 - b_1}{\sqrt{2(\rho^2_a + \rho^2_b)}} \quad \text{and} \tag{10.17}$$

$$SNDR_+(\omega_2) = \frac{B_2}{\sqrt{2}\rho_{a+b}} = \frac{a_2 + b_2}{\sqrt{2(\rho^2_a + \rho^2_b)}}\,. \tag{10.18}$$

We will now examine how precisely we can extract the frequency ω_1, assuming a CRLB limited estimation process as described in Sec. 7.2. According to Eq. (7.10), the variance of CRLB limited frequency estimation will scale like[3][4] $\sigma^2 \sim 1/SNDR^2$. When we estimate the frequencies of $S(t)_a$ and $S(t)_b$, the weighted mean will have a variance

$$\sigma^2_{a,b} \sim \frac{1}{SNDR^2_a + SNDR^2_b} = \frac{2}{a^2/\rho^2_a + b^2/\rho^2_b}\,, \tag{10.19}$$

as given by Eq. (7.24). If we were to estimate the frequencies of $S(t)_-$ and $S(t)_+$, the variance of the combined measurement would be

$$\sigma^2_{-,+} \sim \frac{1}{SNDR^2_- + SNDR^2_+} = \frac{2(\rho^2_a + \rho^2_b)}{(a+b)^2 + (a-b)^2} = \frac{\rho^2_a + \rho^2_b}{a^2 + b^2}\,. \tag{10.20}$$

When we compare Eq. (10.19) and Eq. (10.20), we can state that

---

[2] as it is the case for the dominant phtocurrent shotnoise

[3] We neglect all other factors in Eq. (7.10), because they are constant in these considerations.

[4] To keep the notation a bit shorter we identify $SNDR(\omega_1) \equiv SNDR$ if not further specified.

- in general $\sigma^2_{-,+} \geq \sigma^2_{a,b}$,
- for arbitrary amplitudes a and b we have $\sigma^2_{-,+} = \sigma^2_{a,b}$ if $\rho_a = \rho_b$ and
- for arbitrary noise levels ρ_a and ρ_b we find $\sigma^2_{-,+} = \sigma^2_{a,b}$ if $SNDR_a = SNDR_b$.

We already see that the construction of composite signals generally means a loss in estimation precision, except for the two limiting cases above. The requirements become even more stringent when we return to a more practical scenario. Usually, one would apply the gradiometric technique to suppress unwanted perturbations in the signals that might disturb the frequency estimation process. This means assuming that the π-dephased component ω_1 is our signal of interest, e.g., the ^{3}He FSP and the in-phase component ω_2 the perturbance. Then of course one would rather use only $S(t)_-$ for the frequency determination since the ω_2 component is even increased on $S(t)_+$, as Eq. (10.10) shows. In this case the variance of the frequency estimation is given by

$$\sigma^2_- = \frac{2(\rho_a^2 + \rho_b^2)}{(a+b)^2}\,. \tag{10.21}$$

We now examine the ratio of Eq. (10.19) and Eq. (10.21) to understand under which conditions and by how much the sensitivity will suffer from the formation of gradiometer signals. For this we introduce the amplitude ratio

$$c_a = b/a \qquad \text{and noise ratio} \qquad c_\rho = \rho_b/\rho_a\,. \tag{10.22}$$

When we express the ratio $\sigma^2_{a,b}/\sigma^2_-$ in terms of a, ρ_a, c_a, c_ρ, we find

$$\frac{\sigma^2_{a,b}}{\sigma^2_-} = \frac{(c_a+1)^2 c_\rho^2}{(c_\rho^2+1)(c_a^2+c_\rho^2)}\,. \tag{10.23}$$

The meaning of Eq. (10.23) is explained graphically in Fig. 10.1. The vertical axis shows by which factor the composite variance of frequency estimation from two initial signals $S(t)_a$ and $S(t)_b$ will be smaller than the variance of the frequency estimated from the difference signal $S(t)_- = S(t)_a - S(t)_b$. The horizontal axes give the amplitude and noise density, respectively of $S(t)_b$ as a multiple of these values of $S(t)_a$ (compare definitions Eq. (10.22)). Inspection of Eq. (10.23) reveals that $\sigma^2_{a,b}/\sigma^2_-$ becomes unity under the condition $c_a = c_\rho^2$, denoted as the thick black line in Fig. 10.1. For this special case no loss in sensitivity will occur and we have $\sigma^2_{a,b} = \sigma^2_-$.

To conclude, we see that suppressing a common mode noise component generally means a trade off in estimation precision. The advantage of cleaning the spectrum has to be carefully pondered against the loss in sensitivity in each individual case. The above considerations put aside, gradiometric measurements are still a valuable tool for analysis and identification of noise processes even if not used for the actual data recording. An oscillating perturbation that is in-phase on all CsOPMs for example can be often traced back to an oscillating magnetic field caused by a distant source, the most common case of magnetic noise. A perturbation that has different phases on the individual sensors would rather point to a local source.

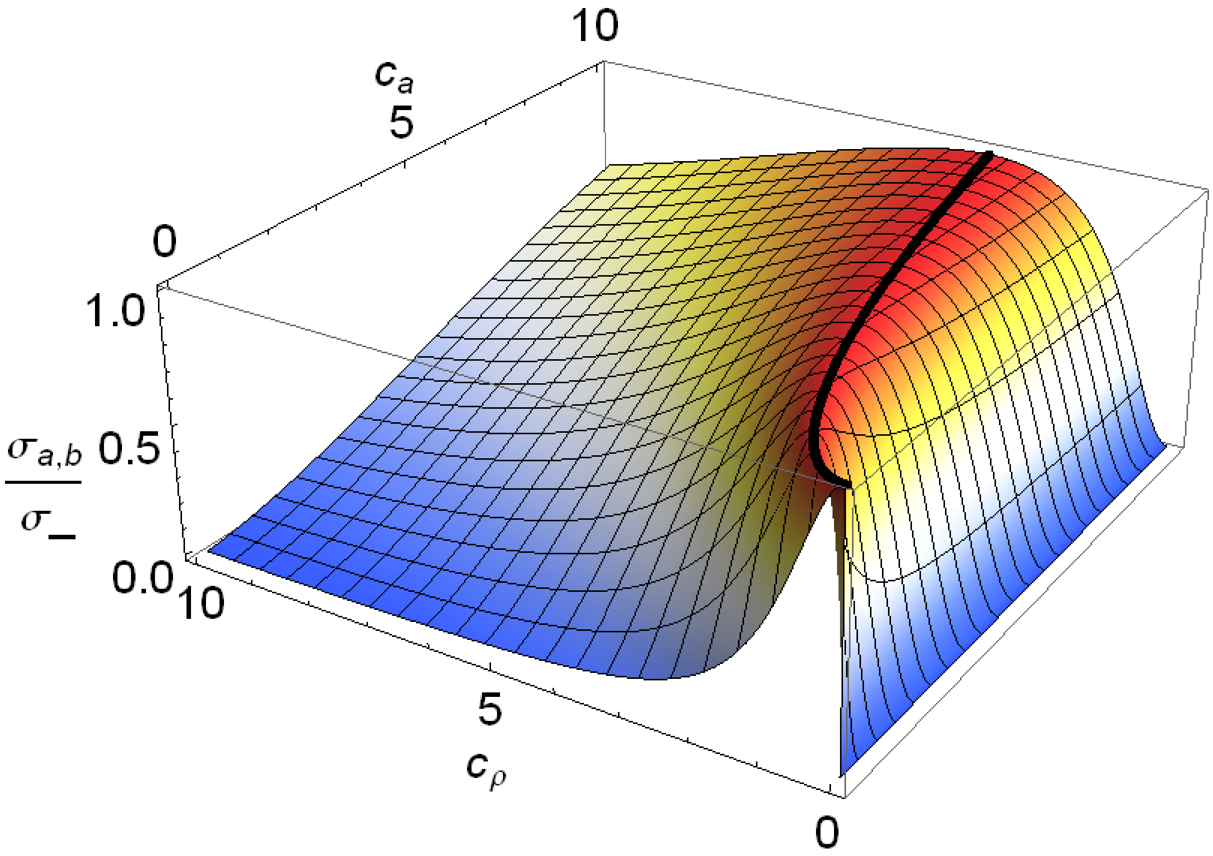

FIGURE 10.1: Ratio of $\sigma^2_{a,b}/\sigma^2_-$ as a function of the amplitude and noise ratios c_a, c_ρ. The solid line denotes the condition under which $\sigma^2_{a,b} = \sigma^2_-$, where no loss in sensitivity occurs. See text for details.

10.2 Gradiometric measurements at PTB

In this section we report on our experimental demonstration of the gradiometric technique described above. To this aim we first inspect the FFT spectra of phase signals simultaneously measured by Cs4 and Cs5 shown in Fig. 10.2. In addition to the peak near 37 Hz (the ^{3}He FSP signal of interest) perturbances are visible, the most prominent of which are at 50 Hz and a double peak around 22 Hz. Figure 10.3 (left) shows the corresponding time series of the signals from Cs4 and Cs5 together with the fits of Eq. (7.16) to the data; the phase shift of π is apparent. The FFT spectrum of the differential signal Cs4-Cs5 is displayed in Fig. 10.3 (right). The 50 Hz perturbation of Fig. 10.2 is not present any more, demonstrating the common noise suppression effect. The double peak structure around 22 Hz is increased in amplitude which leads to the assumption that this perturbation might be dephased on the two signals. The amplitudes and noise levels extracted from the FFT spectra of Cs4, Cs5 and (Cs4-Cs5) are given in Table 10.1. The rightmost column compares the theoretically expected values following the considerations presented in Sec. 10.1 to the experimentally observed ones. It is evident that the amplitudes a_{He} of the ^{3}He signals add up exactly as expected. A slight disagreement with theory is found for the noise level of the gradiometer signal, which was expected to be a factor ~ 0.87 smaller. This observation could be explained by the presence of partially non-Gaussian noise, an assumption which is justified since the signals undergo filtering in the LIA which leads to correlations of the noise. The discrepancy between expected and measured noise level also shows up in the SNDRs given in Table. 10.1. Examination of the double peak structure around 22 Hz shows that their amplitudes add as expected for a π-dephased signal (compare Table 10.1).

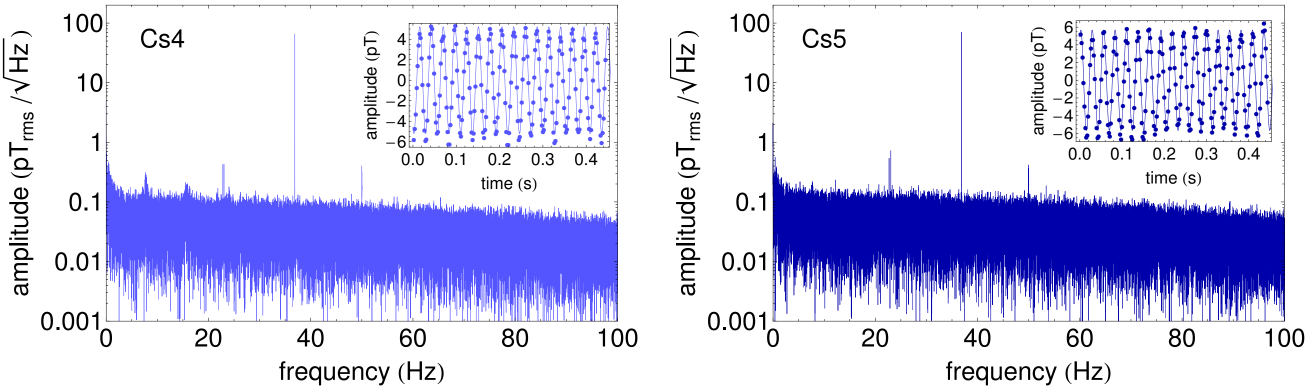

FIGURE 10.2: FFT spectra of phase signals from Cs4 (left) and Cs5 (right) rescaled to magnetic units. The data was recorded at a sampling rate of 450 Hz and effective bandwidth of 60 Hz over a measurement time of 700 s. The time series of the first half second together with the fit by Eq. (7.16) is shown in the small insets. Color coding corresponds to Fig. 5.4.

	Cs4	Cs5	Cs4-Cs5$_{meas}$	theo/meas
$\rho(\mathrm{fT_{rms}}/\sqrt{\mathrm{Hz}})$	47	60	87	0.872
$a_{\mathrm{He}}(\mathrm{pT_{rms}})$	3.578	3.850	7.428	1.000
$\mathrm{SNDR_{He}}(\sqrt{\mathrm{Hz}})$	75.6	64.6	85.2	1.147
$a_{22}(\mathrm{pT_{rms}})$	0.022	0.029	0.049	1.034
$a_{23}(\mathrm{pT_{rms}})$	0.021	0.034	0.052	1.071

TABLE 10.1: Measured signal parameters of phase signals from Cs4 and Cs5 and the gradiometer signal Cs4-Cs5. The square root power spectral density $\rho$of the noise is given under the ^{3}He peak. The rightmost column is the ratio of the expected parameters of the gradiometer signal according to the considerations in Sec. 10.1 and the experimentally observed values and thus has no units.

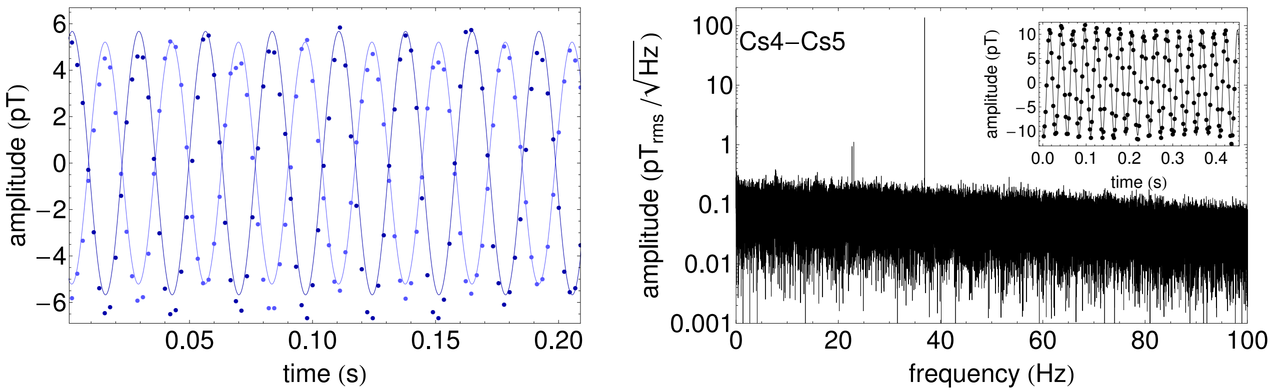

FIGURE 10.3: Time series of Cs4 and Cs5 and fits of signals (left).The phase shift of π is visible. FFT spectrum of gradiometer signal Cs4-Cs5 (right). The 50 Hz perturbation is not present any more in the differential signal, while the double peak structure around 22 Hz is increased in amplitude. Compare Fig. 10.2 and Table 10.1. Time series is shown in the inset.

10.3 Gradiometric measurements at PSI

During the measurements at PTB the gradiometric effects were merely an interesting feature of secondary interest. Due to the magnetically extremely quiet and stable environment it was not necessary to exploit these effects in order to record data of sufficient quality. The potential of the gradiometer technique is more impressively demonstrated by a measurement performed at PSI in early 2015. A ^{3}He/Cs magnetometer consisting of a ^{3}He cell and two CsOPMs in gradiometer configuration was operated in a cylindrical five-layer mu-metal shield at PSI. Due to the close vicinity of high power electric facilities and the lower shielding factor, the 50 Hz magnetic noise is much more pronounced in the PSI environment. This noise component was even stronger than the typical ^{3}He-FSP signal under those conditions. Figure 10.4 (two left figures, blue) shows FFT spectra and time series of two CsOPMs measuring a ^{3}He-FSP to demonstrate the problem. This considerably hinders data analysis, since this strong noise component can not be ignored in the fit routines used to extract the ^{3}He Larmor frequency. The problem was overcome by constructing a gradiometer signal by (off-line) subtraction of one signal from the other. The gradiometer signal is shown in the rightmost part of Fig. 10.4 (black). The 50 Hz component cannot be identified any more in the FFT spectrum and the time series clearly shows the 30 Hz oscillation from the ^{3}He-FSP. In this example the measurement was only made possible by the application of the gradiometer technique.

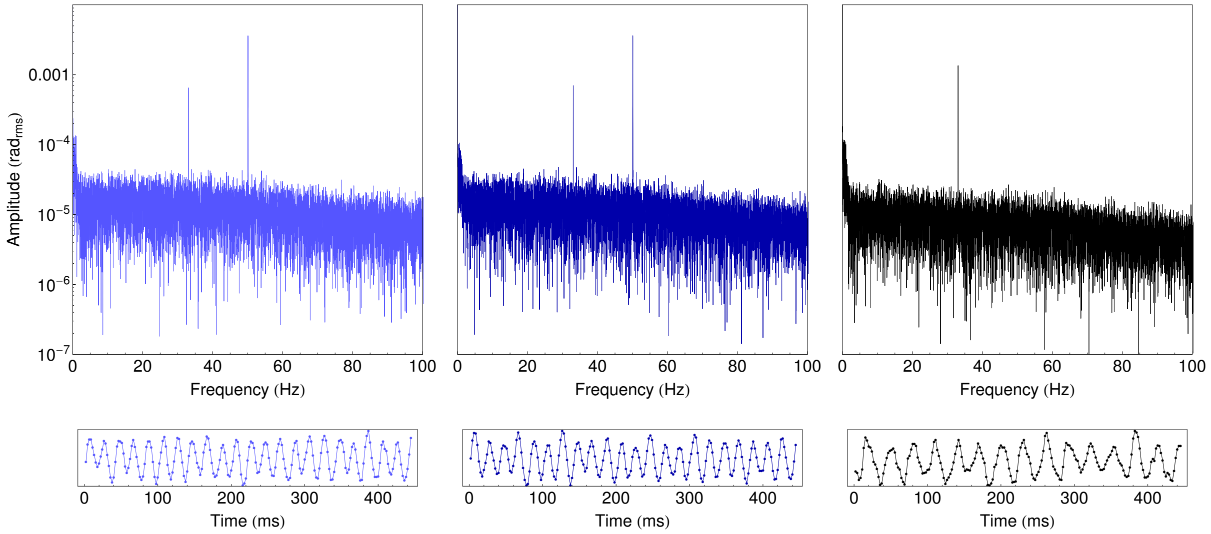

FIGURE 10.4: FFT spectra (upper row) and time series (lower row) of phase signals from CsOPMs measuring ^{3}He-FSP. The two left figures (darker and lighter blue) show the signals from individual sensors. As can be seen, the 50 Hz perturbation is significantly stronger than the ^{3}He signal and completely dominates the time series. The rightmost figure shows the FFT and time series of the gradiometer signal obtained in the off-line analysis. The 50 Hz noise is not present any more in the FFT spectrum and the $\sim$ 30 Hz oscillation from the ^{3}He-FSP becomes visible in the time series.

Chapter 11

Magnetic field measurements

The main purpose of a magnetometer is, of course, the measurement of a magnetic field. In this chapter magnetometric measurements at BMSR-2 will be described and examples of their analysis given. In general, the technique consists in measuring the ^{3}He Larmor frequency and calculating the magnetic field via Eq. (3.24). The ^{3}He FSP was recorded by CsOPMs, as described in Sec. 11.1, which is the basic functionality of the combined magnetometer. The symmetrical placement of the CsOPMs in the magnetometer prototype further allows for an interesting comparison between the field measured via $\omega_{L,He}$ and the CsOPM readings, this will be discussed in Sec. 11.2.1. At BMSR-2 it was also possible to use a SQUID system in parallel, which permits a comparative measurement between ^{3}He/Cs and ^{3}He/SQUID. The latter is described in Sec. 11.2.

11.1 Actual field measurements by the ^{3}He/Cs magnetometer

To demonstrate the magnetometer operation, ^{3}He was polarized, a $\pi/2$ flip applied and the FSP signal recorded. For the reasons described in Sec. 4.4, the CsOPMs were driven in the FF-mode of operation. Thus the recorded signals are phase signals as those described by Eq. (4.25) which can be directly used to obtain the ^{3}He FSP frequency. Six CsOPMs were simultaneously recorded on nominally identical DAQ channels, two additional CsOPMs on a slightly different DAQ (c.f. Sec 6.1.4) which is why they are partially skipped in the analysis. For the analysis, the continuous time series of the phase signal from each CsOPM was split into consecutive 100 s slices. Those slices were fit by Eq. (7.16) to extract the 100 s mean frequencies for each CsOPM and their respective errors. The technique described in Sec. 7.4 was applied in order to impose correct noise levels onto the fit routine. The 100 s mean magnetic field $B^{(\mathrm{i})}_{\mathrm{He/Cs}}$ and its uncertainty $\Delta B^{(\mathrm{i})}_{\mathrm{He/Cs}}$ was calculated for each sensor from the extracted frequencies and their errors using Eq. (3.24). Figure 11.1 shows a plot of $B^{(\mathrm{i})}_{\mathrm{He/Cs}} \pm \Delta B^{(\mathrm{i})}_{\mathrm{He/Cs}}$ as a function of time for all six CsOPMs. First we note that the $B^{(\mathrm{i})}_{\mathrm{He/Cs}}$ agree on an absolute scale within their uncertainties which is a very important result, because it experimentally proves that multiple CsOPMs can indeed be used to measure the same ^{3}He FSP yielding consistent results. Since the reading of each CsOPM can be considered as an independent measurement of the same magnetic field, combining the results from several readout CsOPMs will improve the total magnetometric sensitivity of the ^{3}He/Cs magnetometer. The individual estimation uncertainty $\Delta B^{(\mathrm{i})}_{\mathrm{He/Cs}}$ for a single CsOPM ranges between $100-400$ fT for the 100 s averages displayed here. The large spread in the field estimation errors for different sensors is due to different SNDR which limit the achievable precision. The dependence of the estimation precision on the SNDR has been described in Sec. 7.2 and explanations for the occurence of such large SNDR differences will be given in Chapter 12. Figure 11.1 also shows a weighted mean and its uncertainty $B^{\mathrm{mean}}_{\mathrm{He/Cs}} \pm \Delta B^{\mathrm{mean}}_{\mathrm{He/Cs}}$ of all six sensor readings that was calculated according to Eq. (7.23), (7.24). The uncertainty of the weighted mean is typically below 70 fT in a 100 s measurement time for the data shown here. It is further visible in Fig. 11.1 that the magnetic field was drifting by $\sim$ 1 pT on a timescale of $\sim$ 1000 s. This observation will become important later, when we examine the intrinsic sensitivity of the magnetometer (Chapter 12).

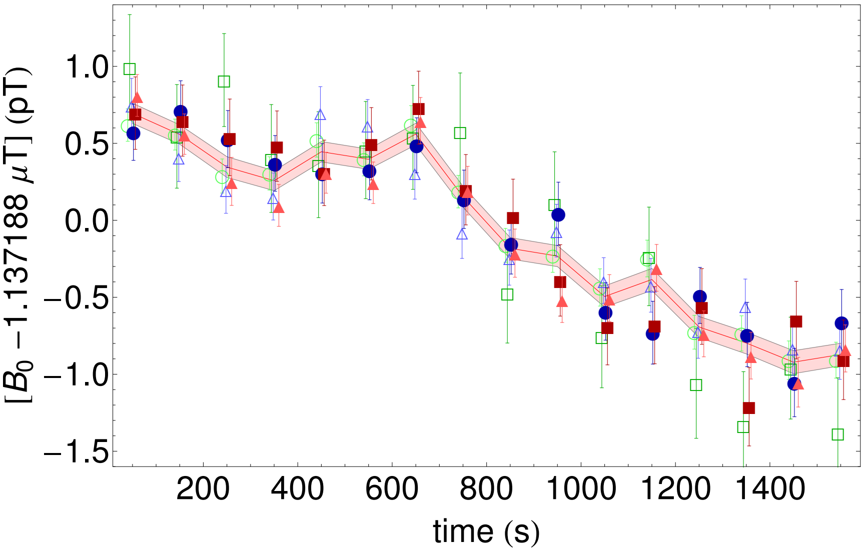

FIGURE 11.1: Time evolution of the magnetic field in the BMSR-2 chamber at PTB, estimated from consecutive 100 s subsets from data segments of six CsOPMs simultaneously detecting the same ^{3}He FSP. Each plot point displays an individual CsOPM reading $B^{(i)}_{\mathrm{He/Cs}}$ and its uncertainty $\Delta B^{(i)}_{\mathrm{He/Cs}}$. The points are slightly displaced horizontally to improve the visibility of the individual error bars. The colors of the plotmarkers refer to Fig. 5.4. The common ordinate is shifted by ~ 1.1 μT. The solid line (red) and the shaded band represent the mean of all sensors' readings $B^{\mathrm{mean}}_{\mathrm{He/Cs}}$ and its corresponding 1σ confidence values $\Delta B^{\mathrm{mean}}_{\mathrm{He/Cs}}$.

11.2 Comparative measurements of ^{3}He/Cs, ^{3}He/SQUID and Cs

During the measurements at PTB we operated different types of magnetometers in parallel. In this section, their simultaneous readings will be compared. The comparison of ^{3}He/Cs and Cs proper will merely aim at gaining knowledge about the spatial dependence of the magnetic field. The ^{3}He/Cs and ^{3}He/SQUID measurements are compared to search for possible systematic effects in the ^{3}He readout by CsOPMs.

11.2.1 Comparing ^{3}He and Cs

The prototype magnetometer consists in fact of 16 magnetometers in one, since every CsOPM (i) gives two readings of the magnetic field, one through its measurement of the ^{3}He FSP frequency $\omega^{(i)}_{\mathrm{L,He}}$ and one through its proper Larmor frequency $\omega^{(i)}_{\mathrm{L,Cs}}$. Since $\omega^{(i)}_{\mathrm{L,He}}$ corresponds to the magnetic field at the position of the ^{3}He cell it should be the same for all CsOPMs, and this is the case, as we have seen in the previous section. Conversely, the $\omega^{(i)}_{\mathrm{L,Cs}}$ from different CsOPMs are generally not identical because they correspond to the magnetic field at the position of the specific CsOPM[1]. So far we have only dealt with the extraction of the magnetic field via $\omega_{\mathrm{L,He}}$ and disregarded the readings from the CsOPMs proper. In Sec. 7.1 an equation was derived that relates the measured phase signal to the magnetic field at the CsOPMs position based on parameters extracted from the sweep responses. Using Eq. (7.2), the readings from each sensor can individually be scaled to magnetic units. During a running ^{3}He FSP measurement the rescaled signal will, as for the raw phase data, consist of a small oscillation at $\omega_{L,He}$ on a constant offset which corresponds to the magnetic field $B^{(i)}_{\mathrm{Cs}}$ at the (i)-th sensor's position. These offsets can be easily determined by the standard fit by Eq. (7.16).

Figure 11.2 shows a plot of these offset fields $B^{(i)}_{\mathrm{Cs}}$ as a function of time for a measurement when all eight CsOPMs were running. Each point denotes the average offset value during a 50 s time slice. The ordinate is individually shifted for each sensor by a value $\langle B^{(i)}_{\mathrm{Cs}}\rangle_{\mathrm{T}}$ corresponding to the time average of the respective sensor over the

---

[1] And may additionally include systematic shifts, as discussed in Sec. 3.3

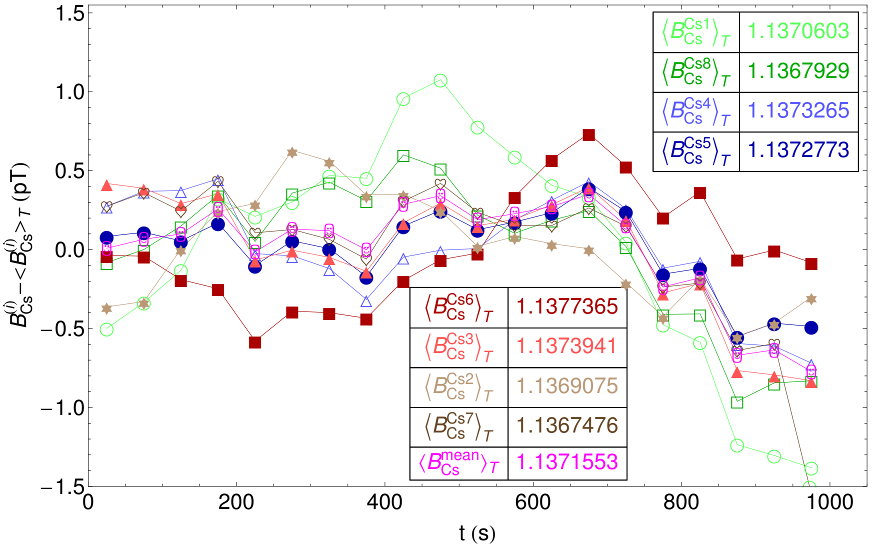

FIGURE 11.2: Magnetic field readings $B^{(i)}_{\mathrm{Cs}}$ calculated from the individual CsOPMs Larmor frequencies $\omega^{(i)}_{\mathrm{L,Cs}}$. The ordinate is shifted individually for each sensor by the time average of the respective sensor's readings $\langle B^{(i)}_{\mathrm{Cs}} \rangle_{\mathrm{T}}$ over the whole measurement time displayed here. The numerical values are given in the inset tables (in μT). Colorcoding corresponds to Fig. 5.4. The mean value $B^{\mathrm{mean}}_{\mathrm{Cs}}$ of all eight sensors is also shown (magenta).

Gradient type	Sensor pair	value (pT/mm)
$\frac{\Delta\lvert\vec{B}\rvert}{\Delta z}$	Cs1,Cs8	4.0
	Cs2,Cs7	2.4
	Cs3,Cs6	-5.1
	Cs4,Cs5	0.7
$\frac{\Delta\lvert\vec{B}\rvert}{\Delta x}$	Cs6,Cs8	12.6
	Cs3,Cs1	4.5
$\frac{\Delta\lvert\vec{B}\rvert}{\Delta y}$	Cs2,Cs4	-5.6
	Cs7,Cs5	-7.1

TABLE 11.1: Variation of the modulus of the magnetic field along the three coordinate axes. The values are calculated from the time-average magnetic fields measured by the individual sensors displayed in the inset table in Fig.11.2

whole measurement time of ~ 1000 s displayed here. This permits to see the commonality of their field fluctuations (~ 1 pT) which are much smaller than their absolute spacing (~ 1 nT). The mean value $B^{\mathrm{mean}}_{\mathrm{Cs}}$ of all eight sensors is also shown (magenta). The significant difference in the $B^{(i)}_{\mathrm{Cs}}$ underlines the observation already made in Sec. 9.1 that quite strong (fluctuating) gradients were present during data recording. We can try to quantify these gradients by exploiting the fact that pairs of CsOPMs can be found along the three axes of the coordinate system as detailed in Sec. 5.3. We recall that the pairs (Cs2, Cs4) and (Cs5, Cs7) are oriented along $\hat{y}$, (Cs1, Cs3) and (Cs8, Cs6) along $\hat{x}$ and (Cs1, Cs8), (Cs2, Cs7), (Cs3, Cs6), (Cs4, Cs5) along the direction of the holding field $\hat{z}$. The design-spacing between the Cs-cell centers for pairs in the $\hat{z}$ direction is $\Delta_z = 67$ mm while in the $\hat{x}$ and $\hat{y}$ direction it is $\Delta_{x,y} = 75$ mm. The spatial variation of the magnetic field is calculated from the time-average fields seen by all eight sensors which are displayed in the inset of Fig 11.2, the results are given in Table 11.1. These measurements suggest the presence of rather large non-linear magnetic field gradients. The (Cs3,Cs6) pair is particularly remarkable since the sign of field variation is opposite to the one of the other pairs measuring the gradient along the same direction.

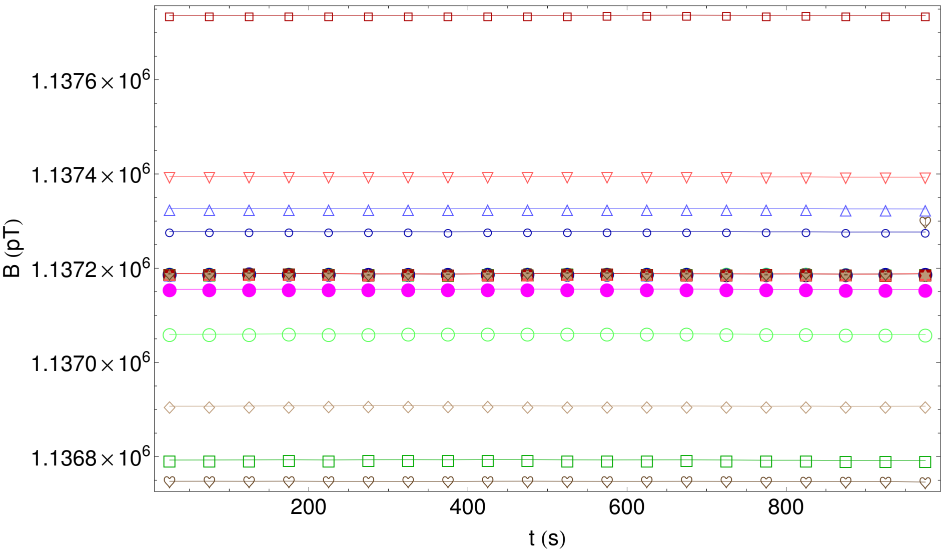

FIGURE 11.3: Comparison of magnetic field $B_{\mathrm{He/Cs}}^{\mathrm{mean}}$ calculated from the ^{3}He FSP frequency and fields $B_{\mathrm{Cs}}^{(\mathrm{i})}$ from the individual CsOPM Larmor frequencies $\omega_{L,Cs}^{(\mathrm{i})}$. The $B_{\mathrm{Cs}}^{(\mathrm{i})}$ are displayed as hollow symbols, color coding corresponds to Fig. 5.4. The magenta line (filled dots) gives their mean value $B_{\mathrm{Cs}}^{\mathrm{mean}}$. The magnetic field $B_{\mathrm{He/Cs}}^{\mathrm{mean}}$ extracted from the ^{3}He FSP frequency is denoted by the brown line (thick, filled symbols). Errors are drawn but too small to be visible.

When we consider the symmetric placement of the CsOPMs around the ^{3}He cell in the prototype magnetometer, we find that in a magnetic field that is homogeneous or contains only contains gradients, B_0^{mean} will correspond to the magnetic field in the center of the magnetometer cube that coincides with the center of the ^{3}He cell[2]. This value can thus be compared with the magnetic field $\widetilde{B}$ calculated from $\omega_{L,He}$. Figure 11.3 shows the magnetic fields already presented in Fig. 11.2 on a common scale (hollow symbols) with their mean value being the magenta line (filled dots). The solid brown dots above represent the weighted mean field readings $B_{\mathrm{He/Cs}}^{\mathrm{mean}}$ obtained from the ^{3}He FSP frequency following the same procedure as described in Sec. 11.1. Closer inspection shows a systematic shift on the order of $B_{\mathrm{He/Cs}}^{\mathrm{mean}} - B_{\mathrm{Cs}}^{\mathrm{mean}} \sim 33\,\mathrm{pT}$.

Several effects are be considered that could lead to a shift of this kind; they are detailed below. The field readings from the CsOPMs are obtained by evaluating the phase offsets of the individual magnetometers. The calibration of this dependence relies on the sweep response measurements. The precision with which the center of the resonance can be determined from these measurements was for our experiments usually $\Delta\omega_{L,Cs}/2\pi \approx 20\,\mathrm{mHz}$. This corresponds to a statistical error of the field estimation ΔB of $\approx 5\,\mathrm{pT}$ assuming that the line shape is adequately described by the fitted model. Since the sweeps were recorded sequentially and not simultaneously, one relies on the magnetic field and its gradients being stable during the corresponding time intervals. The sweep responses which were used for calibration of the measurements presented here took a total time of $\approx 20\,\mathrm{min} \sim 1200\,\mathrm{s}$. As we have seen from Fig. 11.1 a drift of the magnetic field by $\sim 2\,\mathrm{pT}$ is not uncommon on this timescale. In addition, as one can infer from Fig. 11.2, the gradient exhibits a similar drift during this time.

Another effect which has to be considered is a shift of $B_{\mathrm{Cs}}^{\mathrm{mean}}$ due to an incomplete flip of the ^{3}He magnetization. A theoretical expression for $B_{\mathrm{Cs}}^{\mathrm{mean}}$ can be derived from the magnetic field produced by the precessing ^{3}He magnetization described by Eq. (4.7). The modulus of the total field $\left|B_{\mathrm{Cs}}^{(\mathrm{i,theo})}(t)\right| = \sqrt{(\vec{B}_{\mathrm{He}}(\vec{r}_i,t)+\vec{B}_0)^2}$ at each CsOPM's position is calculated using this equation and their mean

$$B_{\mathrm{Cs}}^{\mathrm{mean,theo}} = \frac{\sum_i \left|B_{\mathrm{Cs}}^{(\mathrm{i,theo})}(t)\right|}{8} \tag{11.1}$$

---

[2] This is not coincidence, but was designed such, as described in Sec. 5.3

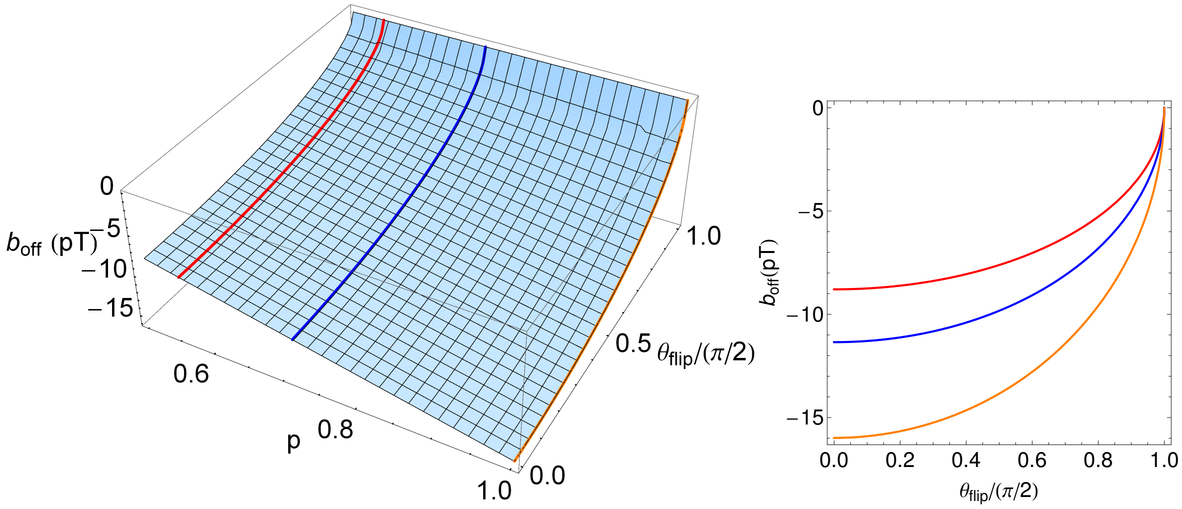

(a) (b)

FIGURE 11.4: Shift of the extrapolated magnetic field value $B_{\text{Cs}}^{\text{mean,theo}} - B_0 = b_{\text{off}}$ at the ^{3}He cell-center calculated from the surrounding CsOPMs phase offsets. (a) The expected measured deviation from the 1 μT holding field is calculated as a function of the ^{3}He polarization p and the normalized flipping angle $\theta_{\text{flip}}/(\pi/2)$. (b) Cuts through the plot of (a) for three different values of ^{3}He polarization ($p = 0.55$, red), ($p = 0.71$, blue) and ($p = 1$, orange).

is evaluated. Due to the symmetric placement of the CsOPMs this expression becomes independent of time (assuming a constant B_0 field) but depends on the flip angle θ_{flip} of the ^{3}He magnetization and the polarization p. By subtraction of the main field we obtain an expression for the observed shift $b_{\text{off}} = B_{\text{Cs}}^{\text{mean,theo}} - B_0$, a plot of this function in the (p,θ_{flip}) parameter space[3] is shown in Fig. 11.4a. Figure 11.4b shows cuts through the surface depicted in Fig. 11.4a for three different values of the ^{3}He polarization. It is visible, that b_{off} attains a maximum for $\theta_{\text{flip}} = 0$ and vanishes for $\theta_{\text{flip}} = \pi/2$. The maximum for a 100 % polarized ^{3}He sample is at $|b_{off}| \approx 16$ pT. The flipping angle and polarization for this measurement are known, they are actually calculated in Sec. 12.2.5. There we find $p = 71(6)$ % which corresponds to the green curve in Figs. 11.4b 11.4a. The flipping angle is $\theta_{\text{flip}} = 68°$ or $\theta_{\text{flip}}/(\pi/2) = 0.755$ which evaluates to a shift $|b_{\text{off}}| = 7.4$ pT as can be read from Fig. 11.4b. We have to clearly state here that this b_{off} does not reflect a real shift of the magnetic field at the ^{3}He cell-center but is due to the high order gradients that are created by the ^{3}He dipole field. These gradients are only averaged out by Eq. (11.1) when the flipping angle is $\theta_{\text{flip}} = \pi/2$.

The probably most important, and yet hardest to assess, possible cause of the observed offset lies within the inhomogeneities of the magnetic field. Finite sized coils[4] produce transverse fields whose effect was clearly witnessed by the values shown in Table 11.1. These gradients have a twofold effect. On one hand, a small geometrical misplacement of the cell can easily lead to a shift of the magnetic field by several pT. On the other hand, they induce systematic shifts of the volume averaged Larmor frequency, as discussed in Sec 3.3. The magnitude of these shifts will depend on the strength and shape of the gradients, only in the case of constant gradients the effect can easily be quantified. Since we observe considerably strong gradients in Table11.1, one may assume that these shifts can be significant as well[5]. To summarize, we conclude that the sum of the effects discussed above could easily lead to a shift of the observed magnitude.

Besides the shift discussed above it is interesting to analyze the correlation of field *changes* measured through the ^{3}He FSP and the CsOPM phase offsets. This can be done by comparing the normalized ^{3}He/Cs mean

---

[3] For calculatory reasons the normalized flipping angle $\theta_{\text{flip}}/(\pi/2)$ is used as a parameter.

[4] and may also be related to the SQUID system, see Sec. 11.2.2

[5] Evaluating Eq. (3.44) for the largest gradient ~ 12 pT/mm from Table 11.1 yields a shift of ~ 9 fT in the high pressure limit which is still negligibly small. However, the gradients encountered here are clearly neither constant nor do they have cylindrical symmetry. Under these conditions Eq. (3.44) is thus not valid anymore.

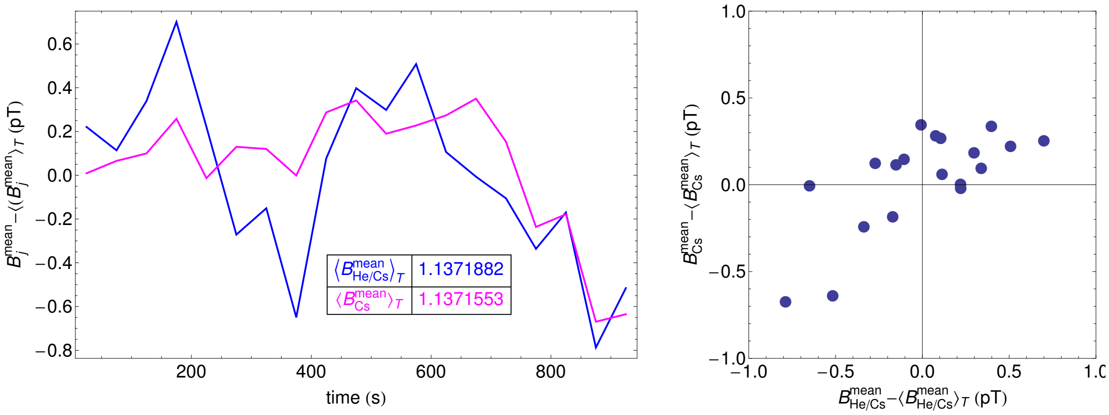

FIGURE 11.5: Left: Plots of normalized magnetic fields from ^{3}He/Cs data (blue) and CsOPM proper data (magenta). The lines are individually shifted by their time average denoted in the inset table, the ~ 33 pT discrepancy between these values which was discussed above can be seen. Right: Correlation plot of the normalized fields. See text for details.

field and normalized CsOPM proper mean field. Normalization is done by subtraction of the respective time-averaged field, yielding $B^{\rm mean}_{\rm He/Cs} - \langle B^{\rm mean}_{\rm He/Cs} \rangle_{\rm T}$ for the ^{3}He/Cs data and $B^{\rm mean}_{\rm Cs} - \langle B^{\rm mean}_{\rm Cs} \rangle_{\rm T}$ for the CsOPM data proper. Both quantities can then be plotted on a common scale, as shown in Fig. 11.5(left). As before, each data point represents a 50 s time average. Figure 11.5(right) depicts one normalized field plot against the other. The correlation of both quantities can be clearly seen, even though not overly pronounced. This can again be explained with fluctuating higher order magnetic field gradients which dynamically shift $B^{\rm mean}_{\rm He/Cs} - \langle B^{\rm mean}_{\rm He/Cs} \rangle_{\rm T}$ and $B^{\rm mean}_{\rm Cs} - \langle B^{\rm mean}_{\rm Cs} \rangle_{\rm T}$ against each other.

11.2.2 Comparing ^{3}He/Cs and ^{3}He/SQUID

As mentioned before, the BMSR-2 chamber at PTB features a multi-channel SQUID system. This offers the unique opportunity to search for systematic differences in the readout of ^{3}He-FSP by SQUIDs and CsOPMs. This was done by analyzing a long over-night measurement during which CsOPMs and SQUIDS were simultaneously detecting the ^{3}He-FSP. The ^{3}He/Cs data was processed as described in Sec. 11.1, but only six CSOPMs were running during this measurement. The average field $B^{\rm mean}_{\rm He/Cs} \pm \Delta B^{\rm mean}_{\rm He/Cs}$ was estimated for time slices of 150 s. The ^{3}He/SQUID data needed an additional step of data processing. Due to the presence of strong noise perturbations close to the ^{3}He frequency, e.g., the 50 Hz peak, digital filtering of the signals was necessary before fitting. A band-pass of ~ 7 Hz width was used for this purpose, filtering was done by a Mathematica routine. Figure 11.6 shows a SQUID signal before (upper row, left) and after (upper row, right) the digital filtering. The ^{3}He oscillation becomes visible in the time series after the filtering only. The corresponding FFT spectra in the lower row of Fig. 11.6 show the effect in the frequency domain. After filtering the fit routine was able to reliably estimate the ^{3}He Larmor frequency. Here as well it was assured that the fit yields realistic error estimates using the methods described in Sec. 7.4. Four SQUIDS with comparatively clean signals were selected and the field $B^{\rm (i)}_{\rm He/SQUID}$ and its error $\Delta B^{\rm (i)}_{\rm He/SQUID}$ calculated from the fitted ^{3}He Larmor frequency for each of them. From the four simultaneous readings the average field and its error $B^{\rm mean}_{\rm He/SQUID} \pm \Delta B^{\rm mean}_{\rm He/SQUID}$ are calculated, in complete analogy to the procedure for the ^{3}He/Cs data detailed in Sec. 11.1. The results are shown in Fig. 11.7a for a total measurement time of 7000 s, details of the visualization are given in the figure caption.

The correlation of the measurements by ^{3}He/Cs and ^{3}He/SQUID is obvious in Fig. 11.7b, where $B^{\rm mean}_{\rm He/SQUID}$ and $B^{\rm mean}_{\rm He/Cs}$ are plotted against each other. However, differences can still be observed that do not seem to be of statistical nature. This is in principle unexpected and suggests the presence of a systematic difference since the

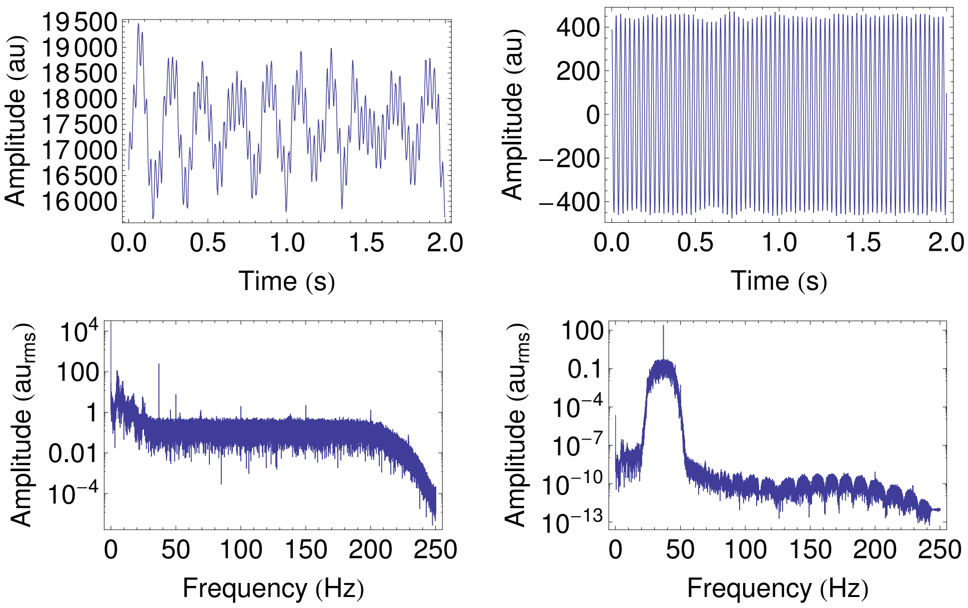

FIGURE 11.6: SQUID signals before and after digital filtering. In the upper row the time series is shown. The lower row depicts the corresponding FFT spectra. The SQUID data was taken at a sample rate $\text{sr}_{\text{SQUID}} = 500\,\text{Hz}$. The FFTs correspond to 200 s of data each.

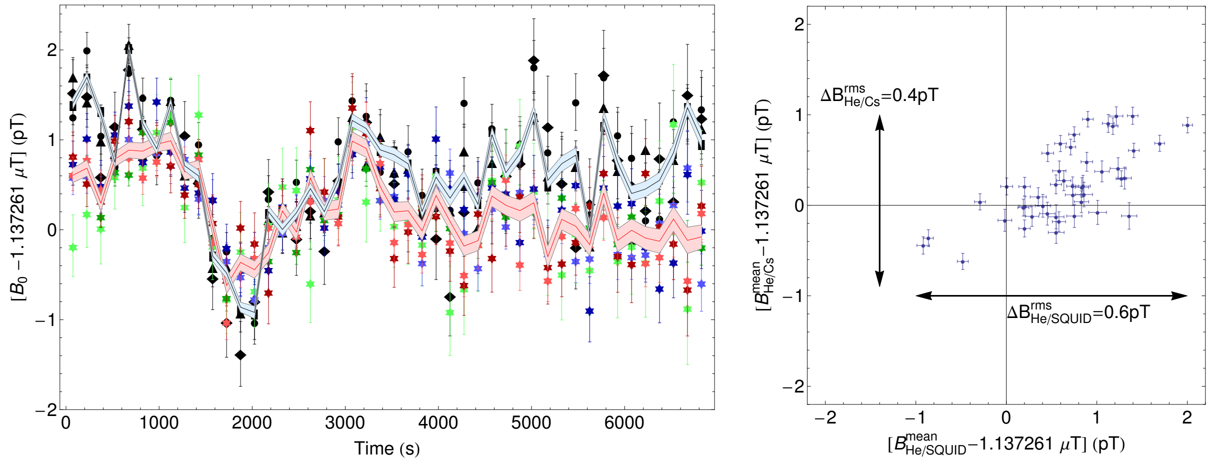

(a)

(b)

FIGURE 11.7: Correlation of field estimates obtained from CsOPMs and SQUIDs simultaneously detecting the ^{3}He-FSP. (a) Time dependence of magnetic field measured by ^{3}He/Cs (colored stars) and ^{3}He/SQUID (black symbols). Six CsOPMs and four SQUIDs are displayed. Each point corresponds to a fit to 150 s of data. The red line with the shaded region around it denotes the average value from the ^{3}He/Cs, $B^{\text{mean}}_{\text{He/Cs}}$ and its 1σ confidence band $\pm\Delta B^{\text{mean}}_{\text{He/Cs}}$. The black line and the shaded region around it signifies the same for the ^{3}He/SQUID readings,e.g., $B^{\text{mean}}_{\text{He/SQUID}} \pm \Delta B^{\text{mean}}_{\text{He/SQUID}}$ The common ordinate is shifted by the value denoted in the plot for better visibility. (b) Correlation plot of $B^{\text{mean}}_{\text{He/SQUID}}$ and $B^{\text{mean}}_{\text{He/Cs}}$. The error bars correspond to $\Delta B^{\text{mean}}_{\text{He/SQUID}}$ and $\Delta B^{\text{mean}}_{\text{He/Cs}}$ for the abscissa and ordinate, respectively. The horizontal and vertical arrows indicate the spreads $\Delta B^{\text{rms}}_{\text{HE/SQUID}}$ and $\Delta B^{\text{rms}}_{\text{HE/Cs}}$ of the magnetometer readings given in the figure.

SQUIDs and CsOPMs were detecting the same ^{3}He-FSP. The origin for this systematic difference is suspected in a flaw in the measurement process already mentioned in Sec. 6.1.4. We had omitted to reference the internal quartz-oscillator of the SQUID DAQ to the stable rubidium atomic clock, as was done for all other devices. Independent measurements characterizing this oscillator[6] show a relative stability of $\sim 10^{-7}$ in a 1 s integration time[Sch], which is already quite good for a quartz. For the frequency estimates based on 150 s time slices this instability leads to an additional statistical uncertainty which is neglegible compared to the statilstical uncertainty of the frequency estimation process. However a temperature dependent drift was also observed which may produce a relative error $\sim 10^{-6}$ in the accuracy of the time-base. This will directly translate into an equally large error of the relative field measurement at all integration times, ~ 1 pT in our case. The temperature dependence of the drift is not exactly known, but the mentioned $\sim 10^{-6}$ effects were observed under standard laboratory conditions. Since the measurements described here took place in July, when comparably large temporal temperature gradients are present, it is reasonable to expect drifts of at least this magnitude. The assumption that the SQUID system drifted is also supported by the fact that the measurements by He/SQUID show a considerably larger spread $\Delta B^{\mathrm{rms}}_{\mathrm{HE/SQUID}} = 0.6\,\mathrm{pT}$ than the corresponding readings from He/Cs, $\Delta B^{\mathrm{rms}}_{\mathrm{HE/Cs}} = 0.4\,\mathrm{pT}$, as denoted in Fig. 11.7b. From this background we conclude that no systematic difference between ^{3}He/Cs and ^{3}He/SQUID were observed within the uncertainties of this measurement.

In this context it is also interesting to note that the SQUID system produces a significant magnetic field during operation. In one measurement the CsOPMs were already measuring the ^{3}He-FSP at the moment when the SQUID system was activated[7]. The moment when the SQUIDs are activated can be clearly identified by a sequence of spikes and a persistent field shift in the CsOPM data. Figure 11.8 shows phase data from Cs1, rescaled to magnetic units (upper plot). The initiation period of the SQUID is marked in red, a shift of the magnetic field by ~ 18 pT during this process can be observed. The process equally shifts the ^{3}He Larmor frequency, as can be seen from the lower part of the figure. There, the field extracted from 50 s measurements of the ^{3}He-FSP by a CsOPM is displayed. The observation that the SQUID system produces a considerable field itself is also interesting in the frame of the discussions in the previous section, since it is expected that this field is strongly inhomogeneous due to its spatially well localized source.

---

[6] Measurements were done on an identical-twin system by the researchers at PTB.

[7] This was merely done because the SQUIDs had lost their lock on several occasions during irradiation of the ^{3}He $\pi/2$ pulse when activated from the beginning on.

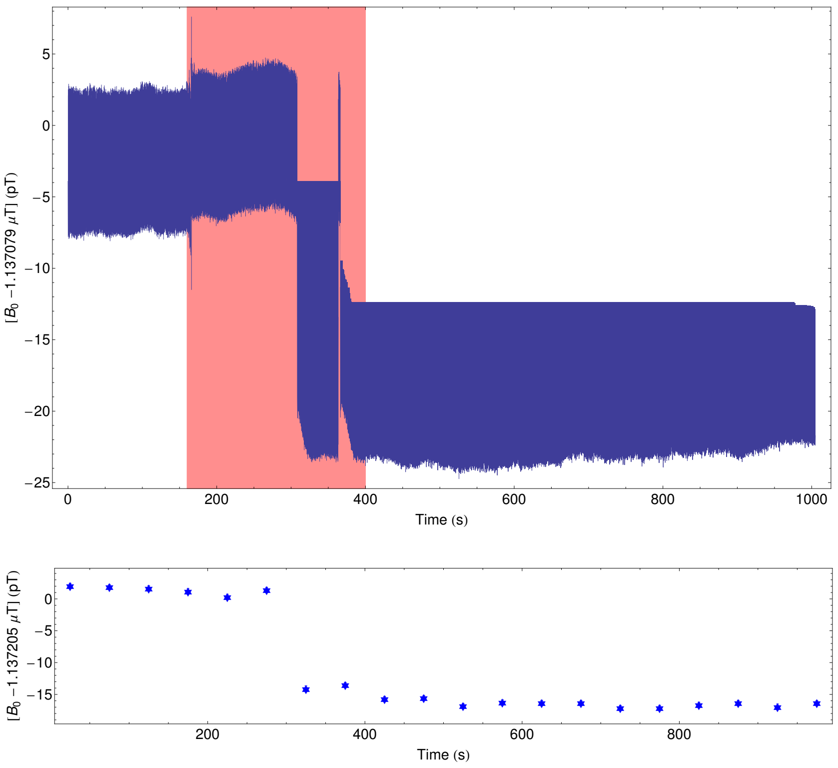

FIGURE 11.8: Shift of the magnetic holding field by activation of the SQUID system. The upper plot shows the phase data of Cs1 scaled to magnetic units, $B_{\mathrm{Cs}}^{\mathrm{Cs1}}$. The period during which the SQUID system is initiated is marked in red. The offset value of the CsOPM jumps by ∼ 18 pT. In the lower plot the magnetic field extracted from the ^{3}He-FSP, $B_{\mathrm{He/Cs}}^{\mathrm{Cs1}}$, during this time is drawn, showing that the ^{3}He magnetometer measured a change on the same order of magnitude.

Chapter 12

Magnetometric sensitivity

A key figure for characterizing a magnetometer's performance is its magnetometric sensitivity or, in other words, the precision with which the field's absolute value (or a change thereof) can be determined in a given measurement time. Investigation of the ^{3}He/Cs magnetometer's sensitivity was the central quantity of interest of this thesis since it defines the performance limits of the device that limit its possible applications, e.g., whether the magnetometer is suitable for the envisioned use in the nEDM experiment. For another type of absolute magnetometer measuring the ^{3}He FSP by SQUIDs, the sensitivity was experimentally proven to be in the lower fT range for measurement times on the order of 100 s[GHK$^+$10]. In the following section an experimental and theoretical investigation of the combined magnetometers sensitivity is presented. An expression is derived that permits to predict the sensitivity of the combined magnetometer and the ultimate sensitivity is estimated. A measurement in PS-mode is presented that demonstrates the predicted improved sensitivity for this scheme due to the higher bandwidth. Finally the expected sensitivity in the n2EDM application is estimated based on these findings and compared to that of the prototype magnetometer.

12.1 Experimental determination of sensitivity

Determining the sensitivity of of a measurement device seems at first sight a trivial task. The straightforward approach consists in repeatedly measuring a known gauge quantity with the device and determining the statistical uncertainty of the measurements. This approach fails when the measured property of the gauge quantity can not be assumed to be constant in time. In that case the fluctuations observed in the measurement values can not be unambiguously attributed to imperfections of the measurement device but might as well be caused by the instability of the gauge quantity. The situation is becoming even worse when the time scale on which the gauge quantity fluctuates is not known. This case applies for the combined ^{3}He/Cs magnetometer, where the quantity to be measured is a magnetic field, the stability of which limits the experimental determination of the magnetometer's sensitivity. In this thesis we have tried to overcome these limitations, at least partially, by simultaneously measuring the magnetic field with several different magnetometers. In this way, fluctuations of the field can be distinguished from fluctuations caused by imperfections of the measurement device.

The magnetic field in the BMSR-2 chamber was measured with the combined ^{3}He/Cs magnetometer and its readings compared to three different types of simultaneously running magnetometers. The combined ^{3}He/Cs magnetometer enables two different ways of assessing the magnetic field, as already detailed in Chapter 11. One is by using the ^{3}He's Larmor frequency $\omega_{\mathrm{L,He}}$ and one by using the CsOPM's Larmor frequency $\omega_{\mathrm{L,Cs}}$ proper. As mentioned in Chapter 6, BMSR-2 offers a built-in SQUID system which provides a third independent measurement of the magnetic field. A fourth way of measuring the magnetic field is by detection of the ^{3}He FSP using the SQUIDs. The stability of the different types of magnetometer readings were investigated by calculating and comparing their ASDs, introduced in Sec. 7.5. For the ^{3}He/Cs (^{3}He/SQUID) the underlying signal is the coherent ^{3}He-FSP found in the CsOPMs phase data (SQUID signal) and recorded over a total time T_{tot}. Calculation of the ASD of these signals takes considerable amount of time and computational power since for each

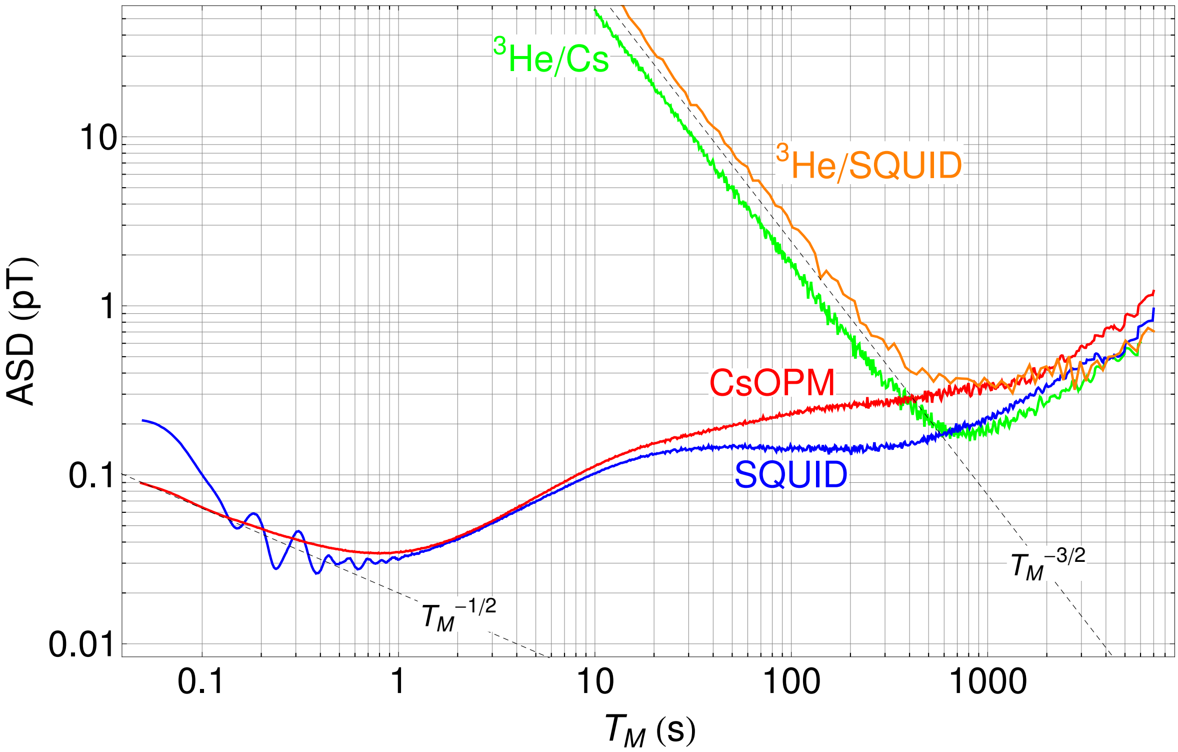

FIGURE 12.1: ASD plot of four different types (^{3}He/Cs, ^{3}He/SQUID, CsOPM-proper, SQUID-proper) of simultaneously running magnetometers. The dashed lines visualize a $\tau^{-1/2}$ and $\tau^{-3/2}$ slope, respectively. For interpretation, see text.

point $ASD(\tau)$ a number of T_{tot}/τ fits of Eq. (7.16) to the data have to be made. For the CsOPM-proper (SQUID-proper) signals, the procedure is more straightforward, as detailed in Sec. 7.5. In order to remove the ^{3}He FSP contribution from these signals, they were digitally low-pass filtered before the ASDs were calculated. This procedure of course restricts the bandwidth of the signals to $f_{\text{BW}} < 30\,\text{Hz}$, which is acceptable since we were mostly interested in the long term stability. The ASDs calculated from all four signals are shown in Fig. 12.1.

The following points are noteworthy:

The CsOPM-proper curve has the characteristic $\tau^{-1/2}$ dependence expected for a signal affected by white noise for integration times $\tau < 1\,\text{s}$ (c.f. Sec. 7.5). In this region the magnetic field measurement is statistically limited by the sensitivity of the CsOPM.

The SQUID-proper curve shows some oscillations for integration times $\tau < 1\,\text{s}$ which are most probably due to mechanical vibrations of the dewar. This makes it difficult to assign a slope to the curve in that region.

Above $\tau \sim 1\,\text{s}$ the CsOPM-proper and SQUID-proper curves are limited by the instability of the applied magnetic field. The fact that they do not overlap perfectly can be explained by their different spatial positions and the presence of magnetic field gradient fluctuations (2nd order field fluctuations). The presence of such fluctuations was already pointed out in Sec. 11.2.1 and documented in Fig. 11.2.

The ^{3}He/Cs (^{3}He/SQUID) curve shows the characteristic $\tau^{-3/2}$ dependence expected for a CRLB-limited frequency estimation of a sinusoidal signal affected by white noise (c.f. Sec. 7.2,7.5) for integration times $\tau < 500\,\text{s}$. In this region the magnetic field measurement is CRLB limited by the sensitivity of the ^{3}He/Cs (^{3}He/SQUID) magnetometer.

CsOPM	$\eta_\mathrm{B}^\mathrm{meas}(\mathrm{pT}\cdot\mathrm{s}^{3/2})$
Cs1	106(1)
Cs8	324(2)
Cs4	175(1)
Cs5	196(2)
Cs6	226(2)
Cs3	147(1)
Cs2	258(2)

TABLE 12.1: Measured sensitivity parameters for seven simultaneously running CsOPMs.

The relative vertical shift between the ^{3}He/Cs and the ^{3}He/SQUID curves depends on the CsOPM's (SQUID's) sensitivity and the distance and orientation with respect to the ^{3}He sample cell, e.g., the SNDR. Although the SQUIDS have a higher sensitivity than the CsOPMs, the ^{3}He/SQUID combination is inferior here because of the larger distance ($\approx 15\,\mathrm{cm}$) and the non-optimal orientation.

Above $\tau \sim 1000\,\mathrm{s}$ the ASD curves of all four magnetometer types overlap. In this region the field measurement precision is limited by a common process that affects all magnetometers equally. This process is the drift of the magnetic field documented in Fig. 11.1.

With the knowledge of the field stability gained from Fig. 12.1, we can investigate the magnetometric sensitivity in more detail. We have learned that the drift of the magnetic field limits the time scale of uninterrupted CRLB limited measurements to several hundreds of seconds. We now examine the error of the magnetic field estimation as a function of the measurement time T_M on this time scale. To this aim, a subset of data was chosen for which the ^{3}He amplitude was relatively large (fresh polarization) $p = 71(6)\,\%$. ASDs up to 300 s length were calculated for all seven running CsOPMs and are displayed in Fig. 12.2. As above, it can be seen that all seven ^{3}He/Cs measurements are limited by the same field drift on long time scales while for short time scales they are statistically limited. A function

$$\sigma_\mathrm{B}^\mathrm{meas} = \frac{\eta_\mathrm{B}^\mathrm{meas}}{T_\mathrm{M}^{3/2}} \tag{12.1}$$

with a fixed $T_\mathrm{M}^{-3/2}$ dependence was fit to the $10-60\,\mathrm{s}$ region of each ASD. It is shown for the lowest curve in Fig. 12.2 denoted by the dashed line, for the other ASDs the fit curves are not displayed in order not to overload the figure. The uncertainties of the ASD points, denoted by the gray envelopes around the curves, were used as weights in the fits. The experimental points follow nicely the anticipated $T_\mathrm{M}^{-3/2}$ dependence of a CRLB-limited estimation procedure that is expected on this time scale. Under this assumption, Eq. (12.1) describes the uncertainty of field estimation as a function of the measurement time. The variable $\eta_\mathrm{B}^\mathrm{meas}$ introduced there is a *sensitivity parameter* that characterizes the performance of the respective magnetometer under investigation. The sensitivity parameters for all ^{3}He/Cs pairs are summarized in Table 12.1.

When comparing Figs. 12.1 and 12.2, one notices that the range of CRLB limited measurements is restricted to shorter time scales in the second case. This is due to the fact that the polarization in the second measurement was considerably higher thereby improving the performance of all ^{3}He/Cs pairs. This shifts the ASD curves downwards and causes them to hit the stability limit of the magnetic field at shorter times already. Inspection of Fig. 12.2 and Table 12.1 reveals a considerable spread of the measured sensitivities. An explanation for this will be given in Sec. 12.2, where an expression is derived that theoretically predicts the sensitivity parameter of a CsOPM reading the ^{3}He FSP based on the parameters of its operation.

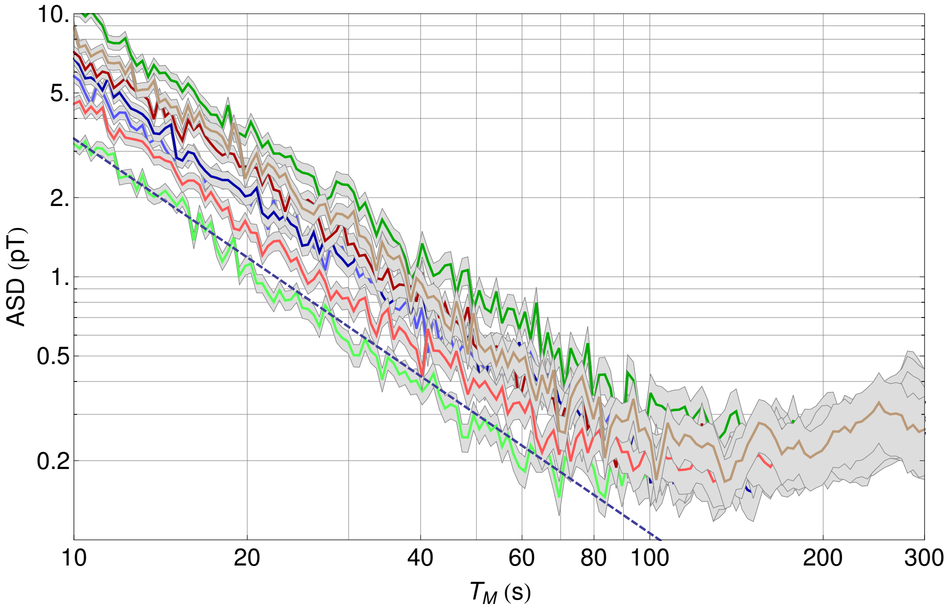

FIGURE 12.2: ASDs of seven simultaneously running CsOPMs measuring the ^{3}He FSP. Each curve is surrounded by a gray envelope that indicates its 1σ confidence region. The thick dashed line denotes a fit of Eq. (12.1) with fixed $T_{\mathrm{M}}^{-3/2}$ slope to the lowermost ASD curve. As in the previous figure, it is visible that a common noise process limits the sensitivity on long timescales.

12.2 Estimation of intrinsic sensitivity

Any measurement is perturbed by different noise processes. Some of them can be reduced or completely avoided, like the pick-up of noise on signal lines due to insufficient shielding. Others have their origin in physical effects that are inherent to the measurement process and as such represent intrinsic sources of noise. The sensitivity of the measurement process is thus fundamentally limited by these intrinsic noise processes. On the other hand, the stability of the to-be-measured magnetic field is also fundamentally limited due to the manner of its production. In this chapter, an estimation of the combined magnetometer's sensitivity is presented assuming only intrinsic sources of noise. This estimation will depend on the individual properties of each CsOPM and help to explain the large spread of the $\eta_{\mathrm{B}}^{\mathrm{meas}}$ parameter reported in the previous section.

12.2.1 Photocurrent shotnoise and CsOPM noise equivalent magnetic field

As described in Sec. 3.1.2, the CsOPMs exploit a double resonance process which is driven by an applied rf field. The shape of the resonance, and thus the magnetometer signals, are influenced by parameters characterizing the Cs vapor cell, the pump light and the rf field. We have already seen in Sec. 3.1.2 that there exists an optimal rf power for a given CsOPM geometry which is a function of the effective relaxation rate. The effective relaxation rate Γ on the other hand reflects the quality of the cell (intrinsic relxation rate) and is affected by the optical power of the pump light P_L. The sensitivity of an individual CsOPM depends on of all three of these parameters in an entangled manner.

Every paraffin-coated Cs vapor cell produced by the FRAP group is characterized by measuring Γ for different points in the $(P_L, \Omega_{\mathrm{rf}})$-parameter space. From these measurements a map of the sensitivity in this space can be extrapolated, which serves as a guide to users to find the optimal working point of each individual Cs cell. A large sample study of the cells produced at FRAP and a detailed account of the dependence of the sensitivity on the different parameters was published in [CBD$^+$09]. The following discussion will be restricted to estimating the intrinsic magnetometric sensitivity of the CsOPMs for the true drive parameters used during the measurements at PTB. These might not be the optimal values, but the sensitivity calculated from them sets a fundamental limit on the achievable sensitivity under the experimental conditions. They can thus be compared to to the experimentally observed sensitivity and help to judge the impact of other, unknown noise sources.

At the very beginning of the signal processing chain of the apparatus is the photodiode that measures the transmitted power of a laser beam traversing the Cs sample cell. The current produced in the photodiode is proportional to this power and consists of a small AC component caused by the modulation of the absorption coefficient on top of a large DC background which is typically in the μA range. As a consequence of its corpusculary nature, each electric current is affected by an intrinsic noise process, a phenomenon known as shotnoise. Shotnoise is a Gaussian noise process and as such can be characterized by a constant square root power spectral density (SQRPSD), given by

$$\rho_{\mathrm{I,PSN}} = \sqrt{2 q_{e^-} I_{\mathrm{DC}}}, \tag{12.2}$$

where I_{DC} is the DC photocurrent and q_{e^-} the elementary charge. The current is fed into a transimpedance amplifier which produces a voltage related to the current by the amplifier gain g. Fluctuations of the current will thus be converted into fluctuations of the output voltage. Since the gain is in general a function of the signal frequency, the resulting voltage noise spectrum after the amplifier, assumed to be adding no additional noise, is obtained by convoluting the current noise spectrum with the gain profile $g(\omega)$. Since in our case the signal is later processed by a LIA, only the noise close to the reference frequency will affect the demodulated signal. For this reason, one can estimate the voltage noise SQRPSD by multiplying the current SQRPSD with the respective gain factor at the reference frequency, $g(\omega_{\mathrm{rf}}) \equiv g_{\mathrm{AC}}$. The gain of the transimpedance amplifier used throughout most of the experiments at PTB was measured and found to be $g_{\mathrm{AC}} = 2.53 \times 10^7\,\mathrm{V/A}$. The major noise contribution will arise from the DC component of the photocurrent that is much larger than the AC component, so that the voltage noise SQRPSD is to a good approximation given by

$$\rho_{\mathrm{V,PSN}} = \rho_{\mathrm{I,PSN}}\, g_{\mathrm{AC}} = \sqrt{2 q_{e^-} I_{\mathrm{DC}}}\, g_{\mathrm{AC}}\,. \tag{12.3}$$

What we are finally interested in is how this voltage change affects the phase φ of the demodulated signal. The relation between these two quantities can be inferred from Fig. 12.3 and reads

$$\rho_{\varphi} = \frac{\rho_{\mathrm{R}}}{R} = \frac{\rho_{\mathrm{V,PSN}}}{a_{\mathrm{Cs}}}\,. \tag{12.4}$$

Again, we have assumed that the LIA's input noise is small compared to $\sigma_{\mathrm{V,PSN}}$ and can be neglected. From this phase noise we can calculate the so-called noise-equivalent magnetic field (NEM), its value is the magnetic noise SQRPSD which would lead to a fluctuation of the phase signal equal to the one caused by photocurrent shotnoise. The NEM is a measure for the sensitivity of the device, since smaller magnetic field changes cannot be resolved with the magnetometer, they are hidden in the intrinsic noise. From Eq. (4.24) one infers

$$\begin{aligned}\frac{\partial}{\partial B}\varphi &= \frac{\partial}{\partial B}\left(\varphi_0 + \frac{\omega_{\mathrm{L,Cs}}}{\Gamma_2} - \frac{\omega_{\mathrm{rf}}}{\Gamma_2}\right)\\ &= \frac{\partial}{\partial B}\left(\varphi_0 + \frac{\gamma_{\mathrm{Cs}} B}{\Gamma_2} - \frac{\omega_{\mathrm{rf}}}{\Gamma_2}\right) = \frac{\gamma_{\mathrm{Cs}}}{\Gamma_2}\end{aligned}$$

and thus for the NEM

$$\mathrm{NEM} = \rho_{\mathrm{B,PSN}} = \frac{\rho_{\varphi}\Gamma_2}{\gamma_{\mathrm{Cs}}} = \frac{\rho_{\mathrm{V,PSN}}\Gamma_2}{a_{\mathrm{Cs}}\gamma_{\mathrm{Cs}}}. \tag{12.5}$$

Since the DC photocurrents I_{DC} were measured repeatedly and the signal amplitudes a_{Cs} and Γ_2 constant can be extracted from the sweep responses also used for the rescaling to magnetic units, the NEM can be calculated for each sensor and individual measurement. For typical values ($I_{\mathrm{DC}} = 2\mu A, \Gamma_2/2\pi = 6\,\mathrm{Hz}, a_{\mathrm{Cs}} = 1\,\mathrm{V}$), this yields $\mathrm{NEM} \approx 38\,\mathrm{fT_{rms}}/\sqrt{\mathrm{Hz}}$. Under optimized conditions a NEM as small as $\sim 7\,\mathrm{fT_{rms}}/\sqrt{\mathrm{Hz}}$ has been reported for the best paraffin-coated cells of this type [CBD$^+$09].

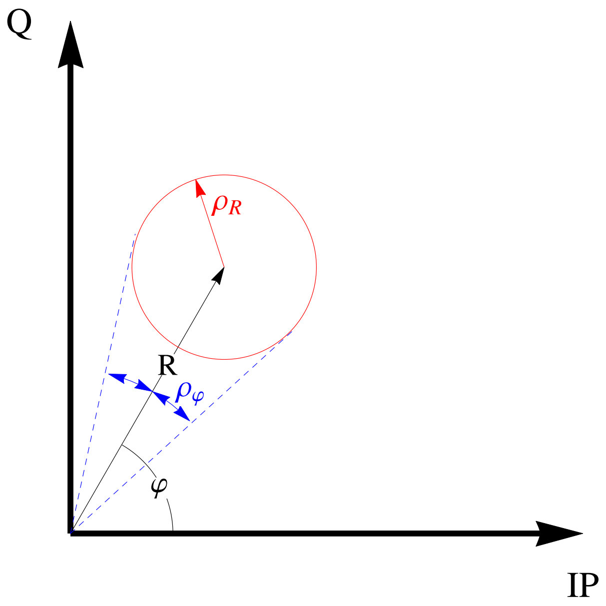

FIGURE 12.3: Phasor plot of a signal with amplitude R and phase φ affected by Gaussian amplitude noise. The noise on the in-phase (IP) and quadrature (Q) component is statistically independent and equally large and can thus be visualized as a circle of radius $\rho_\mathrm{R} = \sqrt{\rho_\mathrm{IP}^2 + \rho_\mathrm{Q}^2}$. The corresponding phase noise SQRPSD $\rho_\varphi = \rho_\mathrm{R}/R$ follows from simple geometrical considerations.

12.2.2 Coil current shotnoise

The measured magnetic field was produced by a current I_C flowing through a coil. From this current arises a shotnoise as well which leads to a fluctuation of the magnetic field amplitude. In analogy to (12.2), we calculate the current shotnoise SQRPSD and multiply by the coil constant g_coil to obtain the SQRPSD of the magnetic noise arising from it,

$$\rho_{B,CSN} = \sqrt{2eI_C}\, g_\mathrm{coil}\,. \tag{12.6}$$

In the measurements presented in this thesis, a ~ 1 μT magnetic field was created by a ~ 19 mA coil current. This corresponds to a current shotnoise of $\rho_I = \sqrt{2eI_C} \approx 78\,\mathrm{pA_{rms}}/\sqrt{\mathrm{Hz}}$. The technical noise of the current source will add to this value. The source used in the experiments described here has an extremely low technical noise specified as $7\,\mathrm{pA_{rms}}/\sqrt{\mathrm{Hz}}$[Gmb11] which can be neglected compared to the shotnoise. This leads to $\rho_{B,CSN} \approx 4.5\,\mathrm{fT_{rms}}/\sqrt{\mathrm{Hz}}$.

12.2.3 Noise processes and CsOPM response

One subtlety that has to be considered is that the coil current's shotnoise and the photocurrent's shotnoise are of substantially different type. The coil current shotnoise discussed in Sec. 12.2.2 produces a magnetic perturbation which is picked up by the CsOPM via the magnetic resonance effect. As such it will be processed by the CsOPM in the same way as the oscillating ^{3}He field. It will thus also be affected by the low-pass filter related with the Cs polarization lifetime τ_Cs discussed in Sec. 4.4.1. As stated in Sec. 7.4, only the noise $\rho_{B,CSN}(f_{He})$[1] at the ^{3}He precession frequency will affect a CRLB-limited estimation process. According to Eq. (7.3) this implies

$$\rho'_{B,CSN}(f_{He}) = T_\mathrm{Cs}(f_{He}) \cdot T_{LIA}(f_{He})\rho_{B,CSN}(f_{He}) \qquad \text{for the noise under the peak and} \tag{12.7}$$

$$b'_{He} = T_\mathrm{Cs}(f_{He}) \cdot T_{LIA}(f_{He}) b_{He} \tag{12.8}$$

---

[1] $f_{He} = \omega_{He}/2\pi$

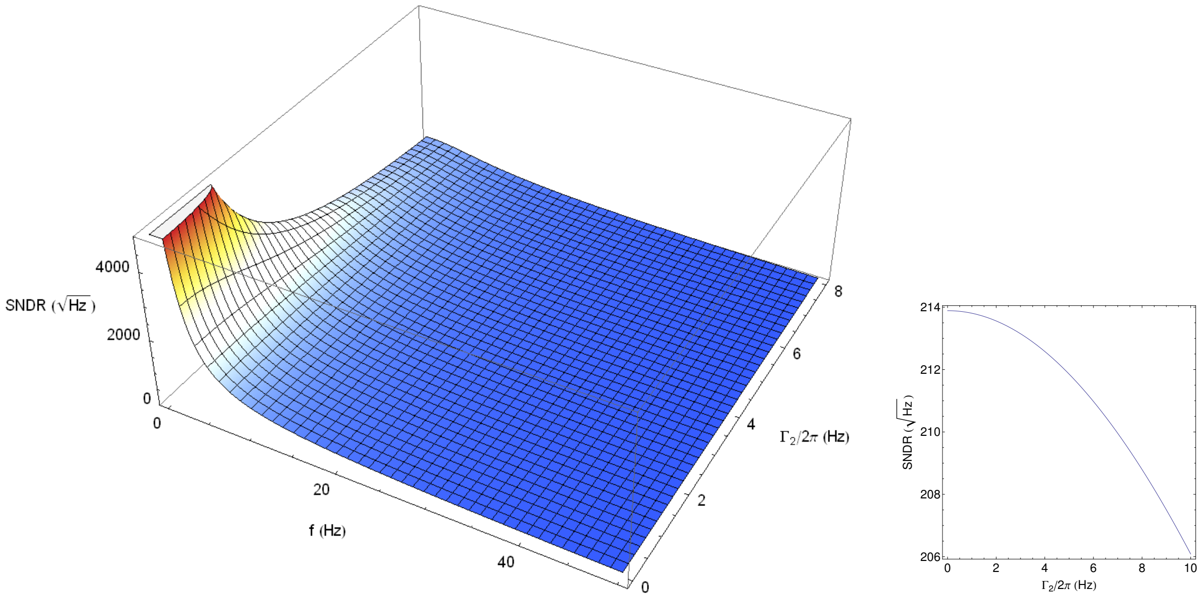

(a) (b)

FIGURE 12.4: SNDR for photocurrent shotnoise and a measured magnetic perturbance at frequency f (e.g. the ^{3}He signal) as expected from Eq. (12.10) assuming typical values, see text for details. (a) SNDR as a function of the CsOPM linewidth Γ_2 and the signal frequency f. (b) Cut through the 3D-plot from (a) at a typical ^{3}He frequency $f = f_{He} = 36\,\text{Hz}$. The SNDR is maximized for small linewidths and signal frequencies.

for the effectively measured signal amplitude. The relevant noise that a CSOPM with linewidth Γ_2 detects will thus scale in the same way as the ^{3}He measurement signal itself. As a consequence, the SNDR is independent of the linewidth Γ_2 for purely magnetic Gaussian noise.

The situation is different for the photocurrent shotnoise. As detailed in Sec. 12.2.1 its origin is not a magnetic field fluctuation but inherent to the measurement process. Thus, unlike the ^{3}He signal it is not affected by the low pass filtering arising from the Cs polarization lifetime but eventually only by the LIA demodulation filter. According to Eq. (12.5) it scales linearly with the linewidth of the CsOPM, $\rho_{\text{B,PSN}} = \frac{\rho_{\text{V,PSN}}\Gamma_2}{a_{\text{Cs}}\gamma_{\text{Cs}}}$. For the effective SNDR$'$ in this case one obtains

$$\text{SNDR}' = \frac{b'_{He}}{\rho'_{\text{B,PSN}}} = \frac{T_{\text{Cs}}(f_{He}) \cdot T_{LIA}(f_{He}) b_{He}}{T_{LIA}(f_{He}) \rho_{\text{B,PSN}}} = \frac{T_{\text{Cs}}(f_{He}) b_{He}}{\rho_{\text{B,PSN}}} \tag{12.9}$$

$$= \frac{a_{\text{Cs}}\gamma_{\text{Cs}} b_{He}}{\rho_{\text{V,PSN}}\Gamma_2\sqrt{1 + (\omega_{He}/\Gamma_2)^2}} = \frac{a_{\text{Cs}}\gamma_{\text{Cs}} b_{He}}{\rho_{\text{V,PSN}}\sqrt{\Gamma_2^2 + \omega_{He}^2}}, \tag{12.10}$$

where in the second line Eq. (4.28) with $\tau = 1/\Gamma_2$ and $n = 1$ and Eq. (12.5) were used. From Eq. (12.10) it is apparent that in the presence of photocurrent shotnoise the SNDR depends on the linewidth[2] of the CsOPM and the ^{3}He FSP frequency. The full dependency on Γ_2 and ω_{He} is shown in Fig. 12.4a. For this plot a typical ^{3}He precession frequency $f_{\text{L,He}} = 36\,\text{Hz}$ and realistic FSP amplitude $b_{He} = 22\,\text{pT}_{\text{rms}}$ and $\rho_{\text{V,PSN}} = 10^{-5}\,\text{V}_{\text{rms}}/\sqrt{\text{Hz}}$ were chosen. It can be seen that the SNDR peaks for small $\omega_{\text{L,He}}$ and linewidth Γ_2.

12.2.4 Sensitivity loss due to off-resonant drive

There is yet another effect that has to be considered when estimating the sensitivity of a ^{3}He/Cs magnetometer arrangement. As was introduced in Sec. 4.4, in the FF-mode of CsOPM operation some (or all) sensors are

---

[2] Note, that this calculation assumes a constant Cs-amplitude a_{Cs} and a constant photocurrent noise power $\rho_{\text{V,PSN}}$. It does thus not model the effects that may arise from different power broadening but only due to the spread in intrinsic relaxation rates. When power broadening is to be considered, one has to include as well the dependence of a_{Cs} and $\rho_{\text{V,PSN}}$ on the light power. A detailed discussion of these dependence is given in [CBD$^+$09].

by default driven off resonance, e.g., $\omega_{\mathrm{L,Cs}} \neq \omega_{\mathrm{rf}}$. The approximations which have been made there, leading from Eq. (4.17) to the simple expression Eq. (4.25) assume that the actual detuning $\delta\omega$ is very small. In this section the effect of a finite detuning on the magnetometer's sensitivity will be quantitatively studied. The line shape of the M_x-magnetometer was derived in Sec. 3.1.2 and reads (see Eq. (3.20),(4.17)) $\tan(\varphi) = -\Gamma_2/\delta\omega$. The approximation that was made exploits that around $\delta\omega \approx 0$ the tangens function has a linear dependence on the detuning[3]. The slope of the phase curve for a given detuning $\delta\omega'$ of a specific CsOPM can be calculated via

$$m(\delta\omega') = \frac{\partial\varphi}{\partial\delta\omega} = \frac{\partial}{\partial\delta\omega}\arctan\left(\frac{-\Gamma_2}{\delta\omega}\right)\Big|_{\delta\omega'} = \frac{\Gamma_2}{\Gamma_2^2 + \delta\omega'^2}\,. \tag{12.11}$$

We see, that Eq. (12.11) is maximal at $m(\delta\omega' = 0) = 1/\Gamma_2$ for the on-resonance value of the phase slope. A CsOPM that is driven off-resonance will thus always exhibit a smaller phase response to a given magnetic perturbation $dB = d\omega/\gamma_{\mathrm{Cs}}$. The factor by which this response is smaller compared to the response of the same magnetometer when it is driven on resonance is given by

$$\epsilon_\varphi(\delta\omega') = \frac{d\varphi'}{d\varphi} = \frac{m(\delta\omega')}{m(\delta\omega = 0)} = \frac{\Gamma_2^2}{\Gamma_2^2 + \delta\omega'^2}\,. \tag{12.12}$$

In analogy to the considerations for the low-pass effect presented in Sec. 12.2.3, this does not affect the SNDR in the presence of purely magnetic noise since the scaling factor for the noise- and the signal-amplitude is the same. Again, the situation is different when a (large) fraction of the measurement noise is attributed to photocurrent shotnoise. This is clearly the case in the measurements under investigation here, as we have seen in Sec. 12.2.1. From Eq. (12.4), we know the dependence of the phase noise on the photocurrent (voltage-) shotnoise,

$$\rho_\varphi = \frac{\rho_{\mathrm{V,PSN}}}{a'_{\mathrm{Cs}}(\delta\omega')}\,, \tag{12.13}$$

where $a'_{\mathrm{Cs}}(\delta\omega') = R(\delta\omega')$ is the amplitude of the R-signal for a given detuning $\delta\omega'$ as given by Eq. (3.19). The ratio of photocurrent shotnoise induced phase noise for a resonantly driven and detuned CsOPM is thus given by

$$\epsilon_\rho(\delta\omega) = \frac{\rho'_\varphi}{\rho_\varphi} = \frac{a_{\mathrm{Cs}}(\delta\omega = 0)}{a'_{\mathrm{Cs}}(\delta\omega')}\,. \tag{12.14}$$

For this case, the SNDR effectively measured by a detuned CsOPM is

$$\mathrm{SNDR}'(\delta\omega) = \frac{\varphi'}{\rho'_\varphi} = \frac{\epsilon_\varphi(\delta\omega')\varphi}{\epsilon_\rho(\delta\omega')\rho_\varphi} = \mathrm{SNDR}\frac{\epsilon_\varphi(\delta\omega')}{\epsilon_\rho(\delta\omega')}\,. \tag{12.15}$$

From the definitions (12.12) and (12.14) it is obvious that in the presence of photocurrent shotnoise in general $\mathrm{SNDR}' < \mathrm{SNDR}$, a CsOPM will thus be less performing when driven off resonance. An analytical expression for $\frac{\epsilon_\varphi(\delta\omega')}{\epsilon_\rho(\delta\omega')}$ can be derived from Eqns. (3.19) and (12.12). It reads

$$\frac{\epsilon_\varphi(\delta\omega')}{\epsilon_\rho(\delta\omega')} = \frac{\Gamma_2^2(\Gamma_1\Gamma_2 + \omega_1^2/2)}{\sqrt{\Gamma_2^2 + \delta\omega'^2}\,(\Gamma_1(\Gamma_2^2 + \delta\omega'^2) + \Gamma_2\omega_1^2/2)}\,. \tag{12.16}$$

Equation (12.16) becomes interesting when Γ_1, Γ_2 and ω_1 for a CsOPM are known. It can then be used to model the sensitivity as a function of the detuning. For the measurements discussed here a more empirical approach will be followed. From the sweep response scans and the known drive frequency ω the detuning $\delta\omega'$ and linewidth Γ_2 can be derived and inserting this into Eq. (12.12), ϵ_φ calculated for each CsOPM. The ratio $\epsilon_\rho(\delta\omega) = \frac{a_{\mathrm{Cs}}(\delta\omega=0)}{a'_{\mathrm{Cs}}(\delta\omega')}$ can be read from the R-signal of the sweep response. This allows to calculate a correction factor

$$c(Cs_i) = \frac{\epsilon_\varphi(Cs_i)}{\epsilon_\rho(Cs_i)} \tag{12.17}$$

---

[3] Actually $1/\Gamma_2$ can be understood as the zero-detuning slope of the phase curve.

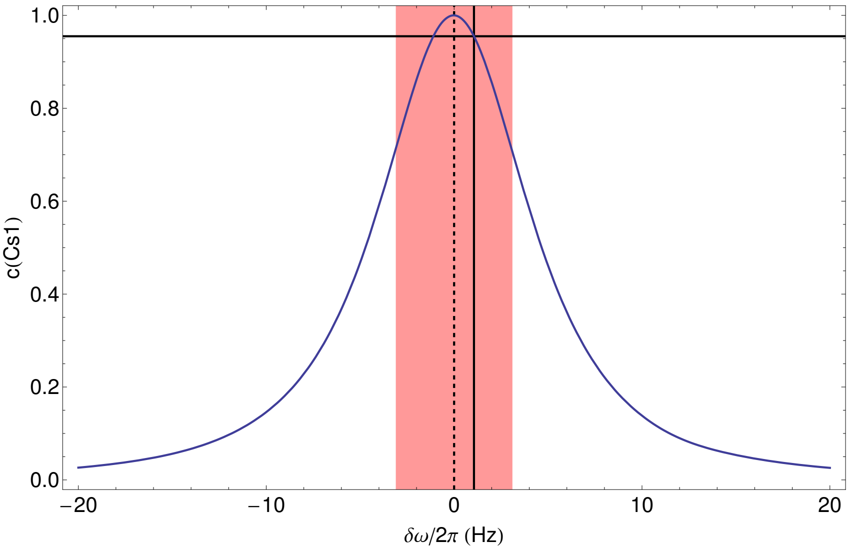

FIGURE 12.5: Plot of $c(Cs_1) = \frac{\epsilon_\varphi(Cs_1)}{\epsilon_\rho(Cs)}$ visualizes the dependence of the CsOPM's sensitivity on the detuning. The values were obtained as described in the text. The shaded red vertical band illustrates the linewidth $\Gamma_2/2\pi = 6.1$ Hz of this magnetometer. The solid vertical line denotes the actual detuning $\delta\omega'/2\pi = 1.06$ Hz of this CsOPM during operation. This leads to a sensitivity reduced by a factor $c = 0.96$ as indicated by the horizontal line.

for each CsOPM[4] that takes the loss of sensitivity due to a (permanent) constant detuning into account. The effect is illustrated in Fig. 12.5 for magnetometer Cs1. Note, that the scaling function Eq. (7.2) that is used in the DC-scaling procedure described in Sec. 7.1.1 takes this effect into account because it uses the accurate arctan() phase/frequency dependence. This means that the amplitudes of phase-oscillations will be transformed to oscillations of the measured magnetic field in a nonlinear way. The data which has been rescaled to magnetic units in this way shows realistic amplitudes of the oscillating magnetic fields. This goes hand in hand with an equally nonlinear transformation of the measurement noise. If PSN is the dominant source of noise in the system, the DC-rescaled spectrum of a CsOPM will thus not reflect the NEM, even under optimal conditions, while the raw phase signal will. We thus see that the raw phase data is more convenient for analyzing noise processes while the (AC/DC-) rescaled signals are more adequate for investigating the signal amplitudes.

12.2.5 Measured ^{3}He-FSP amplitudes

After the discussion of effects that affect the measured amplitudes of oscillating magnetic fields, now we will compare the ^{3}He-FSP amplitudes measured by different CsOPMs. Phase data from a measurement with seven simultaneously running CsOPMs was first rescaled to magnetic units using the DC-scaling procedure introduced in Sec. 7.1.1. As stated in Sec. 12.2.4 this already corrects for the individual amplitude response errors of each CsOPM due to their off-resonant drive. The amplitudes of the rescaled signals were extracted by fits of Eq. (7.16). The true magnitude of the magnetic field oscillations was then calculated from those amplitudes using the AC-scaling procedure described in Sec. 7.1.2. The results before and after the AC-rescaling are summarized in Table. 12.2. Comparison of the values before AC-rescaling yields a considerable spread of ≈ 21 % which reduces to ≈ 9.1 % after rescaling. The remaining spread in the measured ^{3}He-FSP amplitudes is most likely caused by *geometrical* imperfections of the apparatus[5]. Two qualitatively different types of ef-

---

[4] ...(Cs_i) is a short symbolic notation for the relevant parameters (detuning, linewidth and R_0/R ratio) of the i-th CsOPM.

[5] For Cs2 and Cs7 this statement does not strictly hold, because they were demodulated on a LIA of different type. It can not be excluded that this influences the amplitudes in a slightly different way, for example due to a different implementation of the low-pass filter in the LIA device.

CsOPM	$b'_{He}(\mathrm{pT_{rms}})$	$b_{He}(\mathrm{pT_{rms}})$
Cs1	3.12	22.0
Cs8	5.25	22.2
Cs4	3.66	22.4
Cs5	3.95	22.9
Cs6	4.82	24.3
Cs3	3.09	25.3
Cs2	4.09	20.6
Cs7	3.07	18.8
rms-spread	≈ 21 %	≈ 9.1 %

TABLE 12.2: Amplitudes of ^{3}He FSP as obtained from the CsOPMs phase data after DC-rescaling (b'_{He}) and after AC-rescaling (b_{He}). The bottom line gives the relative rms-spread of the values in both columns calculated from the ratio between their standard deviation and their mean.

fects can be considered which originate from possibly unequal distances between the individual CsOPMs and the ^{3}He-cell-center on one hand and misalignments on the other hand. As pointed out in Sec.5.3 the ^{3}He-Cs cell-center-distances can be estimated to be $r_\mathrm{c} = 50(1)\,\mathrm{mm}$. From Eq. (4.7) it is apparent that the amplitude of the oscillating $\hat{z}$-component of the magnetic field created by the ^{3}He FSP has a $1/r^3$ dependence on the distance from the source. The relative spread in the magnetic fields expected from positioning errors is thus $\Delta b_\mathrm{He}/b_\mathrm{He} = 3\Delta r_\mathrm{c}/r_\mathrm{c} = 6\,\%$ which is in good agreement with the observed value in Table 12.2. It can thus be concluded that the AC-rescaling procedures really yield realistic measures for the amplitudes of oscillating magnetic fields. By comparing the AC-rescaled ^{3}He FSP amplitudes to the value $b_\mathrm{He,max}$ obtained for 100 % polarization in Eq. (4.14), the degree of polarization of the gas sample in this measurement can be calculated. For this evaluation, the flipping angle θ_flip needs to be known. The flipping of the magnetization for this measurement run was recorded and is actually displayed in Fig. 8.2. Following the procedure detailed in Sec. 8.2, the flipping angle was calculated for this measurement yielding $\theta_\mathrm{flip} = 68.0(6)\,^\circ$. The degree of polarization is then given by

$$p = \frac{b_\mathrm{He}}{b_\mathrm{He,max}\sin(\theta_\mathrm{flip})}\,, \tag{12.18}$$

the calculation yielding $p = 0.71(6)$. Comparisons with data from other measurement runs show, that the polarization was usually on the order of 70 % after optical pumping.

The second effect which could cause the difference in the readings of different CsOPMs is a geometrical misalignment. Since the combined magnetometer setup has, in principle, many degrees of freedom when one starts to consider the positioning of the individual components, an estimation of the effects which might arise becomes very complex. The simplest form of misalignment which has an influence on the measured ^{3}He FSP amplitudes is met when the symmetry axis of the combined magnetometer does not coincide with the $\hat{B}_0$ direction. This case is particularly interesting for future investigations, because it may possibly allow to infer information on the direction of the applied magnetic field from the measurements.

12.2.6 CRLB-limited sensitivity in shotnoise limit

For the case considered here, the intrinsic noise of the CsOPMs will at least consist of the two contributions discussed above. The situation in which the shotnoise of the involved currents is considered to be the only source of noise is referred to as the *sensitivity in the shotnoise limit.* Since one can assume that these two sources of noise are statistically independent, their combined noise SQRTPSD will be the quadratic sum of the constituents,

$$\rho_{B,tot} = \sqrt{\rho^2_\mathrm{B,PSN} + \rho^2_{B,CSN}}\,. \tag{12.19}$$

CsOPM	$\eta_{\mathrm{B}}^{\mathrm{theo}}(\mathrm{pT}\cdot\mathrm{s}^{3/2})$	$\eta_{\mathrm{B}}^{\mathrm{meas}}(\mathrm{pT}\cdot\mathrm{s}^{3/2})$	$\eta_{\mathrm{B}}^{\mathrm{theo}}/\eta_{\mathrm{B}}^{\mathrm{meas}}$
Cs1	118(11)	106(1)	1.11(10)
Cs8	313(28)	324(2)	0.97(09)
Cs4	161(15)	175(1)	0.92(09)
Cs5	196(18)	196(2)	1.00(09)
Cs6	241(22)	226(2)	1.07(10)
Cs3	156(14)	147(1)	1.06(10)
Cs2	181(17)	258(2)	0.70(07)
Cs7	254(23)	-	-

TABLE 12.3: Measured and predicted sensitivity parameters for different CsOPMs. The measured values are repeated from Table 12.1. For Cs7 no sensitivity could be measured due to a DAQ problem. The large errors on the predicted values are due to the uncertainty of the degree of polarization.

For typical values introduced above, Eq. (12.19) yields $\rho_{B,tot} \approx 38\,\mathrm{fT_{rms}}/\sqrt{\mathrm{Hz}}$. We thus find that under our experimental conditions, the photocurrent shotnoise is by far the dominant contribution[6]. To estimate the intrinsic sensitivity of the combined ^{3}He/Cs magnetometer in the shotnoise limit under the given experimental conditions, we assume a CRLB-limited frequency estimation procedure. Under these assumptions a sensitivity parameter $\eta_{\mathrm{B}}^{\mathrm{theo}}$ in analogy to the one introduced in Eq. (12.1) can be theoretically predicted for each magnetometer. The expression is obtained by calculating the CRLB of a signal with SNDR which is corrected for the effects due to the Cs-lifetime and detuning for each individual CsOPM that were introduced in Sec. 12.2.3 and Sec. 12.2.4. This means effectively that combining Eq. (7.11), (12.10) and (12.17) yields

$$\eta_{\mathrm{B}}^{\mathrm{theo}} = \frac{\sqrt{6}\,\rho_{\mathrm{V,PSN}}\sqrt{\Gamma_2^2+\omega_{He}^2}}{a_{\mathrm{Cs}}\,b_{He}\gamma_{He}\gamma_{\mathrm{Cs}}}\,\frac{\epsilon_\rho}{\epsilon\varphi}\,. \tag{12.20}$$

By including the definitions from Eq. (12.14), Eq. (12.17) and expressing b_{He} in terms of the maximum achievable amplitude $b_{\mathrm{max,He}}$ from Eq. (4.14) and the *effective* degree of polarization $p_{\mathrm{eff}} = p\cdot\sin(\theta_{\mathrm{flip}})$, we find a different form of Eq. (12.20)

$$\eta_{\mathrm{B}}^{\mathrm{theo}} = \frac{\sqrt{6}}{p_{\mathrm{eff}}\,b_{\mathrm{max,He}}\gamma_{He}\gamma_{\mathrm{Cs}}}\,\frac{\rho_{\mathrm{V,PSN}}\sqrt{\Gamma_2^2+\omega_{He}^2}(\Gamma_2^2+\delta\omega'^2)}{a'_{\mathrm{Cs}}(\delta\omega')\Gamma_2^2}\,. \tag{12.21}$$

Evaluating this expression for the parameters of the different CsOPMs during the measurements yields the values presented in Table 12.3 together with their experimental counterparts obtained in Sec. 12.1. The values are also plotted in Fig. 12.6 and a linear regression was performed to analyze their dependence. The fit yields [7] the dependence $\eta_{\mathrm{B}}^{\mathrm{meas}} = 1.11(10)\eta_{\mathrm{B}}^{\mathrm{theo}} - 21.38(16.26)\,\mathrm{pT}\cdot\mathrm{s}^{3/2}$. The theoretically predicted sensitivities calculated from Eq. (12.21) agree with the experimentally observed ones within the uncertainties of the measurement. This result also allows the conclusion that a shotnoise limited measurement was performed, since Eq. (12.21) predicts the sensitivity in the shotnoise limit.

12.2.7 Sensitivity in PS-mode

It was pointed out in Sec. 4.4 that the low-pass character of the CsOPM in FF-mode imposes a severe bandwidth limitation. Since the PS-mode allows to operate the magnetometer with a considerably larger bandwidth, the question arises if an improved magnetometric sensitivity can be achieved in this mode of operation.

To investigate the achievable SNDR in the PS-mode we again have to make a separate case for the PSN which causes fluctuations of the CsOPM's phase signal that are not related to magnetic field fluctuations. The

---

[6] Note that due to the low-pass filtering effect discussed in Sec. 12.2.3 the *measured magnetic noise* arising from the coil current's shotnoise does not have a constant SQRTPSD anymore and is thus not adequately described by $\rho_{B,CSN}$. Since its contribution to the total noise floor is very small, the magnetic fraction of the noise in general and this fact in particular will be neglected in the following estimation.

[7] Cs2 is excluded from this discussion, because it was operated on a substantially different signal processing chain.

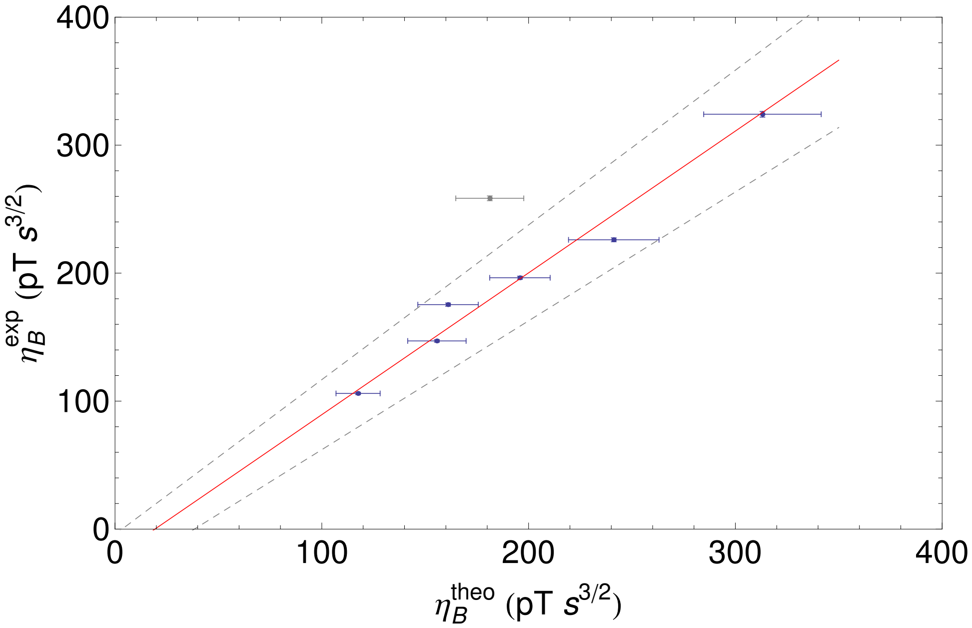

FIGURE 12.6: Plot of measured and predicted sensitivity parameters. A linear regression was performed to analyze the dependence, the gray point belongs to Cs2 and was excluded from the fit because it was handled on a different DAQ system. The fit yields $\eta_{\mathrm{B}}^{\mathrm{meas}} = 1.11(10)\eta_{\mathrm{B}}^{\mathrm{theo}} - 21.38(16.26)\,\mathrm{pT}\cdot\mathrm{s}^{3/2}$.

PSL will equally react to these fluctuations by adjustments of the drive frequency $\omega_{\mathrm{rf}} = \widetilde{\omega}_{\mathrm{PSL}}$ thereby actually detuning the CsOPM from resonance, $\widetilde{\omega}_{\mathrm{PSL}} \neq \omega_{\mathrm{L,Cs}}$. As a result the response of the magnetometer to these adjustments of the drive frequency becomes again bandwidth limited by the lifetime of the Cs polarization. We can express this detuning in magnetic units by a relation similar to Eq. (4.32),

$$\delta\widetilde{B} = \frac{\Gamma_2\delta\phi_{\mathrm{PSL}} + T_{\mathrm{Cs}}(f)\delta\widetilde{\omega}_{\mathrm{PSL}}}{\gamma_{\mathrm{Cs}}} = \frac{\delta\widetilde{\omega}_{\mathrm{PSL}}}{\gamma_{\mathrm{Cs}}}\left(\frac{\Gamma_2}{\kappa(f)} + T_{\mathrm{Cs}}(f)\right) \tag{12.22}$$

where in the last step Eq. (4.31) was used. We assume now a measurement signal originating from an oscillating magnetic field, e.g., the ^{3}He FSP $\delta B = b_{\mathrm{He}}$ and signal noise being caused by PSN $\delta\widetilde{B} = \rho_{\mathrm{B,PSN}} = \mathrm{NEM}$. The SNDR of the PSL frequency signal can be written as

$$\mathrm{SNDR}_{\mathrm{PSL}} = \frac{\delta\omega_{\mathrm{PSL}}}{\delta\widetilde{\omega}_{\mathrm{PSL}}} = \frac{\delta B}{\delta\widetilde{B}}\frac{T_{\mathrm{Cs}}(f) + \Gamma_2/\kappa(f)}{1 + \Gamma_2/\kappa(f)} \tag{12.23}$$

$$= \frac{b_{\mathrm{He}}}{\rho_{\mathrm{B,PSN}}}\frac{T_{\mathrm{Cs}}(f) + \Gamma_2/\kappa(f)}{1 + \Gamma_2/\kappa(f)}. \tag{12.24}$$

Inspection of Eq. (12.24) in the high gain limit ($\kappa(f) \gg \Gamma_2$) shows that the maximum achievable SNDR is

$$\lim_{\kappa(f)\to\infty} \mathrm{SNDR}_{\mathrm{PSL}} = \frac{b_{\mathrm{He}}}{\rho_{\mathrm{B,PSN}}} T_{\mathrm{Cs}}(f), \tag{12.25}$$

which is equal to the SNDR for a CsOPM with zero permanent detuning driven in FF-mode derived in Eq. (12.9). The frequency dependence of the SNDR in both modes of operation is thus identical. To put it in simple words we found that in the PS-mode the signal amplitude is scaled down due the bandwidth limitation of the CsOPM response while the signal noise (PSN) is not bandwidth limited and thus constant. In the FF-mode on the other hand the situation is inverted. The signal amplitudes are constant (within the bandwidth of the PSL) but the signal noise is scaled up due to the same bandwidth limitation of the CsOPM.

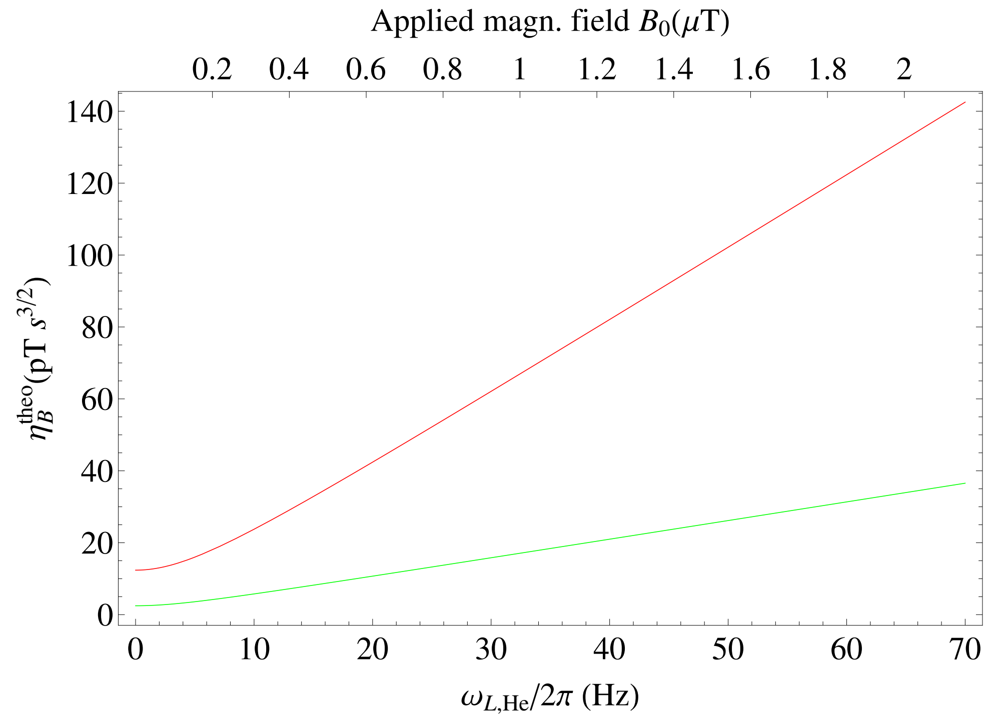

FIGURE 12.7: Plot of the theoretically predicted ultimate sensitivity of the combined ^{3}He/Cs magnetometer as a function of the applied magnetic field. For the green curve, the best paraffin coated Cs vaporcell ever produced by FRAP [CBD$^+$09] is assumed. For comparison the red curve calculated based on the experimental parameters of Cs1 during the measurements reported here is also shown. A 100% polarized ^{3}He sample and CRLB-limited detection in the shotnoise limit is assumed in both cases.

12.2.8 Ultimate sensitivity

At this point we dare to make an estimation of the best achievable sensitivity of a combined ^{3}He/Cs magnetometer in this design. After all previous discussions and by inspecting Eq. (12.20) it is obvious that this means minimizing the CsOPMs NEM and detuning and maximizing the ^{3}He FSP amplitude. We assume, that the positions of the CsOPMs are already optimal, e.g., their distance to the cell is minimal and their angular positions are as derived in Sec. 4.2. The CsOPMs have the smallest NEM for a specific set of drive parameters. As reported in [CBD$^+$09], the best paraffin coated Cs vaporcell ever produced by FRAP has a $\text{NEM}_{\text{min}} = 7\,\text{fT}_{\text{rms}}/\sqrt{\text{Hz}}$ at optimum drive parameters (P_L, Ω_{rf}) and exhibited a linewidth of $\Gamma_2/2\pi = 4.75\,\text{Hz}$ under these conditions. When we rewrite Eq. (12.20) introducing the NEM from Eq. (12.5) as a parameter and setting $p_{\text{eff}} = 1$ while assuming $\delta\omega' = 0$ we find

$$\eta_{\text{B}}^{\text{theo}} = \text{NEM}\frac{\sqrt{6}\sqrt{\Gamma_2^2 + \omega_{\text{L,He}}^2}}{\gamma_{He}\Gamma_2 b_{\text{max,He}}}. \tag{12.26}$$

Inserting the best reported cell parameters cited above, we obtain the ultimate achievable sensitivity for a single CsOPM reading the ^{3}He-FSP as a function of the applied magnetic field. A plot of this function is shown in Fig. 12.7. For a magnetic field of $B_0 = 1\,\mu\text{T}$ Eq.(12.26) evaluates to $\eta_{\text{B}}^{\text{theo}} = 17\,\text{pT}\cdot\text{s}^{3/2}$. For $\omega_{\text{L,He}} = 0$ a value of $\eta_{\text{B}}^{\text{theo}} = 2.5\,\text{pT}\cdot\text{s}^{3/2}$ is found.

12.3 Implications for the n2EDM experiment

The ultimate sensitivity derived in the previous section only applies to the specific geometry of the prototype magnetometer developed in this work. For the n2EDM application, a major difference will be the use of much

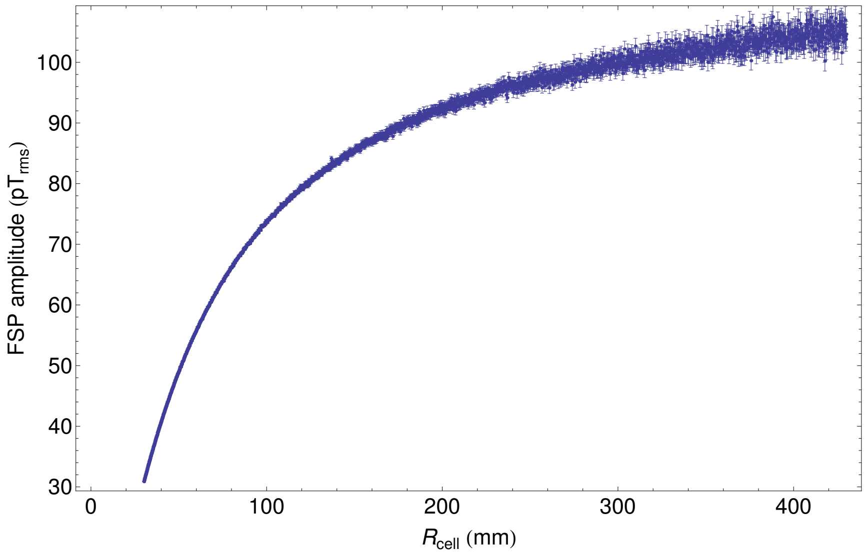

FIGURE 12.8: Dependence of the expected ^{3}He-FSP amplitude b_{He} on the ^{3}He cell-radius. A CsOPM with a cell of 3 cm diameter is assumed, that is at the closest possible distance (both cells touching) under the optimal detection angle. A spherical shape of the ^{3}He cell and 100 % polarized gas are considered. The plot starts at the parameters found in the prototype magnetometer.

larger ^{3}He cells of different shape. In the prototype magnetometer the Cs-cells and the ^{3}He cell are of similar size ($\sim$ 3 cm and $\sim$ 7 cm diameter, respectively). From the considerations in Chapter 4 it is clear that the magnetic field produced at the surface of a polarized ^{3}He sample cell depends on the pressure only, and not on the size, e.g., the radius R_{cell} of the cell. This follows from the fact that at constant pressure the number of atoms in the cell scales with $\sim R_{cell}^3$ while the dipole field drops with $\sim r_c^{-3}$ and every increase of the cell size goes in hand with an equal increase of the distance from the center, r_c. However, the field at a fixed distance r_s from the cell surface does depend on the ratio between R_{cell} and r_s. For $R_{cell} \approx r_s$, which is the case in the magnetometer prototype, considerably smaller magnetic fields are found as for $R_{cell} \gg r_s$, which will be the situation in n2EDM. The dependence of the rms-amplitude of the ^{3}He-FSP on the ^{3}He cell radius (for a spherical ^{3}He cell filled with 100 % polarized gas at 1 mbar) is shown in Fig. 12.8. The values are obtained from a numerical simulation assuming a distance $r_s = 1.5$ cm from the surface of the ^{3}He cell and an optimal detection angle. It is evident that the FSP amplitude rises considerably with increased ^{3}He cell size and saturates at around three times the value found for the current geometry. This suggests that improved sensitivities can be achieved for the larger ^{3}He cells envisioned in n2EDM.

Since the design of the n2EDM spectrometer is still a topic of vivid discussions we only dare to make a tentative approximation of the expected sensitivity. The design of the ^{3}He magnetometer vessels has in any case to foresee the situation where the magnetometer is operated in atmospheric pressure, as this might be useful for various tests and facilitate the handling. These vessels have thus to be built to withstand the large forces which arise from the $\sim$ 1 bar pressure difference in this case, this poses very high stability requirements in particular to the plane lids of the cylinders. First tests [Len09] were therefore performed with cells having lids of thickness 20 mm made from borosilicate glas. From the previous discussions however, we know that we should aim to minimize the distance between the CsOPMs and the ^{3}He volume in order to maximize the ^{3}He FSP amplitude. A stress analysis performed with Autodesk Inventor shows that the thickness can be reduced to 15 mm, still having a reasonable security margin[8]. We thus assume a cylindrical ^{3}He cell of 500 mm inner diameter and inner height 60 mm with lids of thickness 15 mm filled with 100 % polarized gas at 1 mbar pressure. A numerical

---

[8] The maximum acceptable tension of the glass is at all positions of the cell at least two times larger than the calculated tension for the $\sim$ 1 bar pressure difference. One possible n2EDM design scheme also involves a centric axial pillar in the ^{3}He cell which would further improve the mechanical stability and allow for even thinner walls.

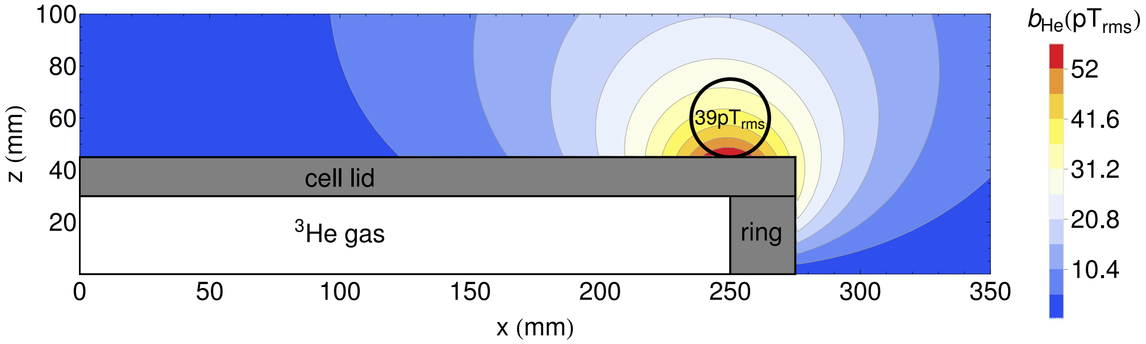

FIGURE 12.9: Simulation of ^{3}He FSP amplitude b_{He} for the expected n2EDM geometry. One quadrant of a cut through the ^{3}He cell (in lower left of figure) in the $\hat{x}$-$\hat{z}$ plane is shown, the gray structure denotes the cell walls. The B_0 field points along $\hat{z}$ and the ^{3}He magnetization precesses in the $\hat{x}$-$\hat{y}$ plane. A filling with 100 % polarized gas at 1 mbar is assumed. A CsOPM, represented by the black circle, is placed at the position of highest amplitude $b_{\mathrm{He}} = 39\,\mathrm{pT_{rms}}$.

simulation of the expected ^{3}He FSP amplitudes as a function of the CsOPM position is shown in Fig. 12.9. It can be seen that for the assumed n2EDM geometry the amplitude attains a maximum $b_{\mathrm{He,max}} \approx 39\,\mathrm{pT_{rms}}$, comparable to the value found in the geometry of the ^{3}He/Cs magnetometer prototype. The expected sensitivity in the n2EDM application will thus be comparable or slightly better than that reported for the prototype magnetometer. However, due to the larger size of the ^{3}He cell a large number $N_{\mathrm{Cs}} > 25$ of CsOPMs can be employed for simultaneous detection of the ^{3}He FSP. Since the overall sensitivity parameter scales[9] as $1/\sqrt{N_{\mathrm{Cs}}}$ this will significantly improve the performance of the magnetometer and also allow for more precise measurements of the flip angle θ_{flip}.

It is worth noting that unlike for the spherical ^{3}He cell the optimal position for the CsOPM in this geometry is not at 45 ° with respect to $\vec{B}_0$ anymore. For the flat cylindrical cell in this simulation the radial position of this maximum almost coincides with the inner radius of the ^{3}He cell, the simulation actually yields $x(b_{\mathrm{He,max}}) = 248\,\mathrm{mm}$.

---

[9] Assuming equal SNDRs of all CsOPMs.

Summary and outlook

The central objective of this work was to examine the applicability of CsOPMs as readout for the free spin precession (FSP) of nuclear polarized ^{3}He gas. The general feasibility had already been shown in earlier work, but the details, achievable performance and limitations were unclear beforehand. In the frame of this thesis it was demonstrated that CsOPMs are very well suited for this purpose. This result makes CsOPMs a convenient choice when it comes to detecting the ^{3}He-FSP in low field applications. Compared to SQUIDs, which are equally well suited, CsOPMs have the great advantage of being operational at room temperature. The integration of a ^{3}He magnetometer thus becomes feasible for all kinds of high precision applications where the need for cryogenic infrastructure poses a major experimental obstacle.

Based on the spatio-temporal dependence of the magnetic field created by the polarized gas and the properties of the CsOPM in M_x-configuration, the optimal detection geometry for the ^{3}He/Cs magnetometer was derived. A geometry was found in which gradiometric effects are maximized. Following these concepts, a compact and versatile prototype magnetometer was built based on which many aspects of the interplay between the ^{3}He sample and the CsOPMs were experimentally investigated. It was shown that the behavior of the ^{3}He/Cs magnetometer can be understood and traced back to the basic underlying mechanisms of nuclear magnetic resonance (NMR) and optically detected magnetic resonance (ODMR). Based on the well established equations describing the lineshapes of the CsOPM in M_x-configuration and the specific detection geometry, the signals of the combined ^{3}He/Cs magnetometer were modeled and found to be in good agreement with the experimental reality.

It was shown that multiple CsOPMs can be used to simultaneously detect the ^{3}He-FSP yielding consistent results. Although expected, this is still an important result since it implies the $C_{\mathrm{Cs}}^{-1/2}$ scalability of the magnetometer's sensitivity by application of a suitable number N_{Cs} of readout CsOPMs.

Different modes of CsOPM operation and their merits and drawbacks for ^{3}He-FSP readout were discussed. Limitations of the magnetometer bandwidth arising in the particular modes of operation were analyzed and understood. It was shown that both modes of operation yield identical magnetometric sensitivity but the measurements suggest that even more elaborate operation schemes may lead to significantly improved sensitivity. Further gains might be possible through optimization of the drive parameters, e.g. increased light power to broaden the Cs resonance line. Other types of magnetometer operation, e.g., the self-oscillating mode [AV13], remain to be investigated in this frame. Exploring the detection of the ^{3}He FSP by magnetically silent FSP-Cs magnetometers seems also very worthwile, since this would eliminate possible Bloch-Siegert shifts that were discussed.

A method was demonstrated that allows a precise measurement of the Rabi-flopping angle and degree of polarization of the ^{3}He by the CsOPMs. On one hand this is a very convenient method to determine good pulse parameters and particularly important when precise flipping is required as, e.g., in the nEDM experiment. On the other hand it serves to experimentally verify the predicted flipping during standard operation. A routine might be developed that infers the flip-angle in real time and produces a constant flip even under changing experimental conditions, e.g., independently of the applied magnetic field.

The intrinsic sensitivity of the magnetometer was experimentally investigated and theoretically modeled. By comparison with other magnetometers it was shown that CRLB-limited measurements are possible with the ^{3}He/Cs type of magnetometer within the constraints posed by the stability of the holding field. A formula was derived that predicts the individual magnetometric sensitivity of a ^{3}He/Cs pair assuming a CRLB-limited estimation in the shotnoise limit. Since it is based on experimentally accessible parameters it is a valuable tool to estimate the achievable performance and judge the quality of the measurement. Excellent agreement was found between these predictions and the measured sensitivities at PTB which leads to the conclusion that the model includes all relevant processes and the measurements at PTB were shotnoise limited within the uncertainties of the predictions. Using this formula, the ultimate sensitivity for this magnetometer arrangement was calculated. The intrinsic sensitivity in a likely n2EDM geometry was also estimated and found to be comparable to that of the prototype magnetometer. However, since the ^{3}He cells in the n2EDM geometry are much larger, an even better performance can be achieved by using a larger number of readout CsOPMs.

It became clear during the work on this subject that the possibilities of the ^{3}He/Cs concept are far from being fully exploited. A combined magnetometer in this or a comparable geometry should in principle also yield measurement information on the direction of the magnetic field. This information is contained in the phase- and amplitude-relations between the different CsOPMs. These effects were investigated but a conclusive analysis was not possible owing to the insufficient precision of time-synchronization of the LIAs (and lacking mechanical precision of the prototype magnetometer). Still, this remains an interesting subject for further research that could possibly eventually lead to a ^{3}He/Cs vector magnetometer.

Provided the convenient readout with CsOPMs and due to the high precision with which the ^{3}He gyromagnetic ratio is known the idea to measure the magnetic moments of different species in terms of that of ^{3}He arises quite naturally. A precision measurement of the gyromagnetic ratio of ^{199}Hg is a good candidate for such investigations and its comparison with ^{3}He could, together with a recent result [ABB$^+$14] eventually even lead to an improved measurement of the neutron's magnetic moment. Comparisons between Cs and ^{3}He also seem very promising, because of the link to the definition of the second in terms of a Cs transition.

Appendices

Appendix A

Derivation of the CRLB for frequency estimation

CRLB of a sinusoidal signal in white Gaussian noise

This section gives a very short derivation of the CRLB for a frequency estimation of an un-damped sinusoidal signal with peak amplitude a embedded in white Gaussian amplitude noise (WGN) from a set of N_s discrete sampling points. We stick to the definitions made in Sec. 7.2 which are repeated here for convenience. Particularly those are the amplitude

$$a_{He}^{rms} = a/\sqrt{2} \qquad \text{and frequency} \qquad \omega_{L,He} = 2\pi f_{He}$$

of the signal, the (white) Gaussian amplitude noise variance $\sigma_{\mathscr{G}}^2$ and power spectral density ρ^2 which relate via

$$\sigma_{\mathscr{G}}^2 = \rho^2 f_{\mathrm{BW}} \qquad \text{where} \qquad f_{\mathrm{BW}} = \frac{f_{\mathrm{SR}}}{2} = \frac{1}{2T_{\mathrm{SR}}}$$

is the sampling rate limited bandwidth of the measurement. Further we have defined the signal to noise-density ratio

$$SNDR = \frac{a_{He}^{rms}}{\rho}.$$

We model the measurement data as a discrete time series of equi-spaced points of the form

$$x[n] = s[n] + wgn[n] = a\cos(2\pi f_{He} T_{\mathrm{SR}} n + \phi) + \mathrm{WGN}[n]. \tag{A.1}$$

The sampling rate is assumed to be constant and T_{SR} is the time between two samples. The total measurement time is thus $T_M = N_s T_{\mathrm{SR}}$ and the bandwidth can be written as

$$f_{BW} = \frac{1}{2T_{\mathrm{SR}}} = \frac{N_s}{2T_M}. \tag{A.2}$$

In words, the CRLB states that the diagonal-components of the inverse Fisher-matrix set a lower bound on the variance of the estimate of the corresponding parameter, i.e.,

$$var(\theta_i) \geq [\boldsymbol{I}^{-1}(\boldsymbol{\theta})]_{ii}, \tag{A.3}$$

where

$$\boldsymbol{\theta} = \begin{pmatrix} A \\ f_{He} \\ \phi \end{pmatrix} \tag{A.4}$$

is the relevant parameter-vector and the Fisher-information-matrix is generally given by

$$[\boldsymbol{I}(\boldsymbol{\theta})]_{ij} = -E[\frac{\partial^2 ln p(\boldsymbol{x};\boldsymbol{\theta})}{\partial\theta_i \partial\theta_j}] \tag{A.5}$$

with E[...] being the expectation value and $p(\boldsymbol{x};\boldsymbol{\theta})$ the likelihood-function.
However, for a signal in WGN, a simpler expression for the Fisher-information-matrix can be derived, as described in[Kay93]. With $s[n;\boldsymbol{\theta}]$ being the signal, as introduced in Eq. (A.1), it is

$$[\boldsymbol{I}(\boldsymbol{\theta})]_{ij} = \frac{1}{\sigma^2} \sum_{n=0}^{N_s-1} \frac{\partial s[n;\boldsymbol{\theta}]}{\partial \theta_i} \frac{\partial s[n;\boldsymbol{\theta}]}{\partial \theta_j} . \tag{A.6}$$

The derivation is now straightforward. The different matrix-elements can be calculated to be

$$[\boldsymbol{I}(\boldsymbol{\theta})]_{11} = \frac{1}{\sigma^2} \sum_{n=0}^{N_s-1} \left(\frac{\partial s[n;\boldsymbol{\theta}]}{\partial A} \right)^2 = \frac{1}{\sigma^2} \sum_{n=0}^{N_s-1} \cos^2\left(2\pi f_{He} n T_{\mathrm{SR}} + \phi\right) , \tag{A.7}$$

$$[\boldsymbol{I}(\boldsymbol{\theta})]_{12} = [\boldsymbol{I}(\boldsymbol{\theta})]_{21} = \frac{1}{\sigma^2} \sum_{n=0}^{N_s-1} \frac{\partial s[n;\boldsymbol{\theta}]}{\partial a} \frac{\partial s[n;\boldsymbol{\theta}]}{\partial f_{He}} = \frac{1}{\sigma^2} \sum_{n=0}^{N_s-1} -2\pi a n T_{\mathrm{SR}} \cos\left(2\pi f_{He} n T_{\mathrm{SR}} + \phi\right) \sin\left(2\pi f_{He} n T_{\mathrm{SR}} + \phi\right) , \tag{A.8}$$

$$[\boldsymbol{I}(\boldsymbol{\theta})]_{13} = [\boldsymbol{I}(\boldsymbol{\theta})]_{31} = \frac{1}{\sigma^2} \sum_{n=0}^{N_s-1} \frac{\partial s[n;\boldsymbol{\theta}]}{\partial a} \frac{\partial s[n;\boldsymbol{\theta}]}{\partial \phi} = \frac{1}{\sigma^2} \sum_{n=0}^{N_s-1} -a \cos\left(2\pi f_{He} n T_{\mathrm{SR}} + \phi\right) \sin\left(2\pi f_{He} n T_{\mathrm{SR}} + \phi\right) , \tag{A.9}$$

$$[\boldsymbol{I}(\boldsymbol{\theta})]_{23} = [\boldsymbol{I}(\boldsymbol{\theta})]_{32} = \frac{1}{\sigma^2} \sum_{n=0}^{N_s-1} \frac{\partial s[n;\boldsymbol{\theta}]}{\partial f_{He}} \frac{\partial s[n;\boldsymbol{\theta}]}{\partial \phi} = \frac{1}{\sigma^2} \sum_{n=0}^{N_s-1} 2\pi n T_{\mathrm{SR}} a^2 \sin^2\left(2\pi f_{He} n T_{\mathrm{SR}} + \phi\right) , \tag{A.10}$$

$$[\boldsymbol{I}(\boldsymbol{\theta})]_{22} = \frac{1}{\sigma^2} \sum_{n=0}^{N_s-1} \left(\frac{\partial s[n;\boldsymbol{\theta}]}{\partial f_{He}} \right)^2 = \frac{1}{\sigma^2} \sum_{n=0}^{N_s-1} (2\pi)^2 n^2 T_{\mathrm{SR}}^2 a^2 \sin^2\left(2\pi f_{He} n T_{\mathrm{SR}} + \phi\right) , \tag{A.11}$$

and

$$[\boldsymbol{I}(\boldsymbol{\theta})]_{33} = \frac{1}{\sigma^2} \sum_{n=0}^{N_s-1} \left(\frac{\partial s[n;\boldsymbol{\theta}]}{\partial \phi} \right)^2 = \frac{1}{\sigma^2} \sum_{n=0}^{N_s-1} a^2 \sin^2\left(2\pi f_{He} n T_{\mathrm{SR}} + \phi\right) . \tag{A.12}$$

Using some algebraic manipulations, one can considerably simplify the Fisher-matrix elements. The products of the trigonometric functions in (A.7) to (A.12) can be split using the well known relations

$$\cos^2(\alpha) = \frac{1}{2} + \frac{1}{2}\cos(2\alpha) \tag{A.13}$$

$$\sin^2(\alpha) = \frac{1}{2} - \frac{1}{2}\cos(2\alpha) \tag{A.14}$$

$$\sin(\alpha)\cos(\alpha) = \frac{1}{2}\sin(2\alpha). \tag{A.15}$$

Then, by using the approximations

$$\frac{1}{N_s^{i+1}} \sum_{n=0}^{N_s-1} n^i \sin\left(4\pi f_{He} n T_{\mathrm{SR}} + 2\phi\right) \approx 0 \tag{A.16}$$

$$\frac{1}{N_s^{i+1}} \sum_{n=0}^{N_s-1} n^i \cos\left(4\pi f_{He} n T_{\mathrm{SR}} + 2\phi\right) \approx 0 \tag{A.17}$$

from [Kay93] [RB74], it follows that

$$[\boldsymbol{I}(\boldsymbol{\theta})]_{12} = [\boldsymbol{I}(\boldsymbol{\theta})]_{21} \approx 0 \tag{A.18}$$

$$[\boldsymbol{I}(\boldsymbol{\theta})]_{13} = [\boldsymbol{I}(\boldsymbol{\theta})]_{31} \approx 0 \tag{A.19}$$

and

$$[\boldsymbol{I}(\boldsymbol{\theta})]_{11} \approx \frac{N_s}{2\sigma^2} , \tag{A.20}$$

$$[\boldsymbol{I}(\boldsymbol{\theta})]_{22} \approx \frac{a^2 (2\pi)^2 T_{\mathrm{SR}}^2}{2\sigma^2} \sum_{n=0}^{N_s-1} n^2 , \tag{A.21}$$

$$[\boldsymbol{I}(\boldsymbol{\theta})]_{23} = [\boldsymbol{I}(\boldsymbol{\theta})]_{32} \approx \frac{a^2 2\pi T_{\mathrm{SR}}}{2\sigma^2} \sum_{n=0}^{N_s-1} n, \tag{A.22}$$

$$[\boldsymbol{I}(\boldsymbol{\theta})]_{33} \approx \frac{N_s a^2}{2\sigma^2}. \tag{A.23}$$

Using the notations

$$S0 = \sum_{n=0}^{N_s-1} = N_s, \tag{A.24}$$

$$S1 = \sum_{n=0}^{N_s-1} n = \frac{N_s(N_s-1)}{2} \tag{A.25}$$

and

$$S2 = \sum_{n=0}^{N_s-1} n^2 = \frac{N_s(N_s-1)(2N_s-1)}{6}, \tag{A.26}$$

the Fisher-information-matrix can be written as

$$I(\boldsymbol{\theta}) \approx \frac{1}{\sigma^2} \begin{pmatrix} \frac{S0}{2} & 0 & 0 \\ 0 & a^2 2\pi^2 T_{\mathrm{SR}}^2 S2 & a^2 \pi T_{\mathrm{SR}} S1 \\ 0 & a^2 \pi T_{\mathrm{SR}} S1 & \frac{S0 a^2}{2} \end{pmatrix}. \tag{A.27}$$

Inversion of this matrix yields

$$I(\boldsymbol{\theta})^{-1} \approx \begin{pmatrix} \frac{2\sigma^2}{S0} & 0 & 0 \\ 0 & -\frac{S0\sigma^2}{2a^2\pi^2(S1^2 - S0S2)T_{\mathrm{SR}}^2} & \frac{S1\sigma^2}{a^2\pi S1^2 T_{\mathrm{SR}} - a^2 S0 \pi S2 T_{\mathrm{SR}}} \\ 0 & \frac{S1\sigma^2}{a^2\pi S1^2 T_{\mathrm{SR}} - a^2 S0 \pi S2 T_{\mathrm{SR}}} & -\frac{2S2\sigma^2}{a^2(S1^2 - S0S2)} \end{pmatrix}. \tag{A.28}$$

Since the interest lies on frequency estimation, according to (A.3) the [2,2] element has to be selected. The CRLB for the frequency estimate can then be expressed as

$$var(f_{He}) \geq [\boldsymbol{I}^{-1}(\boldsymbol{\theta})]_{22} = -\frac{S0\sigma^2}{2a^2\pi^2\left(S1^2 - S0S2\right)T_{\mathrm{SR}}^2} = \frac{12\sigma^2}{2a^2\pi^2\left(N_s^3 - N_s\right)T_{\mathrm{SR}}^2} \tag{A.29}$$

where the last result was obtained by inserting and evaluating $S0$, $S1$ and $S2$ from Eqs. (A.24), (A.25) and (A.26). For $N_s >> 1$ the linear term N_s can be neglected with respect to the N_s^3 term and one obtains

$$var(f_{He}) \geq [\boldsymbol{I}^{-1}(\boldsymbol{\theta})]_{22} = -\frac{N_s\sigma^2}{2a^2\pi^2\left(S1^2 - N_sS2\right)T_{\mathrm{SR}}^2} = \frac{6\sigma^2}{a^2\pi^2 N_s^3 T_{\mathrm{SR}}^2}. \tag{A.30}$$

It is more instructive to have an expression for the CRLB as a function of SNDR and measurement time. Inserting the definitions of the SNDR, bandwidth and measurement time yields

$$\boxed{\sigma_{\mathrm{f}}^2 = var(f_{He}) \geq \frac{6}{(2\pi)^2 SNDR^2 T_M^3}}, \tag{A.31}$$

which is the result reproduced in Eq. (7.10).

CRLB for a damped sinusoidal signal in white Gaussian noise

This paragraph will consider the case of an exponentially damped sinusoidal signal embedded in WGN. Signals like this are expected for all direct readings of FSP processes, e.g., ^{3}He, read by SQUIDS or the Cs-FSP. For a damped signal the SNDR is not constant during the measurement time. It decreases at the decay-rate $1/T_2$ of the spin polarization. It is qualitatively clear that this will lead to an increased variance of the estimation compared to the non-decaying case. The faster the decay is, compared to the measurement time, the more important it becomes to take this effect into account. The derivation of the CRLB for this case proceeds in complete analogy to that of the un-damped signal. The measurement signal is now expected to be of the form

$$x[n] = s[n] + wgn[n] = a\cos(2\pi f_{He} T_{\mathrm{SR}} n + \phi) e^{-\frac{T_{\mathrm{SR}} n}{T_2}} + \mathrm{WGN}[n]\,. \tag{A.32}$$

The parameter-vector for this problem is defined as

$$\boldsymbol{\theta} = \begin{pmatrix} a \\ f_{He} \\ \phi \\ T_2 \end{pmatrix}. \tag{A.33}$$

Starting from Eq. (A.6), the Fisher-information-matrix is now a 4 × 4-matrix that reads

$$I(\boldsymbol{\theta}) = \sum_{n=0}^{N_s-1} \frac{e^{-\frac{2nT_{\mathrm{SR}}}{T_2}}}{\sigma^2}
\begin{pmatrix}
\cos[\alpha_n]^2 & -an\pi T_{\mathrm{SR}} \sin[2\alpha_n] & -a\cos[\alpha_n]\sin[\alpha_n] & \frac{anT_{\mathrm{SR}}\cos[\alpha_n]^2}{T_2^2} \\
-an\pi T_{\mathrm{SR}} \sin[2\alpha_n] & 4a^2n^2\pi^2T^2\sin[\alpha_n]^2 & 2a^2n\pi T_{\mathrm{SR}}\sin[\alpha_n]^2 & -\frac{a^2n^2\pi T_{\mathrm{SR}}^2\sin[2\alpha_n]}{T_2^2} \\
-a\cos[\alpha_n]\sin[\alpha_n] & 2a^2n\pi T_{\mathrm{SR}}\sin[\alpha_n]^2 & a^2\sin[\alpha_n]^2 & -\frac{a^2nT_{\mathrm{SR}}\cos[\alpha_n]\sin[\alpha_n]}{T_2^2} \\
\frac{anT_{\mathrm{SR}}\cos[\alpha_n]^2}{T_2^2} & -\frac{a^2n^2\pi T_{\mathrm{SR}}^2\sin[2\alpha_n]}{T_2^2} & -\frac{a^2nT_{\mathrm{SR}}\cos[\alpha_n]\sin[\alpha_n]}{T_2^2} & \frac{a^2n^2T_{\mathrm{SR}}^2\cos[\alpha_n]^2}{T_2^4}
\end{pmatrix} \tag{A.34}$$

where the shorthand notation for the phase of the n-th measurement point

$$\alpha_n = 2\pi f_{He} n T_{\mathrm{SR}} + \phi \tag{A.35}$$

has been introduced. Using the same approximations as in the previous derivation, it follows that

$$[\boldsymbol{I}(\boldsymbol{\theta})]_{12} = [\boldsymbol{I}(\boldsymbol{\theta})]_{21} \approx 0\,, \tag{A.36}$$

$$[\boldsymbol{I}(\boldsymbol{\theta})]_{13} = [\boldsymbol{I}(\boldsymbol{\theta})]_{31} \approx 0\,, \tag{A.37}$$

$$[\boldsymbol{I}(\boldsymbol{\theta})]_{42} = [\boldsymbol{I}(\boldsymbol{\theta})]_{24} \approx 0\,, \tag{A.38}$$

$$[\boldsymbol{I}(\boldsymbol{\theta})]_{43} = [\boldsymbol{I}(\boldsymbol{\theta})]_{34} \approx 0\,. \tag{A.39}$$

The remaining matrix-elements can be simplified to yield

$$I(\boldsymbol{\theta}) = \begin{pmatrix}
\frac{\mathrm{C0}}{2\sigma^2} & 0 & 0 & \frac{a\mathrm{C1}T_{\mathrm{SR}}}{2\sigma^2T_2^2} \\
0 & \frac{2a^2\mathrm{C2}\pi^2T_{\mathrm{SR}}^2}{\sigma^2} & \frac{a^2\mathrm{C1}\pi T_{\mathrm{SR}}}{\sigma^2} & 0 \\
0 & \frac{a^2\mathrm{C1}\pi T_{\mathrm{SR}}}{\sigma^2} & \frac{a^2\mathrm{C0}}{2\sigma^2} & 0 \\
\frac{a\mathrm{C1}T_{\mathrm{SR}}}{2\sigma^2T_2^2} & 0 & 0 & \frac{a^2\mathrm{C2}T_{\mathrm{SR}}^2}{2\sigma^2T_2^4}
\end{pmatrix} \tag{A.40}$$

where

$$C0 = \sum_{n=0}^{N_s-1} e^{-\frac{2nT_{\mathrm{SR}}}{T_2}}\,, \tag{A.41}$$

$$C1 = \sum_{n=0}^{N_s-1} ne^{-\frac{2nT_{\mathrm{SR}}}{T_2}}\,, \tag{A.42}$$

$$C2 = \sum_{n=0}^{N_s-1} n^2e^{-\frac{2nT_{\mathrm{SR}}}{T_2}} \tag{A.43}$$

denote the sums which include the damping effects. It is interesting to note, that for very small damping, this means for $T_2 \gg T_M$ the sums $C0$, $C1$ and $C2$ simplify greatly and become identical to the sums $S0$, $S1$ and $S2$ from Eqns. (A.24), (A.25), (A.26). Then, the result of the un-damped case Eq. (A.31) is reproduced.

Inversion of the matrix yields for the variances

$$var(\theta_i) \geq \left[\begin{pmatrix} \frac{2\mathrm{C2}\sigma^2}{-\mathrm{C1}^2+\mathrm{C0C2}} & 0 & 0 & \frac{2\mathrm{C1}\sigma^2 T_2^2}{a\mathrm{C1}^2 T_{\mathrm{SR}}-a\mathrm{C0C2}T_{\mathrm{SR}}} \\ 0 & -\frac{\mathrm{C0}\sigma^2}{2a^2(\mathrm{C1}^2-\mathrm{C0C2})\pi^2 T_{\mathrm{SR}}^2} & \frac{\mathrm{C1}\sigma^2}{a^2\mathrm{C1}^2\pi T_{\mathrm{SR}}-a^2\mathrm{C0C2}\pi T_{\mathrm{SR}}} & 0 \\ 0 & \frac{\mathrm{C1}\sigma^2}{a^2\mathrm{C1}^2\pi T_{\mathrm{SR}}-a^2\mathrm{C0C2}\pi T_{\mathrm{SR}}} & -\frac{2\mathrm{C2}\sigma^2}{a^2(\mathrm{C1}^2-\mathrm{C0C2})} & 0 \\ \frac{2\mathrm{C1}\sigma^2 T_2^2}{a\mathrm{C1}^2 T_{\mathrm{SR}}-a\mathrm{C0C2}T_{\mathrm{SR}}} & 0 & 0 & -\frac{2\mathrm{C0}\sigma^2 T_2^4}{a^2(\mathrm{C1}^2-\mathrm{C0C2})T_{\mathrm{SR}}^2} \end{pmatrix}\right]_{ii} \tag{A.44}$$

and in particular for the frequency estimation

$$var(f_{He})_{damp} \geq [\boldsymbol{I}^{-1}(\boldsymbol{\theta})]_{22} = \frac{\sigma^2}{2a^2\pi^2 T_{\mathrm{SR}}^2} \frac{C0}{\left(C0\,C2 - C1^2\right)}. \tag{A.45}$$

In the un-damped case, the factor on the right of Eq. (A.45) would evaluate to $\frac{12}{N_s^3}$, so it makes sense to normalize it to this value. Then Eq. (A.45) reads

$$\boxed{var(f_{He})_{damp} \geq [\boldsymbol{I}^{-1}(\boldsymbol{\theta})]_{22} = \frac{6\sigma^2}{a^2\pi^2 T_{\mathrm{SR}}^2 N_s^3} C = \frac{6}{(2\pi)^2 SNDR^2 T_M^3} C}, \tag{A.46}$$

where

$$\boxed{C = \frac{N_s^3\, C0}{12\left(C0\,C2 - C1^2\right)}}. \tag{A.47}$$

We see that this is the result already obtained above for the un-damped case, multiplied by a factor $C \geq 1$ which includes the damping. The factor Eq. (A.47) can be brought to the alternative form Eq.(7.12) by basic algebraic manipulations.

Appendix B

Publications on ^{3}He/Cs magnetometer

Design and performance of an absolute ^{3}He/Cs magnetometer

An article summarizing the work described in this thesis was published in European Physical Journal D [KBG$^+$15a] and is appended in the following.
The article is available online under under `http://dx.doi.org/10.1140/epjd/e2015-60018-7`.

Eur. Phys. J. D (2015) 69: 202
DOI: 10.1140/epjd/e2015-60018-7

THE EUROPEAN
PHYSICAL JOURNAL D

Regular Article

Design and performance of an absolute ^{3}He/Cs magnetometer

Hans-Christian Koch[1,2,a], Georg Bison[3], Zoran D. Grujić[1], Werner Heil[2], Malgorzata Kasprzak[1], Paul Knowles[1,b], Andreas Kraft[2], Anatoly Pazgalev[5], Allard Schnabel[4], Jens Voigt[4], and Antoine Weis[1]

[1] Physics Department, University of Fribourg, 1700 Fribourg, Switzerland
[2] Department of Physics, Johannes Gutenberg-University, 55122 Mainz, Germany
[3] Paul Scherrer Institute, 5232 Villigen, Switzerland
[4] Physikalisch-Technische Bundesanstalt Institut, 10587 Berlin, Germany
[5] Ioffe Physical Technical Institute, Russian Academy of Sciences, 194021 St. Petersburg, Russia

Received 9 January 2015 / Received in final form 20 June 2015

Abstract. We report on the design and performance of a highly sensitive combined ^{3}He/Cs magnetometer for the absolute measurement of magnetic fields. The magnetometer relies on the magnetometric detection of the free spin precession of nuclear spin polarized ^{3}He gas by optically pumped cesium magnetometers. We plan to deploy this type of combined magnetometer in an experiment searching for a permanent electric dipole moment of ultracold neutrons at the Paul-Scherrer Institute (Switzerland). A prototype magnetometer was built at the University of Fribourg (Switzerland) and tested at Physikalisch-Technische Bundesanstalt (Berlin, Germany). We demonstrate that the combined magnetometer allows Cramér-Rao-limited field determinations with recording times in the range of 10–500 s, measurements above 500 s being limited by the stability of the applied magnetic field. With a 100 s recording time we were able to perform an absolute measurement of a magnetic field of ≈1 μT with a standard uncertainty of $\Delta B \sim 60$ fT, corresponding to $\Delta B/B < 6\times10^{-8}$.

1 Introduction

A new experiment searching for a permanent Electric Dipole Moment of the neutron (nEDM) is currently being developed at Paul-Scherrer Institute (PSI), Switzerland [1]. In the experiment, the degeneracy of the neutron's magnetic sublevels is lifted by the interaction of the neutron's magnetic moment $\boldsymbol{\mu}_n = g_I\mu_N\boldsymbol{I}/\hbar \equiv \mu_n\boldsymbol{I}/I$ with a static magnetic field $\boldsymbol{B}_0$, where $\boldsymbol{I}$ is the neutron's angular momentum. Additionally, a static electric field $\boldsymbol{\mathcal{E}}$ is applied parallel or antiparallel to $\boldsymbol{B}_0$. In case the neutron has an EDM $\boldsymbol{d}_n = d_n\boldsymbol{I}/I$, the external field interaction Hamiltonian is given by

$$H_{ext} = -\frac{\mu_n}{I}\boldsymbol{I}\cdot\boldsymbol{B}_0 - \frac{d_n}{I}\boldsymbol{I}\cdot\boldsymbol{\mathcal{E}}. \tag{1}$$

The Larmor precession frequencies

$$\omega_{\uparrow\uparrow} = \left|\frac{\mu_n B_{0\uparrow\uparrow} - d_n\mathcal{E}}{I\hbar}\right| \quad \text{and} \quad \omega_{\uparrow\downarrow} = \left|\frac{\mu_n B_{0\uparrow\downarrow} + d_n\mathcal{E}}{I\hbar}\right| \tag{2}$$

in transverse (perpendicular to $\boldsymbol{I}$) magnetic fields are given by the sublevel splitting for parallel (↑↑) and antiparallel (↑↓) magnetic and electric fields [2]. In the PSI experiment the precession frequency of spin-polarized ultracold neutrons is measured by Ramsey's method of (time-) separated oscillatory fields [3]. A measurement cycle takes ≈400 s and consists of filling the neutron storage vessel, running a Ramsey cycle, emptying the vessel and measuring the neutrons' spin polarization. The nEDM experiment measures whether or not the (magnetic) spin precession frequency is altered by an electric field applied along the magnetic field.

In practice one compares the precession frequencies in experiments with (↑↑) and (↑↓) configuration. From the difference frequency

$$\omega_{\uparrow\uparrow} - \omega_{\uparrow\downarrow} = \frac{2d_n}{\hbar}\left(\mathcal{E}_{\uparrow\uparrow} + \mathcal{E}_{\uparrow\downarrow}\right) + \frac{2\mu_n}{\hbar}\left(B_{0\uparrow\uparrow} - B_{0\uparrow\downarrow}\right), \tag{3}$$

the nEDM is inferred. From equation (3) it is clear that the magnetic field has to be precisely controlled and known during the precession time of the neutrons (typically ∼180 s), hence the need for very accurate magnetometers. An uncorrected statistically fluctuating difference $B_{\uparrow\downarrow} - B_{\uparrow\uparrow} \neq 0$ would worsen the statistics for the nEDM experiment since the electric-field-induced difference in precession frequencies (if any) is many orders of magnitude smaller than the Larmor frequency itself. Even more severe, a change in the magnitude of the applied magnetic field that is correlated to the electric field direction would be misinterpreted as an nEDM, if not corrected

---

[a] e-mail: `kochhc@googlemail.com`

[b] *Present address:* LogrusData, Vienna, Austria

for. Moreover, magnetic field gradients may lead to geometrical phase effects [2] that could also mimick an nEDM. A high-sensitivity and high-accuracy measurement of the magnetic field and its variation over the neutron storage volume during the free evolution time is therefore of crucial importance for controlling and suppressing several major systematic errors and ensuring good statistics in the nEDM experiment.

2 Magnetometry in the PSI-EDM experiment

The current nEDM experiment at PSI [1] deploys two types of optically pumped magnetometers for measuring the temporal and spatial variations of the magnetic field in and around the neutron storage volume, viz., a Hg comagnetometer and an array of 16 Cs magnetometers (CsOPMs). We first note that the Hg and the Cs magnetometers as well as the magnetometer described in this work are all scalar magnetometers that measure only the modulus of the magnetic field vector at the sensor's location. The working sensitivities of the currently deployed systems (Cs, Hg) are both ∼100 fT in a 100 s measurement time. This is sufficient for the ongoing phase of the project since the statistical sensitivity of the nEDM measurement is currently limited by the neutron counting statistics. The uncertainties arising from this limitation currently allow a tolerance of magnetic field fluctuations up to ≈100 fT during one Ramsey cycle without loss of sensitivity. The Hg co-magnetometer [4] yields a volume-averaged value of the field in the neutron bottle, important for normalization of the neutron precession frequency. The co-magnetometer uses (nuclear) spin-polarized ^{199}Hg vapor that occupies the same storage volume as the neutrons, and the magnetic field is inferred from the frequency of the free spin precession (FSP) of the Hg's spin polarization. The Hg-FSP is monitored by recording the (time dependent) transmitted power of a resonant circularly polarized light beam traversing the Hg vapor. Strictly speaking, the spin precession of the Hg atoms is only 'quasi'-free, since the read-out light beam may affect the spin precession frequency (e.g., by the light shift effect [5]), thereby limiting the magnetometer's accuracy. The relative systematic shift arising from this effect for the given parameters of the current nEDM experiment has been estimated to be on the order of 6×10^{-9} [4]. A limiting factor to the accuracy of field measurements with the Hg magnetometer is the Hg gyromagnetic ratio, which is only known with a relative accuracy of $\sim 10^{-6}$ [6,7].

The Cs magnetometer array builds on an optically detected magnetic resonance process [8], in which the frequency of a weak applied oscillating magnetic field is made identical ('locked') to the Cs atoms' Larmor precession frequency using a feedback loop [9]. The Cs magnetometers offer the possibility to access information on the spatial field distribution outside the UCN precession volume, needed to control magnetic field gradients. The Cs magnetometers are also prone to possible light shift effects, but their accuracy may be more seriously affected by phase errors (and the stability thereof) in their feedback electronics. Moreover, because of the hyperfine interaction, the Cs magnetometer readings are affected by the quadratic Zeeman effect and, being driven magnetometers (in contrast to magnetometers based on free precession), their interaction with the magnetic resonance driving rf field introduces a systematic frequency shift (Bloch-Siegert shift [10]). The systematic effects mentioned above lead to sensor-specific offsets of the magnetometric readings that are generally unknown, not necessarily constant and may depend on other experimental parameters. This spoils the direct comparison of the absolute field value given by different sensors and limits the ability to obtain a consistent picture of the magnetic field inside the apparatus necessary to suppress systematic errors in the EDM measurement such as those mentioned in Section 1 caused by the geometric phase effects [2].

The combined ^{3}He/Cs magnetometer described hereafter offers an important complement to the magnetometers discussed above. It is based on recording the FSP of nuclear spin polarized ^{3}He gas, by detecting the time dependent magnetic field produced by the precessing (and decaying) ^{3}He magnetization with an arrangement of several Cs magnetometers. ^{3}He FSP detection by external magnetometers provides an indirect optical readout non-perturbative to the ^{3}He FSP, avoiding possible systematic effects as they may occur by the read-out beams or the feedback control in the Hg and Cs magnetometers, respectively. In the absence of magnetic field gradients the Larmor precession frequency of ^{3}He is thus an absolute measure of the magnetic field inside the magnetometer cell. When gradients are present, the measured precession frequency corresponds to the volume averaged field in the cell. The details of this averaging process will depend on the dynamic regime in the cell [11]. On the other hand, the systematic effects affecting the CsOPMs are irrelevant for their use as readouts for ^{3}He FSP. The fact that the ^{3}He gyromagnetic ratio is known with a relative precision of 2.5×10^{-8} [7] makes ^{3}He a promising candidate as a reference for magnetic field measurements, as suggested in [12]. One application that is envisioned for the next stage of the nEDM experiment (n2EDM) is a ^{3}He-"quasi comagnetometer". Since in this experiment it is not possible to have ^{3}He cohabiting inside the neutron bottle, flat cylindrical magnetometer vessels will be installed above and below the cylindrical neutron precession chamber. These vessels will have the same geometrical cross section as the precession chamber and will thus be traversed to first order by the same magnetic flux. An array of CsOPMs around the vessels will be used to detect the ^{3}He FSP signal. The magnetic field measurement from the ^{3}He/Cs magnetometer, performed simultaneously with the nEDM measurement proper, can then be used, along with the Hg co-magnetometer, to normalize the neutron precession frequency and to correct for field changes [13,14]. From the double-chamber type of geometry, additional information on magnetic field gradients can be obtained. Another possible application is an array of several compact ^{3}He/Cs magnetometers to measure the magnetic field at different spatial positions around the precession chamber. Since

^{3}He/Cs magnetometers do not suffer from the systematics discussed above, and offsets which they may induce, readings from different ^{3}He/Cs sensors can be more easily compared and their use can thus improve field stabilization and gradient control in the experiment. In this paper, we describe a prototype ^{3}He/Cs magnetometer based on a small, sealed spherical ^{3}He cell surrounded by Cs magnetometers. The prototype is not adapted to later use in the nEDM experiment, but designed as a versatile test device for investigation of the combined magnetometer concept.

2.1 Preparation and detection of polarized ^{3}He

^{3}He gas in a spherical glass cell is polarized by optical pumping of the helium atoms in the metastable 2^3S_1 state populated by collisions in a weak glow discharge, using circularly polarized 1083 nm light from a 2W ytterbium-doped fiber laser. The electronic spin polarization is transferred to nuclear spin polarization of the groundstate atoms by metastable exchange. Metastable exchange optical pumping (MEOP) is a method that is well studied and described in detail, e.g., in references [15,16]. Conversely to Cs and Hg magnetometers, the spin polarization (and hence its dynamics) cannot be detected by optical means because of the large optical excitation energy (20 eV) of the ^{3}He ground state for which no (convenient) light sources are available.

The rotating magnetization $\boldsymbol{m}_{\mathrm{He}}$ that is associated with the precession of the nuclear spin polarization can be detected by pick-up coils [17], which are very inefficient at the low precession frequency ($\sim$30 Hz) occuring here.

SQUIDs (superconducting quantum interference devices) are highly sensitive magnetometers that have been deployed for detecting the ^{3}He FSP [18]. However, the additional technical complexity associated with the cryogenic cooling needed for the SQUID operation is an obstacle for operating these magnetometers under the experimental conditions of a room temperature nEDM experiment. In 1967, Cohen-Tannoudji et al. [19] have demonstrated the suitability of a discharge lamp pumped alkali (Rb) vapor magnetometer for detecting the FSP of ^{3}He nuclei. Based on the results reported in that paper, we estimate their magnetometric sensitivity to be $\approx$80 $\mathrm{pTs}^{3/2}/\mathrm{T}_{\mathrm{m}}^{3/2}$, assuming a Cramér-Rao limited performance (c.f. Sect. 5) in a measurement time T_m.

2.2 ^{3}He/Cs magnetometer principle

During optical pumping the ^{3}He cell is exposed to a homogeneous magnetic field $\boldsymbol{B}_0$ oriented along the pump laser beam. The oriented nuclear magnetic moments give rise to a macroscopic magnetization $\boldsymbol{m}_{\mathrm{He}}$ that produces a magnetic dipole-like field $\boldsymbol{B}_{\mathrm{He}}$ outside of the cell. One readily estimates that the field from a 100 % polarized gas at 1 mbar is on the order of 200 pT on the outside surface of the cell. After optical pumping, the laser and the gas discharge are turned off and a $\pi/2$ rf-pulse is applied to the cell in order to flip $\boldsymbol{m}_{\mathrm{He}}$ to a plane perpendicular to $\boldsymbol{B}_0$, upon which $\boldsymbol{m}_{\mathrm{He}}$ starts freely precessing around $\boldsymbol{B}_0$ at the ^{3}He Larmor frequency

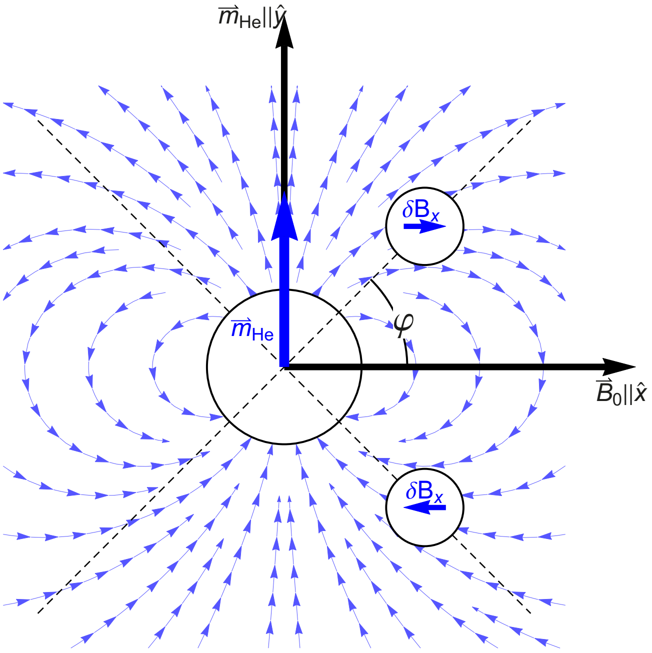

Fig. 1. ^{3}He spin sample cell with its magnetic dipole field in the $(\hat{\boldsymbol{x}},\hat{\boldsymbol{y}})$-plane. The direction of the applied $\boldsymbol{B}_0$ defines the $\hat{\boldsymbol{x}}$-axis, so that the ^{3}He magnetization precesses in the $(\hat{\boldsymbol{y}},\,\hat{\boldsymbol{z}})$-plane. The Cs sensors shown at their different positions record the FSP signal phase-shifted by π. The 45° cones of highest sensitivity are denoted by the dashed lines.

$$\omega_{\mathrm{He}} = \gamma_{\mathrm{He}}\,|\boldsymbol{B}_0|\,, \tag{4}$$

where $\gamma_{\mathrm{He}}/2\pi = 32.43410084(81)\,\mathrm{Hz}/\mu\mathrm{T}$ ($\Delta\gamma_{\mathrm{He}}/\gamma_{\mathrm{He}} = 2.5\times10^{-8}$) is the gyromagnetic ratio of the ^{3}He nucleus [7]. The precessing (and decaying) magnetization produces at the position $\boldsymbol{r}_{\mathrm{Cs}}$ of each Cs magnetometer a magnetic field $\boldsymbol{B}_{\mathrm{He}}(\boldsymbol{r}_{\mathrm{Cs}},t)$ with time-dependent amplitude and orientation.

The Cs magnetometers are scalar magnetometers, i.e., they measure the modulus $B(\boldsymbol{r},t) = |\boldsymbol{B}_0(\boldsymbol{r},t)+\boldsymbol{B}_{\mathrm{He}}(\boldsymbol{r},t)|$ of the total field at their location. Since $B_{\mathrm{He}}\ll B_0$, and B_0 is nominally constant in time one has $B \approx B_0 + \hat{\boldsymbol{B}}_0\cdot\boldsymbol{B}_{\mathrm{He}}(t)$, so that the CsOPMs are, to first order, only sensitive to the component δB_x of the ^{3}He-FSP field along the applied magnetic field $\boldsymbol{B}_0$. A simple calculation shows that – for a given distance r_{Cs} – this time dependent projection has a maximum amplitude when the sensors are located on a double cone with a half-opening angle of $\varphi = 45°$ with respect to $\boldsymbol{B}_0$. In the prototype described below, the centers of all 8 CsOPM cells were located on that double cone, and the relative azimuthal positions on the cones determine the phase relations between the individual FSP signals detected by the different CsOPMs (compare Fig. 1). By pairwise subtraction of CsOPM signals that are dephased by π, common mode magnetic

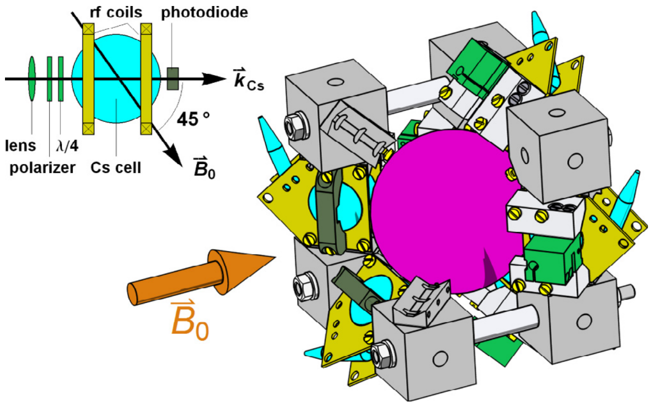

Fig. 2. Schematic drawing of the CsOPM (left) and CAD drawing of the combined ^{3}He/Cs magnetometer (right). The spherical ^{3}He cell (magenta) in the middle of the cubic structure is surrounded by eight CsOPMs (blue) on the edges of the cube, in which the rf coils are laid out on printed circuit boards (yellow). The total dimensions of the combined magnetometer are $\sim(10\,\mathrm{cm})^3$. One corner cube and two CsOPMs are left out for better visibility.

noise components (such as magnetic fields oscillating at the 50 Hz line frequency) that are in-phase on both sensors can be strongly suppressed in the differential signal, while increasing the signal of interest, as shown in Section 5.2. For the chosen geometry of the combined magnetometer, 8 such gradiometer pairs can be formed.

2.3 The Cs magnetometers

The CsOPMs used in this study are laser pumped double-resonance magnetometers, operated in the M_x configuration [8]. A sketch of a CsOPM is shown in Figure 2 (left). Light from a Toptica DLPro diode laser with a frequency actively stabilized to the $F_g = 4 \rightarrow F_e = 3$ transition of the Cs-D$_1$ line at 894 nm is delivered to each magnetometer module via a multimode fiber. The light from each fiber is collimated and given a circular polarization, after which it passes through a room-temperature paraffin-coated [20] 30 mm diameter Cs vapour cell. The cell coating ensures a long-lived coherence ($\sim$30 ms) of the spin polarization created by optical pumping. The light exiting the cell is detected by a photodiode (PD) that measures the Cs vapor's optical transmission. The propagation direction $\hat{\boldsymbol{k}}_{Cs}$ of the incident light makes an angle of 45° with respect to $\boldsymbol{B}_0$ for all CsOPMs since this yields maximal sensitivity [8]. A weak magnetic field (rf field) parallel to $\boldsymbol{k}_{Cs}$ oscillating at frequency ω_{rf} resonantly drives the precession of the Cs vapour's magnetization, thereby modulating the vapour's absorption coefficient and hence the photodiode signal [8]. The (transimpedance-) amplified PD signal is demodulated by a dual channel digital lock-in amplifier referenced to ω_{rf}. Figure 3 shows the dependence of the amplitude and phase of a CsOPM sensor on the detuning from the resonance $\delta = \omega_{\mathrm{rf}} - \omega_{Cs}$. The resonance occurs at the Cs Larmor frequency $\omega_{\mathrm{rf}} = \omega_{\mathrm{Cs}} = \gamma_{\mathrm{Cs}}\,|\boldsymbol{B}_0|$, where $\gamma_{\mathrm{Cs}} \approx 2\pi \times 3.5\,\mathrm{kHz}/\mu\mathrm{T}$ is the Cs ground state's gyromagnetic ratio. In the currently employed mode of operation in the nEDM experiment the rf frequency is tuned near the line center where the phase has a linear dependence on the frequency detuning and the phase signal is used to drive a voltage-controlled oscillator generating the oscillatory voltage for the rf coils. This mode of operation represents a feedback loop that keeps ω_{rf} locked to the Cs Larmor frequency [8]. When multiple CsOPMs are operated in close spatial vicinity one sensor may be parasitically driven by the rf of a neighboring magnetometer. To avoid this effect known as cross talk, it is advisable to drive all CsOPMS at the same common frequency. In the measurements described here the CsOPMs were thus driven at a single, constant frequency ω_{rf} close to ω_{Cs} and the photodiode signals were demodulated at that fixed rf-frequency using digital lock-in amplifiers. The oscillatory magnetic field $B_{\mathrm{He}}(t)$ then leads to an oscillation of the CsOPM's phase signal at ω_{He}, with an amplitude proportional to B_{He}, as long as $B_{\mathrm{He}}\gamma_{\mathrm{Cs}} \ll \Delta\omega$, where $\Delta\omega$ is the linewidth of the resonance of Figure 3. We note that the proportionality factor between the phase response of the CsOPM and B_{He} depends on the Cs cell properties and the parameters of operation. For the CsOPMs driven at fixed frequency, bandwidth limitations arising from the lifetime of the Cs polarization and the lock-in demodulator filter have to be considered. The scaling of the phase signal to magnetic units which we will do in the following

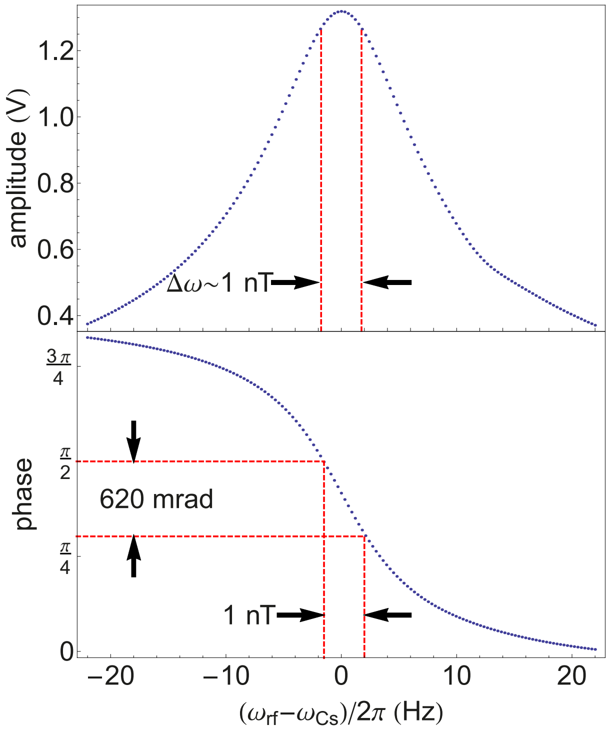

Fig. 3. Amplitude (top) and phase (bottom) response of a CsOPM when sweeping the rf frequency ω_{rf}. The dashed lines represent the change of the CsOPMs Larmor frequency ω_{Cs} and phase response corresponding to a 1 nT variation of the magnetic field B_0.

to make the results more intuitively accessible does not correct for these effects, e.g., the reported amplitudes do not reflect the true values of B_{He}. The true FSP amplitudes are actually roughly a factor of five larger.

3 The prototype magnetometer

A prototype of a combined ^{3}He/Cs magnetometer for studying the ^{3}He FSP readout with laser pumped CsOPMs was built in Fribourg. It consists of a 70 mm diameter spherical cell filled with ^{3}He at a pressure of 1 mbar that is fixed in the center of a mechanical structure holding eight laser-pumped CsOPMs mounted symmetrically on the edges of a cube as shown in Figure 2 (right), thereby fulfilling the optimal sensitivity criterion (45° cone) discussed above. The distance between the ^{3}He cell center and the Cs cell centers is 50.5(5) mm. The He cell carries two electrodes, each consisting of a spiral of copper foil glued to the outside of the cell that are driven by a 1.2 MHz sinusoidal voltage (amplified by a Tesla transformer) to ignite and sustain a weak gas discharge in the cell. The electrodes were designed to achieve a homogeneous illumination of the cell volume by the gas discharge while allowing optical access to a large part of the cell's surface to permit the ^{3}He pump laser beam to traverse the cell.

Figure 2 (left) shows details of a single CsOPM sensor. Each sensor carries its own pair of rf coils and the coils of all 8 sensors were driven at the same, constant rf frequency during measurements. This mode of operation is only possible when the magnetic field gradients over the whole structure are sufficiently small so that the individual Larmor frequencies of all 8 sensors differ by amounts that are much less than the Cs magnetic resonance linewidth $\Delta\omega$. During the measurements described here, the local Larmor frequencies of two CsOPMs $i, j \in \{1, 8\}$ differed by less than $(\omega_i - \omega_j)/(2\pi) < 1.8\,\mathrm{Hz}$.

The apparatus depicted in Figure 2 (right) is surrounded by large coils (Helmholtz configuration, ~30 cm diameter, not shown in the figure) for producing magnetic fields perpendicular to $\hat{\boldsymbol{B}}_0$. They were used to start the FSP by flipping the ^{3}He magnetization by resonant rf-pulses following the pumping process. Having in mind the later mounting of the device in the vacuum chamber of the nEDM spectrometer at PSI, all components were manufactured from nonmagnetic and vacuum compatible (low outgassing) materials.

4 Measurements

A key issue of the present study was the determination of the intrinsic magnetometric sensitivity of the combined ^{3}He/Cs magnetometer. Since the stability of the applied magnetic field sets a limit on the ability to determine the magnetometer sensitivity (c.f. Sect. 5.4 for details), that field has to be kept as stable as possible. After initial tests in Fribourg the measurements reported below were carried out in the magnetically shielded room BMSR-2 [21] at the Physikalisch-Technische Bundesanstalt (PTB) in Berlin, Germany. The BMSR-2 room is one of the magnetically most quiet and stable places on earth. It consists of a 7 layer MU-metal magnetic shield and an additional aluminum layer. It features a built-in multi-channel system of (vector) SQUID magnetometers that were operated together with our test equipment. A three axis Helmholtz coil system [22] was used to produce the B_0 field inside BMSR-2. The coil was driven by a commercial low-noise current source (Magnicon, CSE-1) delivering a current of 19 mA yielding a homogeneous magnetic field $|\boldsymbol{B}_0|$ of $\approx 1\,\mu\mathrm{T}$ in the center of the coil. The ^{3}He optical pumping light from the 1083 nm laser was brought into the chamber by an optical fiber, after which the beam was expanded by a telescope in order to illuminate the whole accessible cross section of the ^{3}He cell. The light was circularly polarized with a polarizing beamsplitter cube followed by a $\lambda/4$ plate. After traversing the ^{3}He cell the pump beam was back-reflected by a mirror for a second passage through the cell, thus increasing the pumping efficiency. The fluorescence from a ^{3}He reference cell located outside BMSR-2 was used to monitor and manually adjust the laser wavelength during optical pumping.

The 894 nm light for operating the 8 CsOPMs was delivered to the sensors by eight multimode fibers. A board containing 8 transimpedance amplifiers (mounted inside BMSR-2) pre-amplified the photodiode currents, and the ensuing voltage signals were transmitted to the data acquisition (DAQ) system located outside of the chamber. The raw signals as well as the demodulated PD signals from a set of six CsOPMs were recorded simultaneously by (nominally) identical DAQ channels. The remaining two CsOPM signals were recorded by a separate DAQ system and were not used for the analysis presented here. The timebase of the DAQ system was referenced to a rubidium atomic clock (SRS PRS10).

Figure 4 shows the demodulated phase signals of six CsOPMs after rescaling to magnetic field units. The ~36 Hz oscillation from the ^{3}He FSP is clearly visible with no additional filtering applied to the phase data. If not specified otherwise, the 36 Hz precession signals from the ^{3}He atoms will be referred to as FSP signals in what follows. The FSP signals in Figure 4 are clearly of varying quality. While Cs1 (upper left in Fig. 4) exhibits a relatively good signal to noise ratio (SNR), Cs8 (lower left in Fig. 4) is obviously performing much worse. These differences are due to different Cs-cell qualities and CsOPM drive parameters. A criterion to quantify the sensors intrinsic sensitivity limitation taking cell quality and drive parameters into account is the noise equivalent magnetic field (NEM) (c.f. Sect. 6 for details). While for Cs1 we find a quite good value of $\mathrm{NEM}_{Cs1} \approx 34\,\mathrm{fT}/\sqrt{\mathrm{Hz}}$, Cs8 yields $\mathrm{NEM}_{Cs8} \approx 158\,\mathrm{fT}/\sqrt{\mathrm{Hz}}$. For the measurements presented here, Cs1 was always performing significantly better than the other CsOPMs. While the drive parameters can be optimized during a measurement, preselection of high quality Cs cells for the combined magnetometer is of crucial importance.

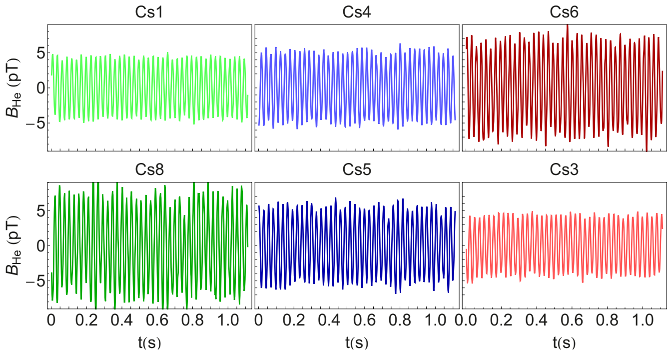

Fig. 4. Raw phase signals of the six CsOPMs used in the analysis, rescaled to magnetic units. All subplots have identical amplitude and time scales. The ∼36 Hz oscillation originating from the ^{3}He FSP is clearly visible. The amplitudes and signal to noise ratios differ due to individual bandwidth limitations of the individual CsOPMs. Note that the amplitudes do not reflect the true magnitude of B_{He}.

5 Data analysis

The data were analyzed off-line using dedicated Mathematica [23] codes.

5.1 Relaxation time

As discussed in [11], the transverse spin relaxation time T_2 of nuclear spin polarized ^{3}He atoms is strongly affected by the presence of magnetic field gradients. The very long T_2 time that can be achieved in high quality glass cells is, in general, limited by field inhomogeneities. We recorded ^{3}He FSP signals for time periods of slightly more than 10 h. The data, recorded at a sampling rate of 450 Hz, was split into 44 s long segments over which the FSP amplitude can be assumed to be constant. Each subset was then individually fitted using a sinusoidal function

$$f(t) = a_{\mathrm{off}} + a(t)\,\sin(\omega_{\mathrm{He}} t + \phi), \tag{5}$$

where a_{off} is the offset field at the individual sensor's position and $a(t)$ the constant FSP amplitude for the respective subset. The time dependence of these amplitudes for a single CsOPM is shown in a semi-logarithmic plot in Figure 5 that illustrates the exponential character of the decay. The FSP signal is described by

$$s(t) = a_0\, e^{-t/T_2}\,\sin(\omega_{\mathrm{He}} t + \phi). \tag{6}$$

From a fit of the data shown in Figure 5 (from a single CsOPM) by the function

$$a(t) = a_0\, e^{-t/T_2}, \tag{7}$$

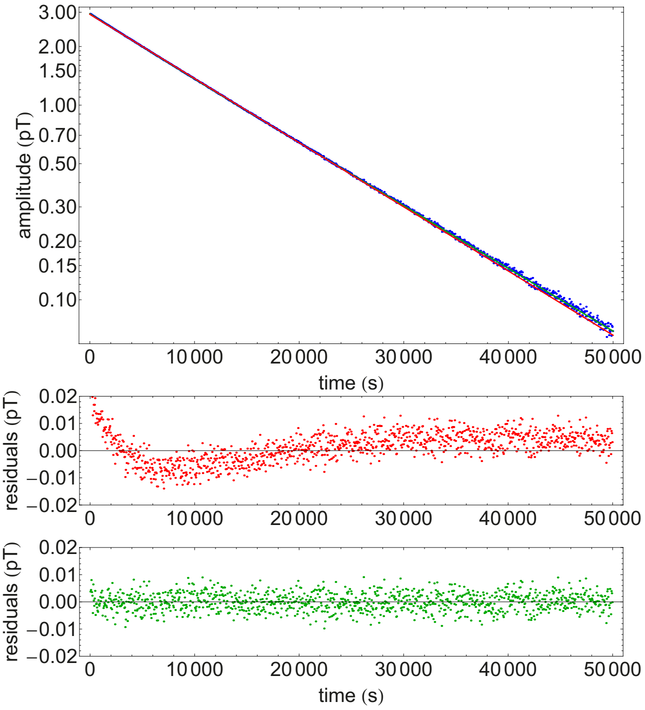

Fig. 5. Measurement of ^{3}He T_2 time. Fit of single exponentially decaying function equation (7) and combined function equation (8), taking into account the relaxation of magnetic field gradients (top). The fit residuals are shown for the simple function (middle, red) and the more complex one (bottom, green). Note that the amplitudes – as in Figure 4- do not reflect the true magnitude of B_{He}.

we infer a decay time T_2 of 13173(4) s ≈ 3.6 h. Closer inspection of the fit residuals reveals a small imperfection of the fit (red curves, middle graph of Fig. 5). This can be explained by variations of magnetic field gradients induced by the magnetic relaxation of the μ-metal shield (essentially the innermost layer) after closure at the beginning of the measurement. This effect has already been observed in BMSR-2 and was described in [24]. An alternative fit function,

$$a(t) = a_1\, e^{-t/T_2^{(1)}} + a_2\, e^{-t/T_2^{(2)}}, \tag{8}$$

empirically takes into account the shield relaxation by introducing a second time constant $T_2^{(2)}$. The fit of equation (8) yields Gaussian-distributed residuals and a decay time $T_2^{(2)}$ of 13505(23) s (green curve, lower in Fig. 5). The same analysis, performed with all six simultaneously running CsOPMs yields the decay rates visualized in in Figure 6. As expected, the values for $T_2^{(1)}$ (and $T_2^{(2)}$ respectively) measured by different CsOPMs agree within their uncertainties. The mean decay times of the ^{3}He polarization, calculated from all six CsOPM measurements, are $T_2^{(1)} = 13532(17)$ s and $T_2^{(2)} = 6621(183)$ s respectively. Although much longer decay times have been reported in the literature (see, e.g., [25]), the value achieved here is largely sufficient in the context of the present study.

In a constant magnetic field the ^{3}He FSP can be represented by a decaying single tone oscillation as introduced in equation (6). Assuming that the data have only white Gaussian noise $\mathcal{G}$ and neglecting the shield relaxation described above, we can model the experimental signal

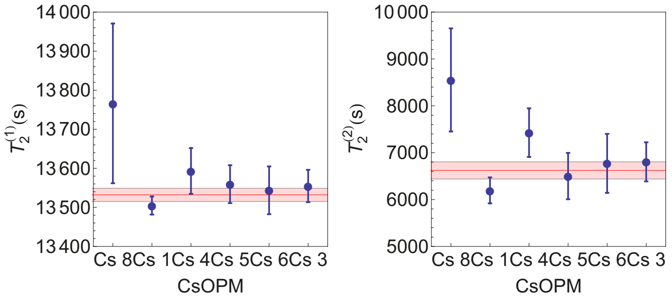

Fig. 6. Decay times of ^{3}He spin polarization simultaneously measured by multiple CsOPMs. The red horizontal lines denote the weighted mean and the shaded band around it gives the 1σ confidence region. Compare equation (8) for meaning of variables.

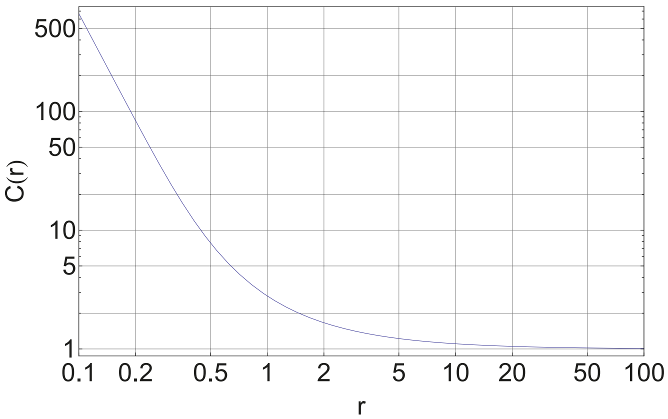

Fig. 7. Plot of CRLB degradation function $C(r)$ from equation (13) for a damped sine wave as a function of $r = T_2/T_M$, the ratio of decay to measurement time.

as a discrete time series of equi-spaced data points

$$S_n = a\, e^{n\,T/T_2}\, \sin(\omega\, n\, T + \phi_0) + \mathcal{G}(n), \tag{9}$$

where $T = (\mathrm{f}_{sr})^{-1}$ is the inverse of the sampling rate f_{sr}, i.e., the spacing between consecutive points in the time series and $\mathcal{G}(n)$ the Gaussian noise contribution to the nth data point. The noise is completely characterized by its power spectral density ρ^2 or variance $\sigma^2_{\mathcal{G}} = \rho^2 f_{bw}$ where $f_{bw} = f_{sr}/2$ is the bandwidth of the measurement. The precision of the frequency determination of such a coherent signal over a given measurement time T_M is fundamentally limited as described by information theory. It has first been studied by Cramér and Rao [26,27] who derived a lower bound for the frequency estimation variance of a signal of constant amplitude (CRLB)[28]. The corresponding bound for a damped oscillation was derived in [18] and reads

$$\sigma_{\mathrm{f}}^2 \geq \frac{6}{(2\pi)^2\, \mathrm{SNR}^2\, T_M^3} C(T_M, T, T_2), \tag{10}$$

with

$$C(T_M, T, T_2) = \frac{T_M^3}{6\,T^3} \frac{(1 - e^{-2T/T_2})^3\,(1-\alpha)}{e^{-2T/T_2}(1-\alpha)^2 - (T_M/T)^2\,\alpha(1-e^{-2T/T_2})^2} \tag{11}$$

where

$$\alpha = e^{-2T_M/T_2}. \tag{12}$$

In equation (10), SNR $= a_{rms}/\rho$ represents the signal to noise-density ratio with $a_{rms} = a/\sqrt{2}$ being the rms-amplitude of the FSP signal. $C(T_M, T, T_2)$ is a factor that takes damping into account. For sufficiently high sampling rates ($T \ll 2\pi/\omega_{\mathrm{He}}$), an approximative form of equation (11) that is independent of T can be found and reads

$$C(r) = \frac{e^{2/r} - 1}{3r^3 \cosh\left(\frac{2}{r}\right) - 3r\left(r^2+2\right)}, \tag{13}$$

where $r = T_2/T_M$ is the ratio of the decay and measurement time. A plot of this function is shown in Figure 7. For vanishing damping, $T_2 \gg T_M$ the factor $C(T_M, T, T_2)$ becomes unity, thus reproducing the result of [28]. Since the decay time T_2 in our system is ∼13 000 s, one sees from Figure 7 that C is ≈1 for measurement times up to several thousand seconds and can thus be neglected. It turns out that up to integration times of several hundreds of seconds the fit results do not differ when the decay is neglected. This justifies the use of the simple fit function (5) up to relatively long integration times for which the signal amplitude can be considered constant.

5.2 Common noise suppression

Noise suppression effects in differential CsOPM signals as described in Section 2.1 were investigated. For this, the phase signal from one CsOPMs (Cs5) was subtracted from a second CsOPM signal that is, by construction, dephased by π (Cs4). Both signals carry perturbations from the 50 Hz line frequency, as shown in the Fourier spectra in the top row of Figure 8. These perturbations are in-phase on both signals, whereas the ^{3}He FSP signal is dephased by π, as visible in the lower left plot of Figure 8. In the differential signal, the 50 Hz perturbation has vanished, as evidenced by the Fourier spectrum on the lower right of Figure 8. It is expected that the (random) noise amplitude spectral densities of the two signals $\rho_4 = 48\,\mathrm{fT}/\sqrt{\mathrm{Hz}}$ and $\rho_5 = 59\,\mathrm{fT}/\sqrt{\mathrm{Hz}}$ add quadratically in the differential signal $\rho_{\mathrm{diff}} = \sqrt{\rho_4^2 + \rho_5^2}$, assuming no correlation between the white noise contribution to both signals. One also expects the signal amplitudes $a_4 = 3.58\,\mathrm{pT_{rms}}$ and $a_5 = 3.86\,\mathrm{pT_{rms}}$ to add in the combined signal, $a_{\mathrm{diff}} = a_4 + a_5$. The expected signal to noise ratio of the differential signal can thus be written as

$$\mathrm{SNR_{diff}} = \frac{a_4 + a_5}{\sqrt{\rho_4^2 + \rho_5^2}}, \tag{14}$$

yielding $\mathrm{SNR_{diff}} \approx 98\sqrt{\mathrm{Hz}}$ for the values given above. Analysis of a Fourier spectrum of the differential signal shows that only a reduced SNR of $\approx 85\sqrt{\mathrm{Hz}}$ is observed

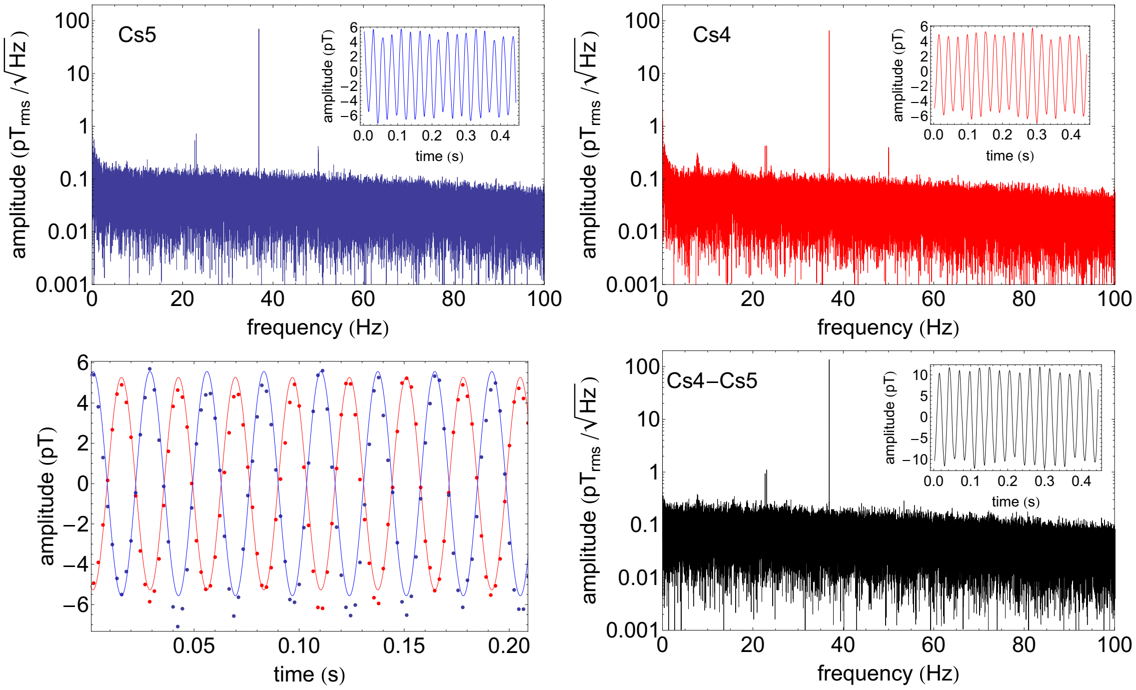

Fig. 8. Upper row: Fourier spectra of two CsOPMs dephased by π. Perturbations from the 50 Hz line frequency and around $\sim$22 Hz are visible. Lower row: time series of both signals, dephasing is visible (lower left), Fourier spectrum of differential signal. The 50 Hz pertubation has vanished but the $\sim$22 Hz perturbations persist and are even increased (lower right). Each Fourier spectrum contains 700 s of measurement data.

in the signal. A closer analysis reveals that the amplitudes add, as expected, to $\approx$7.43 pT, while the noise of the differential signal is increased more than expected to a level of $\approx$87 fT/$\sqrt{\rm Hz}$. This discrepancy can be explained by non-Gaussian perturbations which are correlated between the two signals. The presence of such noise components is witnessed by the double-peak around $\sim$22 Hz in the Fourier spectra of Figure 8. Such perturbations may originate from higher order magnetic field fluctuations (gradient oscillations) that affect the individual sensors located in different spatial positions differently, but in a correlated manner. Such noise processes are not suppressed by the gradiometer, their amplitudes might even add up in the combined signal, as visible in Figure 8 (lower right). Nevertheless, the suppression of the common noise component was successfully demonstrated. This technique becomes an important tool when in-phase perturbations are strong and may lead to systematic errors in the extraction of the ^{3}He Larmor frequency.

5.3 Magnetic field measurements

In order to demonstrate the performance of the combined magnetometer we measured the magnetic field in the BMSR-2 chamber by analyzing consecutive 100 second long time series of the continuously recorded phase signal. We analyzed data from the six CsOPMs that have recorded simultaneously the same ^{3}He FSP. The average frequency of each time series and its standard error were extracted by fitting equation (5) to the data. Special care was taken to ensure that the fit routine correctly estimates the standard errors. Since the phase data undergoes filtering in the lock-in amplifier, the noise might not be purely Gaussian anymore. To prevent the fit routine from underestimating the error, the variance was extracted from a Fourier spectrum of each dataset and explicitly imposed on the fit. The magnetic field B_i and its uncertainty $\varDelta B_i$ were calculated for each CsOPM using (4). The weighted average $\widetilde{B}$ and its uncertainty $\varDelta\widetilde{B}$ were calculated for the readings of all individual CsOPMs according to

$$\widetilde{B} = \frac{\sum \frac{B_i}{\varDelta B_i^2}}{\sum \frac{1}{\varDelta B_i^2}} \tag{15}$$

with standard error

$$\varDelta\widetilde{B} = \left(\sum \frac{1}{\varDelta B_i^2}\right)^{-1/2}. \tag{16}$$

Equations (15) and (16) are only valid assuming a constant magnetic field which is justified for 100 s subsets of data as shown in Section 5.4. The uncertainities $\varDelta B_i$ of the field estimations from data of an individual CsOPM range between 100 and 350 fT in 100 s, depending on the signal to noise ratio of the respective CsOPM and the field fluctuations during the measurements. The error $\varDelta\widetilde{B}$ of the weighted mean is typically well below 70 fT for these 100 s time slices.

Figure 9 shows, that the magnetic field in the BMSR-2 chamber drifts by several pT on a time scale of $\approx$1000 s.

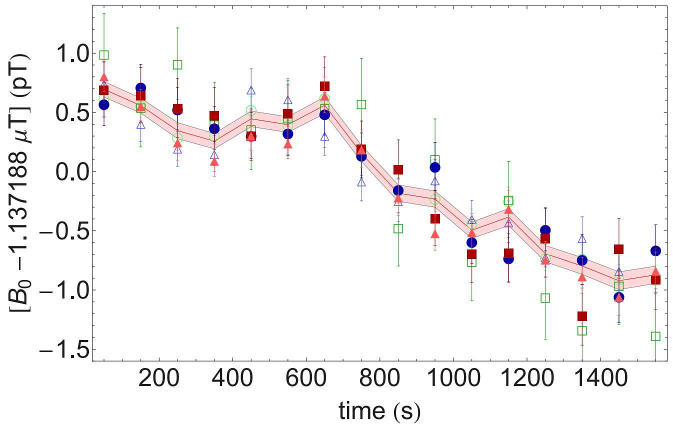

Fig. 9. Time evolution of the magnetic field in the BMSR-2 chamber at PTB, estimated from consecutive 100 s subsets from data segments of six CsOPMs simultaneously detecting the same ^{3}He FSP. Each plot point displays an individual CsOPM reading B_i and its uncertainity ΔB_i. The common ordinate is shifted by $\sim 1.1\,\mu$T. The solid line (red) and the shaded band represent $\widetilde{B}$ and its corresponding 1σ confidence values $\widetilde{B} \pm \Delta\widetilde{B}$.

We will see below that these instabilities limited the determination of the combined magnetometer's sensitivity.

5.4 Experimental determination of sensitivity

The noise of any magnetometer signal will contain in general contributions from both technical and intrinsic (fundamental) noise sources. In the best possible case the technical noise is due to the instability of the applied magnetic field. The two sources of noise cannot be distinguished in general. In this study we have operated simultaneously four different types of magnetometers, viz., the ^{3}He read out by CsOPMs, the ^{3}He read out by SQUIDs, the CsOPMs alone, and the SQUID(s) alone. We can make use of this fact to distinguish noise processes that are common to all sensors from processes that affect the individual sensors. When different types of magnetometers are operated in the same magnetic field, the technical noise contributions resulting from field fluctuations should be correlated, except for instabilities of the magnetic field gradients, since the different magnetometers are located at different spatial positions. The Allan standard deviation (ASD) [29] is a powerful tool to examine noise processes and signal stability. A detailed account of its application to magnetometric measurements is given by Groeger et al. [30].

We have extracted the magnetic field from the ^{3}He/SQUID data using the same procedure as for the ^{3}He/Cs signal analysis, i.e., by fitting equation (5) to the data. The magnetometric field readings from the SQUIDs proper and from the Cs magnetometers proper were retrieved from the original data using a digital low-pass filter (bandwidth $\sim$25 Hz) that removes the modulation from the ^{3}He FSP. We note that these filtered magnetometer signals do not represent absolute field readings since they may be affected by detector specific offsets. Nevertheless, as long as those potential offsets are constant, they will not affect the ASD of the signals and can thus be used for comparing the signal fluctuations. The ASD of the measured magnetic field was calculated over a wide range of integration times for all four types of magnetometers. Typical results are shown in Figure 10. The region of CRLB limited measurements up to integration times $T_M \sim 500$ s is restricted by the drift of the magnetic field witnessed in Figure 9. One sees that the ASDs of all sensors, independent of the sensor type, end up on the same rising slope for sufficiently long integration times $T_M > 500$ s. The fact that the different ASDs do not overlap perfectly for long integration times can be explained by fluctuations of magnetic field gradients, since the different sensors were not located at exactly the same spot. These observations support the assumption that the long-term stability of the magnetic field limits indeed the determination of the magnetometric sensitivity. Note that for the data which entered the analysis displayed in Figure 10 the initial ^{3}He polarization was $\sim$20 % smaller than for the measurements presented in Section 5.3.

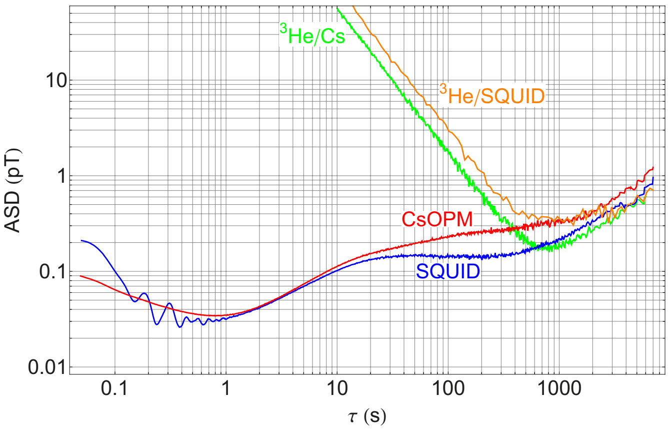

Fig. 10. Allan standard deviation of simultaneous field measurements with the ^{3}He/Cs (green), the CsOPM (red), the SQUID (blue) magnetometer, and the ^{3}He/SQUID (orange) respectively. For long integration times the sensitivity of all magnetometers is limited by a common noise process. The oscillatory component of the SQUID data is most probably due to mechanical vibrations of the setup. Note that the ^{3}He/Cs curve lies deeper than the ^{3}He/SQUID only due to the lower SNR of ^{3}He/SQUID which is caused by the larger distance to the ^{3}He cell.

In order to experimentally determine the sensitivity of the ^{3}He/Cs magnetometer we selected a measurement with a large ^{3}He polarization and calculated the ASD of the magnetic field determined from ω_{He} following the same procedure as above. The result is shown in Figure 11, the shaded band giving the 1σ confidence region for each measurement. Where the field estimation process is CRLB limited, we find the characteristic $\tau^{-3/2}$ slope of the ASD curve, e.g., up to integration times of $\sim$55 s. We determine the experimental sensitivity in this range by fitting a function

$$\sigma_B^{\text{meas}} = \eta_B^{\text{meas}} / T_M^{3/2}, \tag{17}$$

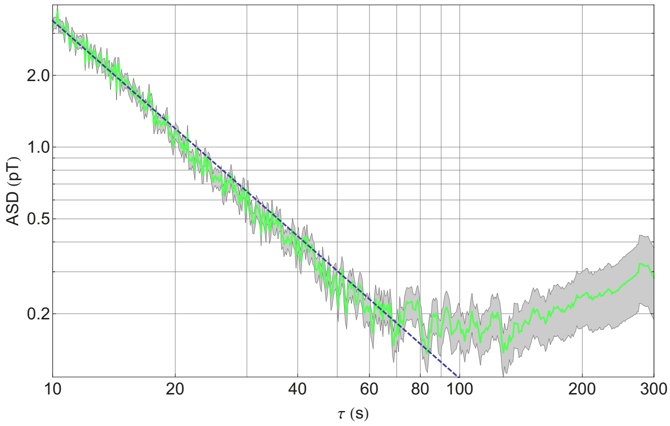

Fig. 11. ASD of magnetic field calculated from ω_{He} measured by the ^{3}He/Cs magnetometer. The gray region around the curve denotes the 1σ confidence band for each ASD point. A fit of equation (17) to the data up to $\tau \leq 55\,\mathrm{s}$ is displayed as the dashed line.

to the data (up to $\tau \leq 55\,\mathrm{s}$). The fitted function is denoted by the dashed line in Figure 11. The uncertainties of the ASD points are used as weights in this fit. We find for the sensitivity parameter $\eta_B^{meas} = 107.0(5)\,\mathrm{pT\ s}^{3/2}$.

We note that due to the higher ^{3}He polarization compared to the data shown in Figure 10, the ASD reaches its minimum imposed by the instability of the magnetic field already at shorter integration times.

6 Sensitivity in shotnoise limit

In this section we will quantify the intrinsic noise level that is inherent to the measurement process with the given experimental parameters. We can then compare this value to the observed noise floor to judge the quality of our measurement, allowing us to quantify the impact of technical noise (such as electromagnetic pick-up, amplifier noise, ...) on the signals. We will furthermore estimate the ultimate achievable sensitivity of the combined magnetometer under optimized experimental parameters.

The discrete nature of the charges constituting the relevant electric currents in the experiment is a fundamental source of noise. This shotnoise is assumed to be a zero-average Gaussian process. We calculate the intrinsic noise level of the measurement due to the shotnoise of the CsOPMs' photodiode currents and the shotnoise of the B_0-coilcurrent. We refer to this fundamental noise level as the shotnoise limit in the following. The fundamental intrinsic noise floor of the measurement will thus have two contributions, one from the magnetic field noise, σ_{field}, and one from the CsOPM noise, σ_{Cs}. Since the two Gaussian sources of noise are uncorrelated one can set

$$\sigma_{\mathcal{G}} = \sqrt{\sigma_{Cs}^2 + \sigma_{\mathrm{field}}^2}. \tag{18}$$

As described in [20], the intrinsic noise of a CsOPM depends on the laser power, rf-power and the cell properties and can be expressed in terms of the noise-equivalent magnetic field (NEM). For optimized rf- and laser power one obtains a minimal NEM$^{\mathrm{min}}$ of $\approx 12\,\mathrm{fT}/\sqrt{\mathrm{Hz}}$ for the type of cells used. To estimate the NEM in the shotnoise limit under given experimental conditions, e.g., non-optimal rf and light power, we start from the square-root power spectral density of the photocurrent shotnoise

$$\rho_{\mathrm{I,PSN}} = \sqrt{2e\,I_{DC}}, \tag{19}$$

where I_{DC} is the measured DC-photocurrent and e the elementary charge. The voltage shotnoise is then given by

$$\rho_{\mathrm{V,PSN}} = \rho_{\mathrm{I,PSN}}\,g = \sqrt{2e\,I_{DC}}\,g, \tag{20}$$

where $g = 2.53 \times 10^7\,\mathrm{V/A}$ is the gain of the used transimpedance amplifier. The phase change $\delta\phi$ corresponding to a voltage change δU of the input signal is (see [31])

$$\delta\phi = \frac{\delta U}{a_{Cs}}, \tag{21}$$

where a_{Cs} denotes the amplitude of the signal after the transimpedance amplifier, and the NEM can finally be calculated using

$$\mathrm{NEM} = \rho_{Cs} = \frac{\delta\phi\,\Gamma_2}{\gamma_{Cs}}, \tag{22}$$

with Γ_2 being the transverse relaxation rate of the Cs spin polarization. For the best-performing CsOPM under true experimental conditions (Cs1: $\mathrm{I}_{DC} = 3.25\,\mu\mathrm{A}$, $a_{Cs} = 1.3\,\mathrm{V}$, $\Gamma_2/2\pi = 6.1\,\mathrm{Hz}$) this calculation yields $\mathrm{NEM}_{Cs1} \approx 34\,\mathrm{fT}/\sqrt{\mathrm{Hz}}$. The photocurrents I_{DC} were repeatedly measured for each sensor during the experiment. The values of a_{Cs} and $\Gamma_2/2$ can be obtained by fits to the frequency sweep-responses of the individual sensors shown in Figure 3 which were also repeatedly recorded.

The second source of noise in equation (18) comes from Gaussian fluctuations of the magnetic field B_0 due to the coilcurrent's shotnoise. In the shotnoise limit ρ_{field} is obtained for a given coilcurrent ($I_C = 19\,\mathrm{mA}$) and coil constant ($g_{\mathrm{Coil}} = 60\,\mu\mathrm{T/A}$) is given by

$$\rho_{\mathrm{field}} = \sqrt{2e\,I_c}\,g_{\mathrm{coil}} = 4.7\,\mathrm{fT}/\sqrt{\mathrm{Hz}}. \tag{23}$$

Inserting these values into equation (18) leads to the shotnoise limit under the given experimental conditions of $\rho_{\mathcal{G}}^{SN} = 35\,\mathrm{fT}/\sqrt{\mathrm{Hz}}$. It is obvious that $\rho_{\mathcal{G}}^{SN}$ is dominated by ρ_{Cs}, the contribution from the coilcurrent ρ_{field} playing only a negligible role. This value can be compared to the experimentally observed noise level $\rho_{\mathcal{G}}^{exp} = 27\,\mathrm{fT}/\sqrt{\mathrm{Hz}}$. In order to make this comparison consistent, we still have to consider the effect of the lock-in demodulation filter which has a transfer function $T_{\mathrm{LIA}}(\omega_{\mathrm{He}}) = 0.82$, the noise before the lock-in is thus $\rho_{\mathcal{G}}^{exp}/_{\mathrm{LIA}}(\omega_{\mathrm{He}}) \approx 35\,\mathrm{fT}/\sqrt{\mathrm{Hz}}$. We find that the observed noise floor agrees with the expected shotnoise limit. Using equations (4), (10) and (17), we calculate the expected sensitivity parameter in the shotnoise limit from the above value of $\rho_{\mathcal{G}}^{SN}$ and the ^{3}He-FSP amplitude ($a = 4.15\,\mathrm{pT}$), yielding

$$\eta_B^{SN} = \sigma_B^{SN}(\rho_{\mathcal{G}}^{SN}, a) \cdot T_M^{3/2} \approx 111\,\mathrm{pT\ s}^{3/2}.$$

If we compare the measured sensitivity from equation (17) and the shotnoise limited sensitivity we find $\eta_B^{meas} \approx \eta_B^{SN}$. We can thus state that the measurement was shotnoise limited. In the same way we can compare our results to the estimated sensitivity of [19]. We use the magnitude of the magnetic field produced by the ^{3}He FSP $a_{\mathrm{CT}} = 6\,\mathrm{pT}$ reported in their paper and $\rho_{\mathcal{G}}^{exp} = 27\,\mathrm{fT}/\sqrt{\mathrm{Hz}}$ to find $\eta \approx 77\,\mathrm{pT\ s}^{3/2}$. This value is comparable to the estimated sensitivity of [19] given at the end of Section 2.1, we thus conclude that the two measurements were equally sensitive. We note that because the measurements described in [19] were done in a very weak magnetic field, the Larmor frequency is only $\omega_{\mathrm{He}}/2\pi = 3\,\mathrm{mHz}$. At this low frequency the bandwidth limitations imposed by the readout magnetometer are not relevant.

We will now estimate the ultimate sensitivity $\eta_B^{\min}$, under the assumption of a perfectly stable magnetic field. This limit is reached by maximizing SNR $= a_{\mathrm{rms}}/\rho_{\mathcal{G}}$ in equation (10). We thus consider a ^{3}He FSP with maximum amplitude, measured by a shotnoise limited CsOPM with minimal NEM. For our best paraffin-coated cells, operated under optimized conditions, a minimal NEM of $\sim 7\,\mathrm{fT}/\sqrt{\mathrm{Hz}}$ has been reported [20]. The FSP amplitude is maximized for 100 % ^{3}He polarization. We further consider a detection of the FSP without the bandwidth limitations imposed by the CsOPMs driven in the fixed frequency mode. This could be achieved by a CsOPM driven in the phase-stabilized mode by a PLL with high bandwidth (or by a self-oscillating Cs magnetometer [32]). For the ~1mbar cell used this corresponds to $a_{\mathrm{rms}}^{\max} = 41\mathrm{pT}$ at the CsOPM position. Combining $a_{\mathrm{rms}}^{\max}$ and NEM$^{\min}$ from above leads to a maximum SNR of $\approx 5800\,\sqrt{\mathrm{Hz}}$. Using equation (10) we thus find $\eta_B^{\min} \approx 2\,\mathrm{pT\ s}^{3/2}$ for the intrinsic sensitivity of a combined ^{3}He/Cs magnetometer in this configuration.

7 Conclusion

We have described the design of a compact ^{3}He/Cs magnetometer prototype for absolute measurements of weak magnetic fields at room temperature, and have investigated its performance. It was shown that the magnetometer is capable of performing CRLB limited measurements within the constraints imposed by the stability of the applied magnetic field. We demonstrated that a combined ^{3}He/Cs magnetometer consisting of a ^{3}He cell and a single CsOPM as readout-magnetometer can measure the absolute value of a $1.1\,\mu\mathrm{T}$ magnetic field with a standard uncertainty of 100 fT in a measurement time of 100 s, which corresponds to a relative error below 10^{-7}. Measurements with simultaneous readout by multiple CsOPMs were presented and show that the standard error of the weighted mean field estimate decreases statistically with the number of CsOPMs, reaching $\Delta\widetilde{B} \approx 60\,\mathrm{fT}$ in 100 s. This result is important because it implies that the magnetometric sensitivity of a combined ^{3}He/Cs magnetometer fulfills the requirements of the current and future nEDM (and other) experiments by applying a suitable number of readout CsOPMs. A gradiometric measurement was presented in which common-mode noise could be suppressed in the differential signal. We estimated the intrinsic sensitivity of the prototype magnetometer for single CsOPM readout, corresponding to a standard of field estimation error of 2 fT in a measurement time of 100 s. For the nEDM application larger ^{3}He cells are foreseen which will also increase the FSP amplitude compared to the cell used here where CsOPM- and ^{3}He-cell were of similar size, leading to an even higher sensitivity. The results show that combined ^{3}He/Cs magnetometers are suitable for the absolute, high precision determination of magnetic fields in fundamental physics experiments.

The described work was only made possible by the outstanding support from the mechanical workshops of the Physics Department at the University of Fribourg and the University of Mainz. This work was supported by grants from the Deutsche Forschungsgemeinschaft (HE2308/14-1) and the Swiss National Science Foundation (200020_140421).

The studies presented in this paper are part of the Ph.D. thesis of H.-C. Koch who was leading all aspects of the investigations. The other authors contributed to particular subtasks as follows:

- A. Weis, Z.D. Grujić, P. Knowles, M. Kasprzak and W. Heil were involved in the conceptual planing and construction of the device and in the development of data acquisition methods;
- Z.D. Grujić, P.Knowles, G. Bison, A. Schnabel and J. Voigt contributed to the data taking at PTB;
- A. Weis, Z.D. Grujić, G. Bison and W. Heil participated in the data analysis and the discussion of the results;
- A. Kraft, A. Pazgalev, Z.D. Grujić, P.Knowles and M. Kasprzak contributed to important precursor measurements at Johannes Gutenberg University Mainz.

References

1. C.A. Baker, G. Ban, K. Bodek, M. Burghoff, Z. Chowdhuri, M. Daum, M. Fertl, B. Franke, P. Geltenbort, K. Green, M.G.D. van der Grinten, E. Gutsmiedl, P.G. Harris, R. Henneck, P. Iaydjiev, S.N. Ivanov, N. Khomutov, M. Kasprzak, K. Kirch, S. Kistryn, S. Knappe-Güneberg, A. Knecht, P. Knowles, A. Kozela, B. Lauss, T. Lefort, Y. Lemière, O. Naviliat-Cuncic, J.M. Pendlebury, E. Pierre, F.M. Piegsa, G. Pignol, G. Quéméner, S. Roccia, P. Schmidt-Wellenburg, D. Shiers, K.F. Smith, A. Schnabel, L. Trahms, A. Weis, J. Zejma, J. Zenner, G. Zsigmond, Phys. Proc. **17**, 159 (2011), 2nd International Workshop on the Physics of fundamental Symmetries and Interactions – PSI2010
2. J.M. Pendlebury, W. Heil, Yu. Sobolev, P.G. Harris, J.D. Richardson, R.J. Baskin, D.D. Doyle, P. Geltenbort, K. Green, M.G.D. van der Grinten, P.S. Iaydjiev, S.N. Ivanov, D.J.R. May, K.F. Smith, Phys. Rev. A **70**, 032102 (2004)
3. N.F. Ramsey, Phys. Rev. **78**, 695 (1950)

4. M.C. Fertl, Ph.D. thesis, Diss., Eidgenössische Technische Hochschule ETH Zürich, Nr. 21638, 2013
5. A. Kastler, J. Opt. Soc. Am. **53**, 902 (1963)
6. B. Cagnac, Ph.D. thesis, Université Paris, 1960
7. P.J. Mohr, B.N. Taylor, D.B. Newell, J. Phys. Chem. Ref. Data **41**, 043109 (2012)
8. S. Groeger, G. Bison, J.-L. Schenker, R. Wynands, A. Weis, Eur. Phys. J. D **38**, 239 (2006)
9. P. Knowles, G. Bison, N. Castagna, A. Hofer, A. Mtchedlishvili, A. Pazgalev, A. Weis, Nucl. Inst. Meth. A **611**, 306 (2009)
10. F. Bloch, A. Siegert, Phys. Rev. **57**, 522 (1940)
11. G.D. Cates, S.R. Schaefer, W. Happer, Phys. Rev. A **37**, 2877 (1988)
12. B.W. Petley, J.L. Flowers, M.G. Richards, Metrologia **30**, 75 (1993)
13. P.G. Harris, C.A. Baker, K. Green, P. Iaydjiev, S. Ivanov, D.J.R. May, J.M. Pendlebury, D. Shiers, K.F. Smith, M. van der Grinten, P. Geltenbort, Phys. Rev. Lett. **82**, 904 (1999)
14. A. Kraft, H.-C. Koch, M. Daum, W. Heil, T. Lauer, D. Neumann, A. Pazgalev, Y. Sobolev, A. Weis, Eur. Phys. J. Tech. Instrum. **1**, 8 (2014)
15. W. Happer, Rev. Mod. Phys. **44**, 169 (1972)
16. M. Leduc, P.J. Nacher, G. Tastevin, E. Courtade, Hyperfine Interactions **127**, 443 (2000)
17. F.D. Colegrove, L.D. Schearer, G.K. Walters, Phys. Rev. **132**, 2561 (1963)
18. C. Gemmel, W. Heil, S. Karpuk, K. Lenz, Ch. Ludwig, Yu. Sobolev, K. Tullney, M. Burghoff, W. Kilian, S. Knappe-Grüneberg, W. Müller, A. Schnabel, F. Seifert, L. Trahms, St. Baeßler, Eur. Phys. J. D **57**, 303 (2010)
19. C. Cohen-Tannoudji, J. Dupont-Roc, S. Haroche, F. Laloë, Phys. Rev. Lett. **22**, 758 (1969)
20. N. Castagna, G. Bison, G. Domenico, A. Hofer, P. Knowles, C. Macchione, H. Saudan, A. Weis, Appl. Phys. B **96**, 763 (2009)
21. F. Thiel, A. Schnabel, S. Knappe-Grüneberg, D. Stollfuß, M. Burghoff, Rev. Sci. Instrum. **78**, 035106 (2007)
22. I. Hilschenz, D. Gutkelch, S. Hartwig, N. Höfner, R. Körber, H.J. Scheer, J. Voigt, M. Burghoff, L. Trahms, Biomed. Technik/Biomedical Eng. **55**, 227 (2010)
23. *Mathematica*. 8th edn. (Wolfram Research, Inc., Champaign, Illinois, 2010)
24. K. Tullney, Ph.D. thesis, Johannes Gutenberg-Universitaet, 2013
25. W. Heil et al., Ann. Phys. **525**, 539 (2013)
26. C. Radhakrishna Rao, Bull. Calcutta Math. Soc. **37**, 81 (1945)
27. H. Cramér, *Mathematical methods of statistics* (Princeton university Press, 1946)
28. D.C. Rife, R.R. Boorstyn, IEEE Trans. Inf. Theory **20**, 591 (1974)
29. D.B. Sullivan, D.W. Allan, D.A. Howe, F.L. Walls, *Characterization of clocks and oscillators*, US Department of Commerce, National Institute of Standards and Technology, 1990
30. S. Groeger, G. Bison, P.E. Knowles, A. Weis, Eur. Phys. J. Appl. Phys. **33**, 221 (2006)
31. G. Bison, Ph.D. thesis, University of Fribourg, Switzerland, 2004
32. E.B. Alexandrov, A.K. Vershovskiy, *M_x and M_z magnetometers*, in *Optical Magnetometry*, edited by D. Budker, D.J.F. Kimball (Cambridge University Press, 2013), p. 60

Investigation of the intrinsic sensitivity of a ^{3}He/Cs magnetometer

A second article focusing on the investigations of the sensitivity described in Chapter 12 was published in European Physical Journal D [KBG$^+$15b] and is appended in the following.
This article is available under `http://dx.doi.org/10.1140/epjd/e2015-60509-5`.

Eur. Phys. J. D (2015) 69: 262
DOI: 10.1140/epjd/e2015-60509-5

THE EUROPEAN
PHYSICAL JOURNAL D

Regular Article

Investigation of the intrinsic sensitivity of a ^{3}He/Cs magnetometer

Hans-Christian Koch[1,2,a], Georg Bison[3], Zoran D. Grujić[1], Werner Heil[2], Malgorzata Kasprzak[1,b], Paul Knowles[1,c], Andreas Kraft[2], Anatoly Pazgalev[5], Allard Schnabel[4], Jens Voigt[4], and Antoine Weis[1]

[1] Physics Department, University of Fribourg, 1700, Fribourg, Switzerland
[2] Department of Physics, Johannes Gutenberg-University, 55122 Mainz, Germany
[3] Paul Scherrer Institute, 5232 Villigen, Switzerland
[4] Physikalisch-Technische Bundesanstalt, 10587 Berlin, Germany
[5] Ioffe Physical Technical Institute, Russian Academy of Sciences, 194021 St. Petersburg, Russia

Received 8 September 2015 / Received in final form 8 October 2015

Abstract. We report on extensive studies on the intrinsic sensitivity of a combined ^{3}He/Cs magnetometer. The magnetometer relies on the detection of the free spin precession of nuclear spin polarized ^{3}He by optically pumped cesium magnetometers. We characterize the relevant processes involved in the detection and quantify their impact on the total sensitivity of the magnetometer. An expression is derived that predicts the sensitivity of this magnetometer scheme and the results are compared to experiments. Excellent agreement is found between theory and experiments, and implications for an application of a ^{3}He/Cs magnetometer in an experiment searching for a permanent neutron electric dipole moment are discussed.

1 Introduction

Many fundamental physics experiments require the precision knowledge and control of an applied magnetic field. The searches for permanent electric dipole moments (EDM) of elementary particles, atoms or molecules are among such experiments. A high precision experiment, currently conducted at Paul Scherrer Institute (PSI), Switzerland, searches for the existence of a neutron EDM (nEDM) [1]. The existence of a finite-valued nEDM is closely tied to long persisting questions of cosmology, such as the baryon asymmetry of the universe [2]. In the experiment the spin precession frequency of stored ultracold neutrons in homogeneous parallel and anti-parallel electric and magnetic fields is measured using Ramsey's technique of separated oscillatory fields [3]. A next generation nEDM experiment is currently being developed at PSI (n2EDM) and is expected to further constrain the value of the nEDM. In order to suppress and control systematic effects the experiment requires the precise measurement of an applied magnetic field of $\sim$1 μT and the tuning of field gradients. For this task we plan to integrate in the apparatus a ^{3}He magnetometer recording the free spin precession (FSP) frequency of nuclear spin polarized ^{3}He gas. During the FSP the ^{3}He magnetization precesses at the Larmor frequency

$$\omega_{\mathrm{L,He}} = |\boldsymbol{B}|\,\gamma_{\mathrm{He}} \tag{1}$$

which will be measured by detecting the associated rotating magnetic field with optically pumped Cesium magnetometers (CsOPMs). Compared to superconducting quantum interference devices, which are widely used to detect nuclear magnetic resonance, CsOPMs offer the advantage of operating at room temperature, thus easing the spatially-distributed positioning of a large number of individual sensors.

In a recent publication we have described the design and performance of a ^{3}He/Cs magnetometer prototype built to investigate this magnetometric scheme [4]. We have demonstrated that CsOPMs provide a convenient way to detect the ^{3}He FSP, permitting Cramér-Rao lower bound (CRLB) limited measurements of a 1 μT magnetic field that yield sensitivities as low as $\Delta B \sim 50$ fT with a 100 s integration time. In this paper we report on an extended study of the intrinsic sensitivity of the combined ^{3}He/Cs magnetometer concept. We have developed a semi-empirical formula which predicts the CRLB and shotnoise-limited magnetometric sensitivity of a ^{3}He/Cs magnetometer based on specific experimental parameters. The predictions are compared to experimental results obtained at the magnetically shielded room (BMSR-2) of Physikalisch Technische Bundesanstalt (PTB) in Berlin [5] and find excellent agreement with model estimations.

---

[a] e-mail: kochhc@googlemail.com
[b] *Present address:* Instituut voor Kern- en Stralingsfysica, Katholieke Universiteit Leuven, 3001 Leuven, Belgium
[c] *Present address:* LogrusData, Vienna, Austria

2 Magnetometer principle

The ^{3}He/Cs magnetometer concept is based on detecting (by CsOPMs) the weak rotating magnetic field accompanying the precessing of nuclear spin polarized ^{3}He atoms. The CsOPMs build on an optically-detected magnetic resonance effect. The sensor proper is an evacuated, paraffin-coated glass cell of 30 mm diameter that holds a droplet of cesium in an appendix which is connected to the main volume by a capillary to reduce depolarizing collisions of Cs vapor atoms with the bulk Cs [6]. The Cs vapor is optically pumped using circularly-polarized laser radiation resonant with the D1 transition, $\lambda \sim 895$ nm. The cell is enclosed in a pair of Helmholtz coils used to drive the magnetic resonance transitions by a weak rf field, $\boldsymbol{B}_{\mathrm{rf}}(t)$, oscillating at the Cs Larmor frequency $\omega_{\mathrm{rf}} \approx \omega_{\mathrm{L,Cs}}$ that is related to the modulus of the total magnetic field $\boldsymbol{B}$ via

$$\omega_{\mathrm{L,Cs}} = \gamma_{\mathrm{Cs}} \left|\boldsymbol{B}\right| \tag{2}$$

where $\gamma_{\mathrm{Cs}}/2\pi \approx 3.5$ kHz/μT is the cesium atom's gyromagnetic ratio. The magnetometers are operated in the so-called M_x configuration [7] with the rf field along the laser beam, $\hat{B}_{\mathrm{rf}} \parallel \hat{k}_{\mathrm{Cs}}$. The light power transmitted by the Cs cell is detected by a photodiode and the transimpedance amplified photocurrent signal demodulated by a lock-in amplifier referenced to ω_{rf}. Analytical expressions describing the lineshapes of the M_x magnetometer can be derived from the Bloch equations in the rotating wave approximation, yielding

$$S_R = \sqrt{S_{IP}^2 + S_{QU}^2} = \frac{G_0\sqrt{\Gamma_2^2 + \delta\omega^2}\omega_1\Gamma_1}{\sqrt{2}(2\Gamma_1(\Gamma_2^2+\delta\omega^2)+\Gamma_2\omega_1^2)} \tag{3}$$

$$\tan\left(\frac{\pi}{2}+\phi\right) = \frac{S_{QU}}{S_{IP}} = -\frac{\delta\omega}{\Gamma_2} \tag{4}$$

for the amplitude (S_R)-phase (ϕ) parametrization of the demodulated signal [8]. Here, S_{IP} and S_{QU} denote the in-phase and quadrature components of the signal, respectively. G_0 is a saturation parameter that depends on the laser power and Γ_1, Γ_2 are the longitudinal and transverse relaxation rates of the Cs polarization, respectively. We have also introduced the detuning of the rf frequency from resonance

$$\delta\omega = \omega_{\mathrm{L,Cs}} - \omega_{\mathrm{rf}} \tag{5}$$

and expressed the rf field strength in terms of its associated Larmor frequency $\omega_1 = \gamma_{\mathrm{Cs}} B_{\mathrm{rf}}$.

The magnetic dipole field produced by a spherical volume of polarized ^{3}He at the magnetometer position $\boldsymbol{r}$ with respect to the sphere center is given by:

$$\boldsymbol{B}_{\mathrm{He}} = \frac{3\hat{r}(\hat{\mu}\cdot\hat{r}) - \hat{\mu}}{r^3}\frac{N_{\mathrm{He}}p\mu_{\mathrm{He}}\mu_0}{4\pi}. \tag{6}$$

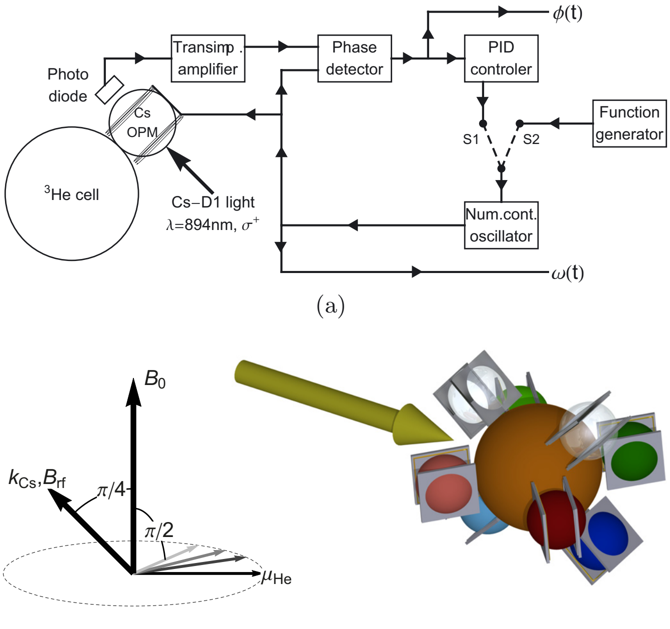

(a)

(b)

Fig. 1. (a) Schematic sketch of experiment and processing electronics. If the switch is set to position S1, the phase detector, PID controller and numerically controlled oscillator form a phase feedback loop and the CsOPM is operated in PS-mode. If set to S2 position the CsOPM can be operated in FF-mode (function generator supplies constant output) or frequency sweep measurements as shown in Figure 2 can be recorded (function generator supplies ramp). In the experiments described here, phase detector, PID controller, function generator and numerically controlled oscillator are all digitally implemented in a single device. (b) Left: geometry of the experiment. The ^{3}He magnetization $\boldsymbol{\mu}_{\mathrm{He}}$ is precessing in a plane perpendicular to $\boldsymbol{B}_0$, the $\boldsymbol{k}_{\mathrm{Cs}}$ of the CsOPM readout laser is at 45°. Right: geometry of the combined magnetometer. The large(orange) sphere in the center is the ^{3}He cell. The surrounding smaller spheres are the CsOPMs with the gray planes indicating the orientation of the printed circuit boards holding the individual rf coils. The (yellow) arrow denotes the direction of the B_0 field.

Here p and μ_{He} are the nuclear spin polarization and magnetic moment of the ^{3}He, while $\hat{\mu}$ represents the spatial orientation of the ^{3}He magnetization. Assuming a (room temperature) pressure of ∼1 mbar, the ∼70 mm diameter ^{3}He cell contains $N_{\mathrm{He}} \approx 3\times10^{18}$ atoms following the ideal gas law. Evaluating equation (6) shows that the magnetic field of interest is on the order of pico-Tesla in the vicinity of the cell. In the experiments described in this work we have $B_0 \sim 1\ \mu\mathrm{T} \gg B_{\mathrm{He}}$, in which case equation (2) reduces to $\omega_{\mathrm{L,Cs}}(t) \propto |\boldsymbol{B}| = |\boldsymbol{B}_0 + \boldsymbol{B}_{\mathrm{He}}| \approx |\boldsymbol{B}_0| + \hat{B}_0\cdot\boldsymbol{B}_{\mathrm{He}}(t)$. Under this condition the CsOPM is to first order only sensitive to the component of the ^{3}He field along $\boldsymbol{B}_0$. The precession of the ^{3}He magnetization can be expressed by a time dependent $\hat{\mu}(t)$ in equation (6). Assuming $\hat{B}_0 = \hat{z}$ and $\boldsymbol{\mu}$ rotating in an orthogonal plane (cf. Fig. 1b, left), the relevant component of the oscillating magnetic field is given by:

$$B_{\mathrm{He,z}} = \frac{N_{\mathrm{He}}p\mu_{\mathrm{He}}\mu_0}{4\pi r^3}3\cos(\omega_{\mathrm{L,He}}t - \phi)\cos(\theta)\sin(\theta) \tag{7}$$

introducing standard spherical coordinates. The field component given by equation (7) will thus be maximized for $\theta = 45°$, so that the loci of optimal CsOPM positions are represented by two symmetric cones around $\hat{B}_0$ with tips centered at the ^{3}He cell center. The CsOPMs should thus be placed on these cones at a minimal distance $|\boldsymbol{r}|$ from the ^{3}He cell.

3 The experimental apparatus

The measurements presented below were performed in the magnetically shielded room BMSR-2 of Physikalisch Technische Bundesanstalt in Berlin using the combined ^{3}He/Cs magnetometer prototype described in detail in reference [4]. It consists of a 70 mm diameter spherical ^{3}He cell mounted in a structure that holds eight CsOPMs in the optimal detection geometry discussed above (cf. Fig. 1b, right). Nuclear spin polarization is created in the ^{3}He gas by metastable exchange optical pumping with 1.08 μm laser radiation traversing a plasma discharge in the ^{3}He cell. The maximal amplitude of the field oscillation created by the ^{3}He FSP that can be expected at the Cs cell centers can be calculated from equation (7). Inserting the dimensions of the ^{3}He cell (69–72 mm diameter, 2 mm wall thickness) and the CsOPMs (30 mm diameter) the calculation yields $\left|B_{\mathrm{He}}^{(\mathrm{max})}\right| = 34\ \mathrm{pT}_{\mathrm{rms}}$. Each CsOPM has an individual rf coil pair. In order to avoid that the magnetic resonance in a given CsOPM is driven by the parasitic rf field from a neighboring sensor, an effect known as rf cross-talk, all magnetometers are driven at the same ω_{rf}.

Two different modes of operation were investigated, viz., the fixed-frequency mode (FF-mode) and the phase-stabilized mode (PS-mode). Figure 1a shows a schematic drawing of the data processing electronics for both modes of operation. In the FF-mode of operation the frequency ω_{rf} is kept constant, and magnetic field changes are detected via corresponding phase changes, following equation (4). If the magnetic field gradients are sufficiently small ω_{rf} can be chosen to have good overlap with the resonances of all CsOPMs and they can all be driven by the same rf. In the PS-mode of operation one CsOPM (master) is operated in a phase feedback loop. An error signal is derived from the phase difference between the magnetometer signal and the output of a numerically-controlled oscillator (NCO) that supplies the rf frequency for the CsOPM [9]. A PID controller minimizes this error signal by adjusting the frequency of the NCO. Under ideal conditions the CsOPM is thus always driven on resonance $\omega_{\mathrm{rf}}{=}\omega_{\mathrm{L,Cs}}$. This dynamically controlled ω_{rf} is then also used to drive the remaining CsOPMs (slaves). In the presence of (fluctuating) gradients this implies that the slaves are in general not driven exactly on resonance. Furthermore, due to the dependence of the ^{3}He FSP signal's phase on the relative position of the CsOPM (cf. Eq. (7)), the signals from the slaves will be qualitatively different and all depending on the master's performance. Such effects can be exploited in gradiometric measurements [10].

4 The measurement parameters

The sensitivity of the combined magnetometer depends on a set of parameters describing the properties of the optically detected magnetic resonance (ODMR) process in the CsOPM and the FSP of the ^{3}He gas. A detailed account of all effects affecting the CsOPM sensitivity is given in reference [6]. In the following we will separately address the most relevant effects and quantify their contribution to the total sensitivity.

4.1 Bandwidth limitation of CsOPM

As evidenced by the expressions describing the magnetometer signal lineshapes (Eqs. (3) and (4)), the CsOPM in M_x configuration can be considered as a driven harmonic oscillator with resonance frequency $\omega_{\mathrm{L,Cs}}$ periodically excitated at ω_{rf}. In general, the excitation frequency ω_{rf} is detuned from the resonance frequency $\omega_{\mathrm{L,Cs}}$ by an amount $\delta\omega$ given by equation (5). The detuning is affected both by variations of the magnetic field and of the excitation frequency. Following a change of the detuning, the ODMR process in the CsOPM undergoes a transient phase (and frequency) change during which the Cs spin precession adapts to the changed conditions. The settling time of this process depends on the lifetime $\tau{=}\varGamma_2^{-1}$ of the Cs polarization in the cell, where $\varGamma_2$ is the transverse spin relaxation rate. In perfect analogy with mechanical or electronic driven oscillators, the settling time can be related to the resonance's quality factor Q via

$$Q = \frac{\omega_{L,Cs}}{2\varGamma_2}. \tag{8}$$

Periodic changes of the detuning $\delta\omega \sim \cos(\omega_{\mathrm{mod}} t)$ are of particular interest for the present discussion. In that case, the settling process implies a frequency-dependent response of the system with a first-order low pass characteristic [11] $T_{\mathrm{Cs}}(f) = T^{(1)}(f)$, where

$$T^{(n)}(f) = \left[\frac{1}{1 + (2\pi f\,\tau)^2}\right]^{n/2}, \tag{9}$$

is the generalized transfer function of an nth order filter. $T_{\mathrm{Cs}}(f)$ describes the response of the photodiode signal to a change of the detuning. The relaxation rate in the Cs cell will in general depend on different parameters, e.g., the quality of the coating, the size of the cell and the power of the resonant pump and readout light. It can be conveniently measured by recording the response of the magnetometer to a sweep of the rf frequency. The result of such a measurement is shown in Figure 2.

As described in Section 3, the CsOPMs can be operated in two different modes of operation. In the FF-mode, where ω_{rf} is being kept constant, any change of the detuning induced by a change of the magnetic field at the CsOPM's position will change the local Larmor frequency $\omega_{\mathrm{L,Cs}}$. The oscillating field produced by the ^{3}He-FSP introduces a periodic change of the detuning, and the frequency dependence of the CsOPM's response will be given

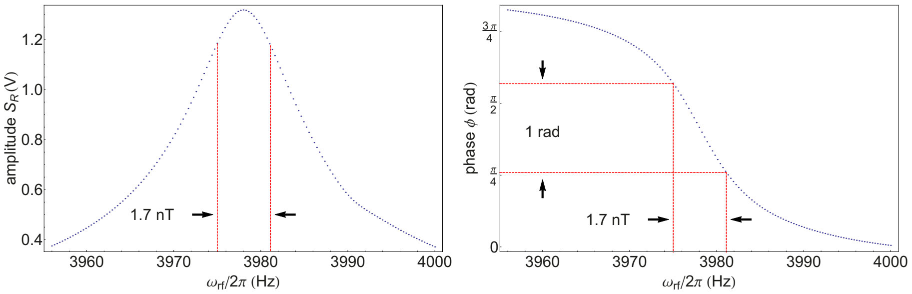

Fig. 2. S_R- and ϕ-signal of CsOPM when the rf frequency is tuned across the magnetic resonance. Graphs shown for $\Gamma_2/2\pi = 6.1$ Hz, equivalent to 1.7 nT.

by the transfer function $T^{(1)}_{\mathrm{Cs}}(f)$. Since the typical lifetime of the Cs polarization in the paraffin coated cells is $\tau \sim 26$ ms, the low pass described by equation (9) has a -3dB cutoff frequency of typically $f_{\text{-3dB}} \approx 6$ Hz. This represents a severe bandwidth limitation for measurements performed in the FF-mode. An additional bandwidth limitation arises from the low-pass filter in the lock-in amplifier's demodulator used to extract the phase signal, an effect that can be characterized by a second transfer function, $T_{\mathrm{LIA}}(f)$. Assuming only small variations of the magnetic field $\gamma_{\mathrm{Cs}}\delta B \ll \Gamma_2$ and using equation (4) the response of the CsOPM's phase signal to a change of the magnetic field can be expressed as:

$$\delta\phi = \frac{\delta\omega}{\Gamma_2} T_{\mathrm{tot}} = \frac{\gamma_{\mathrm{Cs}}\,\delta B}{\Gamma_2} T_{\mathrm{tot}}, \tag{10}$$

where

$$T_{\mathrm{tot}} = T_{\mathrm{LIA}}\, T_{\mathrm{Cs}} \tag{11}$$

is the combined transfer function of the system caused by the two processes mentioned above. This assumption can be verified experimentally by measuring the response of the CsOPM to small periodic variations applied to the holding field B_0. The results of such a measurement in which the field modulation frequency f_{mod} is changed (at constant modulation amplitude) are shown in Figure 3. For each value of f_{mod}, the amplitude $\delta\phi$ of the corresponding phase oscillation was inferred from the FFT spectrum of the time dependent phase signal. The experimental results are in excellent agreement with the theoretical predictions.

In the PS-mode of operation the phase-stabilized loop dynamically readjusts ω_{rf} to track changes of the Larmor frequency. In the ideal case one has $\omega_{\mathrm{L,Cs}} = \omega_{\mathrm{rf}}$ at all times, so that the CsOPM is always driven at resonance and no change of detuning occurs. In this mode of operation, the CsOPM is free from the bandwidth limitation imposed by the 'free-running' FF-mode. In reality the bandwidth is limited by the frequency characteristics of the feedback loop whose bandwidth, however, can be considerably larger than the one imposed by $T_{\mathrm{LIA}}T_{\mathrm{Cs}}$ under free-running conditions. In Section 7 implications for the magnetometric sensitivity in this mode of operation will be discussed.

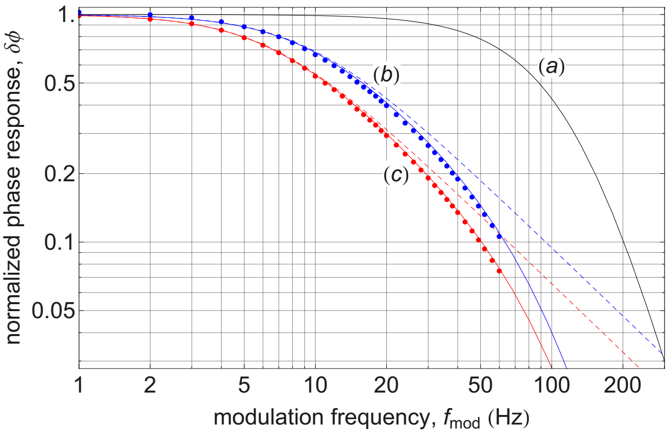

Fig. 3. Experimental and theoretical frequency response of two CsOPMs driven in FF-mode. (a) Transfer function $T_{LIA} = T^{(4)}$ of the used 4th order (-24 dB/oct) lock-in amplifier demodulation filter calculated according to equation (9) with $\tau = 1.16$ ms. (b,c) dashed lines: Transfer functions T_{Cs}=$T^{(1)}$ of two CsOPMs, corresponding to a 1st order filter with $\tau = 1/\Gamma_{Cs}$. The lifetimes are $\tau \approx 17$ ms for the blue curve and $\tau \approx 24$ ms for the red curve, respectively. (b,c) Solid lines: Combined transfer functions $T_{LIA}T_{Cs}$ for the two CsOPMs. The dots represent experimentally measured points.

4.2 Sensitivity loss due to permanent detuning

An additional effect has to be considered when operating multiple CsOPMs at an identical fixed frequency. Due to unavoidable inhomogeneities of the magnetic field, the Larmor frequencies of the individual CsOPMs will in general differ $\omega^{(i)}_{\mathrm{L,Cs}} \neq \omega^{(j)}_{\mathrm{L,Cs}}$. This results in some, or all CsOPMs being effectively driven at a finite detuning, even in a perfectly stable field. We consider two effects that are caused by such a permanent detuning. On one hand, the spread of Larmor frequencies will reduce the amplitude $a_{Cs}(\delta\omega)$ of the demodulated signal. On the other hand, the spread will affect the effective slope of the phase curve. Both effects can be experimentally quantified by measurements of the frequency sweep response functions, such as shown in Figure 2. Based on equation (4), the off-resonance value of the phase slope for a constant detuning

$\delta\omega'$ is given by:

$$m(\delta\omega')=\frac{\partial\phi}{\partial\delta\omega}\bigg|_{\delta\omega'}=\frac{\partial}{\partial\delta\omega}\arctan\left(\frac{-\Gamma_2}{\delta\omega}\right)\bigg|_{\delta\omega'}=\frac{\Gamma_2}{\Gamma_2^2+\delta\omega'^2}. \tag{12}$$

The on-resonance slope $m(\delta\omega'=0)=1/\Gamma_2$ will be reduced for detunings $\delta\omega'\neq 0$. A permanently detuned CsOPM will thus produce a smaller response signal to a given magnetic perturbation. The response reduction is given by:

$$\epsilon_\phi(\delta\omega')=\frac{m(\delta\omega')}{m(\delta\omega'=0)}=\frac{\Gamma_2^2}{\Gamma_2^2+\delta\omega'^2}. \tag{13}$$

As noted above, the amplitude S_R also depends on the detuning and will be maximal for $\delta\omega=0$. The consequences for the signal/noise ratio arising from this will be discussed in Section 5.

5 Signal to noise ratio and sensitivity

Even under optimal experimental conditions the magnetometer signal will exhibit a fundamental noise level caused by processes inherent to the detection mechanism. The most prominent of such processes is the photocurrent shotnoise (PSN), a fluctuation of the current produced by the photodiode due to the corpuscular nature of light and electric current. Since the relatively weak ($I_{\mathrm{AC}}<0.1\ \mu$A) oscillatory current carrying the magnetometric information is superimposed on a much larger ($I_{\mathrm{DC}}\sim 3\ \mu$A) DC current, it is reasonable to assume that the PSN is dominated by fluctuations of I_{DC}, whose spectral density is given by:

$$\rho_{\mathrm{I,PSN}}=\sqrt{2\,e\,I_{\mathrm{DC}}}, \tag{14}$$

where e is the elementary charge. Other sources of noise, such as fluctuations of the magnetic field (magnetic field noise, MN) or electronic pick-up by the signal cables that may be present will add quadratically to this fundamental noise floor. The optimal case, in which the PSN is the only source of noise is referred to as the shotnoise limit.

It is important to understand that different noise processes, such as the PSN and MN affect the phase signal in qualitatively different manners. Let us first consider the case of purely magnetic field noise. MN affects the magnetic resonance process and its effect on the phase signal – evaluated using equation (10) – is subject to the bandwidth-limiting atomic filtering of the magnetic resonance process. Since the signal of interest (magnetic field oscillation) and the signal noise (magnetic field fluctuations) are equally bandwidth limited, e.g., undergo the same filtering by T_{tot}, the signal to noise-density ratio (SNDR) is independent of this bandwidth limitation. This independence also holds under the assumption of a permanently detuned magnetometer, as introduced in Section 4.2. In order to illustrate this we consider a periodic magnetic field fluctuation, e.g., the oscillating field $\delta B=b_{\mathrm{He}}$ created by the ^{3}He-FSP at the position of the CsOPM and assume a Gaussian magnetic noise spectral density ρ_{B}. The $SNDR_B$ for the magnetic quantities and the $SNDR_\phi$ on the phase signal are

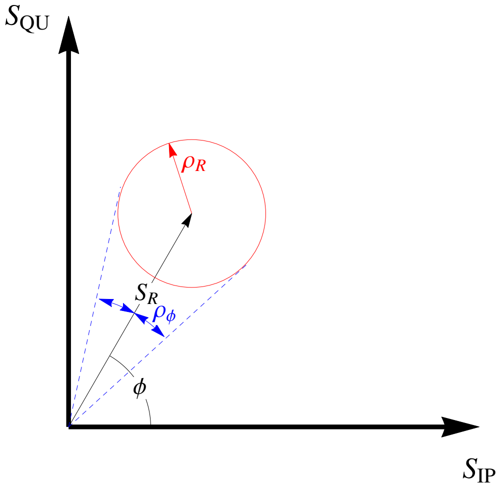

Fig. 4. Phasor plot of a signal with amplitude S_R and phase ϕ affected by Gaussian amplitude noise. The noise densities on the in-phase (S_{IP}) and quadrature (S_{QU}) components are statistically independent and of equal magnitude. They can thus be visualized by a circle, and it follows that $\rho_R=\sqrt{\rho_{IP}^2+\rho_{QU}^2}$. The root power spectral density of the corresponding phase noise $\rho_\phi=\rho_R/S_R$ follows from simple geometrical considerations.

$$SNDR_B=\frac{b_{\mathrm{He}}}{\rho_{\mathrm{B}}}=\frac{\delta\phi}{\rho_\phi}=SNDR_\phi. \tag{15}$$

A different situation occurs with PSN-produced signal fluctuations. This case is particularly interesting since it is often encountered with magnetically well shielded experimental conditions where the PSN is by far the dominant noise process of the measurement. Starting from equation (14) we can calculate the impact of the PSN on the phase signal. We first consider that the photodiode current is converted to a voltage signal by a transimpedance amplifier (TA) with frequency dependent gain $g_{V/A}(f)$. Since the lock-in amplifier in the subsequent step of the processing chain extracts only the signal close to the reference frequency $\omega_{\mathrm{rf}}\approx\omega_{\mathrm{L,Cs}}$, and assuming again that the noise is mainly caused by the fluctuating DC component of the photocurrent we can approximate the voltage noise spectral density after the TA as:

$$\rho_{\mathrm{V,PSN}}=\rho_{\mathrm{I,PSN}}g_{V/A}(\omega_{\mathrm{L,Cs}})=\rho_{\mathrm{I,PSN}}g_{\mathrm{AC}}. \tag{16}$$

Here we have defined $g_{V/A}(\omega_{\mathrm{L,Cs}})=g_{\mathrm{AC}}=2.53\times10^7$ V/A as the AC gain of the TA at the Cs Larmor frequency. The PSN will thus translate into noise of the in-phase and quadrature components of the lock-in detection process, so that the resulting effect on the phase signal can be deduced from Figure 4 to be given by:

$$\rho_{\phi,PSN}=\frac{\rho_{\mathrm{V,PSN}}}{S_R}, \tag{17}$$

where $S_R = \sqrt{S_{IP}^2 + S_{QU}^2}$ is the (detuning-dependent) amplitude of the lock-in signal. One can define a noise equivalent magnetic field NEM, i.e., the magnetic field fluctuation that leads to a signal noise identical to the PSN, by scaling the phase noise to magnetic field units. Using equation (10) one finds

$$NEM = \rho_{B,PSN} = \frac{\rho_{\phi,PSN}\,\Gamma_2}{\gamma_{\mathrm{Cs}}} = \frac{\rho_{\mathrm{I,PSN}}\,g_{\mathrm{AC}}\,\Gamma_2}{S_R\,\gamma_{\mathrm{Cs}}}. \qquad (18)$$

We now discuss the implications for the SNDR assuming a ^{3}He-FSP signal b_{He} which is detected by a CsOPM in the shotnoise limit. Due to the filtering processes introduced above, the CsOPM will effectively detect a smaller oscillation amplitude

$$b'_{\mathrm{He}} = T_{\mathrm{tot}}(\omega_{\mathrm{L,He}})\,b_{\mathrm{He}}. \qquad (19)$$

The NEM, on the other hand, is only subject to the LIA filter, so that

$$\rho'_{B,PSN} = \rho_{B,PSN} T_{\mathrm{LIA}}. \qquad (20)$$

Combining the last two equations we find for the effective SNDR

$$SNDR' = \frac{b'_{\mathrm{He}}}{\rho'_{B,PSN}} = \frac{T_{Cs}(f_{\mathrm{He}})\,T_{LIA}(f_{\mathrm{He}})\,b_{\mathrm{He}}}{T_{LIA}(f_{\mathrm{He}})\,\rho_{B,PSN}} \qquad (21)$$

$$= \frac{a_{Cs}\,\gamma_{Cs}\,b_{\mathrm{He}}}{\rho_{V,PSN}\sqrt{\Gamma_2^2 + \omega_{\mathrm{He}}^2}}, \qquad (22)$$

where we used equations (9) and (18) in the last line. The important conclusion of equation (22) is that in the shotnoise limit the SNDR depends on the linewidth of the CsOPM and the frequency of the signal to be measured.

The considerations presented so far were restricted to a CsOPM with a zero permanent detuning. We will now address the case $\delta\omega' \neq 0$. Equation (13) describes the dependence of the phase response to magnetic perturbations in that case. If we consider again a situation in which the dominant measurement noise is the PSN, we find that – due to the reduced value of S_R – the resulting phase noise of the detuned magnetometer will be larger than the corresponding noise in the $\delta\omega = 0$ case. Replacing S_R by $a'_{Cs}(\delta\omega')$ in equation (17) we can relate the phase noise of the detuned CsOPM to the PSN, and the ratio of the noise densities for both cases is found to be

$$\epsilon_\rho(\delta\omega) = \frac{\rho'_\phi}{\rho_\phi} = \frac{a_{Cs}(\delta\omega = 0)}{a'_{Cs}(\delta\omega')}. \qquad (23)$$

The effect of the permanent detuning can thus be expressed by the factor

$$c(Cs_i) = \frac{\epsilon_\phi(Cs_i)}{\epsilon_\rho(Cs_i)} \qquad (24)$$

for each individual CsOPM. Figure 5 shows a plot of this factor for a CsOPM under real measurement conditions. It can be seen that the effect stays negligibly small for small detunings but becomes considerable when the detuning approaches the linewidth of the CsOPM.

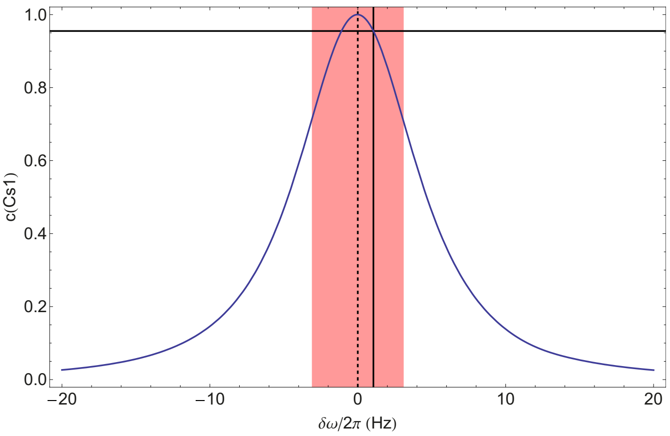

Fig. 5. Plot of $c(Cs_1) = \epsilon_\phi(Cs_1)/\epsilon_\rho(Cs_)$. The values were obtained as described in the text. The shaded red vertical band illustrates the linewidth $\Gamma_2/2\pi = 6.1$ Hz of this magnetometer. The solid vertical line denotes the actual detuning $\delta\omega'/2\pi = 1.06$ Hz of the CsOPM during operation, leading to a sensitivity reduction by $c = 0.96$ as indicated by the horizontal line.

Finally, we combine the effects of bandwidth limitation and permanent detuning to derive the following expression for the detection SNDR

$$\mathrm{SNDR}'' = \mathrm{SNDR}'\frac{\epsilon_\rho}{\epsilon_\phi} = \frac{a_{Cs}\,b_{\mathrm{He}}\gamma_{Cs}}{\rho_{V,PSN}\sqrt{\Gamma_2^2 + \omega_{\mathrm{He}}^2}}\frac{\epsilon_\rho}{\epsilon_\phi}. \qquad (25)$$

6 Sensitivity of the combined magnetometer

Using the results derived above we are now able to predict the sensitivity of a ^{3}He/Cs magnetometer consisting of a ^{3}He cell and a single CsOPM. The precision with which the magnetic field can be determined depends on the precision with which the average frequency of the ^{3}He FSP can be measured in a given integration time T_M. Information theory sets a fundamental limit to this precision, the so called Cramér-Rao lower bound (CRLB) [12,13], which states that the variance of frequency estimation from a discrete-sample signal [14] is bound to obey

$$\sigma_{\mathrm{f}}^2 \geq \frac{6}{(2\pi)^2\,\mathrm{SNDR}^2\,T_M^3}, \qquad (26)$$

which implies

$$\sigma_{\mathrm{B}}^2 \geq \frac{6}{\mathrm{SNDR}^2\,T_M^3\gamma_{\mathrm{He}}^2}. \qquad (27)$$

for the measurement of the magnetic field.

We note that in general we are dealing with a slightly more complicated situation because the amplitude of the ^{3}He-FSP signal decays over time due to relaxation. This is taken into account by introducing an additional factor $C \geq 1$ in equations (26) and (27) that takes the damping into account [15]. However, under homogeneous magnetic field conditions, the ^{3}He polarization decays very slowly so that for sufficiently short measurement times $T_M \ll \Gamma^{-1}$ the FSP amplitude can be considered constant, so that $C \approx 1$. For the measurements presented in the following section the decay time of ^{3}He was $\Gamma^{-1} \sim 13\,000$ s which allows this simplified treatment for measurement times up to several hundreds of seconds. Following the notation in reference [4], we parametrize the performance of the combined magnetometer by a sensitivity parameter η which absorbs the SNDR dependence of the detection,

$$\eta = \sigma_{\rm B} T_M^{3/2} = \frac{\sqrt{6}}{{\rm SNDR}\,\gamma_{\rm He}}. \qquad (28)$$

Evaluating this expression for the effective SNDR of each individual CsOPM yields a corresponding (sensor-specific) sensitivity parameter.

As a last step we assume the effects of a partially polarized ^{3}He sample, or an imperfect $\pi/2$ spin-flip. Both imperfections lead to a decrease of the FSP amplitude according to

$$b_{\rm eff} = p\,\sin(\theta_{\rm flip})\,b_{\rm max,He} = p_{\rm eff}\,b_{\rm max,He} \qquad (29)$$

where we have introduced an effective polarization $p_{\rm eff} \leq 1$. Merging the results of equations (25), (28) and (29) we find

$$\eta_B^{theor} = \frac{\sqrt{6}\,\rho_{V,PSN}\,\sqrt{\Gamma_2^2 + \omega_{\rm He}^2}\,(\Gamma_2^2 + \delta\omega'^2)}{a'_{Cs}(\delta\omega')\,\Gamma_2^2\,p_{\rm eff}\,b_{\rm max,He}\,\gamma_{\rm He}\,\gamma_{Cs}}. \qquad (30)$$

7 CsOPMs driven in PS mode

As we have seen, the FF-mode of operation, although very convenient and transparent, introduces a severe bandwidth limitation. This degrades the performance of the combined magnetometer at high fields in conditions where the PSN is the dominant noise source. In the PS-mode the measurement bandwidth is defined by the characteristics of the feedback loop [11]. In this mode of operation much higher bandwidths can be achieved which will lead to increased amplitudes of the ^{3}He oscillation in the measurement signal. The question arises if this goes hand in hand with an increase of SNDR and thus improved sensitivities can be expected in this mode of operation.

Let us assume a constant magnetic field B_0 and loop adjusted such that the CsOPM's phase is $\phi = 0$ on resonance $\omega_{\rm rf} = \omega_{\rm L,Cs} = \gamma_{\rm Cs} B_0$. A change of the magnetic field δB leads to a change of the CsOPMs phase $\delta\phi = \frac{\delta B \gamma_{\rm Cs}}{\Gamma_2}$ (in the absence of any bandwidth limitations). The loop reacts to this phase change by an adjustment of the loop frequency $\delta\omega_{\rm PS}$ thereby minimizing the error signal

$$\delta\phi_{\rm PS} = \delta\phi - \frac{\delta\omega_{\rm PS}}{\Gamma_2}. \qquad (31)$$

In case of the ^{3}He FSP detection we deal with a periodic magnetic perturbation at frequency f. The minimization will only work properly if the feedback loop's bandwidth $f_{\rm BW}$ is larger than the oscillation frequency $f_{\rm BW} \gg f$. Even at sufficient bandwidth, a finite phase error (error signal) $\delta\phi_{\rm PS}$ is maintained the magnitude of which depends on the gain characteristics of the loop via

$$\delta\omega_{\rm PS} = \delta\phi_{\rm PS}\kappa(f), \qquad (32)$$

where $\kappa(f)$ is a gain factor at the oscillation frequency f. From equation (31) we see that for a properly working feedback loop the full magnetic oscillation amplitude is given by:

$$\delta B = \frac{\Gamma_2 \delta\phi_{\rm PS} + \delta\omega_{\rm PS}}{\gamma_{\rm Cs}}. \qquad (33)$$

Combining this with equation (32), we obtain

$$\delta B = \frac{\delta\omega_{\rm PS}}{\gamma_{\rm Cs}}\left(\frac{\Gamma_2}{\kappa(f)} + 1\right). \qquad (34)$$

To investigate the achievable SNDR in the PS mode we again have to make a separate case for the PSN which causes fluctuations of the CsOPM's phase signal that are not related to magnetic field fluctuations. The feedback loop will equally react to these fluctuations by adjustments of the drive frequency $\omega_{\rm rf} = \widetilde{\omega}_{\rm PS}$ thereby actually detuning the CsOPM from resonance, $\widetilde{\omega}_{\rm PS} \neq \omega_{\rm L,Cs}$. As a result the response of the magnetometer to these adjustments of the drive frequency becomes again bandwidth limited by the lifetime of the Cs polarization. We can express this detuning in magnetic units by a relation similar to equation (33),

$$\delta\widetilde{B} = \frac{\Gamma_2 \delta\phi_{\rm PS} + T_{\rm Cs}(f)\delta\widetilde{\omega}_{\rm PS}}{\gamma_{\rm Cs}} = \frac{\delta\widetilde{\omega}_{\rm PS}}{\gamma_{\rm Cs}}\left(\frac{\Gamma_2}{\kappa(f)} + T_{\rm Cs}(f)\right), \qquad (35)$$

where in the last step equation (32) was used. We assume now a measurement signal originating from an oscillating magnetic field, e.g., the ^{3}He FSP $\delta B = b_{\rm He}$ and signal noise being caused by PSN $\delta\widetilde{B} = \rho_{\rm B,PSN} = {\rm NEM}$. The SNDR of the loop frequency signal can be written as

$$\begin{aligned} {\rm SNDR}_{\rm PS} &= \frac{\delta\omega_{\rm PS}}{\delta\widetilde{\omega}_{\rm PS}} = \frac{\delta B}{\delta\widetilde{B}}\,\frac{T_{\rm Cs}(f) + \Gamma_2/\kappa(f)}{1 + \Gamma_2/\kappa(f)} & (36)\\ &= \frac{b_{\rm He}}{\rho_{\rm B,PSN}} \times \frac{T_{\rm Cs}(f) + \Gamma_2/\kappa(f)}{1 + \Gamma_2/\kappa(f)}. & (37)\end{aligned}$$

Inspection of equation (37) in the high gain limit $(\kappa\,(f) \gg \Gamma_2)$ shows that the maximum achievable SNDR is

$$\lim_{\kappa\to\infty} {\rm SNDR}_{\rm PS} = \frac{b_{\rm He}}{\rho_{\rm B,PSN}} T_{\rm Cs}(f), \qquad (38)$$

which is equal to the SNDR for a CsOPM with zero permanent detuning driven in FF-mode derived in equation (21). The frequency dependence of the SNDR in both modes of operation is thus identical.

Finally we visualize the frequency dependence of the sensitivity (for both modes of CsOPM operation) by a plot of η as a function of the signal frequency. We assume a CsOPM with given linewidth and NEM driven at

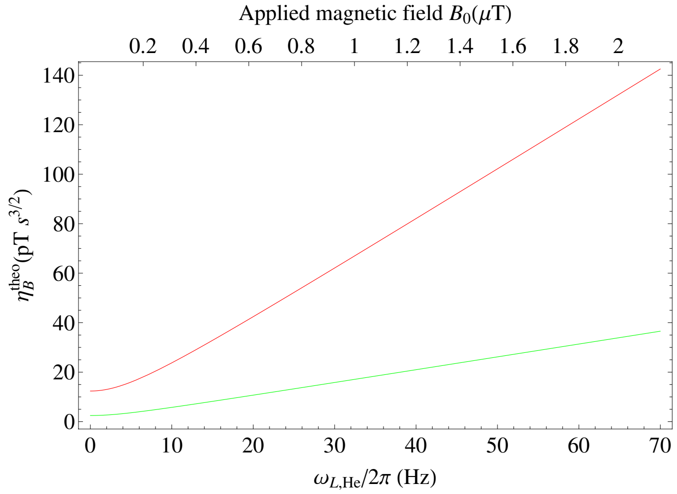

Fig. 6. Dependence of the magnetometric sensitivity on the frequency of the FSP signal, e.g., the magnitude of the holding field. The upper (red) curve corresponds to parameters obtained for Cs1 during the measurements presented here. The lower curve assumes the parameters of the best Cs cell reported in reference [6] ($\Gamma_2/2\pi = 4.75$ Hz, NEM $= 7$ fT/$\sqrt{\text{Hz}}$). Both cases assume $|B_{\text{He}}^{(\text{max})}| = 34$ pT$_{\text{rms}}$, see text for details.

zero permanent detuning. We further assume a 100% polarized cell and ideal spin flip, meaning a maximal FSP amplitude $\left|B_{\text{He}}^{(\text{max})}\right| = 34$ pT$_{\text{rms}}$ (cf. Sect. 3). Under these assumptions equation (30) reduces to

$$\eta_B^{theo} = \text{NEM}\frac{\sqrt{6}\sqrt{\Gamma_2^2 + \omega_{L,\text{He}}^2}}{\gamma_{\text{He}}\Gamma_2\left|B_{\text{He}}^{(\text{max})}\right|}. \tag{39}$$

A plot of this function for two different Cs cells is shown in Figure 6, see figure caption for details.

8 Measurements

We have checked the validity of equation (30) by comparing the predicted sensitivity parameters to experimental values. The experimental sensitivity parameters were obtained by recording simultaneously the phase signals of all CsOPMs detecting the ^{3}He-FSP. The CsOPMs were driven in the FF-mode of operation at a common frequency chosen to have good overlap with the magnetic resonances in all individual sensors. In an offline analysis, a sinusoidal function

$$s(t) = a_0 + a\cos(\omega_{\text{L,He}}t - \phi_0) \tag{40}$$

was fit to the data in order to extract the FSP frequency $\omega_{\text{L,He}}$. The Allan standard deviations (ASD) [16] of the resulting seven frequency estimates (the signals from one of the sensors could not be used because of DAQ problems) are shown in Figure 7. As expected for a CRLB limited estimation process they exhibit the characteristic $T_M^{-3/2}$ dependence for short integration times $T_M < 100$ s while for longer times the ASD grows due to instabilities of the magnetic field. A function

$$ASD = \eta_B^{meas}T_M^{-3/2} \tag{41}$$

was fit to the CRLB limited part of the data shown in Figure 7 to extract the experimental sensitivity parameter η_B^{meas}, the fitted function is shown for the lowest-lying curve. The results of these fits are summarized in Table 1 together with the theoretically predicted values derived by equation (30). The effective polarization which enters in the calculations of the η_B^{theo} was calculated from independent measurements of p and θ_{flip}. Details of the θ_{flip} measurement can be found in reference [8] and will be published in a later paper. The flipping angle was found to be $\theta_{\text{flip}} = 68.0(6)^\circ$. The determination of the spin polarization has to be taken with some caution since it is based on comparing the measured FSP amplitudes to theoretical expectations. This requires a precise knowledge of the pressure and size of the sample cell. The amplitudes may also be affected by mechanical imperfections such as slightly different distances of the CsOPMs from the ^{3}He cell due to imperfect sphericity. The calculation assumes furthermore the validity of the bandwidth- and detuning-dependent CsOPM responses presented in Sections 4.2 and 4.1. The procedure yields $p = 0.71(6)$ where the large error is caused by the mechanical imperfections mainly. This is also the major cause for the rather large error on η_B^{theo} in Table 1.

An additional systematic uncertainty is connected to the measurement of the PSN through I_{DC}. Although this was done rather shortly before the measurements which went into the analysis of the sensitivity, it can not be excluded that the actual light power of each sensor was

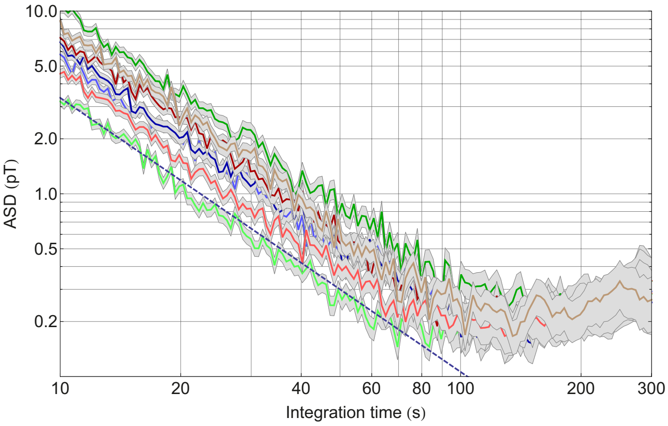

Fig. 7. ASDs of seven CsOPMs simultaneously detecting the ^{3}He-FSP. The gray regions around the curves represent the 1σ confidence band. The relative vertical position of the individual curves depends on the individual SNDR. For short integration times the characteristic $T_M^{-3/2}$ dependence for a CRLB-limited estimation is visible. For longer times the ASD becomes limited by the stability of the applied magnetic field. For the lowest curve the fit by equation (41) is also shown.

Table 1. Measured and predicted sensitivity parameters η_B for different CsOPMs. The sensor Cs7 suffered from a DAQ problem and produced no reliable signals. The large errors on the predicted values are due to the uncertainty of the degree of polarization. Note that Cs2 and Cs7 were handled by a different DAQ system and are thus not directly comparable.

CsOPM	$\eta_B^{theo}(\mathrm{pT}\cdot\mathrm{s}^{3/2})$	$\eta_B^{meas}(\mathrm{pT}\cdot\mathrm{s}^{3/2})$
Cs1	118(11)	106(1)
Cs8	313(28)	324(2)
Cs4	161(15)	175(1)
Cs5	196(18)	196(2)
Cs6	241(22)	226(2)
Cs3	156(14)	147(1)
Cs2	181(17)	258(2)
Cs7	254(23)	–

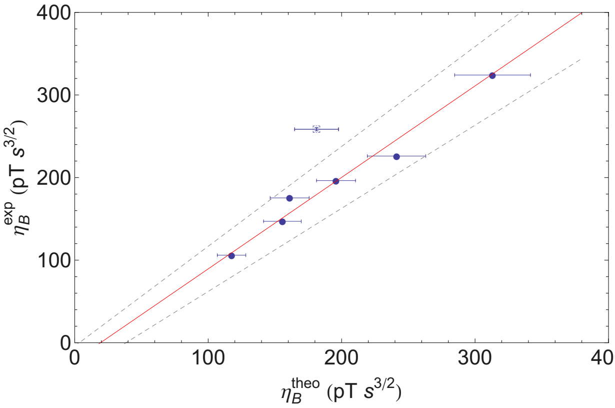

Fig. 8. Measured versus predicted sensitivity parameters. The dependence is given by $\eta_B^{meas} = 1.11(10)\eta_B^{theo} - 21.4(17.3)$ pT s$^{3/2}$. The vertical errors are too small to be visible. The data point depicted by the open square belongs to Cs2. Since this CsOPM was handled on a different DAQ system, this point was not included in the analysis.

slightly different during data taking due to a drift of the laser output power.

The predicted and measured sensitivities are plotted against each other in Figure 8. A linear regression was performed to extract the dependence. It can be seen that the predictions agree with the measured values within the uncertainties of the measurement. We thus conclude that equation (30) adequately describes the sensitivity in the FF-mode of operation and that our measurements were indeed shotnoise- and CRLB-limited since equation (30) predicts the sensitivity under these assumptions.

9 Implications for the n2EDM experiment

As discussed in reference [4] and elsewhere [17] the current design of the n2EDM experiment foresees two large, flat cylindrical ^{3}He magnetometer cells installed symmetrically above and below the cylindrical neutron precession chambers. In the experiment a homogeneous magnetic field $B_0 \approx 1$ μT will be applied along the cylinder axis $\hat{z}$. Based on our studies we can estimate the achievable sensitivity of a ^{3}He/Cs magnetometer in the n2EDM experiment at PSI. Since design details are still under discussion, we make some reasonable assumptions about a likely geometry. For safety reasons the ^{3}He cells have to withstand the large forces that may arise in case the magnetometer is to be operated in atmospheric pressure. We chose a cylindrical cell of 60 mm inner height and 250 mm radius filled with 100% polarized ^{3}He gas at 1 mbar for the example in Figure 9. The cells will be made from borosilicate glass and consist of a ring of radial width 25 mm and height 60 mm and two lid plates of thickness 15 mm. Figure 9 visualizes the results of a simulation in terms of a contour plot of the ^{3}He FSP amplitude in the $\hat{x}$-$\hat{z}$ plane (the ^{3}He magnetization is precessing in the $\hat{x}$-$\hat{y}$ plane). It can be seen that in this geometry a maximum ^{3}He FSP amplitude of $B_{\mathrm{He}}^{\mathrm{max,n2EDM}} = 39$ pT$_{\mathrm{rms}}$ can be expected which compares well to the $B_{\mathrm{He}}^{\mathrm{max,proto}} = 34$ pT$_{\mathrm{rms}}$ found for the prototype magnetometer. We can thus estimate the ultimate achievable magnetometric sensitivity per CsOPM in the n2EDM experiment by scaling the values from Figure 6 by $B_{\mathrm{He}}^{\mathrm{max,proto}}/B_{\mathrm{He}}^{\mathrm{max,n2EDM}} \approx 0.87$. Considering typical neutron storage times used in the current nEDM experiment this translates into a statistical measurement uncertainty of $\Delta B \approx 16$ fT in 100 s ($\Delta B \approx 6$ fT @ 200 s) measurement time per CsOPM. Because of the large size of the ^{3}He cell a large number ($N_{\mathrm{Cs}} > 25$) of readout CsOPMs can be envisioned. The error of the simultaneous measurement of the ^{3}He Larmor Frequency by all these CsOPMs will scale as $N_{\mathrm{Cs}}^{-1/2}$ as was shown in reference [4].

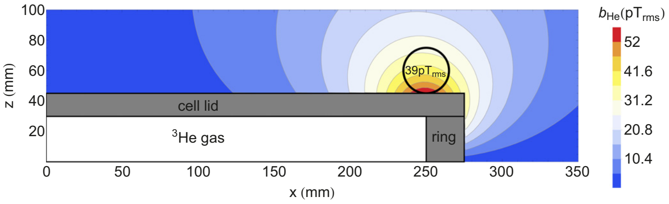

Fig. 9. Simulation of the ^{3}He FSP amplitude for a possible n2EDM geometry as a function of the CsOPM position, only one quadrant is shown. A cylindrical ^{3}He cell of inner height 60 mm and radius 250 mm filled with 100 % polarized gas at 1 mbar was assumed. The cell walls are denoted by the filled gray region, the black circle identifies the optimal position for a CsOPM.

In addition, the magnetic field readings of the two ^{3}He magnetometer cells will yield information about magnetic field gradients which represent a major cause of systematic errors in the nEDM measurement [18]. While the measurement of longitudinal gradients $\partial B_0/\partial z$ is straightforward, the combined magnetometer will also give a potential access to transverse gradients $\partial B_0/\partial r$. The ^{3}He will be nuclear spin polarized and filled into the cells by a dedicated external compressor unit [19]. Since this technique allows to fill the ^{3}He cells at different pressures, the magnetometer can be operated in different dynamic regimes. Exploiting the pressure- and gradient-dependence of the volume averaged Larmor frequency change $\varDelta\varOmega_0$ investigated by Cates et al. [20],

$$\varDelta\varOmega_0 \approx \frac{R_{cell}^2}{10\varOmega_0}\left(|\boldsymbol{\nabla}\varOmega_{1,x}|^2+|\boldsymbol{\nabla}\varOmega_{1,y}|^2\right) \qquad (42)$$

may open ways to infer these gradients[1].

10 Conclusion

We have performed an extensive study of the sensitivity of a combined ^{3}He/Cs magnetometer. We analyzed the performance of two different CsOPM modes of operation and found them to be identical in terms of magnetometric sensitivity. We have presented an expression which permits to predict the achievable sensitivity as a function of the signal frequency. The calculation is based on experimentally accessible parameters and thus provides a useful tool to judge the actual performance of a magnetometer system. The predictions were compared to measurements and an excellent agreement was found. Our results suggest that a deeper study of the laser power dependent effects in the ODMR process (power broadening of the magnetic resonance) might bring interesting insights, potentially leading to a selection criterion for Cs cells to be used in this application. The investigations of the PS-mode of operation suggest that a more elaborate driving scheme for the CsOPMs might lead to significantly improved sensitivity. We have estimated the expected sensitivity for the n2EDM geometry and found it to be compatible with the values reported in our experiments. Possible techniques to measure magnetic field gradients, which are a major source of systematic error in the n2EDM experiment, were discussed.

An additional option which is currently discussed is the installation of several small ^{3}He/Cs magnetometers inside the n2EDM apparatus. These magnetometers could be similar in design to the prototype described here and would yield measurements of the magnetic field at their respective position which could also be used to infer magnetic field gradients.

Author contribution statement

This work was made possible by the excellent support from the mechanical workshops of the Physics Department at the University of Fribourg and the University of Mainz. This work received financial support by grants from the Deutsche Forschungsgemeinschaft (HE2308/14-1) and the Swiss National Science Foundation (200020_140421). The studies presented in this paper are part of the Ph.D. thesis of H.-C. Koch who was leading all aspects of the investigations. The other authors contributed to particular subtasks as follows:

- A. Weis, Z.D. Grujić, P. Knowles, M. Kasprzak and W. Heil were involved in the conceptual planing and construction of the device and in the development of data acquisition methods.
- Z.D. Grujić, P.Knowles, G. Bison, A. Schnabel and J. Voigt contributed to the data taking at PTB.
- A. Weis, Z.D. Grujić, G. Bison and W. Heil participated in the data analysis and the discussion of the results.
- A. Kraft, A. Pazgalev, Z.D. Grujić, P.Knowles and M. Kasprzak contributed to important precursor measurements at Johannes Gutenberg University Mainz.

References

1. C.A. Baker, G. Ban, K. Bodek, M. Burghoff, Z. Chowdhuri, M. Daum, M. Fertl, B. Franke, P. Geltenbort, K. Green, M.G.D. van der Grinten, E. Gutsmiedl, P.G. Harris, R. Henneck, P. Iaydjiev, S.N. Ivanov, N. Khomutov, M. Kasprzak, K. Kirch, S. Kistryn, S. Knappe-Güneberg, A. Knecht, P. Knowles, A. Kozela, B. Lauss, T. Lefort, Y. Lemière, O. Naviliat-Cuncic, J.M. Pendlebury, E. Pierre, F. M. Piegsa, G. Pignol, G. Quéméner, S. Roccia, P. Schmidt-Wellenburg, D. Shiers, K.F. Smith, A. Schnabel, L. Trahms, A. Weis, J. Zejma, J. Zenner, and G. Zsigmond, Phys. Proc. **17**, 159 (2011), 2nd International Workshop on the Physics of fundamental Symmetries and Interactions – PSI2010.
2. A. Riotto, M. Trodden, Ann. Rev. Nucl. Part. Sci. **49**, 35 (1999)
3. N.F. Ramsey, Phys. Rev. **76**, 996 (1949)
4. H.-C. Koch, G. Bison, Z.D. Grujić, W. Heil, M. Kasprzak, P. Knowles, A. Kraft, A. Pazgalev, A. Schnabel, J. Voigt, A. Weis, Eur. Phys. J. D **69**, 202 (2015)
5. J. Bork, H.D. Hahlbohm, R. Klein, A. Schnabel, in *Biomag2000, Proc. 12th Int. Conf. on Biomagnetism*, edited by J. Nenonen, R.J. Ilmoniemi, T. Katila (Helsinki University of Technology, Espoo, Finland, 2001), pp. 970–973
6. N. Castagna, G. Bison, G. Di Domenico, A. Hofer, P. Knowles, C. Macchione, H. Saudan, A. Weis, Appl. Phys. B **96**, 763 (2009)
7. S. Groeger, G. Bison, J.-L. Schenker, R. Wynands, A. Weis, Eur. Phys. J. D **38**, 239 (2006)
8. H.-C. Koch, Ph.D. thesis, Johannes Gutenberg-Universitaet Mainz (2015)
9. P. Knowles, G. Bison, N. Castagna, A. Hofer, A. Mtchedlishvili, A. Pazgalev, A. Weis, Nucl. Inst. Meth. A **611**, 306 (2009)
10. G. Bison, R. Wynands, A. Weis, Appl. Phys. B **76**, 325 (2003)
11. G. Bison, R. Wynands, A. Weis, J. Opt. Soc. Am. B **22**, 77 (2005)
12. R.C. Rao, Bull. Calcutta Math. Soc. **37**, 81 (1945)
13. H. Cramér, *Mathematical methods of statistics* (Princeton University Press, 1946)
14. D.C. Rife, R.R. Boorstyn, IEEE Trans. Inf. Theory **20**, 591 (1974)

---

[1] Note that Cates et al. derived equation (42) for a spherical ^{3}He cell assuming only constant magnetic field gradients. See reference [20] for the definition of the variables.

15. C. Gemmel, W. Heil, S. Karpuk, K. Lenz, Ch. Ludwig, Yu. Sobolev, K. Tullney, M. Burghoff, W. Kilian, S. Knappe-Grüneberg, W. Müller, A. Schnabel, F. Seifert, L. Trahms, St. Baeßler, Eur. Phys. J. D **57**, 303 (2010)
16. D.B. Sullivan, D.W. Allan, D.A. Howe, F.L. Walls, *Characterization of clocks and oscillators* (National Institute of Standards and Technology, 1990)
17. I. Altarev, G. Ban, G. Bison, K. Bodek, M. Burghoff, M. Cvijovic, M. Daum, P. Fierlinger, E. Gutsmiedl, G. Hampel, W. Heil, R. Henneck, M. Horras, N. Khomutov, K. Kirch, St. Kistryn, S. Knappe-Grneberg, A. Knecht, P. Knowles, A. Kozela, J.V. Kratz, F. Kuchler, M. Kuniak, T. Lauer, B. Lauss, T. Lefort, A. Mtchedlishvili, O. Naviliat-Cuncic, S. Paul, A.S. Pazgalev, G. Petzoldt, E. Pierre, C. Plonka-Spehr, G. Qumner, D. Rebreyend, S. Roccia, G. Rogel, T. Sander-Thoemmes, A. Schnabel, N. Severijns, Yu. Sobolev, R. Stoepler, L. Trahms, A. Weis, N. Wiehl, J. Zejma, G. Zsigmond, Nucl. Instrum. Methods A **611**, 133 (2009)
18. S. Afach, C.A. Baker, G. Ban, G. Bison, K. Bodek, Z. Chowdhuri, M. Daum, M. Fertl, B. Franke, P. Geltenbort, K. Green, M.G.D. van der Grinten, Z. Grujic, P.G. Harris, W. Heil, V. Hélaine, R. Henneck, M. Horras, P. Iaydjiev, S.N. Ivanov, M. Kasprzak, Y. Kermaïdic, K. Kirch, P. Knowles, H.-C. Koch, S. Komposch, A. Kozela, J. Krempel, B. Lauss, T. Lefort, Y. Lemière, A. Mtchedlishvili, O. Naviliat-Cuncic, J.M. Pendlebury, F.M. Piegsa, G. Pignol, P.N. Prashant, G. Quéméner, D. Rebreyend, D. Ries, S. Roccia, P. Schmidt-Wellenburg, N. Severijns, A. Weis, E. Wursten, G. Wyszynski, J. Zejma, J. Zenner, G. Zsigmond, Eur. Phys. J. D **69**, 225 (2015)
19. A. Kraft, H.-C. Koch, M. Daum, W. Heil, Th. Lauer, D. Neumann, A. Pazgalev, Yu. Sobolev, A. Weis, Eur. Phys. J. Tech. Instrum. **1**, 1 (2014)
20. G.D. Cates, S.R. Schaefer, W. Happer, Phys. Rev. A **37**, 2877 (1988)

Appendix C

Curriculum vitae

Removed following the regulations for privacy protection

References

[AAB+] S. Afach, N. J. Ayres, C. A. Baker, G. Ban, G. Bison, K. Bodek, M. Fertl, B. Franke, P. Geltenbort, K. Green, W. C. Griffith, M. van der Grinten, Z. D. Grujic, P. G. Harris, W. Heil, V. Helaine, P. Iaydjiev, S. N. Ivanov, M. Kasprzak, Y. Kermaidic, K. Kirch, H.-C. Koch, S. Komposch, A. Kozela, J. Krempel, B. Lauss, T. Lefort, Y. Lemiere, M. Musgrave, O. Naviliat-Cunic, J. M. Pendlebury, F. M. Piegsa, G. Pignol, C. Plonka-Spehr, P. N. Prashanth, G. Quemener, M. Rawlik, D. Rebreyend, D. Ries, S. Roccia, D. Rozpedzik, P. Schmidt-Wellenburg, N. Severijns, D. Shiers, J. A. Thorne, A. Weis, E. Wursten, J. Zejma, J. Zenner, and G. Zsigmond. Gravitational Depolarization of Ultracold Neutrons: Comparison with Data. Accepted by Phys. Rev. D.

[ABB+14] S. Afach, C. A. Baker, G. Ban, G. Bison, K. Bodek, M. Burghoff, Z. Chowdhuri, M. Daum, M. Fertl, B. Franke, P. Geltenbort, K. Green, M. G. D. van der Grinten, Z. Grujic, P. G. Harris, W. Heil, V. Hélaine, R. Henneck, M. Horras, P. Iaydjiev, S. N. Ivanov, M. Kasprzak, Y. Kermaidic, K. Kirch, A. Knecht, H.-C. Koch, J. Krempel, M. Kuźniak, B. Lauss, T. Lefort, Y. Lemière, A. Mtchedlishvili, O. Naviliat-Cuncic, J. M. Pendlebury, M. Perkowski, E. Pierre, F. M. Piegsa, G. Pignol, P. N. Prashanth, G. Quéméner, D. Rebreyend, D. Ries, S. Roccia, P. Schmidt-Wellenburg, A. Schnabel, N. Severijns, D. Shiers, K. F. Smith, J. Voigt, A. Weis, G. Wyszynski, J. Zejma, J. Zenner, and G. Zsigmond. A measurement of the neutron to ^{199}Hg magnetic moment ratio. *Physics Letters B*, 739(0):128 – 132, 2014.

[ABB+15a] S. Afach, C. A. Baker, G. Ban, G. Bison, K. Bodek, Z. Chowdhuri, M. Daum, M. Fertl, B. Franke, P. Geltenbort, K. Green, M. G. D. van der Grinten, Z. Grujic, P. G. Harris, W. Heil, V. Hélaine, R. Henneck, M. Horras, P. Iaydjiev, S. N. Ivanov, M. Kasprzak, Y. Kermaïdic, K. Kirch, P. Knowles, H.-C. Koch, S. Komposch, A. Kozela, J. Krempel, B. Lauss, T. Lefort, Y. Lemière, A. Mtchedlishvili, O. Naviliat-Cuncic, J. M. Pendlebury, F. M. Piegsa, G. Pignol, P. N. Prashant, G. Quéméner, D. Rebreyend, D. Ries, S. Roccia, P. Schmidt-Wellenburg, N. Severijns, A. Weis, E. Wursten, G. Wyszynski, J. Zejma, J. Zenner, and G. Zsigmond. Measurement of a false electric dipole moment signal from 199hg atoms exposed to an inhomogeneous magnetic field. *The European Physical Journal D*, 69(10), 2015.

[ABB+15b] S. Afach, G. Ban, G. Bison, K. Bodek, Z. Chowdhuri, M. Daum, M. Fertl, B. Franke, P. Geltenbort, Z. D. Grujić, L. Hayen, V. Hélaine, R. Henneck, M. Kasprzak, Y. Kermaidic, K. Kirch, S. Komposch, A. Kozela, J. Krempel, B. Lauss, T. Lefort, Y. Lemière, A. Mtchedlishvili, O. Naviliat-Cuncic, F. M. Piegsa, G. Pignol, P. N. Prashanth, G. Quéméner, M. Rawlik, D. Ries, D. Rebreyend, S. Roccia, D. Rozpedzik, P. Schmidt-Wellenburg, N. Severijns, A. Weis, E. Wursten, G. Wyszynski, J. Zejma, and G. Zsigmond. A device for simultaneous spin analysis of ultracold neutrons. *Eur. Phys. J. A*, 51(11):143, 2015.

[ABB+15c] S. Afach, G. Ban, G. Bison, K. Bodek, Z. Chowdhuri, Z. D. Grujić, L. Hayen, V. Hélaine, M. Kasprzak, K. Kirch, P. Knowles, H.-C. Koch, S. Komposch, A. Kozela, J. Krempel, B. Lauss, T. Lefort, Y. Lemière, A. Mtchedlishvili, O. Naviliat-Cuncic, F. M. Piegsa, P. N. Prashanth, G. Quéméner, M. Rawlik, D. Ries, S. Roccia, D. Rozpedzik, P. Schmidt-Wellenburg, N. Severjins, A. Weis,

E. Wursten, G. Wyszynski, J. Zejma, and G. Zsigmond. Highly stable atomic vector magnetometer based on free spin precession. *Opt. Express*, 23(17):22108–22115, Aug 2015.

[AIV77] E. Arimondo, M. Inguscio, and P. Violino. Experimental determinations of the hyperfine structure in the alkali atoms. *Rev. Mod. Phys.*, 49(1):31, 1977.

[AV13] E. B. Alexandrov and A. K. Vershovskiy. Chapter 4.3.2. - m_x magnetometers. In D. Budker and D. J. F. Kimball, editors, *Optical Magnetometry*, pages 75 – 79. Cambridge University Press, 2013.

[Bat11] M. Batz. *Metastability exchange optical pumping in ^{3}He gas up to 30 mT: Efficiency measurements and evidence of laser-induced nuclear relaxation.* PhD thesis, Johannes Gutenberg-Universitaet Mainz, 2011.

[BBB$^+$11] C. A. Baker, G. Ban, K. Bodek, M. Burghoff, Z. Chowdhuri, M. Daum, M. Fertl, B. Franke, P. Geltenbort, K. Green, M. G. D. van der Grinten, E. Gutsmiedl, P. G. Harris, R. Henneck, P. Iaydjiev, S. N. Ivanov, N. Khomutov, M. Kasprzak, K. Kirch, S. Kistryn, S. Knappe-Grüneberg, A. Knecht, P. Knowles, A. Kozela, B. Lauss, T. Lefort, Y. Lemière, O. Naviliat-Cuncic, J. M. Pendlebury, E. Pierre, F. M. Piegsa, G. Pignol, G. Quéméner, S. Roccia, P. Schmidt-Wellenburg, D. Shiers, K. F. Smith, A. Schnabel, L. Trahms, A. Weis, J. Zejma, J. Zenner, and G. Zsigmond. The search for the neutron electric dipole moment at the paul scherrer institute. *Physics Procedia*, 17(0):159 – 167, 2011. 2nd International Workshop on the Physics of fundamental Symmetries and Interactions - PSI2010.

[BBDM13] G. Bevilacqua, V. Biancalana, Y. Dancheva, and L. Moi. Chapter three - Optical atomic magnetometry for ultra-low-field {NMR} detection. volume 78 of *Annual Reports on {NMR} Spectroscopy*, pages 103 – 148. Academic Press, 2013.

[BCC$^+$71] J. A. Barnes, A. R. Chi, L. S. Cutler, D. J. Healey, D. B. Leeson, T. E. McGunigal, J. A. Mullen, W. L. Smith, R. L. Sydnor, R. F. C. Vessot, et al. Characterization of frequency stability. *Instrumentation and Measurement, IEEE transactions on*, 1001(2):105–120, 1971.

[BCV60] M. A. Bouchiat, T. R. Carver, and C. M. Varnum. Nuclear polarization in ^{3}He gas induced by optical pumping and dipolar exchange. *Phys. Rev. Lett.*, 5:373–375, Oct 1960.

[BDG$^+$06] C. A. Baker, D. D. Doyle, P. Geltenbort, K. Green, M. G. D. van der Grinten, P. G. Harris, P. Iaydjiev, S. N. Ivanov, D. J. R. May, J. M. Pendlebury, J. D. Richardson, D. Shiers, and K. F. Smith. Improved experimental limit on the electric dipole moment of the neutron. *Phys. Rev. Lett.*, 97(13):131801, 2006.

[BGK$^+$02] D. Budker, W. Gawlik, D. F. Kimball, S. M. Rochester, V. V. Yashchuk, and A. Weis. Resonant nonlinear magneto-optical effects in atoms. *Rev. Mod. Phys.*, 74(4):1153–1201, November 2002.

[BHK$^+$07] M. Burghoff, S. Hartwig, W. Kilian, A. Vorwerk, and L. Trahms. Squid systems adapted to record nuclear magnetism in low magnetic fields. *Applied Superconductivity, IEEE Transactions on*, 17(2):846–849, 2007.

[BLL74] René Barbé, Michèle Leduc, and Franck Laloë. Résonance magnétique en champ de radiofréquence inhomogène-2 e partie: Vérifications expérimentales; mesure du coefficient de self-diffusion de 3he. *Journal de Physique*, 35(12):935–951, 1974.

[BNL92] N. P. Bigelow, P. J. Nacher, and M. Leduc. Accurate optical measurement of nuclear polarization in optically pumped ^{3}He gas. *Journal de Physique II*, 2(12):2159–2179, 1992.

[BWW03] G. Bison, R. Wynands, and A. Weis. Dynamical mapping of the human cardiomagnetic field with a room-temperature, laser-optical sensor. *Opt. Express*, 11(8):904–909, April 2003.

[Cag60] B. Cagnac. *Orientation nucléaire par pompage optique des isotopes impairs du mercure.* PhD thesis, Université Paris, 1960.

[CBD$^+$09] N. Castagna, G. Bison, G. Domenico, A. Hofer, P. Knowles, C. Macchione, H. Saudan, and A. Weis. A large sample study of spin relaxation and magnetometric sensitivity of paraffin-coated cs vapor cells. *Appl. Phys. B*, 96:763–772, 2009.

[CMN$^+$02] E. Courtade, F. Marion, P. J. Nacher, G. Tastevin, K. Kiersnowski, and T. Dohnalik. Magnetic field effects on the 1083 nm atomic line of helium. *The European Physical Journal D-Atomic, Molecular, Optical and Plasma Physics*, 21(1):25–55, 2002.

[Cra46] H. Cramér. *Mathematical methods of statistics.* Princeton university press, 1946.

[CSH88] G. D. Cates, S. R. Schaefer, and W. Happer. Relaxation of spins due to field inhomogeneities in gaseous samples at low magnetic fields and low pressures. *Phys. Rev. A*, 37:2877–2885, Apr 1988.

[CSW63] F. D. Colegrove, L. D. Schearer, and G. K. Walters. Polarization of ^{3}He gas by optical pumping. *Physical Review*, 132(6):2561, 1963.

[CTDRHL69] C. Cohen-Tannoudji, J. Dupont-Roc, S. Haroche, and F. Laloë. Detection of the static magnetic field produced by the oriented nuclei of optically pumped ^{3}He gas. *Phys. Rev. Lett.*, 22:758–760, 1969.

[CWC$^+$88] G. D. Cates, D. J. White, T. R. Chien, S. R. Schaefer, and W. Happer. Spin relaxation in gases due to inhomogeneous static and oscillating magnetic fields. *Physical Review A*, 38(10):5092, 1988.

[Fer13] M. C. Fertl. *A laser based mercury co-magnetometer for the neutron electric dipole moment search.* PhD thesis, Diss., Eidgenössische Technische Hochschule ETH Zürich, Nr. 21638, 2013, 2013.

[FTW69] W. A. Fitzsimmons, L. L. Tankersley, and G. K. Walters. Nature of surface-induced nuclear-spin relaxation of gaseous ^{3}He. *Phys. Rev.*, 179:156–165, Mar 1969.

[GBS$^+$06] S. Groeger, G. Bison, J.-L. Schenker, R. Wynands, and A. Weis. A high-sensitivity laser-pumped M_x-magnetometer. *Eur. Phys. J. D*, 38(2):239–247, May 2006.

[GHK$^+$10] C. Gemmel, W. Heil, S. Karpuk, K. Lenz, Ch. Ludwig, Yu. Sobolev, K. Tullney, M. Burghoff, W. Kilian, S. Knappe-Grüneberg, W. Müller, A. Schnabel, F. Seifert, L. Trahms, and St. Baeßler. Ultrasensitive magnetometry based on free precession of nuclear spins. *Eur. Phys. J. D*, 57(3):303–320, 2010.

[GKBW15] Z. D. Grujić, P. A. Koss, G. Bison, and A. Weis. A sensitive and accurate atomic magnetometer based on free spin precession. *The European Physical Journal D*, 69(5), 2015.

[GLYO$^+$84] M. B. Gavela, A. Le Yaouanc, L. Oliver, O. Pène, J.-C. Raynal, and T. N. Pham. Contribution of the triangle graphs to the neutron electric dipole moment. *Zeitschrift für Physik C Particles and Fields*, 23(3):251–261, 1984.

[Gmb11] MAGNICON GmbH. Technical notes to CSE-1 extension board, 2011. Online; accessed 10-June-2015.

[GRL91] R. D. Golub, D. J. Richardson, and S. K. Lamoreaux. *Ultra-cold Neutrons.* Adam Hilger, Bristol, Philadelphia, New York, 1991.

[Gro14] Duran Group. Optical properties of Duran. http://www.duran-group.com/en/about-duran/duran-properties/optical-properties-of-duran.html, 2014. Online; accessed 14-November-2014.

[GW13] Z. D. Grujić and A. Weis. Atomic magnetic resonance induced by amplitude-, frequency-, or polarization-modulated light. *Physical Review A*, 88(1):012508, 2013.

[Hap72] W. Happer. Optical pumping. *Rev. Mod. Phys.*, 44(2):169–249, April 1972.

[HGH+10] I. Hilschenz, D. Gutkelch, S. Hartwig, N. Höfner, R. Körber, H. J. Scheer, J. Voigt, M. Burghoff, and L. Trahms. Coil system für low field mri and neuronal current detection. *Biomed Tech*, 55, 2010.

[HGK+13] W. Heil, C. Gemmel, S. Karpuk, Yu. Sobolev, K. Tullney, F. Allmendinger, U. Schmidt, M. Burghoff, W. Kilian, S. Knappe-Grüneberg, A. Schnabel, F. Seifert, and L. Trahms. Spin clocks: Probing fundamental symmetries in nature. *Annalen der Physik*, 525(8-9):539–549, 2013.

[HMP+00] P. G. Harris, D. J. R. May, J. M. Pendlebury, D. Shiers, K. F. Smith, M. van der Grinten, C. A. Baker, K. Green, P. Iaydjiev, S. Ivanov, and P. Geltenbort. The neutron EDM experiment at the ILL. *Nuclear Instruments and Methods in Physics Research Section A: Accelerators, Spectrometers, Detectors and Associated Equipment*, 440(3):479 – 482, 2000.

[Jac62] J. D. Jackson. *Classical electrodynamics*, volume 3. Wiley New York, 1962.

[JDS03] RE Jacob, Bastiaan Driehuys, and Brian Saam. Fundamental mechanisms of ^{3}He relaxation on glass. *Chemical physics letters*, 370(1):261–267, 2003.

[JR76] R. Jackiw and C. Rebbi. Vacuum periodicity in a yang-mills quantum theory. *Phys. Rev. Lett.*, 37:172–175, Jul 1976.

[Kas63] A. Kastler. Displacement of energy levels of atoms by light. *JOSA*, 53(8):902–906, 1963.

[Kay93] S. M. Kay. *Fundamentals of Statistical Signal Processing, Volume I: Estimation Theory.* Prentice-Hall signal processing series. Prentice Hall PTR, Upper Saddle River, New Jersey 07458, 1993.

[KBC+09] P. Knowles, G. Bison, N. Castagna, A. Hofer, A. Mtchedlishvili, A. Pazgalev, and A. Weis. Laser-driven cs magnetometer arrays for magnetic field measurement and control. *Nucl. Inst. Meth. A*, 611(2–3):306–309, 2009. Particle Physics with Slow Neutrons, May 29–31, 2008, Grenoble, France.

[KBG+15a] H-.C. Koch, G. Bison, Z. D. Grujić, W. Heil, M. Kasprzak, P. Knowles, A. Kraft, A. Pazgalev, A. Schnabel, J. Voigt, and A. Weis. Design and performance of an absolute ^{3}He/Cs magnetometer. *Eur. Phys. J. D*, 69(8):202, 2015.

[KBG+15b] H-.C. Koch, G. Bison, Z. D. Grujić, W. Heil, M. Kasprzak, P. Knowles, A. Kraft, A. Pazgalev, A. Schnabel, J. Voigt, and A. Weis. Investigation of the intrinsic sensitivity of a ^{3}He magnetometer. *Eur. Phys. J. D*, 69(11):262, Dec 2015.

[KKD+14] A. Kraft, H.-C. Koch, M. Daum, W. Heil, Th. Lauer, D. Neumann, A. Pazgalev, Yu. Sobolev, and A. Weis. Development of a ^{3}He magnetometer for a neutron electric dipole moment experiment. *EPJ Techniques and Instrumentation*, 1(1):1–15, 2014.

[KM73] M. Kobayashi and T. Maskawa. CP-violation in the renormalizable theory of weak interactions. *Prog.Theor.Phys.*, 49:652, 1973.

[Kra12] A. Kraft. *Aufbau und Inbetriebnahme eines hochsensitiven ^{3}He-Magnetometers fuer ein zukuenftiges Experiment zur Bestimmung eines elektrischen Dipolmoments des freien Neutrons.* PhD thesis, Johannes Gutenberg-Universitaet Mainz, 2012.

[KSD+11] Eiichiro Komatsu, KM Smith, J Dunkley, CL Bennett, B Gold, G Hinshaw, N Jarosik, D Larson, MR Nolta, L Page, et al. Seven-year wilkinson microwave anisotropy probe (wmap) observations: cosmological interpretation. *The Astrophysical Journal Supplement Series*, 192(2):18, 2011.

[Lab00] Ernest O. Lawrence Berkeley National Laboratory. The Berkeley Laboratory Isotopes Project's. http://ie.lbl.gov/education/isotopes.htm, 2000. Online; accessed 28-November-2014.

[Lau10] Th. Lauer. *Investigation of a superthermal ultracold neutron source based on solid deuterium converter for the TRIGA Mainz reactor.* PhD thesis, Johannes Gutenberg-Universitaet Mainz, 2010.

[Len09] K. Lenz. Test eines ^{3}He magnetometers für ein nedm experiment am psi. Diploma thesis, Johannes Gutenberg-Universitaet Mainz, 2009.

[LNTC00] M. Leduc, P. J. Nacher, G. Tastevin, and E. Courtade. Kinetics of helium 3 laser optical pumping. *Hyperfine Interactions*, 127(1-4):443–449, 2000.

[LSB$^+$08] M. P. Ledbetter, I. M. Savukov, D. Budker, V. Shah, S. Knappe, J. Kitching, D. J. Michalak, S. Xu, and A. Pines. Zero-field remote detection of nmr with a microfabricated atomic magnetometer. *Proceedings of the National Academy of Sciences*, 105(7):2286–2290, 2008.

[LZ57] G. Lüders and B. Zumino. Some consequences of TCP-invariance. *Phys. Rev.*, 106:385–386, 1957.

[McG90] D. D. McGregor. Transverse relaxation of spin-polarized ^{3}He gas due to a magnetic field gradient. *Phys. Rev. A*, 41:2631–2635, Mar 1990.

[MTN12] P. J. Mohr, B. N. Taylor, and D. B. Newell. Codata recommended values of the fundamental physical constants: 2010a). *Journal of Physical and Chemical Reference Data*, 41(4):043109, 2012.

[NBC$^+$93] N. R. Newbury, A. S. Barton, G. D. Cates, W. Happer, and H. Middleton. Gaseous ^{3}He-^{3}He magnetic dipolar spin relaxation. *Phys. Rev. A*, 48:4411–4420, Dec 1993.

[NL85] P. J. Nacher and M. Leduc. Optical pumping in ^{3}He with a laser. *Journal de Physique*, 46(12):2057–2073, 1985.

[PFR93] B. W. Petley, J. L. Flowers, and M. G. Richards. A measurement of the nuclear magnetic moment of the helium-3 atom in terms of that of the proton. *Metrologia*, 30:75–87, 1993.

[PHS$^+$04] J. M. Pendlebury, W. Heil, Yu. Sobolev, P. G. Harris, J. D. Richardson, R. J. Baskin, D. D. Doyle, P. Geltenbort, K. Green, M. G. D. van der Grinten, P. S. Iaydjiev, S. N. Ivanov, D. J. R. May, and K. F. Smith. Geometric-phase-induced false electric dipole moment signals for particles in traps. *Phys. Rev. A*, 70(3):032102, 2004.

[PR50] E. M. Purcell and N. F. Ramsey. On the possibility of electric dipole moments for elementary particles and nuclei. *Phys. Rev.*, 78(6):807, June 1950.

[PR05] M. Pospelov and A. Ritz. Electric dipole moments as probes of new physics. *Annals of Physics*, 318(1):119 – 169, 2005. Special Issue.

[Ram49] N. F. Ramsey. A new molecular beam resonance method. *Phys. Rev.*, 76(7):996, October 1949.

[Ram50] N. F. Ramsey. A molecular beam resonance method with separated oscillating fields. *Phys. Rev.*, 78(6):695–699, June 1950.

[Ram55] N. F. Ramsey. Resonance transitions induced by perturbations at two or more different frequencies. *Phys. Rev.*, 100:1191–1194, Nov 1955.

[RB74] D. C. Rife and R. R. Boorstyn. Single-tone parameter estimation from discrete-time observations. *IEEE Trans. Inf. Theory*, 20(5):591–598, 1974.

[RP70] S. D. Rosner and F. M. Pipkin. Hyperfine structure of the 2^3s_1 state of ^{3}He. *Phys. Rev. A*, 1:571–586, Mar 1970.

[RR45] C. Radhakrishna Rao. Information and the accuracy attainable in the estimation of statistical parameters. *Bull. Calcutta Math. Soc.*, 37:81–91, 1945.

[RT99] Antonio Riotto and Mark Trodden. Recent progress in baryogenesis. *Ann. Rev. Nucl. Part. Sci.*, 49(1):35–75, 1999.

[SAHW90] D. B. Sullivan, D. W. Allan, D. A. Howe, and F. L. Walls. *Characterization of clocks and oscillators.* US Department of Commerce, National Institute of Standards and Technology, 1990.

[Sak67] A. D. Sakharov. Violation of CP invariance, C asymmetry and baryon asymmetry of the universe. *Pisma Zh. Eksp. Teor. Fiz.*, 5:32–35, 1967. [JETP Lett., **5**, 24–27, (1967)].

[Sch] A. Schnabel. Personal communication.

[Sch67] L. D. Schearer. Collision-induced mixing in the 2 p 3 levels of helium. *Physical Review*, 160(1):76, 1967.

[SHD91] S. D. Stoller, W. Happer, and F. J. Dyson. Transverse spin relaxation in inhomogeneous magnetic fields. *Phys. Rev. A*, 44:7459–7477, Dec 1991.

[SHM95] B. Saam, W. Happer, and H. Middleton. Nuclear relaxation of ^{3}He in the presence of o_2. *Phys. Rev. A*, 52:862–865, Jul 1995.

[SHO$^+$06] J. Schmiedeskamp, W. Heil, E. W. Otten, R. K. Kremer, A. Simon, and J. Zimmer. Paramagnetic relaxation of spin polarized ^{3}He at bare glass surfaces. *The European Physical Journal D - Atomic, Molecular, Optical and Plasma Physics*, 38(3):427–438, 2006.

[SMB$^+$13] A Saunders, M Makela, Y Bagdasarova, HO Back, J Boissevain, LJ Broussard, TJ Bowles, R Carr, SA Currie, B Filippone, et al. Performance of the los alamos national laboratory spallation-driven solid-deuterium ultra-cold neutron source. *Review of Scientific Instruments*, 84(1):013304, 2013.

[SNS$^+$86] A. Steyerl, H. Nagel, F.-X. Schreiber, K.-A. Steinhauser, R. Gähler, W. Gläser, P. Ageron, J.M. Astruc, W. Drexel, G. Gervais, and W. Mampe. A new source of cold and ultracold neutrons. *Physics Letters A*, 116(7):347 – 352, 1986.

[Tul13] K. Tullney. *Search for a spin-dependent short-range force between nucleons with a ^{3}He, ^{129}Xe clock-comparison experiment.* PhD thesis, Johannes Gutenberg-Universitaet Mainz, 2013.

[Wei07] A. Weis. Polarized light and polarized atoms: Two-level systems and beyond. University Lecture, 2007.

[Wol04] M. Wolf. *Erzeugung höchster ^{3}He Kernspinpolarisation durch metastabiles optisches Pumpen.* PhD thesis, Johannes Gutenberg-Universitaet Mainz, 2004.

[YGK$^+$04] V. V. Yashchuk, J. Granwehr, D. F. Kimball, S. M. Rochester, A. H. Trabesinger, J. T. Urban, D. Budker, and A. Pines. Hyperpolarized xenon nuclear spins detected by optical atomic magnetometry. *Phys. Rev. Lett.*, 93:160801, Oct 2004.

[Zen13] J. Zenner. *The search for the neutron electric dipole moment.* PhD thesis, Johannes Gutenberg-Universitaet Mainz, 2013.

List of Figures

List of acronyms

AC	Alternating current
ASD	Allan standard deviation
BAU	Baryon asymmetry of the universe
$BMSR-2$	Berlin magnetically shielded room - 2
BS	Bloch-Siegert shift
C	Charge conjugation
$C_1 - C_9$	$2^3S \rightarrow 2^3P$ transitions of ^{3}He
$CRLB$	Cramér-Rao lower bound
Cs	Cesium
$CsOPM$	Optically pumped cesium magnetometer
D_1	$6p_{1/2} \rightarrow 6s_{1/2}$ transitions of cesium
DC	Direct current
DAQ	Data acquisition
$ECPU$	External compact ^{3}He polarizer unit
EDM	Electric dipole moment
FC	Fiber coupler
$FF-mode$	Fixed frequency mode
FFT	Fast Fourier transform
$FRAP$	Fribourg atomic physics group
FSP	Free spin precession
$FSP-Cs$	Cesium magnetometer based on free spin precession
ILL	Institute Laue-Langevin
IP	In phase signal component
LIA	Lockin amplifier
$MEOP$	Metastability exchange optical pumping
$nEDM$	Electric dipole moment of the neutron
$n2EDM$	Second generation experiment in search of neutron electric dipole moment at Paul Scherrer Institut
NEM	Noise-equivalent magnetic field

$NEPBW$	Noise-equivalent bower bandwidth
NMR	Nuclear magnetic resonance
$ODMR$	Optically detected magnetic resonance
$oILL$	Current experiment in search of neutron electric dipole moment at Paul Scherrer Institut
P	Parity transformation
PD	Photo diode
PID	Proportional- integral- differential- feedback circuit
$PL-mode$	Phase locked mode
PLL	Phase locked loop
PSD	Power-spectral density
PSI	Paul Scherrer Institute
PTB	Physikalisch-Technische Bundesanstalt Berlin
Q	Quadrature signal component
RBS	Ramsey-Bloch-Siegert shift
rf	Radio frequency
RWA	Rotating wave approximation
SM	Standard model of particle physics
$SNDR$	Signal to noise density ratio
SNR	Signal to noise ratio
$SQUID$	Superconducting quantum interference device
$SQRTPSD$	Square root power-spectral density
$SR-LIA$	Lockin amplifier from Stanford Research Systems
T	Time reversal
UCN	Ultra-cold neutrons
VCO	Voltage controlled oscillator
WGN	White Gaussian noise
$ZI-LIA$	Lockin amplifier from Zurich Instruments

List of symbols

a_{Cs}	Amplitude of CsOPM signal
a'_{Cs}	Amplitude of CsOPM signal detuned from resonance
$\vec{B}$	Magnetic field (general)
$\vec{B}_0$	Homogeneous holding field
$\vec{B}_1(t)$	Oscillating magnetic field
$B_{\uparrow\uparrow,\uparrow\downarrow}$	Magnetic fields in Ramsey experiment
$\vec{B}_{eff}$	Effective field in the rotating frame
$\vec{B}_{He}$	Magnetic field created by ^{3}He magnetization
b_{He}	Amplitude of oscillating magnetic field created by precesing ^{3}He magnetization
$b_{max,He}$	Maximum achievable amplitude of oscillating magnetic field created by precessing ^{3}He magnetization
$B^{(i)}_{Cs}$	Proper field reading of i-th CsOPM
$B^{(i)}_{He/Cs}$	Field reading through measurement of ^{3}He FSP by i-th CsOPM
$B^{(i)}_{He/SQUID}$	Field reading through measurement of ^{3}He FSP by i-th SQUID
$\delta\omega$	Detuning (general)
$\Delta\omega_{RBS}$	Ramsey-Bloch-Siegert shift
$\vec{d}$	Dipole moment (general)
$\vec{d}_n$	Neutron electric dipole moment
$\vec{d}_f$	False electric dipole moment (general)
$\vec{\mathcal{E}}$	Electric field (general)
η^{meas}_B	Sensitivity parameter of combined magnetometer (experimentally determined)
η^{theo}_B	Sensitivity parameter of combined magnetometer (theoretically predicted)
η_{Asym}	Baryon to photon ratio
f_{BW}	Bandwidth of measurement
f_c	-3dB cut-off frequency of low-pass filter
f_{SR}	Sampling rate
γ_{Cs}	Gyromagnetic ratio of Cesium
γ_{He}	Gyromagnetic ratio of ^{3}He
Γ_1	Longitudinal relaxation rate

Γ_2	Transverse relaxation rate
g_{AC}	AC gain of transimpedance amplifier
g_{DC}	DC gain of transimpedance amplifier
g_F	Landé factor
$\hbar$	Reduced Planck constant
I_{DC}	DC-photocurrent
$\vec{k}_{Cs}$	Wave vector of Cesium-D1 resonant pump light
λ	wavelength (general)
μ	Magnetic moment (general)
μ_0	Vacuum permeability
μ_B	Bohr magneton
$\vec{\mu}_n$	Magnetic moment of neutron
$\vec{\mu}_{He}$	Magnetic moment of the ^{3}He nucleus
N_{Cs}	Number of CsOPMs used for simultaneous detection of the ^{3}He FSP
N_{He}	Number of ^{3}He atoms
N_n	Number of neutrons
N_s	Number of samples
p	Polarization (general)
p_{eff}	Effective polarization of ^{3}He
P	Pressure (general)
q	Charge (general)
q_{e^-}	Electron charge
Q	Quality factor of damped oscillator
ρ	Square root power spectral noise density (general)
$\rho_{V,PSN}$	Voltage-square-root power spectral noise density of CsOPM signal caused by photocurrent shotnoise
$\rho_{I,PSN}$	Current-square-root power spectral noise density of CsOPM signal caused by photocurrent shotnoise
ρ_{IP}	Square-root power spectral noise density of demodulated CsOPM in-phase-signal
ρ_{φ}	Square-root power spectral density noise of demodulated CsOPM φ-signal
ρ_R	Square-root power spectral noise density of demodulated CsOPM R-signal
ρ_Q	Square-root power spectral noise density of demodulated CsOPM in-quadrature-signal

ρ_{IP}	Square-root power spectral noise density of demodulated CsOPM in-phase-signal
R_{cell}	Radius of sample cell
$R(\omega t, \hat{x})$	Time dependent rotation matrix
$\rho_{B,CSN}$	Magnetic-square-root power spectral noise density of CsOPM signal caused by coilcurrent shotnoise
$\rho_{B,PSN}$	Magnetic-square-root power spectral noise density of CsOPM signal caused by photocurrent shotnoise
$\rho_{V,PSN}$	Total magnetic-square-root power spectral noise density of CsOPM signal
σ	Square root variance (general)
σ_B	Square root variance of magnetic field estimation
σ_f	Square root variance of frequency estimation
$\vec{\mathscr{S}}$	Bloch vector
$\vec{\mathscr{S}}_{eq}$	Equilibrium state of the Bloch vector
$SNDR$	Signal to noise-density ratio
τ	Time constant (general)
θ_{flip}	Rabi nutation angle
θ_k	Angle between Cesium-D1 resonant pump-light $\vec{k}_{Cs}$ and holding field $\vec{B}_0$
T	Temperature
$T(f)$	Transfer function (general)
$T_{LIA}(f)$	Transfer function of lockin amplifier
$T_{tot}(f)$	Combined transfer function
$T_{Cs}(f)$	Transfer function of CsOPM in FF-mode
T_p	Precession time
T_2^{grad}	Time constant of gradient relaxation
T_M	Measurement time
T^{wall}	Time constant of wall relaxation
T_{SR}	Inverse of sampling rate
T_θ	Rabi flipping time
$\omega_{E,n}$	Electric contribution to neutron precession frequency (in case of an nEDM)
ω_L	Larmor frequency (general)
$\omega_{L,He}$	Larmor frequency of ^{3}He
$\omega_{L,n}$	Larmor frequency of neutrons

$\omega_{L,Cs}$	Larmor frequency of Cesium
ω_{rf}	Frequency of applied rf field
ω_R	Reference frequency in Ramsey experiment
$\omega_{\uparrow\uparrow,\uparrow\downarrow}$	Precession frequency of neutron in Ramsey experiment
ζ	Density operator

Declaration / Erklärung

I hereby declare that i have written this thesis myself without any illicit aid. I have not used any sources other than those cited and appropriately identified all quotations.

Ich versichere hiermit, dass ich die vorliegende Arbeit selbstständig und ohne unerlaubte Hilfe verfasst habe. Ich habe keine anderen als die angegebenen Quellen und Hilfsmittel benutzt sowie Zitate kenntlich gemacht.

Villigen (Schweiz), den 3. Dezember 2015

Hans-Christian Koch

Thanks

Removed following the regulations for privacy protection